# STUDIES ON THIN FILMS OF Zr, ZrN AND ZrAlN PREPARED BY PULSED MAGNETRON SPUTTERING: MICROSTRUCTURES, THERMAL EXPANSION, NANOMECHANICAL AND TRIBOLOGICAL PROPERTIES

*By*

**AKASH SINGH**

(Enrollment No: - ENGG-02 2009 04022)

**Indira Gandhi Centre for Atomic Research, Kalpakkam**

*A thesis submitted to the*
*Board of Studies in Engineering Sciences*
*In partial fulfillment of requirements*
*For the Degree of*

**DOCTOR OF PHILOSOPHY**

*of*

**HOMI BHABHA NATIONAL INSTITUTE**

**January, 2013**

# Homi Bhabha National Institute

## Recommendations of the Viva Voce Board

As members of the Viva Voce Board, we certify that we have read the dissertation prepared by Akash Singh entitled "Studies on Thin Films of Zr, ZrN and Zr-Al-N Prepared by Pulsed Magnetron Sputtering: Microstructures, Thermal Expansion, Nanomechanical and Tribological Properties" and recommend that it may be accepted as fulfilling the dissertation requirement for the degree of Doctor of Philosophy.

..............................................................................Date: 24 Sept. 2013

Chairman: Dr. T. Jayakumar

..............................................................................Date: 24/9/13

Guide/Convener: Dr. P. Kuppusami

M. Vijayalakshmi

..............................................................................Date:

Member 1: Dr. M. Vijayalakshmi

..............................................................................Date:

Member 2: Dr. A. K. Tyagi

..............................................................................Date: 24/9/2013

Examiner:

Final approval and acceptance of this dissertation is contingent upon the candidate's submission of the final copies of the dissertation to HBNI.

I hereby certify that I have read this dissertation prepared under my guidance and recommend that it may be accepted as fulfilling the dissertation requirement.

**Date:** 24/9/13

**Place: Kalpakkam**

**Guide: Dr. P. Kuppusami**

# STATEMENT BY AUTHOR

This dissertation has been submitted in partial fulfillment of requirements for an advanced degree at Homi Bhabha National Institute (HBNI) and is deposited in the Library to be made available to borrowers under rules of the HBNI.

Brief quotations from this dissertation are allowable without special permission, provided that accurate acknowledgement of source is made. Requests for permission for extended quotation from or reproduction of this manuscript in whole or in part may be granted by the Competent Authority of HBNI when in his or her judgment the proposed use of the material is in the interests of scholarship. In all other instances, however, permission must be obtained from the author.

Akash Singh

AKASH SINGH

# DECLARATION

I, hereby declare that the investigations presented in the thesis have been carried out by me. The work is original and has not been submitted earlier as a whole or in part for a degree/diploma at this or any other institution/University.

Akash Singh

AKASH SINGH

Dedicated

to

My Beloved Parents

# ACKNOWLEDGEMENTS

First and foremost I offer my sincere gratitude to my supervisor, Dr. P. Kuppusami, former Head, X-ray Diffraction and Surface Engineering Section and Professor, Homi Bhabha National Institute, who has supported me throughout my thesis with his patience and knowledge. I thank him for his keen interest, constructive suggestion and motivation throughout the course of investigation.

I am grateful to Dr. T. Jayakumar Doctoral Committee Chairman and Director, Metallurgy and Materials Group and members Dr. M. Vijayalakshmi, Associate Director, Physical Metallurgy Group and Dr. A. K. Tyagi, Head, Surface and Nanomaterials Division for their support and evaluation of the progress of my research work and for valuable suggestions at various stages.

I express my sincere gratitude to Shri S. C. Chetal, Director, IGCAR and Dr. Baldev Raj, former Director, IGCAR for their support and permission for perusing higher studies in HBNI.

My sincere thanks to Shri E. Mohandas, Head, MSSCD and Dr. R. Divakar, Head, HRMCS for their constant support, guidance and encouragement during the research work. I would also like to extend my acknowledge to Dr. S. Murugesan for his support.

I thank all of my colleagues and friends in Physical Metallurgy Group for their help and cooperation during the course of this work. I am particularly grateful to Shri R. Thirumurugesan, Smt. M. Jyothi, Ms. Shabana Khan and Ms. Maneesha Mishra for their help and constant support during all the stages of this work. I am also thankful to Shri Arun Kumar Panda for his help during preparation of the thesis.

I am thankful to many of the members of Material Science Group for their help in carrying out various measurements. Special mention must be made to Dr. M. Kamaruaddin, Dr. R. Ramaseshan, Dr. Niranjan Kumar, Shri Sachin Srivastava and Shri Thanigaiarasu.

My special thanks to Shri Chandramohan of WSCD and Dr. Ramya of CSTG for Raman studies, Dr. V. Ganesan, UGC-DAE-CSR, Indore for AFM and Dr. C. Sudha, Ms. T.N.Prasanthi of PMG and Dr. Aloke Paul, IISc Bangalore for helping me in EPMA analysis.

I would like to express my sincere gratitude to my father Shri N. B. Singh and Mother Smt. Indu Singh for their encouragement, affection and love. I am very thankful to my wife Pratibha for her care, understanding and continuous support to complete the thesis. I thank my dear daughter Avanija for providing a cheerful atmosphere at home. And last but not the least, I express my humble regards to all my family members, relatives and friends for their support, and continuous encouragement during my research period.

# ABSTRACT of SYNOPSIS

ZrN based hard coatings are of great interest in a number of technological applications due to their improved tribological, corrosion, mechanical and physical properties . Also, the addition of Al to ZrN has been reported to progressively modify the texture, improve the resistance against oxidation and also increase significantly the hardness of the films. In the present work, a systematic investigation is reported on the structural and nanomechanical properties of thin films of Zr, ZrN and alloyed ZrAlN deposited on (100) Si and D-9 alloy substrates by pulsed DC magnetron sputtering as a function of substrate temperature and nitrogen partial pressure. A study has been undertaken to investigate the thermal stability and thermal expansion behavior of these thin films. Also, the inter- relationship between microstructures, nanomechanical, and tribological properties of these films is investigated.

Formation of α-phase of zirconium with [001] preferred orientation was noticed in the temperature range 300–873 K. It was found that crystallite size increased with increasing temperature. Nanoindentation and microhardness measurements of Zr films showed that the hardness of the films was in the range 6–10 GPa. Scratch test results indicated that the films deposited at higher substrate temperature have better adhesion. High temperature x-ray diffraction showed that Zr films were stable up to 773 K.

The effect of substrate temperature and nitrogen flow rate on the growth characteristics, nanomechanical and tribological properties and phase stability of ZrN films were studied. Only fcc -ZrN was obtained by reactive sputtering at lower flow rates of nitrogen (< 2sccm). At higher flow rates of nitrogen (≥ 2sccm), small amounts of orthorhombic -$Zr_3N_4$ phase was formed along with ZrN. TEM studies also confirmed the presence of ZrN along with small

amount of $Zr_3N_4$ phase at higher nitrogen flow rates. HTXRD study showed that ZrN films were stable up to 1073 K. Nanomechanical properties of ZrN films showed peak values of hardness (H) and elastic modulus (E) for the films deposited at 1-2 sccm flow rate of nitrogen. The effect of nitrogen flow rate on the nanomechnical properties indicated an enhancement in hardness and elastic modulus and showed a peak value for the resistance to plastic deformation ($H^3/E^2$) at lower flow rates of nitrogen. The tribological properties of ZrN thin films were found to be influenced by the deposition temperature and sliding counter bodies.

$Zr_{1-x}Al_xN_y$ films have been studied with the Al concentration range of $0 \leq x \leq 0.36$ Al and it was found that (Zr,Al) N was in solid solution up to 36 at. % of Al. Alloyed films of ZrAlN exhibited a fcc structure. As the Al content was increased up to 36 at.% , lattice parameter decreased due to the substitution of Zr by Al of lower atomic radius. HTXRD results of $Zr_{1-x}Al_xN_y$ thin films indicated that the addition of Al improved the phase stability at higher temperature in comparison with ZrN. The average linear thermal expansion coefficient of $Zr_{1-x}Al_xN_y$ thin films showed increase in the thermal expansion coefficient with increasing Al content up to 28 at.%Al. It was also observed that values of hardness and Young's modulus of the alloyed ZrAlN films were in the range of 9-18 GPa and 235-365 GPa, respectively. Tribological studies of ZrAlN thin film showed that the COF of alloyed films of ZrAlN was lower for the steel ball (100Cr6 steel) than that for the $Al_2O_3$ ball up to 36 at. % of Al. However, no clear trend in the COF was noticed as a function of Al addition. The variations in the nanomechanical and tribological properties have been discussed in relation with the microstructures of these films.

# Contents

# List of Figures

**Figure No.** **Title** **Page No.**

# List of Tables

# Chapter 1

# Introduction

## 1.1 Introduction

Thin films have been used in many types of engineering systems and have been adapted to fulfill some of the following functions:

(i) To protect structural materials in high temperature environments

(ii) To combat friction and wear

(iii) To prepare micro-electro-mechanical systems to serve as sensors or actuators.

Generally the term “thin film” is applied to layers which have thicknesses of the order of few micron or less (1 micron = $10^{-6}$ meters) and may be as thin as a few atomic layers. Often the properties of thin films are affected by the properties of the underlying material (substrate) and can vary through the thickness of the film. Therefore there is a critical thickness for thin films above which the films show properties similar to that of a bulk material. Thin film deposition process is one in which the overlay material is deposited atom-by-atom. The resulting film can range from single crystal to amorphous, fully dense to less than fully dense, pure to impure, and thin to thick. Thin film deposition can be done in vacuum, plasma, gaseous, or electrolytic environment [1].

Thin film is an effective method to improve the durability of the materials used in the aggressive environment. By properly selecting thin film method and materials, it is possible to extend the service life of the substrate material and increase the commercial value of the products [2]. In this chapter general characteristics of nitrides, transition metal nitrides, crystal structure of Zr, ZrN and ZrAlN and their applications are discussed.

## 1.2 General Characteristics of Nitrides

By convention, the term nitride is applied to those compounds that nitrogen forms with elements of lower or about equal electronegativity [3]. The nitrides can be classified in five general categories, based on their electronic structure and bonding characteristics i.e., interstitial, covalent, intermediate, saltlike and molecule forming nitride [4-7]. In the five categories listed above ZrN, alloyed ZrAlN comes under the category of interstitial nitrides. Three general and interrelated atomic characteristics play an essential role in the formation of nitrides: (i) the difference in the electronegativity between the element nitrogen and the other forming nitride, (ii) the size of the respective atoms, and (iii) the electronic bonding characteristics of these atoms.

Interstitial nitrides are crystalline compounds of a host metal and nitrogen where the nitrogen atom occupies specific interstitial sites in the metal structure which is generally close packed. This places a lower limit on the size of the metal atom in order for the nitrogen atom to fit in the available sites of the metal structure. The metals of the nine early-transition elements, i.e. titanium, zirconium and hafnium of Group IV, vanadium, niobium and tantalum of Group V, and chromium, molybdenum and tungsten of Group VI fit the criteria of size and site availability and form intersistitial nitrides [8].

Transition elements qualify as host structures for interistitial nitrides, since the ratio of the radius of the nitrogen atom to the radius of the host metal is less than 0.59. The radii ratio is smallest for the nitrides of Group IV and it is 0.463 for ZrN. There are two types of interstitial sites in the closed-packed structure of transition metals, i.e., the tetrahedral sites and the octahedral sites. The nitrogen atom occupies only the octahedral sites since the tetrahedral sites are too small to accommodate them. There is one octahedral site per atom of the host metal [9].

These metal nitrides exhibit varying composition, usually expressed as $MN_{1-x}$ (M= Metal). This notation shows that the nitrogen content is variable and is the result of incomplete filling of the available sites. The mononitrides (with the exception of WN) have a face centered cubic (fcc) structure where the successive layers follow the sequence ABCABC and the coordination number of the metal atom is 12. The next important nitrides have $M_2N$ composition and these nitrides usually have a hexagonal close-packed (hcp) structure where the atoms of the first layer are directly over those of the third layer. It is expressed as ABAB with hexagonal symmetry with a coordination number of the metal atom of 12. The hcp structure is found in the nitrides of Group V and VI but not in those of Group IV. Another structure is the simple hexagonal structure (hex) such as that of tungsten mononitride where the metal atom layers form a sequence of layers AA or BB. Such structures are not close-packed and do not form octahedral sites. This structure cannot form if the ratio of the nitrogen/metal atomic radii is small, as is the case in the ZrN and HfN [9].

## 1.3 Transition Metal Nitrides

Transition metal nitrides and oxy-nitrides are very attractive compounds because of their excellent mechanical, thermal, electrical and catalytic properties [8]. For example, AlN possesses a high electrical resistivity, a good thermal conductivity and stability up to very high temperatures [10]. These properties make it very interesting material for microelectronic devices. TiN combines characteristics of both covalent compounds, such as extreme hardness and high melting point, and of metallic compounds such as good thermal and electrical conductivity [11, 12]. TiN is extensively used in cutting tools and in semiconductor applications [13]. Concerning catalytic activity of nitrides, molybdenum nitride is known to be active in dehydronitrogenation of pyridine and on the Al-P-O-N oxynitride catalysts [14]. Massinon et al. [15] have shown that the substitution of oxygen by nitrogen during nitridation influences surface properties.

Today, thin films such as ZrN, CrN and HfN, continue to draw attention of tool industry and tools with these coatings are on the market. However, alternative coatings are also manufactured, by deposition of two or more components to enhance both hardness and wear resistance. Recently ZrN coatings have been investigated due to their promising tribological properties. It is reported that mechanical, wear and corrosion properties of ZrN coatings were better than those of TiN coatings. Thus, they have been increasingly used in industry for specific applications such as coatings of tools for machining non-ferrous materials (aluminium or nickel alloys) [16]. Titanium nitride (TiN) can be easily oxidized above 773 K and this may cause the performance degradation of TiN coatings on cutting tools or in diffusion barrier application for microelectronic technology [13].

Recently zirconium nitride (ZrN) has been well recognized due to its lower electrical resistivity (13.6μΩcm at 300 K) and better corrosion resistance among the transition metal nitrides. Additionally, ZrN suggests better thermal chemical stability because of higher negative heat of formation (-87.3 kcal/mol) compared with that of TiN (-80.4 kcal/mol) [17]. ZrN has been considered to be a potential candidate as diffusion barrier in Cu/Si contacts and a metal gate in MOS devices [18]. Since zirconium has a higher melting point, lower vapor pressure, and higher contamination susceptibility by oxygen and carbon, it is more difficult to deposit ZrN film than TiN or CrN films.

Also, ZrN has been extensively studied for industrial applications as hard coatings [19-20], diffusion barrier in semiconductor technology [21-23], optical applications for heat mirrors [24-28] and decorative coatings [29-32] because of their outstanding properties. The optical and mechanical properties of ZrN have been reported to depend on nitrogen composition [33-35]. For instance, the stoichiometric ZrN is metallic-like with a golden color and is a thermodynamically stable phase. $Zr_3N_4$, on the other hand is a metastable phase and is insulating in nature and almost transparent [35]. ZrN is known to be a good reflective material in the IR wavelength range [36] due to the metallic structure of the stoichiometric ZrN. Although nitrides are thermodynamically stable, they are readily oxidized even at room temperature [37-38]. This oxidation or contamination by oxygen can be a major problem, since it completely modifies the properties and reactivities of the solids.

It is also reported that the microstructure and properties of ZrN film vary with different deposition techniques and processing parameters [39-41]. The improvement of a particular film property (e.g. hardness, chemical inertness) of a binary nitride compound MN (e.g. TiN, ZrN, NbN, CrN) can be achieved by addition of a third element X (e.g. Al, B, Cr, Si, Ge) for obtaining a ternary compound [42-52]. Even in small quantity, this third element plays a decisive role in the modification of chemical bonding, structure and morphology of the film. In this type of ternary metallic nitride (M–X–N) thin films, the macroscopic properties (e.g. thermal stability, electrical conductivity, strength or hardness) are influenced by the microscopic properties of the films as morphology, chemical bonding and local composition [53–55]. The formation of a single phase or of a composite multiphase films depends on the chemical reactivity of the M, X and N atoms and on the deposition parameters (substrate temperature, nitrogen partial pressure, atomic fluxes). In the last decades, aluminum based ternary transition metal nitrides, MeAlN and nanocomposites, MeN/SiNx thin films (Me=transition metal) have been reported mainly in the field of protective coatings against wear and hot corrosion at high temperatures. Among the ternary Me–Al–N systems, Ti–Al–N and Cr–Al–N are the most investigated thin films [56-66], while only a few studies have been dedicated to the Zr–Al–N system [67]. Lamni et.al. [68- 69] reported on the electronic and mechanical properties of the Zr–N system as well as on those of Zr–Cr–N and Zr–Al–N systems. Cubic ternary MeAlN nitrides are metastable compounds; therefore thermal annealing or higher working temperatures can produce phase separation into cubic MeN and hexagonal AlN phases which constitute the equilibrium system [70-72].

## 1.4 Zirconium and Zirconium Based Nitrides

### 1.4.1 Crystal structure and application of zirconium

Zirconium is a IV$^{th}$ -group transition element which is widely employed in nuclear reactors. Zirconium has hexagonal closed packed crystal structure with primitive lattice and P63/mmc space group with lattice parameters, $a=3.232$ Å and $c=5.147$ Å (Fig.1.1). At normal pressure and room temperature, bulk zirconium exists in the α-phase, which has two atoms in hexagonal close packed structure. At normal pressure and above 1135 K, it transforms to β-phase occurs (bcc structure) [73]. At room temperature and at high pressure (above 8 ± 2 GPa), an ω-phase with three atoms in hexagonal structure [74] was first reported by Bridgmann in 1952 [75- 76].

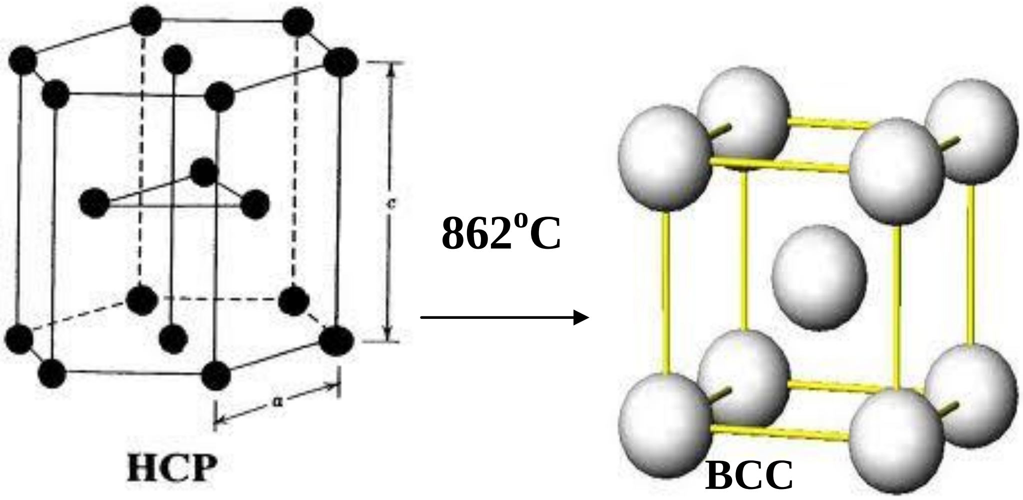

**Fig.1.1** Zr transformation from α (hcp) → β (bcc) phase at higher temperature [8].

It has been reported that a ω→ β transition may occur under very high pressure (30±60 GPa) [77-78]. Most of investigations on the zirconium structures principally deal with the ω → β [75, 76] or α → ω transitions. According to several authors, the latter shows an important hysteresis and the ω -phase has been found to remain metastable at ambient conditions. Usually, the ω phase is obtained by applying hydrostatic pressure in a diamond anvil cell [78, 82] or under shock loaded techniques [79, 81]. In titanium, which is a IV group material close to zirconium, the ω -phase has been produced by heavy ion implantation [83-84]. However, in zirconium, under such treatments, formation of ω -phase was not reported [83]. On the other hand, the ω -phase was recently observed in some ultra-rapid quenched zirconium-base alloys (Zr-V, Zr-Cr, Zr-Ni, Zr-Co, Zr-Fe) with solute additions beyond 2.5 at.% [85]. In any case, all these studies were dealing with bulk zirconium and the occurrence of $\omega$ -phase has been reported, when chromium is used as the interlayer in the case of thin films [105].

In the past decades, structural and mechanical properties of bulk zirconium and its alloys have been extensively studied [86-96]. Since zirconium has superior corrosion resistance against concentrated nitric acid at elevated temperature, it has been used as a material for chemical plants to produce nitric acid or spent nuclear fuel reprocessing plants. Zirconium occurs in more than 30 recognized mineral species and its chemical compounds, such as oxides and phosphates are often used in refractory applications for their resistance to thermal shock and for their extremely low thermal conductivity [97]. Good refractory properties of oxides and high hardness and electrical conductivity of nitrides provide wide scope for these materials for industrial applications [98-103].

Zirconium oxides and nitrides are also widely employed in industry because of their interesting properties: good refractory properties for oxides and high hardness and electrical conductivity for nitrides [8]. In that case, knowledge of the initial Zr film microstructure is of prime importance as it can influence on the reaction and the final product. The initial structure may be strongly dependent on the conditions used for the deposition process especially when using non equilibrium growth mechanisms occurring with highly energetic ion bombardment. Thin films of zirconium oxides and nitrides can be prepared by the treatment of Zr thin films under oxidizing or nitriding atmospheres [104]. It was reported that the formation of $\alpha$ -Zr is sometimes hindered by the growth of $\omega$ -phase of zirconium films because of the compressive stresses or due to the nature of the substrate [105]. Chakraborty et al. [106] have recently reported high in-plane compressive stress in Zr films deposited by dc magnetron sputtering which is found to decrease with increasing film thickness.

Zr based hard coatings are of great interest in a number of technological and medical implant [107] applications due to their improved tribological, corrosion, mechanical and physical properties. Zirconium and its alloys in bulk and thin film forms are widely used in nuclear industry and in reprocessing plants owing to their exceptional resistance to corrosion [108].

**Table 1.1 Properties of α - zirconium [8]**

| | |
|---|---|
| ***Lattice parameter, a and c*** | ***: 0.323 and 0.514 nm*** |
| ***Atomic Number*** | ***: 40*** |
| ***Atomic weight*** | ***:91.2*** |
| ***Appearance*** | ***: Metallic Silver*** |
| ***Melting Point*** | ***: 2128K*** |
| ***Electrical Resistivity (300 K)*** | ***: 4210 μΩ-cm*** |
| ***Vickers Hardness*** | ***:0.9 GPa*** |
| ***Density*** | ***:6.52 g.cm$^{-3}$*** |
| ***Thermal expansion coefficient*** | ***:5.7×10$^{-6}$ K$^{-1}$*** |

Also, polycrystalline zirconium films are used in thin multilayers for various applications such as metallic superlattice formation [94-96]. Zirconium thin films have been suggested as a diffusion barrier between U-Mo fuel and aluminum cladding in order to maintain the integrity of the fuel plates and to prevent fuel plate swelling and possible rupture during reactor operation [109]. Zirconium and titanium films have been also deposited on copper substrate to produce neutrons through deuterium-deuterium (D-D) and deuterium-tritium (D-T) reactions for neutron generator applications [110-111]. Properties of the $\alpha$ - zirconium are listed in Table 1.1.

### 1.4.2 Zirconium nitride crystal structure and its application

Zirconium nitride has a cubic NaCl crystal structure with face centered lattice, Fm3m space group and lattice parameter, *a* is 4.577 Å (Fig.1.2). Zirconium nitride (ZrN) thin films have been widely used in different technological areas [112-115] because of their interesting properties (high hardness, wear and corrosion resistance, chemical stability, etc.).

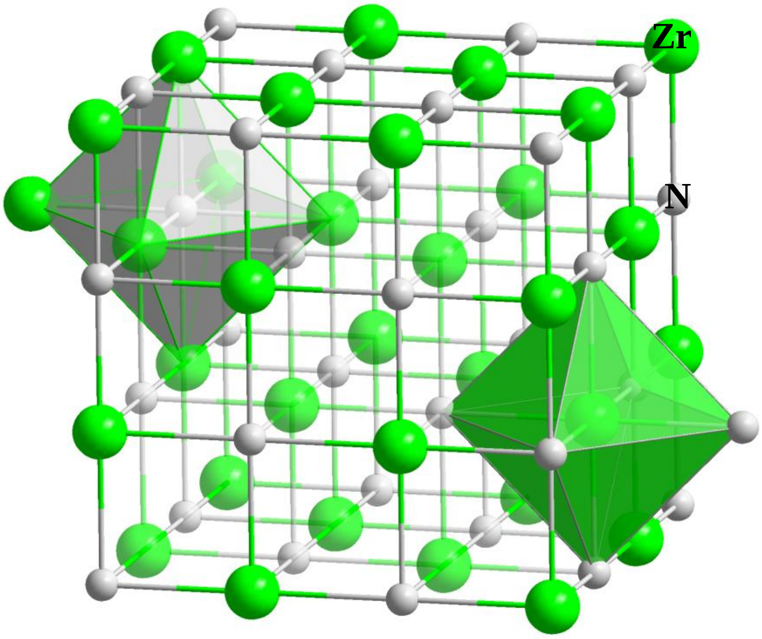

**Fig.1.2** Crystal structure of zirconium nitride [8].

ZrN thin films with their shiny and golden appearance are highly attractive for applications such as protective and decorative coatings in several industrial and commercial sectors [116-117].

**Table 1.2 Properties of ZrN [8]**

| | |
|---|---|
| ***Structure*** | ***: fcc*** |
| ***Lattice parameter (a)*** | ***: 0.456 nm*** |
| ***Composition*** | ***:*** $ZrN_{0.55}$ ***to*** $ZrN_{1.0}$ |
| ***Molecular weight*** | ***:105.23*** |
| ***Appearance*** | ***: Pale yellow*** |
| ***Melting Point*** | ***: 3253K*** |
| ***Electrical Resistivity (300 K)*** | ***: 13.6 µΩ-cm*** |
| ***Vickers Hardness*** | ***:15 GPa*** |
| ***Density*** | ***:*** $7.09\ g.cm^{-3}$ |
| ***Thermal expansion coefficient*** | ***:*** $7.24\times10^{-6}\ K^{-1}$ |

ZrN thin films on type 316 LSS have shown excellent compressive residual stress and mechanical strength resulting in improvement in the fatigue performance of the base steel [118].Gruss et al. [119] have deposited ZrN coatings by cathode arc evaporation onto Incoly 825. Klesoglu et al. [120] have reported the influence of high flux ion bombardment on the corrosion characteristics of ZrN coated on plain carbon steel. A study of nanocrystalline nitride coatings deposited on high density graphite by DC/RF magnetron sputtering has been carried out in molten uranium for the cathode processor crucible used in pyrochemical reprocessing application [121].The corrosion resistance of ion plated Zr, ZrN and Zr/ZrN films coated on commercial type 304 stainless steel investigated by potentiodynamic polarization technique indicated that Zr/ZrN bilayer showed excellent corrosion resistance than those of Zr and ZrN coatings [122]. Properties of the zirconium nitride are listed in Table 1.2.

### 1.4.3 ZrAlN thin films

Cubic ternary MeAlN (Me-metal) nitrides are metastable compounds; and thermal annealing at higher working temperatures can produce phase separation into cubic MeN and hexagonal AlN phases [123-125]. The ternary Zr-Al-N system is an extended system of ZrN with the addition of Al and is not as well studied as the Ti-Al-N system. Theoretical studies show that these systems have the largest miscibility gap of the ternary transition metal aluminum nitrides investigated [126-127]. Cubic-$Zr_{1-x}Al_xN$ with NaCl structure is predicted to be stable for $x < 0.50$ while an hexagonal structure is energetically favorable for higher Al contents [126,128]. It is known that ZrN has a lower coefficient of friction than TiN and other transition metal nitrides, and is relatively hard [129,130]. However, its poor oxidation resistance hampers a broader range of applications. The Al addition changes the lattice parameter of Zr-N system and also improves the resistance against oxidation with significant hardness [131]. Recent experimental studies have shown that only the face-centered cubic (fcc, NaCl-type) $Zr_{1-x}Al_xN$ solid solution exists for $0 < x < 0.43$, and the hardness increases from 21 to 28 GPa when the Al content increase from $x = 0$ to 0.43 [132]. With further addition of Al, hexagonal close packed (hcp, ZnS-type) AlN appears and the hardness of the coatings decreases. H. Klostermann et. al. [133] deposited $Zr_{1-x}Al_xN$ layers in the full compositional range ($x$ = 0…1) by adjusting the working temperature and pulse times using reactive pulsed magnetron co-sputtering of aluminum and zirconium targets and reported no enhanced hardness for $Zr_{1-x}Al_xN$ in a range $x$ = 0.3…0.9. However, films with a fraction of only a few atomic percent aluminum exhibit enhanced hardness up to 30 GPa, which is well above the hardness of ZrN or AlN (25 GPa).

TiAlN and other variants of the alloyed films with Si, C, B, W, and Mo have been investigated and are considered as cutting-edge wear resistant coatings [134,135]. $Ti_{1-x}Al_xN$ itself forms a nanocomposite structure of nanocrystalline (nc) cubic rock salt structure of (Ti,Al)N and hexagonal wurtzite structure of AlN in the compositional range $x$ = 0.5-0.7, which is due to the segregation of AlN once the solubility threshold of Al in (Ti,Al)N is reached or surpassed ($x \geq 0.52$) [59].

Fig. 1.3 shows the phase diagram for Zr-Al-N for the Al content in the range of 0-100%. The phase diagram suggests that ZrN based thin films can dissolve up to 40 at.% of Al and the phase is stable up to 1273 K. Beyond 40 at. % Al, the phase separates into fcc ZrN and hexagonal AlN. Decomposition of the $Zr_{1-x}Al_xN$ solution phase can occur either by nucleation and growth or by spinodal mechanism [136–143]. The spinodal mechanism occurs when the second derivative of the Gibbs energy of the solution phase is negative (‘‘chemical spinodal’’) and the interfacial misfit strain energy is sufficiently small compared to the demixing energy of the mixed phase (‘‘coherent spinodal’’). When the demixing energy is of the order of a few 10 kJ $mol^{-1}$, as in the case of the majority of metallic alloys and in the $Ti_{1-x}Al_xN$ system [144-146], the spinodal mechanism is possible only when the final, stable phases are coherent [143]. Veprek et. al. [147] have reported that for the composition $x \leq 0.472$, $Zr_{1-x}Al_xN$, solid solutions are more stable in fcc than in hcp structure, which is in a good agreement with the experimentally reported value of $x < 0.43$. They show that fcc $Zr_{1-x}Al_xN$ solution coatings should undergo phase decomposition into fcc ZrN and fcc AlN. However, considering the relatively large lattice mismatch between the fcc ZrN and the fcc AlN, the coherent spinodal decomposition may probably be hindered due to rapid phase transformation from fcc AlN to the stable hcp AlN. Experimentally, no intermediate fcc AlN has so far been observed in the Zr–Al–N system.

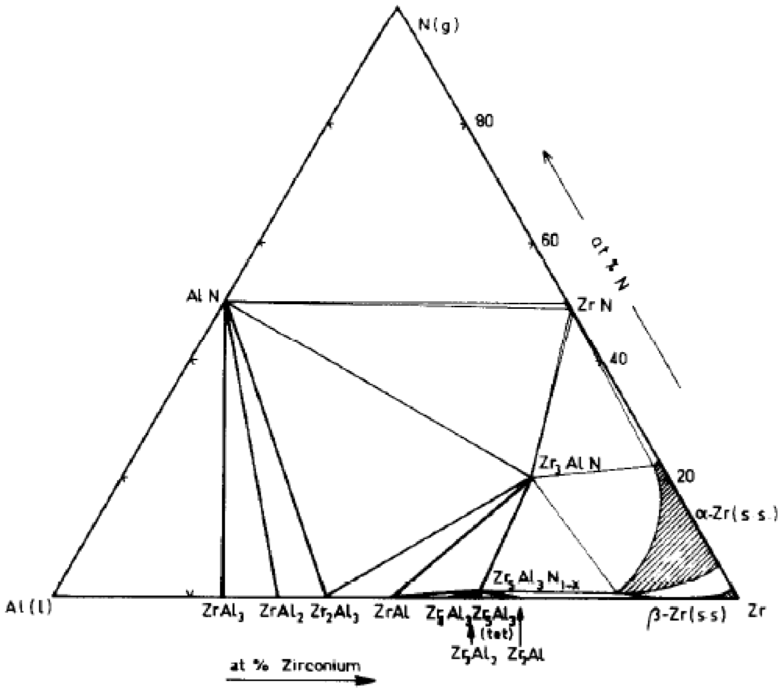

**Fig. 1.3** Isothermal section of Zr-Al-N phase diagram at 1273 K[147].

Among ternary transition metals nitrides, TiAlN and CrAlN films are investigated, whereas less work on ZrAlN [148] films has been reported so far. It was pointed out that ZrAlN films can be used as a diffusion barrier between Cu and Si up to

1073 K. Therefore, it is expected that ZrAlN films can offer better oxidation resistance than ZrN and provide an alternative as a potential diffusion barrier material. Lamni et al. [69] studied the chemical composition, crystal structure, optical and electrical properties of ZrAlN films.

## 1.5 Thin Film Deposition Methods

Physical vapor deposition (PVD) and chemical vapor deposition (CVD) are the most common methods for transferring material atom by atom or molecule by molecule from one or more sources to the growth surface of a film being deposited onto a substrate. If the vapor is created by physical means without a chemical reaction, the process is classified as PVD and if the material deposited is the product of a chemical reaction, the process is classified as CVD. Many variations of these basic vapor deposition methods have been developed to balance the advantages and disadvantages of various strategies based on the requirements of film purity, structural quality, the rate of growth, temperature constraints and other factors. Although CVD is widely used to deposit many coatings, the high deposition temperature is a major constraint of this method [149]. Especially for tool steels or stainless steels, the high temperature during deposition may soften the substrate materials, and the coatings fail accordingly. Since 1985, PVD methods have become popular because lower processing temperature can be used to deposit films on various substrate materials [150], including metals with low melting points and plastic substrates. Moreover, tight environmental protection laws have made PVD the favored deposition process.

### 1.5.1 Sputter deposition

Physical vapor deposition is a technique whereby physical processes, such as evaporation, sublimation or ionic impingement on a target, facilitate the transfer of atoms from a solid or molten source onto a substrate. Evaporation and sputtering are the two most widely used PVD methods for depositing films.

In sputter deposition, ions of a sputtering gas, typically Ar, are accelerated toward the target at high speed by an imposed electric field. The initial concentration of charge carriers in the system is significantly increased with an increase in the dc voltage, as the ions collide with the cathode, thereby releasing secondary electrons, and with the neutral gas atoms. As critical numbers of electrons and ions are created through such avalanches, the discharge becomes self-sustaining. The target is referred to as the cathode since it is connected to the negative side of the direct current power supply. The chamber is evacuated and then Ar gas, at a pressure of approximately 13.3 Pa ($10^{-1}$ torr), is introduced for the purpose of maintaining a visible glow discharge. The Ar+ ions bombard the target or cathode, and the ensuing momentum transfer causes the neutral atoms of the target source to be dislodged. These atoms transit through the discharge and condense onto the substrate, thus providing film growth.

The number of atoms sputtered per ion known as sputtering yield (S) increases with ion energy and with decreasing binding energy of the atom to the target. The sputter yield depends on how close to the surface the Ar loses its energy. For a given ion energy, the higher the atom density in the target and the shorter the mean free path between collisions, the higher the yield. It also depends on crystal orientation as well as the mass ratio. There is a minimum energy for an ion to produce sputtering. S generally increases with the atomic number (Z) of target atoms, but there is wide variation because of the difference in binding energy (Fig 1.4). The surface binding energy for metals is in the range of 3-9 eV [151-152].

The sputtering yield varies with the angle of incidence, Φ, of the ions. As Φ increases, atoms near the surface get more energy and have higher chance of being sputtered. The atoms are sputterd from the target with a range of energies, Stuart and Wehner [153-154] measured values for Cu sputtered by Hg, Ne, Kr and Xe and shows that a few atoms are ejected with low energy and few with high energy, but most atoms have an energy of a few eV. For sputtering with incident ion energy $E_i < 500$ eV ions, the number of atoms being sputtered with energy E is approximately $N(E) \sim E/(E+E_b)^3$, where $E_b$ is the surface binding energy [155].

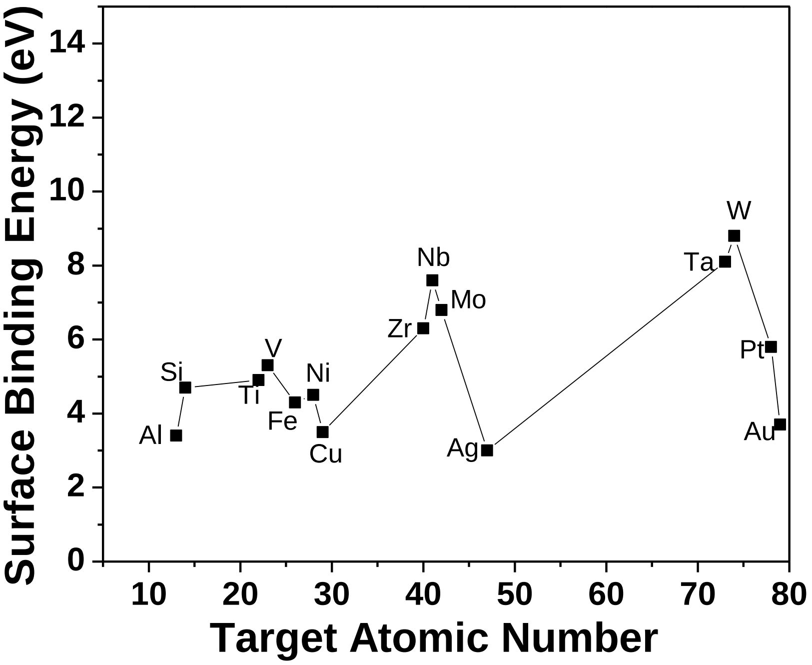

**Fig. 1.4** Surface binding energy curve for different metals [151].

Several different sputtering methods are widely used for the deposition of thin films: (i) dc sputtering (also commonly referred to as cathodic or diode sputtering), (ii) radio frequency (rf) sputtering with frequency of 13.5 MHz, (iii) magnetron sputtering, where a magnetic field is applied in superposition with a parallel or perpendicularly oriented electric field between the substrate and the target source, and (iv) bias sputtering, where either a negative dc or rf bias voltage is applied to the substrate so as to vary the energy and flux of the incident charged species.

### 1.5.2 Magnetron sputtering

In the magnetron sputtering, the ion bombardment is well known to modify the film structure, to improve the film properties and to increase the film density [156-160]. Magnetron sputtering is one of the promising techniques for metal thin film deposition because of several advantages. The precise control of the grain size in the nanocomposite films prepared by magnetron sputtering could be achieved by optimizing the process parameters such as substrate temperature, bias voltage, discharge current, and partial pressure of reactive gas. To improve efficiency, the magnetron uses a magnetic field to prevent electrons from escaping the target region before they produce a number of ions. Magnetrons have three basic configurations: (i) cylindrical [161], (ii) central anode [162] and (iii) planar [163-164]. In a planar magnetron (Fig. 1.5), the magnetic field (B) is neither parallel to the target at all points nor does it have constant magnitude; that is B varies in both magnitude and direction over the target surface. The magnetic field is usually produced by an array of permanent magnets behind the target. For a circular target, there is a central magnetic pole (say a north pole) and an annular (south) pole so that the magnetic field lines between the poles have circular symmetry. At any point above the target, the magnetic field can be resolved into a horizontal component parallel to the target surface and a vertical component normal to the target. The horizontal component provides the magnetic trapping. The vertical component of B prevents the electrons from escaping from the magnetic tunnel because of Lorentz force on electrons moving outward or inward.

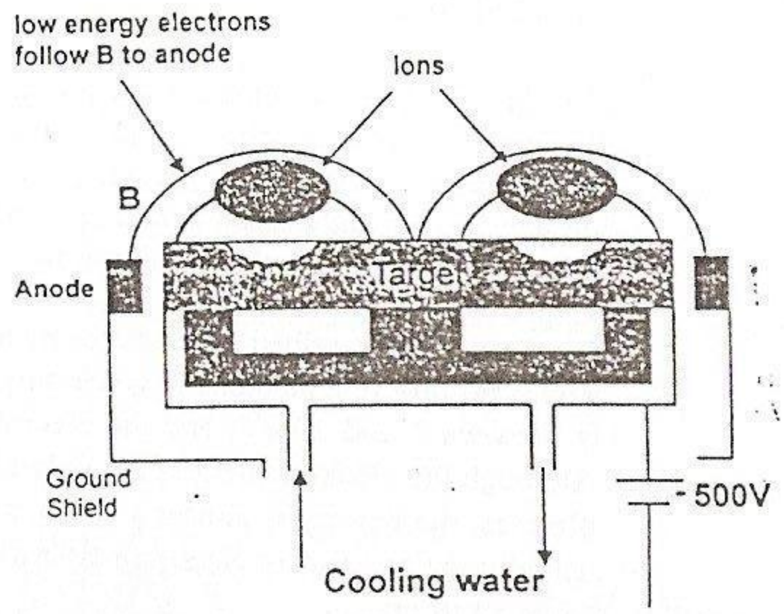

**Fig. 1.5** Schematic diagram of a planar magnetron[159].

Initially, the power supplies for magnetrons were simple DC supplies with current control since the target voltage did not change significantly with increasing power. As target currents were increased, arcing became a problem, especially in reactive processes. As a result, new types of supplies have been developed. Arching results from the buildup of positive charges on an area of the target that is not electrically conducting. This could be because of an insulating oxide forming on the target surface or embedded in the target.

An RF source can be applied to a magnetron system to sputter insulating targets. Conducting targets may also be used with the RF supply, but this only adds complexity. Insulating targets usually have poor thermal conductivity, so there will be a significant thermal gradient across the target for high power densities, required for high sputtering rates. The lowest density target consists of loosely pressed powders. Obtaining high sputtering rates requires high target powers, however high power RF supplies are expensive and require a matching network.

### 1.5.3 Pulsed magnetron sputtering

With the recent advancement in power supplies, pulsed dc magnetron sputtering process has become an attractive production deposition technology [165-167]. The technique is capable of reducing the arcing event, which results from charge accumulation on target surfaces. It consequently prevents the deterioration of film properties and maintains a stable deposition process. The technique also provides higher ratios of the fluxes of bombarding ions.

The pulsed-dc power supply can be operated in both symmetric and asymmetric modes of operation. The bipolar pulsed DC power supplies produce either a bipolar symmetric or asymmetric pulse. In both bipolar symmetric and asymmetric pulsed DC power supplies, sputtering takes place from the target during the negative pulse, whereas discharging of the target surface takes place during the positive pulse. Asymmetric bipolar pulsed DC is the optimum solution to the target poisoning problem because it sets up conditions which cause the insulators on the target to be sputtered first and with a higher sputter yield  and eliminates target poisoning. For the asymmetric pulsed DC power supplies (Fig. 1.6), the positive pulse voltage is only a fraction of the negative pulse voltage. The pulse changes from positive to negative without off time. Asymmetric bipolar pulsed DC technology has been proven to be particularly beneficial for the enhancement of the film qualities.

A pulsed DC power supply driving a magnetron prevents breakdown by providing electrons to the target for 1-5 µs and ions for a 40-50 µs. The positive voltage on the target is typically 5-15% of the magnitude (+40 V) of the negative voltage (i.e. -400 V) for sputtering and this positive voltage is useful for collecting electrons (Fig. 1.7a). Because electron has higher mobility, the number of electrons and ions arriving at the target can be equal so that there is no charge builds up.

An arc detection circuit is often added to these supplies (Fig. 1.7b). If an arc is detected during the -400 V pulse, the supply immediately applies +40 V to the target to suppress the arc. Schneider and Sproul [168] reviewed the pulsed DC process and the control of the reactive sputtering process. Ohsaki et. al [169 ] used a high speed camera to show that the plasma almost disappeared during the positive pulse. Posadowaki [170] and Scholl [171 ] have discussed the detailed operation of these pulses. Kelly et.al.[172] compared DC, pulsed DC and mid frequency supplies for sputtering $Al_2O_3$. For DC, there was considerable arching, and the films were porous with granular structure. The pulsed DC significantly reduces arcing and the films are dense. Frach et.al. [173 ]used the pulsed power supply with polarity reversal to suppress arcs. Belkind et.al. [174 ] showed that the critical frequency to prevent arcs depends on the reverse voltage time.

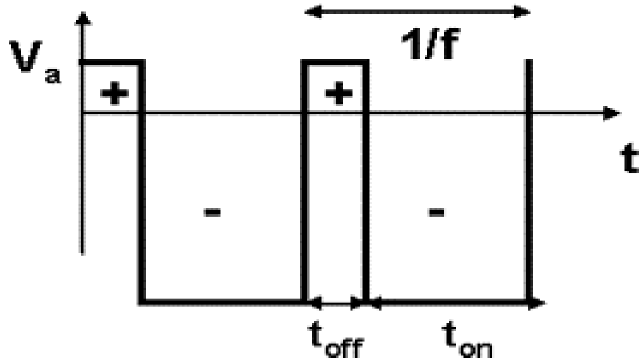

**Fig. 1.6** A waveform of an asymmetric bipolar power supply.

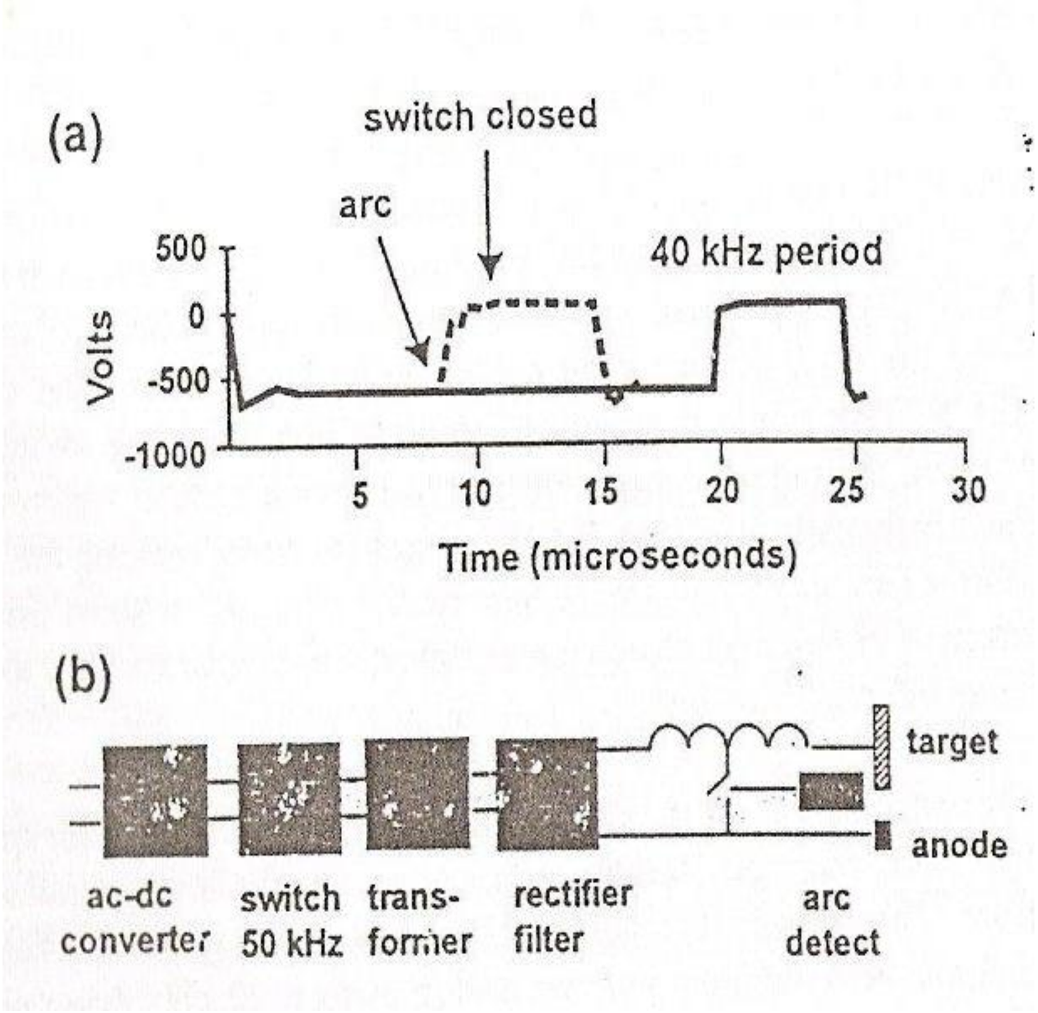

**Fig. 1.7** (a) A typical pulsed DC wave form applied to a magnetron target relative to anode. The dotted line is the response of an arc detection and suppression circuit shown diagrammatically in (b)[168].

The reactive sputtering is a variant of sputtering to facilitate a chemical interaction with the sputtered species by adding a reactive gas or gases to the sputtering system. Although sputtering itself is a purely physical process of ejection of atoms, a chemical reaction is required to form new material. The chemical reaction may be controlled to dope the film with the desired concentration of the reactive element. The chemical reactions take place at the surface of the substrate in the sputtering system. Surface reactions do not occur unless the $N_2$ is dissociated and it requires dissociation energy of 5.2 eV [175]. When $N_2$ is introduced to a plasma such as in the magnetron, electron collision produce $N^{2+}$, which are then accelerated to the target to cause sputtering. Akazawa and Murata [176] measured threshold energy of 40 eV for the impact dissociation of $N^{2+}$ on Pt surfaces. Some of these energetic N atoms will sputter the target, some will be reflected and some react chemically with the target. The reaction mostly occurs at a surface in order to conserve energy and momentum.

## 1.6 Thin Film Growth

The formation of a thin film is accomplished in three stages. The first stage is nucleation during which small nuclei are formed and are statistically distributed over the substrate surface. The nuclei thereafter grow in size so that large islands of deposit form. Eventually the islands coalesce and form a more or less continuous film. In the general case, we have to treat the condensation from a supersaturated vapor onto a solid, which is usually of a different material than the vapour. The phenomenon is referred to as heterogeneous nucleation.

The Gibbs free energy of the cluster increases initially with size until a critical size is reached. Above the critical size, growth occurs with a decrease in the Gibbs free energy. The rate of nucleation is then obtained as the product of the concentration of critical nuclei and the frequency with which they grow by the addition of one molecule. The spontaneous formation of nuclei in the bulk of a supersaturated vapor is known as homogeneous nucleation.

The atomistic model of heterogeneous nucleation involves groups of atoms, such as dimers to represent the critical nucleus size. Walton, Hirth and Halpern [177] provided the treatment of nucleation when adatoms are bound to a substrate and move by discrete diffusion steps. The theory is statistical in nature and describes the nucleation process when the critical nucleus consists of a very small number of atoms, typically less than 10. The binding energy of the individual atoms and the substrate is taken into account, and the clusters of atoms are treated as molecules. A cluster of fixed size is stable in an interval of supersaturation, which is larger as the cluster size gets smaller. The classical nucleation theory prescribes a critical size for the nucleus, and this is valid only when the size of the aggregate is large. Hence, in the atomistic theory of nucleation, the single nucleus size should be operative over a range of temperatures and atom arrival rate. Furthermore, when the size of the nucleus is small, its shape does not remain constant as adopted by the classical theory [177].

Extensive experimental and theoretical studies of deposits at different stages of growth, have been established and it was reported that there are three distinguishable modes of nucleation and growth, which can occur. The three basic modes are: (i) island growth (Volmer–Weber model), (ii) layer by layer growth ( Frank–Van der Merwe model) and (iii) layer plus island growth (Stranski–Krastanov model). A schematic illustration of each of these modes of growth is illustrated in Fig. 1.8.

In the Volmer–Weber model, equilibrium exists in a three-dimensional crystal of the film in contact with the substrate, while the rest of the substrate is devoid of any condensed phase. Nucleation of film occurs in the form of discrete three dimensional nuclei on the surface of the substrate (e.g. lead on graphite). Both the number of nuclei and the size of a given nucleus increase. Eventually, the nuclei grow in size until they intergrow with each other to form a continuous film.

In the Frank and Van der Merwe model, nucleation occurs in the form of monolayer island of the deposit. Eventually the monolayers grow together to form a complete continuous monolayer of the deposit. The process repeats itself so that deposit grows in a layer-by-layer manner (e.g. rare gases on graphite). In this growth, the interaction between substrate and layer atoms is stronger than that between neighboring layer atoms. Layer-by-layer growth is hindered by elastic constraints at the solid–solid interface.

Stransky and Krastanov model combines the features of layer-by-layer growth and discrete three-dimensional nucleation (e.g. Pb on Ge (111)). In this model, nucleation and growth occurs as in the layer-by-layer mode so that finite number of monolayers are produced. Subsequent formation of film occurs by formation of discrete nuclei. The lattice mismatch between the substrate and the deposit cannot be accommodated when the layer thickness increases so that the three-dimensional growth follows the layer-by-layer growth. Alternatively, symmetry or orientation of the over layers with respect to the substrate might be responsible for the production of this growth mode. Freund and Suresh present a detailed thermodynamic analysis of the three modes of growth.

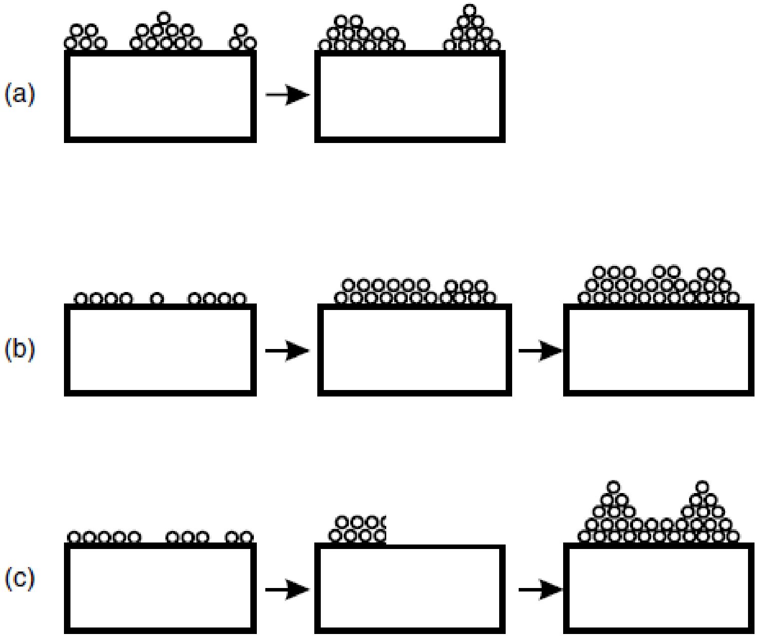

**Fig. 1.8** Thin film growth models (a) Volmer-Weber, (b) Frank-Van der Merwe and (c) Stranski-Krastanov model[177].

The actual mode of growth depends on the materials involved, temperature of the substrate and the degree of supersaturation of the vapor. The transition from two dimensional to three dimensional growth can be described using the analogy of a liquid droplet on the surface. If the droplet wets the surface, a continuous 2D film will form, whereas non wetting surface results in 3D growth. If the thermodynamics of the film and substrate are considered, the equilibrium growth mode is determined by the relative free energies of the substrate surface ($\sigma_s$), film surface ($\sigma_f$) and the film- substrate interface ($\sigma_i$) provided that the strain energy in the system is neglected. The island growth is driven by a high interface energy and substrate surface energy such that it is more favorable for deposit atoms to stick together rather than wet the substrate.

## 1.7 Scope of the Work

In the present work, a systematic investigation is reported on the structural properties of thin films of Zr, ZrN and alloyed ZrAlN prepared by pulsed DC magnetron sputtering as a function of substrate temperature and nitrogen partial pressure. A study has been undertaken to investigate the thermal stability and thermal expansion behavior of these thin films, since these materials are considered to be used as protective coatings against wear applications. Also, a detailed correlation between microstructures, nanomechanical, and tribological properties of these films is investigated.

# Chapter 2

# *Experimental and Characterisation Methods*

## 2.1 Introduction

This Chapter gives a detailed experimental procedure in two parts. First part outlines the details of thin film deposition by magnetron sputtering system, substrate preparation, target mounting, substrate heating, pre sputtering etc. Second part of the Chapter describes the principles and experimental procedure of all the characterization methods that have been used to characterize the thin films in the present work.

## 2.2 Thin Film Synthesis

### 2.2.1 Magnetron sputtering system

Thin films have been deposited by pulsed DC magnetron sputtering system. The sputtering was carried out in a custom built magnetron sputtering system (Fig 2.1(a) and (b)) which consisted of a stainless steel chamber of 45 cm diameter and 20 cm deep using Mighty Mak US sputtering gun of 3 inch diameter [178]. A target disc of 76 mm diameter and 2 mm thickness was used as a sputtering target. The deposition chamber was evacuated to a base pressure of $8\times10^{-4}$ Pa using a pumping system consisting of a rotary and turbo molecular pumps (Alcatel, France). The flow rate of Ar (99.99% purity) was set at 50 standard cubic centimeter per minute (sccm) using MKS make mass flow controller during the sputtering. Nitrogen gas (99.99% purity) has been used for reactive sputtering. A RPG-50 asymmetric bipolar pulsed DC power supply (MKS Instruments, USA) was used as the electrical power source for the thin film deposition.

An experimental flow chart consisting of all the steps followed during the experiment is given in Fig 2.1 (c).

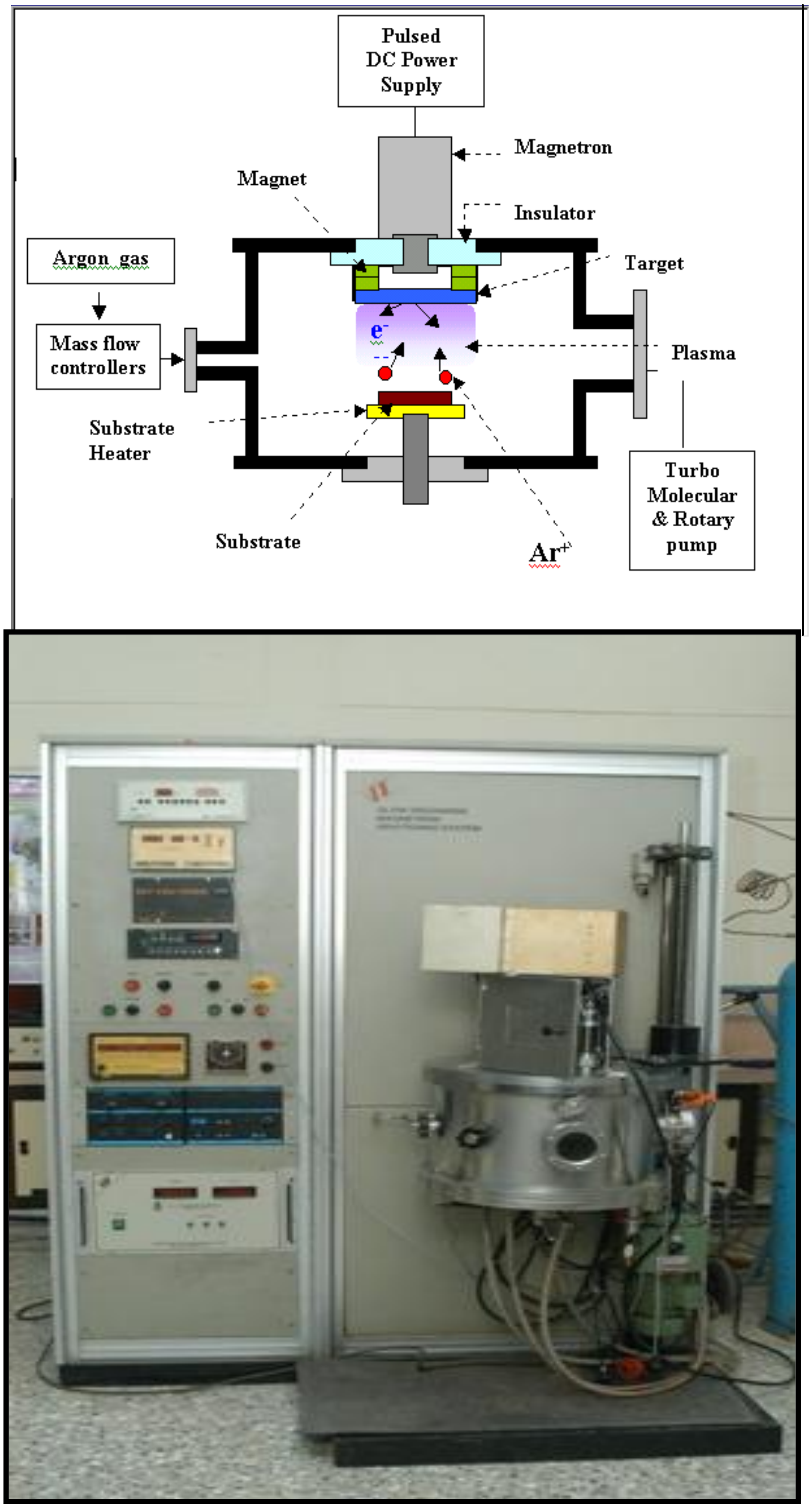

**Fig. 2.1**(a) Schematic diagram of magnetron sputtering system and (b) Sputtering unit used for deposition.

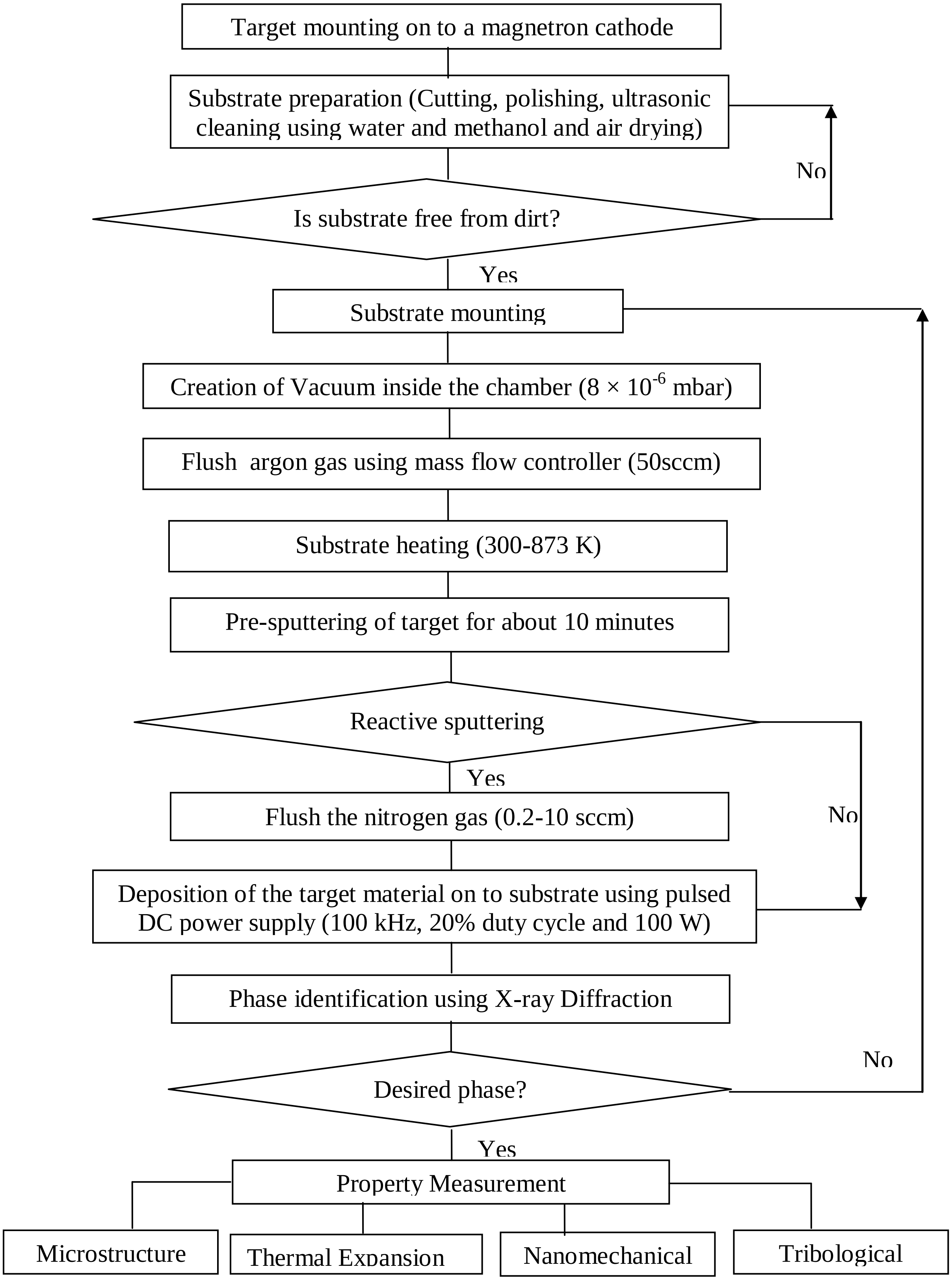

**Fig. 2.1**(c) Experimental flow chart.

### 2.2.2 Target mounting

Zirconium (purity 99.9%) and zirconium nitride target (purity 99.5%) were used in the present study and Zr-Al-N thin films were prepared by mounting an Al strip (purity 99.9%) over the ZrN target and in the presence of reactive environment of nitrogen gas (purity 99.99%). One of the targets was mechanically mounted to a cathode assembly using conducting silver paste. In the present experimental configuration, the target was kept vertically upward, while the substrates have been placed on the base plate in the vertically downward direction. After mounting the target, continuity between target and the base plate was checked to ensure that there was no shorting. The distance between target and substrate was kept at 60 mm throughout the experiments.

### 2.2.3 Substrate preparation and substrate heating

Si (100) and D-9 alloy substrates have been used for the film deposition. Si has been chosen since it is widely used in the electronic industry, while D-9 alloy is Ti modified austenitic stainless steel used as clad material in the fast breeder reactor[179]. Si substrates of  size of 10 mm x 10 mm x 0.5 mm were cut from Si (100) wafer and D-9 alloy substrates of the size of 10 mm x 10 mm x 5 mm is cut from a square rod of D-9 alloy. However, no etching treatment for oxide removal was carried out for Si substrate. The composition of the D-9 alloy has been given in the Table 2.1. The substrates of Si were cleaned with soap solution to remove any contamination due to dust particle onto the surface followed by ultrasonic cleaning with water and methanol ($CH_3OH$). D-9 alloy substrates were polished using successive grade of silicon carbide emery paper followed by mechanical polishing by oxide dispersed silica suspension.

**Table 2.1 Chemical composition (wt.%) of titanium modified austenitic stainless steel (D-9 alloy)**

| **Element** | C | Ni | Cr | Mo | Ti | Si | Mn | P | B | N | Fe |
|---|---|---|---|---|---|---|---|---|---|---|---|
| **wt.%** | 0.05 | 14.9 | 14.7 | 2.2 | 0.18 | 0.65 | 1.3 | 0.008 | 0.0015 | <0.04 | Bal |

D-9 alloy substrates were also cleaned with soap solution followed by cleaning with water and acetone. After cleaning, the substrates were dried by a drier and placed onto the base plate inside the chamber. Si substrates were used for the microstructural study and for the determination of coefficient of thermal expansion, while D-9 alloy substrates were used for tribological and nanomechanical studies.

A halogen lamp (800 W, 6.3 A) heater has been kept below the base plate for the substrate heating. The temperature has been controlled and monitored by externally kept digital programmable temperature controller unit. The substrate temperature was varied from 300 to 873 K with accuracy of ±1 K. A chromel alumel thermocouple was placed at the top of the base plate and substrates were kept near to a thermocouple during the experiments. Preheating of the substrates to a desired set temperature for about 0.5 h was carried out during all the experiments.

### 2.2.4 Thin film deposition

Zirconium thin films were deposited from zirconium target of 99.9% purity in pure argon atmosphere, while zirconium nitride films were deposited by reactive sputtering in nitrogen and argon gas mixture. Zirconium nitride films was also deposited using ZrN target. In this case, lower flow rate of nitrogen gas was required during reactive sputtering. Zr-Al-N thin films were deposited by reactive sputtering in nitrogen and argon atmosphere using ZrN target with Al strip mounted over the ZrN target. A schematic of composite target has been given in Fig. 2.2.

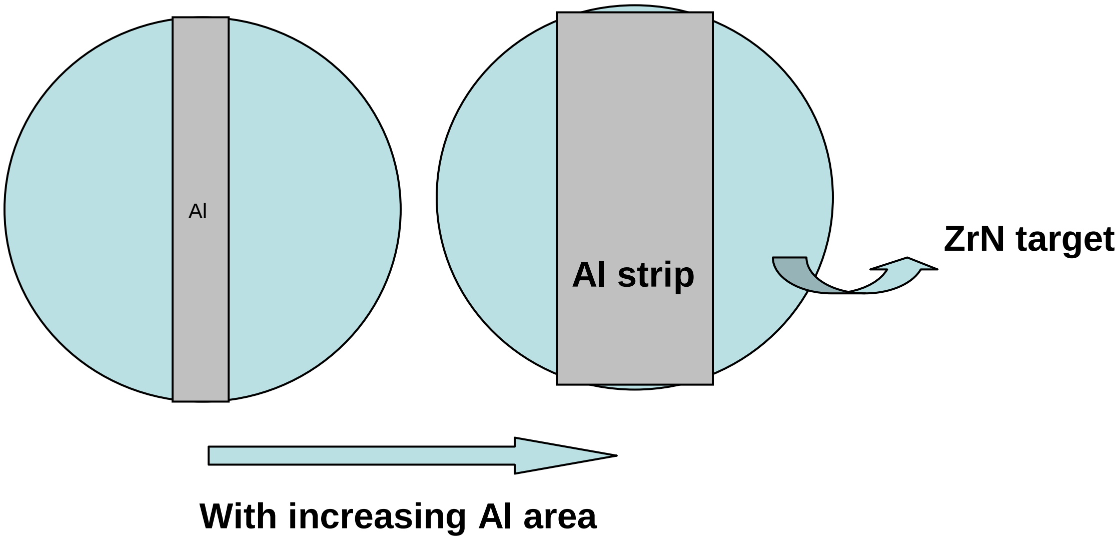

**Fig. 2.2** Composite target used for the deposition of alloyed films of ZrAlN.

The composition of ZrAlN thin films was varied by varying the Al strip area.The flow rate of argon (99.99% purity) and nitrogen (99.99% purity) was controlled in such a manner that the total flow rate inside the chamber was at 50 standard cubic centimeter per minute (sccm) using a MKS make mass flow controller during the sputtering. Table 2.2 lists typical ranges of process and pulsed power supply parameters used for the deposition of Zr, Zr-N and Zr-Al-N thin films.

**Table 2.2 Typical experimental parameters for deposition of Zr, ZrN and alloyed ZrAlN thin films**

| | |
|---|---|
| *Base pressure* | $\sim 8\times 10^{-4}$ *Pa* |
| *Operating pressure* | $7.5\times10^{-1}$ *Pa* |
| *Substrate temperature* | *300–873 K* |
| *Pulse power* | *50-125 W* |
| *Duty cycle* | *10-40%* |
| *Pulse frequency* | *50-200 kHz* |
| *Argon flow rate* | *50-40 sccm* |
| *Nitrogen flow rate* | *0-10 sccm* |
| *Substrate to target distance* | *60 mm* |

The deposition chamber was evacuated to a base pressure of about $8 \times 10^{-4}$ Pa and working pressure was kept constant at $7.5\times10^{-1}$ Pa for all the experiments during the sputtering.

Before the deposition of the films, pre-sputtering of the target was carried out for 10 minutes in the argon atmosphere to remove the surface contamination of the target. During this process a shutter was placed in between target and the substrate, to avoid film deposition during pre-sputtering. The deposition conditions used for Zr, ZrN and alloyed ZrAlN films are presented in the respective chapters.

## 2.3 Characterisation Methods

### 2.3.1Thickness measurement

There are many methods such as profilometer, spectroscopic reflectometer and ellipsometer etc, by which thickness of a film can be measured. In the present work, thickness of the films were measured by a profilometer (DEKTAK6M-stylus profiler), and the method is useful to measure a thickness in the range of 20 nm-1mm with 1 nm accuracy. To measure the thickness of the film, a step was created using a mask. The tip of the stylus was moved on the surface across the step. The step size was measured by taking the difference between the height of coated and uncoated regions of the sample.

### 2.3.2 X-ray diffraction

X-ray diffraction is a non destructive technique used to identify phases, texture, strain, defects, crystallite size etc. of the crystalline materials.

The physical state of the crystalline materials can be loose powder, thin films and bulk materials. X-ray diffraction pattern provides information on intensity and diffraction angle. In the diffraction pattern, 2 θ represents the angle of diffraction of a particular plane from which the d-spacing as well as lattice parameter can be derived. The angle (2θ) at the maximum diffraction intensity is related to the lattice spacing (d) of the diffraction (hkl) plane and the wavelength λ by Bragg’s law,

$$n\lambda = 2d\sin\theta \quad \text{……………………..........................................2.1}$$

The lattice parameter of bulk and thin film at various parameters were refined by the method of least square fitting using the unit cell program [180]. The basic equations used for calculating lattice parameter for cubic and hexagonal phases of Zr based thin films are given in equations 2.2 and 2.3 [181], respectively.

$$\frac{1}{d^2} = \frac{(h^2 + k^2 + l^2)}{a^2} \quad \text{………………………………………2.2}$$

$$\frac{1}{d^2} = \frac{4}{3}\left[\frac{(h^2 + hk + k^2)}{a^2}\right] + \frac{l^2}{c^2} \quad \text{……………………………… .2.3}$$

X-ray peaks have been fitted with Gaussian profile and the unit cell program [185] was used for the calculation of lattice parameter. The full width at half maximum (FWHM) values of the peak has been used for crystallite size determination.

The crystallite size was calculated using the Scherrer's formula [182-183]:

$$D = \frac{k\lambda}{\cos\theta\sqrt{\left(B^2 - b^2\right)}} \quad \ldots\ldots\ldots\ldots\ldots\ldots\ldots\ldots\ldots\ldots\ldots\ldots\ldots 2.4$$

where λ is the wavelength of the X-rays used, k is the correction factor, θ is the diffraction angle, B is the full width at half maximum (FWHM) of a reflection of the film, and b is the FWHM of the instrumental broadening. The instrumental broadening was corrected using standard silicon powder received from National Physical Laboratory, New Delhi. However, broadening due to strain was not considered.

It is also possible to get the qualitative value of the preferred orientation by monitoring the intensity ratio of strong reflections of the phases present in the XRD pattern. The value of texture coefficient (Tc) can be calculated using the equation 2.5 [181]:

$$\text{Texture Coefficient (Tc):} \quad \frac{\dfrac{I_m\left(hkl\right)}{I_0\left(hkl\right)}}{\dfrac{1}{n}\sum\dfrac{I_m\left(hkl\right)}{I_0\left(hkl\right)}} \quad \ldots\ldots\ldots\ldots\ldots\ldots\ldots\ldots 2.5$$

Where n, the total number of reflections; Im (hkl) is the reflected intensity from hkl crystallographic planes in the textured specimen and $I_0$ (hkl) is the standard intensity.

Structural properties of the films were characterized by X-ray diffraction equipment using an INEL XRG-3000 Diffractometer with glancing angle of incidence (ω) of 5◦ using Cu K$\alpha_1$ (1.5406 Å) radiation. Sample was loaded onto a holder and spinned during the experiment to collect the data from whole sample. Curved position sensitive detector was used to collect the diffracted data in the 2θ range of 10 to $90^o$ with an angular resolution of $0.0125\,^o$. Residual stress present in the film also can be measured using $\mathrm{Sin}^2\psi$ technique [181], however in the present study this method has not been followed to measure the residual stress and only qualitative values are presented in this study based on the shift in the d- spacing.

### 2.3.3 High temperature x-ray diffraction

High temperature X-ray diffraction (HTXRD) is used to study phase stability and to determine the coefficient of thermal expansion (CTE) of the thin films. HTXRD experiments were carried out using an INEL XRG – 3000 diffractometer with glancing angle incidence ($\omega$) of 5° and Cu $K_\alpha$ radiation (Fig. 2.3). Buhler HDK 2.4 high temperature camera with tantalum as a heating holder was used for the high temperature measurements in the two theta range 20 to $90^0$ at $2.8 \times 10^{-6}$ mbar with the heating rate of 10 K/min, with a step size of 100 K from room temperature to 1373 K. After reaching the desired temperature, equilibration time of 3 minutes was provided to ensure the stability of the temperature and then data was acquired for about 15 minutes. Samples were kept on a tantalum base and was heated in the temperature range of 300-1373 K and XRD patterns were recorded simultaneously. After heating up to 1373 K, samples were cooled to room temperature with a rate of 50 K/min. Lattice parameters were calculated from HTXRD pattern and from the lattice parameter data, average and instantaneous coefficient of thermal expansions were determined using equations 2.6 and 2.7 respectively [169,184].

$$\alpha_a = \frac{1}{a_{RT}}\left[\frac{a_T - a_{RT}}{T - RT}\right] \qquad \ldots\ldots\ldots\ldots\ldots\ldots\ldots\ldots\ldots\ldots 2.6$$

$$\alpha_i = \frac{1}{a_{T_1 - T_2}}\left[\frac{a_{T_1} - a_{T_2}}{T_1 - T_2}\right] \text{……………………………………..2.7}$$

Where $\alpha_a$ is the average thermal expansion coefficient, $a_T$ and $a_{RT}$ are the lattice parameter values at temperature T and room temperature (RT), respectively and $\alpha_i$ is the instantaneous thermal expansion coefficient along a axis, $a_{T1}$ and $a_{T2}$ are the lattice parameter values at two consecutive temperature $T_1$and $T_2$ respectively.

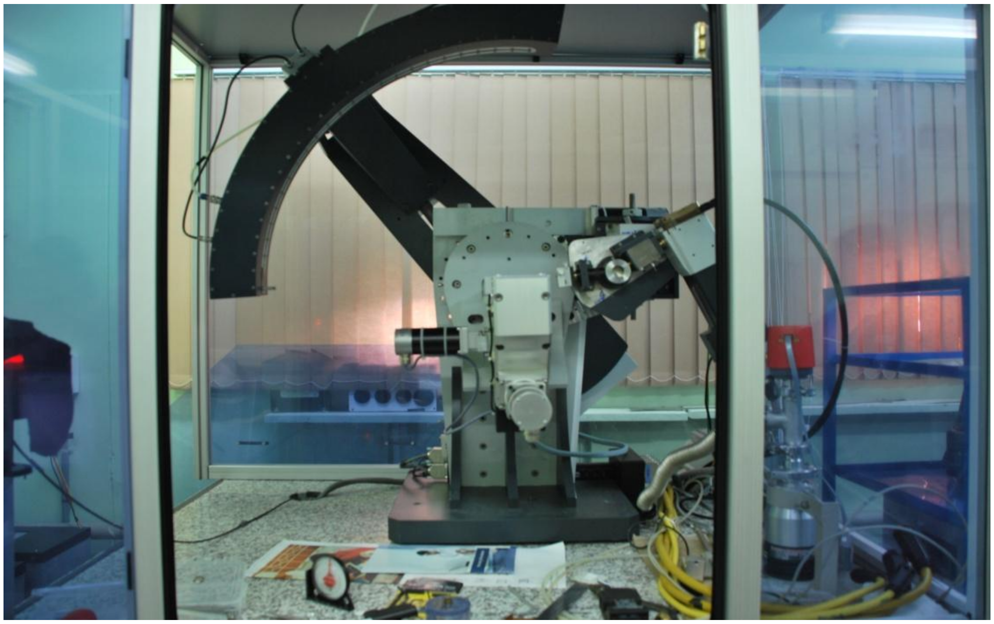

**Fig. 2.3** X-ray Diffractometer used for XRD analysis.

### 2.3.4 Electron probe micro analyzer

An electron probe micro-analyzer (EPMA) is a microbeam instrument used primarily for the *in situ* non-destructive chemical analysis of solid samples. In this, a beam of electrons strikes the specimen surface, interacting with atoms of the specimen to produce x-rays, by measuring the wavelength and intensity of the x-rays produced, it is possible to determine the elements present in the specimen and their concentration. The general design of the EPMA has the following main components:

(i) Electron optics to produce a small-diameter electron beam. This consists of an electron gun plus electron lenses.

(ii) One or more x-ray spectrometers to measure the wavelength and intensity of the characteristic x-ray radiation produced.

(iii) A light microscope to locate an area in the specimen to be examined.

The electron microprobe is capable of carrying out chemical analysis over the complete concentration range from 0.1 to 100% with an acuuracy of ± 2% and sometimes ± 1%. With adequate care in measuring the x-ray intensity and appropriate corrections applied, it is possible to obtain the concentration of the elements with better accuracy.

Microchemical analysis of the films and wear tracks were carried out using a Cameca SX50 electron probe micro analyzer (EPMA) operating at an accelerating voltage of 20 kV and a beam current of 20 nA. X-ray generation volume was restricted to 1 μm. A LiF crystal was used for detecting Fe Kα, Ni Kα and a pseudo crystal PC2 for O Kα, N Kα and C Kα.

### 2.3.5 Scanning electron microscope

A scanning electron microscope (SEM) is a type of electron microscope that produces images of a sample by scanning it with a focused beam of electrons from a tungsten filament or a field emission gun. These electrons interact with electrons in the sample, producing a variety of signals at the surface of solid specimens that can be detected.

The signals that derive from electron-sample interactions contain information about the sample including surface topography, chemical composition, and crystalline structure. XL30 ESEM Philips scanning electron microscope (SEM) fitted with an energy dispersive analysis by X-rays (EDAX) (Fig. 2.4) and a SUPRA 55 Carl Zeiss field emission scanning electron microscope (FESEM) were used to analyze the surface morphology of the films.

**Fig. 2.4** Scanning electron microscope used for characterization.

### 2.3.6 Atomic force microscopy

Atomic force microscopy (AFM) is a nondestructive surface characterization technique, used to analyze the surface morphology, from a few angstroms to micron ranges. Unlike that of scanning tunneling microscope (STM), the AFM technique can be used to analyze conducting as well as insulating materials. The main advantage of AFM is to analyze the surface at ambient condition, without any special sample preparation [185].

In an AFM instrument, a cantilever tip is used to scan the sample surface, while maintaining a constant force (can be attractive or repulsive) between sample surface and tip. The tip radius determines the resolution limit of AFM instruments. Laser light is allowed to fall onto the tip and the deflected laser light is detected by a photo diode. As the cantilever moves across the sample surface, the tip is deflected in z direction in order to maintain a constant force. The deflection in tip results in a deflection in the laser light which in turn is converted to digital signals to form an AFM image.

An AFM instrument can be used in different modes: (i) contact mode, (ii) non-contact mode and (iii) tapping mode [186-187]. In contact mode, when the distance between the cantilever tip and the sample is about a few angstroms, the force is repulsive. In the non-contact mode the cantilever is held at some tens of angstroms from the sample surface by Vander waals forces. Tapping mode images are produced from the force of the intermittent contacts of the tip with the sample surface.

All the images were taken using a Nanoscope E Digital instrument (INC, USA) in the contact mode. A diode laser was used as a light source, a photo diode as detector and a cantilever made up of $Si_3N_4$ with tip radius of 20 nm. Surface roughness was not measured after wear study because of the debris and uneven tribolayer formation which can pose problem to the AFM tip.

### 2.3.7 High resolution transmission electron microscopy

When electron beam in transmission electron microscope (TEM) incidences onto a crystal, the beam is diffracted at certain angles satisfying Bragg's law. The diffracted beams are collected at the back focal plane and observed as electron diffraction pattern. In electron microscope analysis, when transmitted beam is selected to generate images it is called bright field (BF) image, while the diffracted beam is selected it is called dark field (DF) image [188-189].

When more than two beams are used to form electron microscopic images (using a large objective aperture), the mode is called high resolution transmission electron microscopy (HRTEM). As the images are formed due to the phase difference between transmitted and diffracted beam, HRTEM is also called phase contrast microscopy [189]. As the sample is very thin, only phase of incident electron wave gets changed, whereas amplitude remains constant.

The instrumentation of the HRTEM consists of following parts: electron gun, condenser lens, objective lens, magnification and projection systems and detector. Electron beam produced by the gun is focused onto the sample of ~ 100 nm thickness using a condenser lens. The electron beam passes through the sample and the image is formed and recorded on a photographic film or is captured in digital form. The image that is formed is not the atom position; rather it corresponds to the projection of atoms. The contrast in HRTEM is strongly dependent on the sample thickness.

For plane view analysis, films deposited on Si substrates were cut into a dimension of 2 mm × 2 mm × 0.5 mm. The samples were thin down from the opposite of the film side to around 30 μm by grinding followed by dimpling. Then the samples were ion milled using and ion miller (Technoorg Linda IV 4 ion miller) up to electron transparency. Extreme care was taken to remove the surface damage induced by the high-energy ion milling by low energy ion milling in a Technoorg Linda IV 6 Gentle Mill.

**Fig. 2.5** JEOL 2000 EX II High resolution Transmission Electron Microscope**.**

For transmission electron microscopy (TEM) study, a few of the samples of Zr, ZrN and Zr-Al-N of thickness ~50 nm were also deposited at 673 K on KCl crystal in argon and reactive environment of nitrogen. The films deposited on KCl crystal were dissolved in distilled water and some portions of the films were collected on holey carbon coated copper grids. In addition to this, a few samples were directly deposited on holey carbon coated copper grids at 673 K. Typical films thickness was kept about 80 nm based on the deposition rate calculated for the Zr, ZrN and alloyed ZrAlN film deposition. These samples were seen directly in HRTEM without any additional sample preparation steps.

HRTEM studies were carried out in a JEOL 2000 EX II (T) (Fig. 2.5) transmission electron microscope having a point resolution of 0.19 nm at an operating voltage of 200 kV. Phase identification was made from high resolution digital images by calculating power spectra from ~ 10 nm wide crystalline regions and analysing them from inter-planar spacings and angles.

### 2.3.8 Raman spectroscopy

Raman spectroscopy is a nondestructive technique, used to identify the structure, symmetry, crystallinity and phase of material [190]. Raman spectroscopy deals with the inelastic scattering of light with material, resulting in a difference in incident and scattered energy. In Raman spectroscopy, the scattered light is observed in perpendicular direction to the incident light. Scattered light consists of two types of light: (i) light due to Rayleigh scattering, where the frequency is same as that of the frequency of incident light ($\nu_0$) and (ii) Raman scattering where the light frequency is either greater or lesser than that of the incident light. In Raman spectroscopy, the shift in frequency from that of the incident frequency is measured. The shift in the frequency ($\Delta\nu$) in Raman spectroscopy can be written as

$$\boldsymbol{\Delta\nu = \nu_0 \pm \nu_m} \quad \text{..........................(2.8)}$$

Where $\nu_0 - \nu_m$ and $\nu_0 + \nu_m$ lines are called the Stokes and anti-Stokes lines, respectively [191].

Raman spectroscopy was performed using a spectrometer (HR 800, Jobin Yvon, France) with spectral resolution of 1 $cm^{-1}$ equipped with 1800 grooves/mm holographic grating. The samples were placed under an Olympus BXFM-ILHS optical microscope mounted at the entrance of the Raman spectrograph. Argon ion ($Ar^+$) laser of wavelength 488 nm and 514 nm (depending on material) was used as an excitation source. The laser spot size of 3 mm diameter was focused tightly on the sample surface using a diffraction limited (numerical aperture = 0.25 at 10x) long distance objective. The laser power at the sample was kept at 15 mW. The slit width of the monochromator was 400 µm. The back scattered Raman spectra were recorded using supercooled (~383 K) charge-coupled device (CCD) detector.

### 2.3.9 X-ray photo electron spectroscopy

X-ray photoelectron spectroscopy (XPS) is a quantitative spectroscopic technique that can be used to analyze the surface chemistry of a material. It measures the elemental composition, chemical and electronic state of the elements that exist a material. XPS spectra are obtained by irradiating a material with a beam of X-rays while simultaneously measuring the kinetic energy and number of electrons that escape from the top 1 to 10 nm of the material being analyzed. XPS requires ultra-high vacuum (UHV) conditions.

XPS was carried out in a SPECS spectrometer operating at an anode voltage of 13 kV and power level of 300 W. Monochromatic Al Kα was used as the primary source with an energy of 1486.6 eV at base vacuum better than 2.9 x $10^{-9}$ mbar. Ar ions at 5 kV and 50 µA were used for sputtering the specimen surface. Spectra were collected using Specs Lab2 data analysis software and de-convolution of the spectra was performed using CASA XPS system (version 2.3.13Dev30).

### 2.3.10 Nano-indentation

Nano-indentation is used for measuring the mechanical properties at nano scale. In a traditional indentation test, an indenter is pressed into a sample with a known load and is subsequently removed [192-193]. The hardness is then defined as load divided by indentation area, which is the resistance of the material to plastic deformation. But in nano-indentation instrument, load and displacement of the indenter are continuously recorded as the indenter is driven into the sample and removed from it. This technique is widely used for determining the mechanical properties of thin films, coatings, embedded phases, and patterned structures [194-195]. In nano-indentation instrument, the loads are applied electro-magnetically, electro statically or by deflection of a spring. A capacitance gauge or linear variable differential transformer (LVDTs) is used to measure the displacement. The most commonly used tip in the nano-indentation is the Berkovich tetrahedral indenter, which delivers a sharp and axis-symmetric indentation. The typical indentations have depths of 10 to 20 nm and these appear as equilateral triangle with curved sides.

The main purpose of the nano-indentation would be to measure the load - displacement relationship, which can give much information such as Young's Modulus and hardness. The load (P) and indentation displacements (h) are measured during both loading and unloading cycles [196]. In the load-displacement curve, the unloading is generally assumed as purely elastic region. There are three important quantities that must be measured from the load displacement curves (P-h curves). The maximum load ($P_{max}$), maximum displacement ($h_{max}$), and stiffness ($S = dP/dh$), equaling the slope of the upper portion of the unloading curve are determined. Measurement of the properties of thin film on a substrate is a challenging task as the information volume needs to be free from substrate influence. This is achieved by restricting indentation depth to a value of 10% of film thickness. The unloading is a totally elastic recovery process, so the Young's Modulus can be calculated from the unloading curve. The unloading stiffness, S is proportional to the modulus. Therefore, the steeper the unloading curve is, the larger the modulus is. The hardness of the material in general increases as the modulus increases.

Resistance to plastic deformation behaviour is typically characterised by a long elastic strain to failure, which can be described in terms of the ratio between the hardness (H) and the elastic modulus (E). It has been recognised by several authors that the ranking of materials according to their H/E ratio can provide extremely close agreement to their ranking in terms of wear [197]. For thin films toughness cannot be measured directly, various authors report H/E ratio as a ranking parameter since Oberle’s early study [198-200]. In addition to the ratio, H/E determination of $H^3/E^2$ is also considered to evaluate the resistance to plastic deformation from the values of H and E [201].

In this work, indentation hardness and modulus studies were performed using a, nanoindenter (CSM, Switzerland) at a loading rate 10 mN/min and unloading rate 10 mN/min for all samples.

### 2.3.11 Scratch testing

Micro scratch tester (CSM, Switzerland) has been used for characterising the surface mechanical properties of thin films, e.g. adhesion and deformation. The scratch tester characterises the film- substrate system and quantify parameters such as friction and adhesive strength. The technique involves generating a controlled scratch with a sharp tip on a selected area. The tip material (commonly diamond or hard metal (WC)) is drawn across the coated surface under a constant, incremental or progressive load ( Fig. 2.6). At a certain critical load the film will start to fail. The critical loads are very precisely detected by means of an acoustic sensor attached to the load arm but can also be confirmed and collated with observations from a built-in optical microscope.

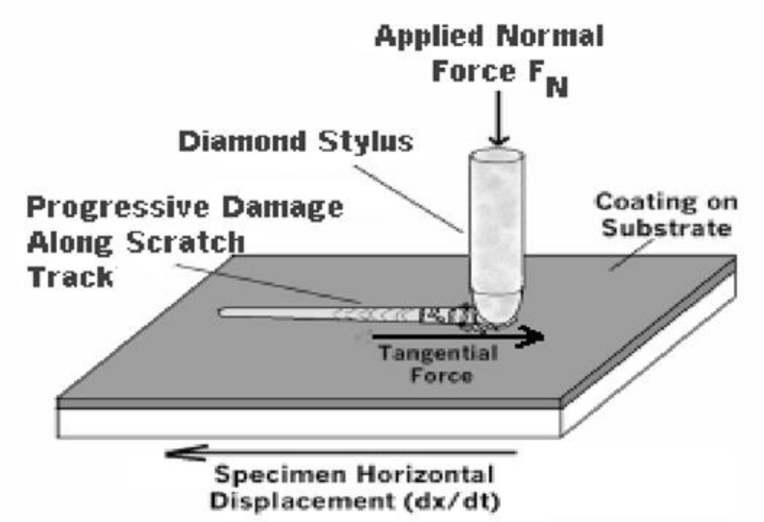

**Fig. 2.6** Scratch test method schematic.

The critical load data is used to quantify the adhesive properties of different film-substrate combinations. In addition to acoustic emission, the scratch tester measures the applied normal force, the tangential force and the penetration depth. These parameters, together with the acoustic emission data, provide the mechanical properties of the film.

### 2.3.12 Tribometry

Tribometer determines the magnitude of friction and wear as two surfaces rub together. A spherical probe is placed on the test sample and loaded with a precisely known weight. The sample is either rotating or reciprocating in a linear track. The resulting frictional forces acting between probe and the sample are measured. The friction coefficient is determined during the test by measuring the deflection of the elastic arm. Wear coefficients for the pin and disk materials are calculated from the volume of material lost during the test. This simple method facilitates the study of friction and wear behaviour of almost every solid state material combination with or without lubricant. Furthermore, the control of the test parameters such as speed, frequency, contact pressure, time and environmental parameters (temperature, humidity and lubricant) allows simulation of the real life conditions of a practical wear situation.

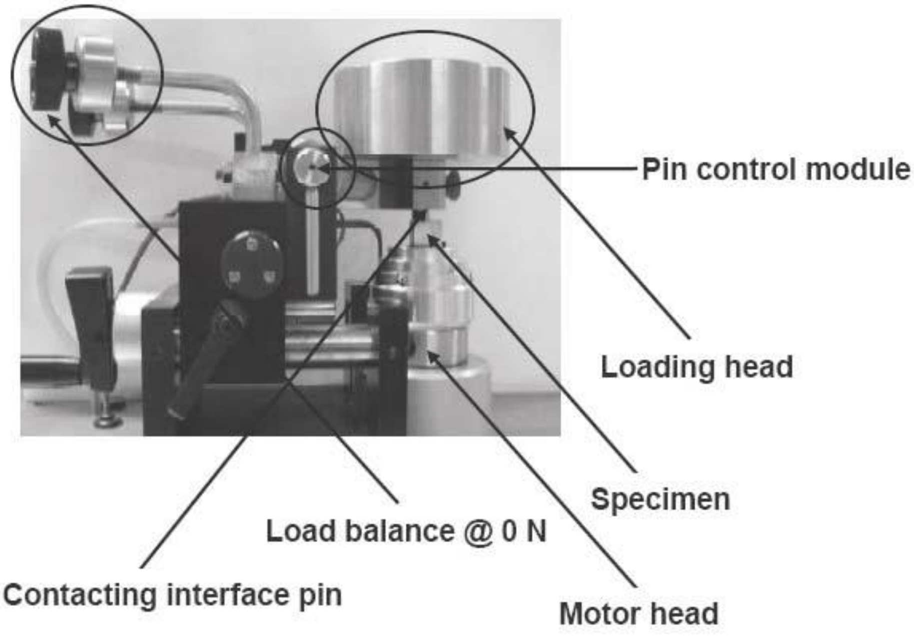

**Fig. 2.7** Experimental set up for tribological study.

The linear tribometer reproduces the reciprocating motion, typical of many real world mechanisms. The instrument measures (Fig. 2.7) a friction coefficient for both the forward and backward displacement of the stroke and the software generates data on Hertzian pressure, static partner and sample wear rates. The reciprocating technique is also very useful for studying the variation over time of the static coefficient of friction. Ball-on-disc CSM micro-tribometer (Switzerland) was used to investigate the wear behavior of the coated and uncoated samples. Three counter bodies namely steel, alumina and silicon nitride ball, with 6 mm diameter, which were loaded with a normal force of 1 N. The tested specimen was slid against the ball at a velocity of 1 cm/s for 1000 cycles. The experiments were performed in ambient and unlubricated condition with relative humidity of 64 to 80 %.

# Chapter 3

# Synthesis and Characterisation of Magnetron Sputtered Zr Thin Films

## 3.1 Introduction

Zirconium (Zr) with hexagonal close packed crystal structure (α-Zr) at room temperature is widely used in nuclear industry and in reprocessing plants owing to its low neutron absorption cross section and its exceptional resistance to corrosion [108]. Structure and mechanical properties of bulk zirconium and its alloys have been extensively studied [86-93]. Though zirconium films have been suggested for different applications [202], only very few studies are reported.

Studies on deuterium and tritium as substitutes for hydrogen in metallic hydrides are of considerable interest for the development of solid targets for the production of neutrons in the $^1$H(d, n)$^3$He and $^3$H(d, n)$^4$He reactions using low-energy (100 kV) accelerators [203]. Characteristics of solid targets such as lifetime, thermal stability, neutron yield, average energy and energy spread of neutrons have been investigated extensively [204-220]. Zirconium and titanium films on high thermal conductivity substrate (Cu, Mo, Ag, Al, W) have been used as deuterium and tritium absorbing metals. These targets have been used for neutron production studies and measurement of its energy [110], calibration of detectors [111] etc. An optimum thickness of target is an important point to access suitable lifetime and maximum neutron yield [221-222].

Basic knowledge of the initial Zr film microstructure is of prime importance as it can influence the reaction and the final product when it is deposited on substrates. Experiments were carried out to see the effect of pulsed DC power supply parameters over the microstructure of thin films. For this purpose Zr films were deposited on a Si (100) substrate and the effects of pulse parameters have been studied.

In the present work, the effect of substrate temperature on the growth characteristics of zirconium films prepared by pulsed DC magnetron sputtering is investigated. The effect of substrate temperature on the surface morphology, nanomechanical and tribological properties is also reported. Results on the scratch test on these films are also presented since it is a widely used method for investigating adhesion of the films with the substrates [223-225]. These data are necessary for the development of Zr films for the applications discussed in Chapter 1.

## 3.2 Pulse Parameters of Pulsed DC Magnetron Power Source

Zirconium target of 99.9% purity was used to deposit zirconium films of thickness in the range 1.2–1.5 µm on to Si (100) substrates with native oxide film. Some of the films for measurement of nanomechanical properties were deposited on titanium modified austenitic stainless steel (D-9 alloy), whose composition is given in Table 2.1. Si was chosen because of its wide application in electronic industry, while D-9 alloy is used as a clad material in breeder reactors.

The effect of pulse parameter and substrate temperature on microstructural properties was studied. During the sputtering, negative pulses were applied to the target, and the duration of pulses can be adjusted by varying the duty cycle of the pulse. Duty cycle can be defined as the ratio of on time and total time of the pulse. Duty cycle, pulse frequency and pulse power were varied to study the effect of these parameters on the microstructure of Zr films.

The effect of substrate temperature on nanomechanical and tribological properties was also measured. The microstructural characterization of Zr films was done using XRD, AFM, SEM and HRTEM. HTXRD was used to study the phase stability at higher temperature. Hardness and elastic modulus were determined by nanoindenation study. Adhesion of the films was tested with scratch tester and tribological studies were carried out using micro tribometer.The deposition conditions and pulse parameters used in the present investigations are given in Table 3.1

**Table 3.1** Experimental parameters for deposition of Zr thin films

| | |
|---|---|
| *Base pressure* | $8\times 10^{-4}$ *Pa* |
| *Operating pressure* | $7.5\times10^{-1}$ *Pa* |
| *Target voltage* | *205–230 V* |
| *Substrate temperature* | *300–873 K* |
| *Pulse power* | *100 W* |
| *Duty cycle* | *20%* |
| *Pulse frequency* | *100 kHz* |
| *Argon flow rate* | *50 sccm* |
| *Substrate to target distance* | *60 mm* |

## 3.3 Results

In the following section, firstly, the effect of some important pulse parameters of the pulsed DC power supply is briefly presented. Secondly, the synthesis and properties of the Zr films prepared at fixed pulse parameters are discussed as a function of substrate temperature.

### 3.3.1 Effect of Pulse Power Supply Parameters

In this section, the effect of pulse frequency, duty cycle and pulse power on the microstructure of Zr films deposited at 773 K is investigated.

### 3.3.1.1 The role of pulse frequency

Fig.3.1 (a) shows XRD patterns of α-Zr films deposited on D-9 alloy substrate at 773 K and at various pulse frequencies (50, 100, 150, 200 kHz) and constant pulse power and duty cycle of 100 W and 20%, respectively. XRD pattern shows that films are polycrystalline in nature and all the reflections are from α-Zr. For the calculation of crystallite size (002) and (101) reflections have been considered at different pulse frequencies and it is found that, the crystallite size decreases more rapidly above 100 kHz of pulse frequency (Fig. 3.1(c)). The deposition rate also decreases as pulse frequency increases (Fig. 3.1 (b)).

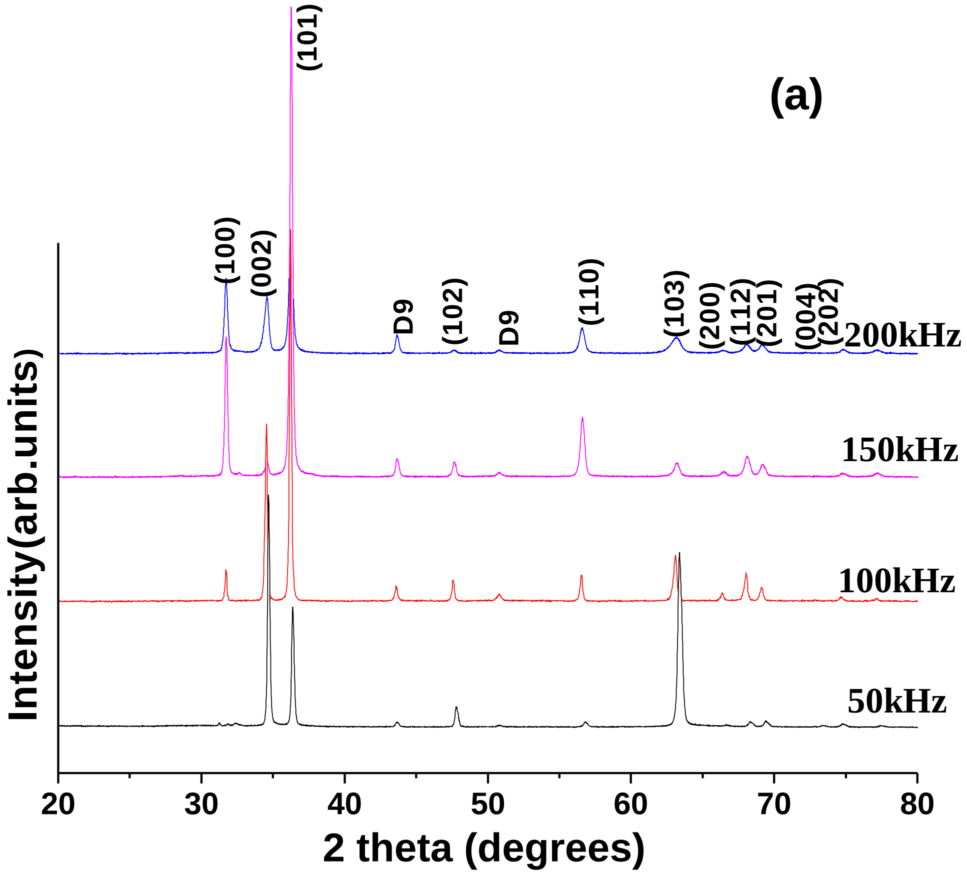

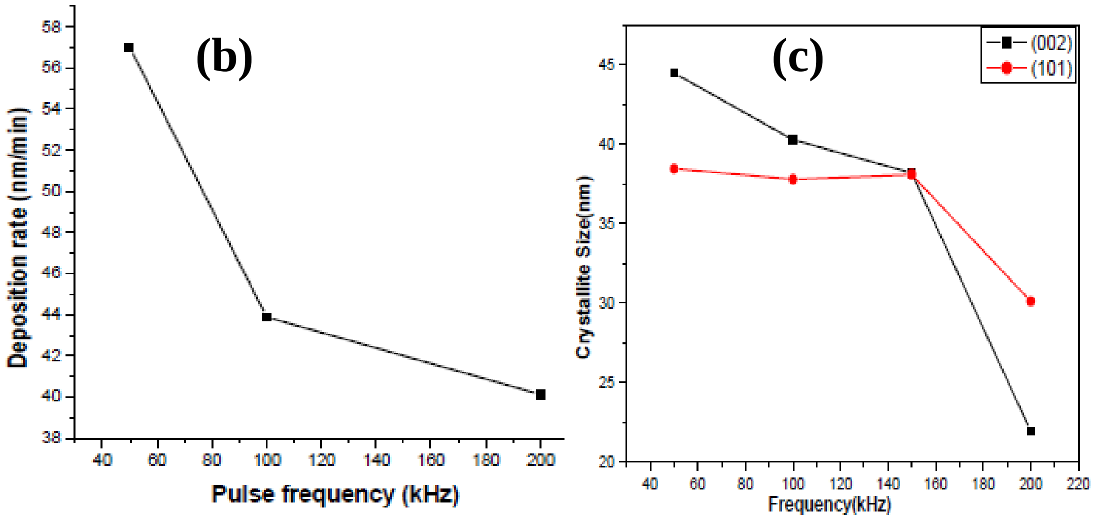

**Fig. 3.1** (a) XRD pattern of Zr thin films as a function of pulse frequency, (b) Deposition rate and (c) Crystallite size versus pulse frequency.

#### 3.3.1.2 The role of duty cycle

Fig. 3.2 (a) shows XRD patterns of α-Zr films deposited on D-9 alloy substrate at 773 K and various duty cycles (10%, 20%, 30% and 40%) at constant pulse power of 100 W and constant pulse frequency of 100 kHz. It is noticed that all the reflections present in the XRD pattern belongs to α-hcp phase of Zr. The crystallite size was calculated using (002) reflection and is found to be decreasing with increasing pulse width. The XRD results also indicate that crystallinity decreases with the increase in the duty cycle (Fig. 3.2(c)). It is also noticed that the deposition rate increases with increase in duty cycle (Fig.3.2 (b)).

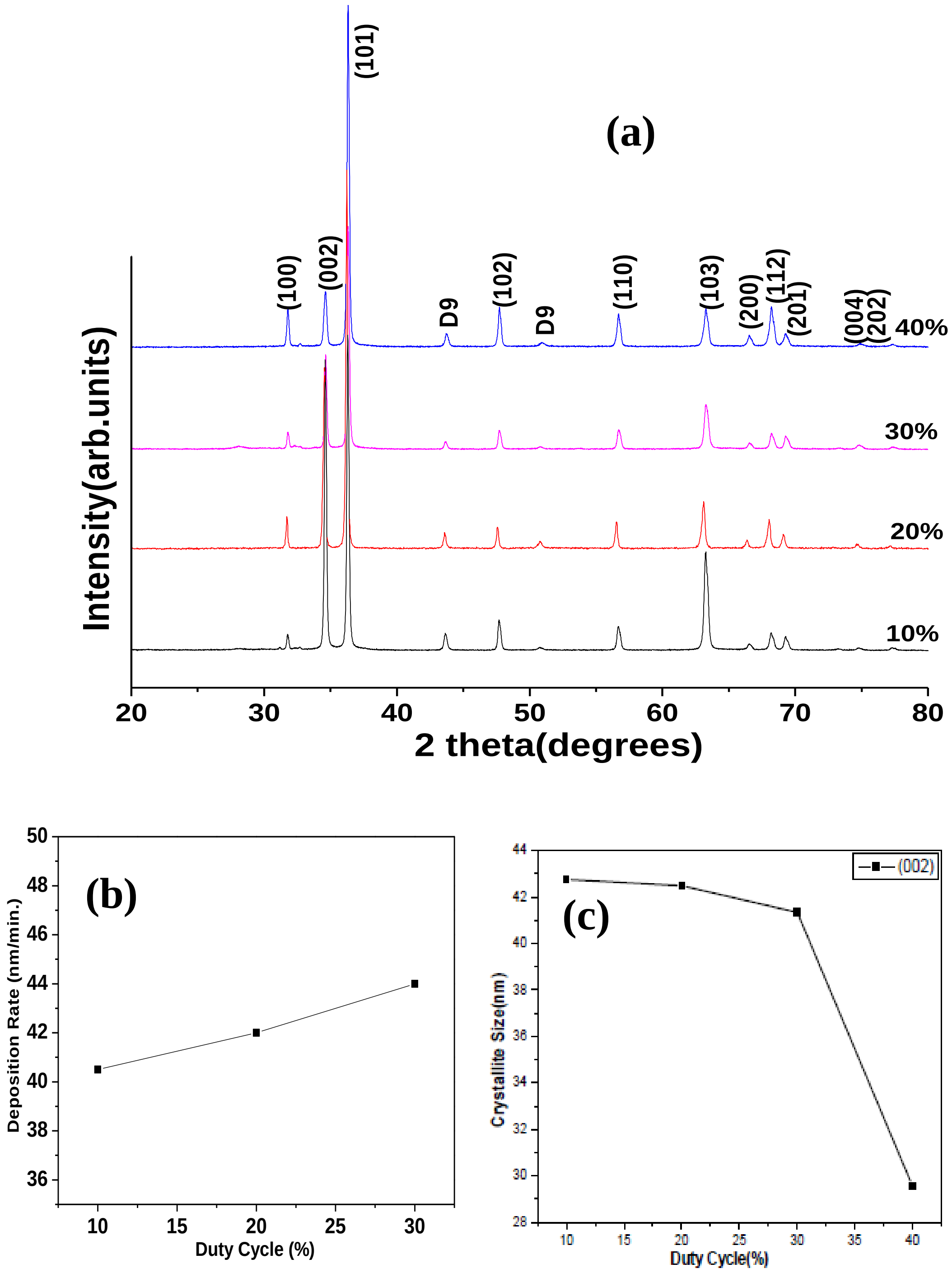

**Fig. 3.2** (a) XRD pattern of Zr thin films as a function of pulse width, (b) Deposition rate and (c) Crystallite size versus duty cycle.

#### 3.3.1.3 The role of pulse power

Fig. 3.3 (a) shows the XRD pattern of Zr thin films deposited on D-9 alloy substrate at 773 K at pulse power of 50, 75, 100 and 125 W, at constant frequency of 100 kHz and constant duty cycle of 20%. Fig. 3.3 (c) demonstrates the qualitative dependence of the crystallite size on the pulsed DC power. It is also noticed that the crystallite size and deposition rate (Fig.3.3 (b) & (c)) increases with increasing power. Crystallite size was calculated using Scherrer's formula for the (002) and (101) reflections of the Zr pattern obtained as a function of different pulse power.

Based on preliminary experiments carried out as a function of pulsed DC power supply parameters, we found that films were crystalline in nature. In all the cases substrate temperature was kept constant at 773 K. We also noticed that except crystallite size change there was no significant change in the surface morphology based on SEM and AFM micrograph. All the films were smooth and no cracks were noticed. Nanoindentation measurement also indicate that the hardness of the film was about 6-8 GPa as a function of pulse frequency and duty cycle variation. It was decided to keep the pulse frequency, duty cycle and pulse power values as 100 kHz, 20% and 100 W, respectively for all the depositions since these values were appearing in the mid range of the respective power supply parameters. The deposition was carried out for a constant duration of 30 minutes.

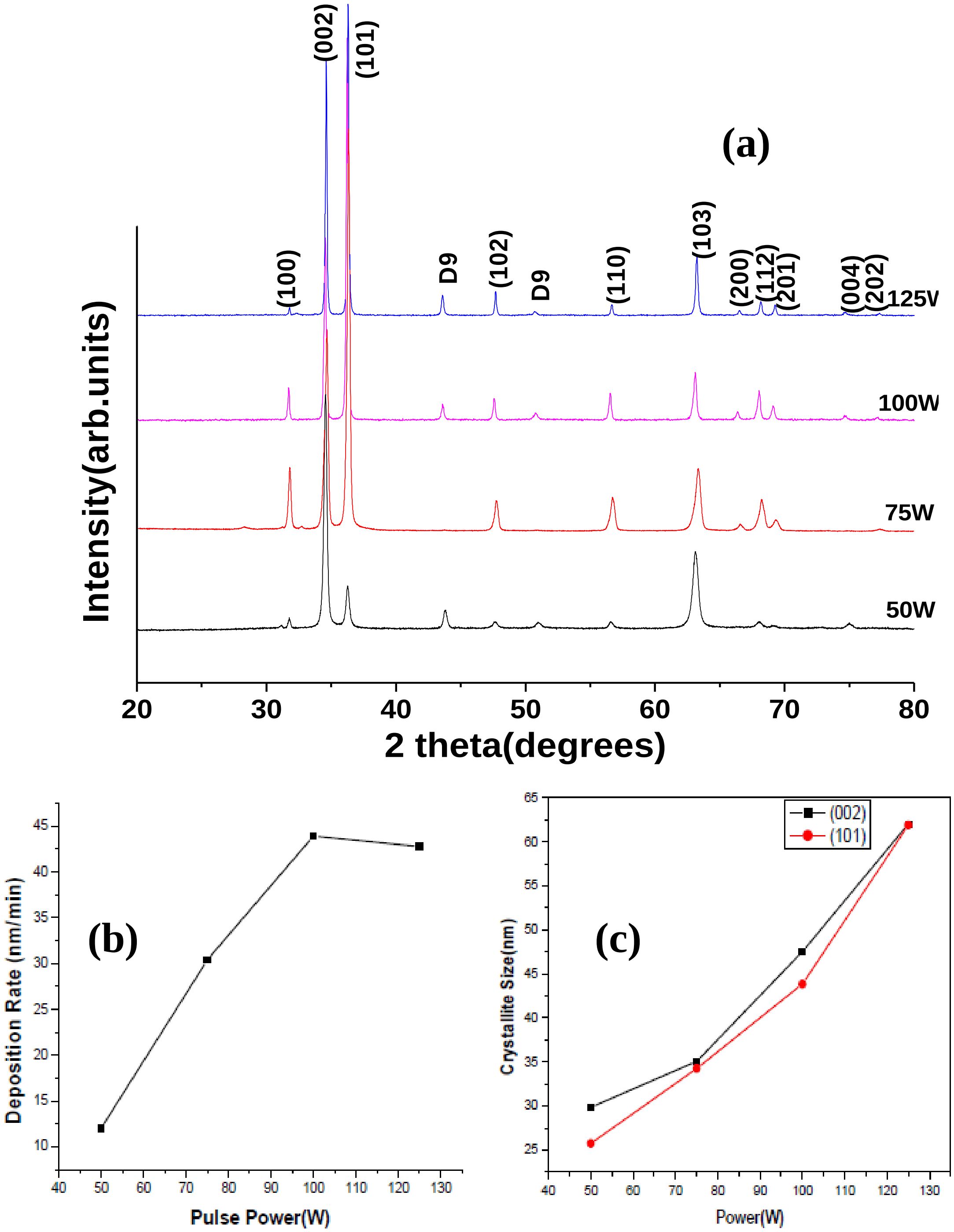

**Fig. 3.3** (a) XRD pattern of Zr thin films as a function of pulse power, (b) Deposition rate and (c) Crystallite size versus pulse power.

### 3.3.2 Microstructural Characterisation

Fig. 3.4 shows the XRD pattern of the films deposited on Si and D-9 alloy substrates in the temperature range 300–873 K. The films are generally polycrystalline in nature and are crystalline even at room temperature. ‘Unit cell program’ has been used to calculate the lattice constant of the films and all the peaks have been considered for the determination of the lattice parameter. The lattice parameters, *a* and *c* are found to be in the range 3.238–3.253 ± 0.002 Å and 5.157–5.21 ± 0.002 Å, respectively in the temperature range 300–873 K (Fig. 3.5). Though the deposition time of 30 minutes was followed in all the experiments, there was reduction in the thickness deposited on D-9 alloy than that on Si substrate. Therefore, in some cases the substrate peaks were noticed.

Though the variation in lattice parameter, *a* is significantly small (<1%), the lattice parameter, *c* increases slightly resulting in the overall increase in the unit cell volume expansion with substrate temperatures $\geq$ 673 K. The crystallite size was calculated using (101) and (002) reflections, since these are the dominant peaks in the diffraction pattern and the variation in the crystallite size corresponding to both the reflections is shown in Fig. 3.6. It is clear that the crystallite size of the films determined using Scherrer’s equation shows a similar trend for both (101) and (002) reflections. For instance, the crystallite size of Zr deposited on D-9 alloy substrate corresponding to (101) reflection increases from ~14 nm to 44 nm with the increase of substrate temperature up to 773 K and there is a decrease in the crystallite size at 873 K.

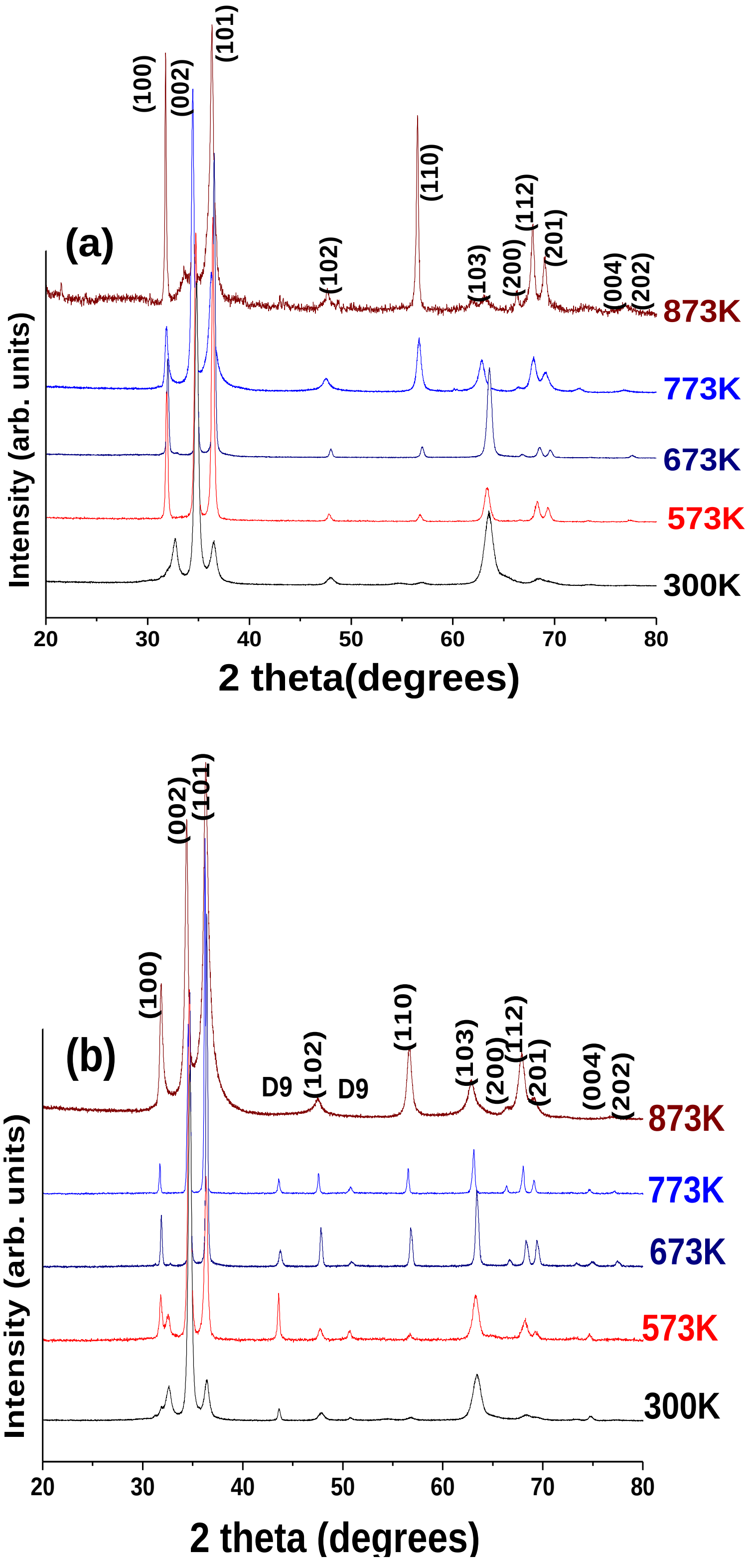

**Fig. 3.4** XRD pattern of Zr films deposited on (a) Si substrate and (b) D-9 alloy substrates as a function of substrate temperature.

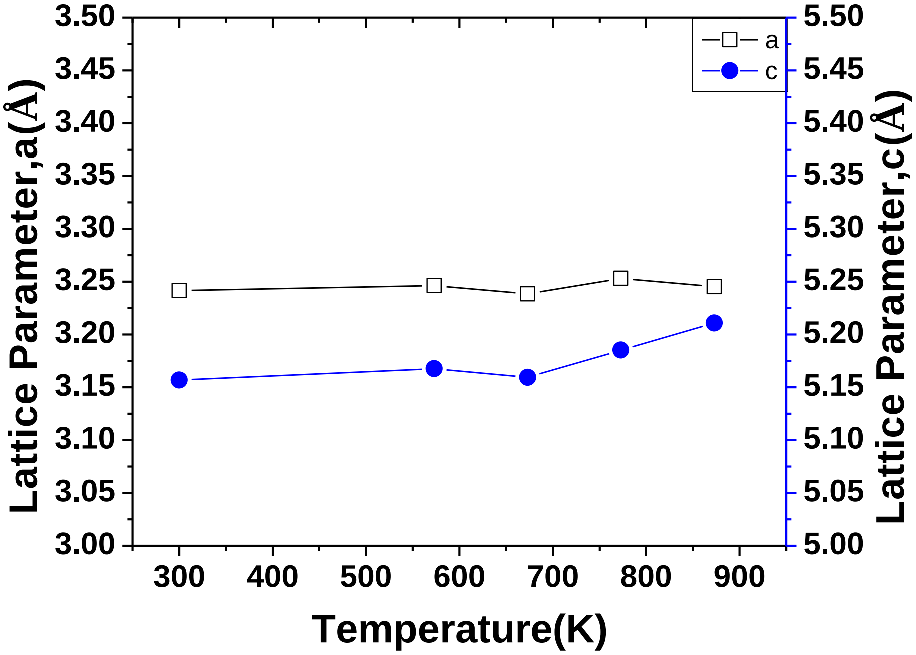

**Fig. 3.5** Variation of lattice parameter of Zr thin films deposited on D-9 alloy substrate as a function of substrate temperature.

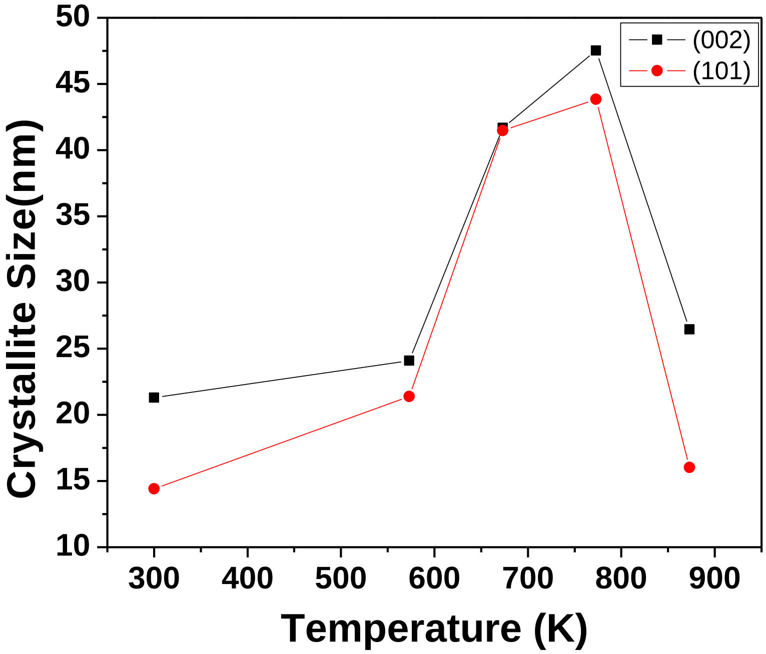

**Fig. 3.6** Variation of crystallite size of Zr thin films deposited on D-9 alloy substrate as a function of substrate temperature.

The crystallite size calculated for films deposited on Si substrates also showed a similar trend. However, the average crystallite size is higher with metallic D-9 substrate compared to that obtained on semiconducting substrate such as Si.

There is also a change in the preferred orientation of the films with increasing substrate temperature and is qualitatively calculated from the texture coefficient of (002) and (101) reflections. The film deposited at 300 K shows predominantly [001] orientation as it is evident from the higher intensity of (002) reflection and it is noticed that with increase in the substrate temperature, [001] orientation decreases slightly. Fig. 3.7 is a histogram describing the interrelationship between the texture coefficient and the substrate temperature.

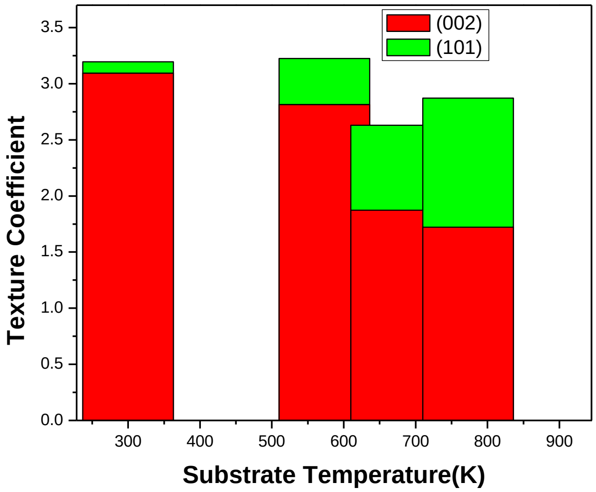

**Fig. 3.7** Variation of the texture coefficient of Zr thin films deposited on D-9 alloy substrate as a function of the substrate temperatures.

Surface morphology of the films was examined in SEM and a typical surface morphology of the film deposited at 773 K on Si substrate (Fig. 3.8 (a)) indicated that the film has a uniform granular structure. A typical cross-sectional image shown in Fig. 3.8

(b) for the film deposited at 773 K, revealed a uniform film thickness and a columnar structure.

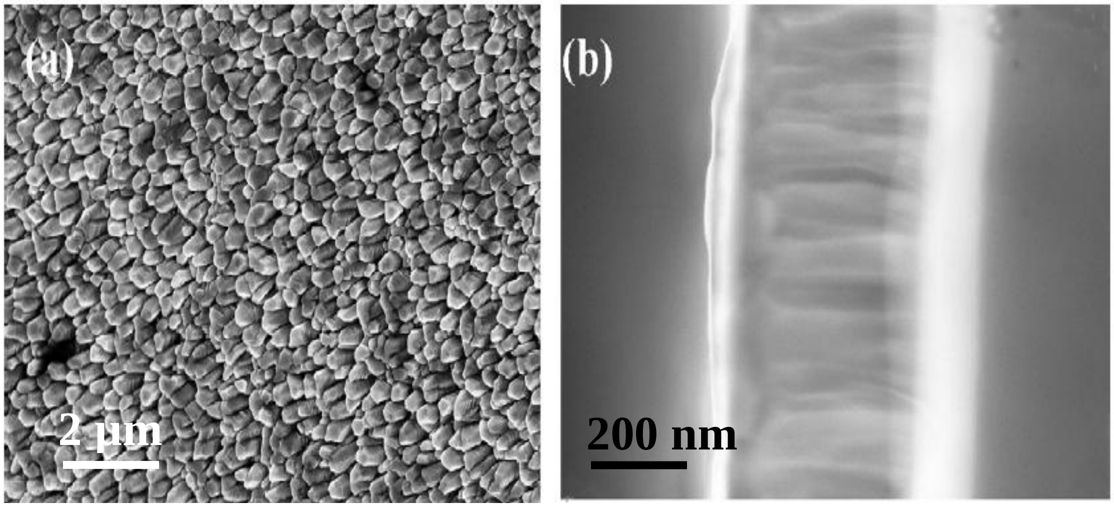

**Fig. 3.8** Zr thin films deposited at 773 K on Si substrate (a) SEM micrograph and (b) Cross sectional image.

AFM images (Fig. 3.9) showed an increased crystallite size with increasing substrate temperature in the range 300–773 K. There is a clear change in the morphology of the crystallites as a function of the substrate temperature. The crystallites are small and the film is porous at temperatures less than 773 K, while the films contain hexagonal shaped crystallites at 773 K. These crystallites appear to grow along the surface normal to the substrate surface (c-axis oriented) in accordance with the x-ray analysis. However, dense and spherically shaped smaller Zr crystallites are seen at 873 K. The root mean square (RMS) roughness of the films as a function of the substrate temperature was also measured by AFM. The RMS roughness is found to decrease from ~ 20 nm to ~ 4 nm with the increase in the substrate temperature from 300 K to 773 K.

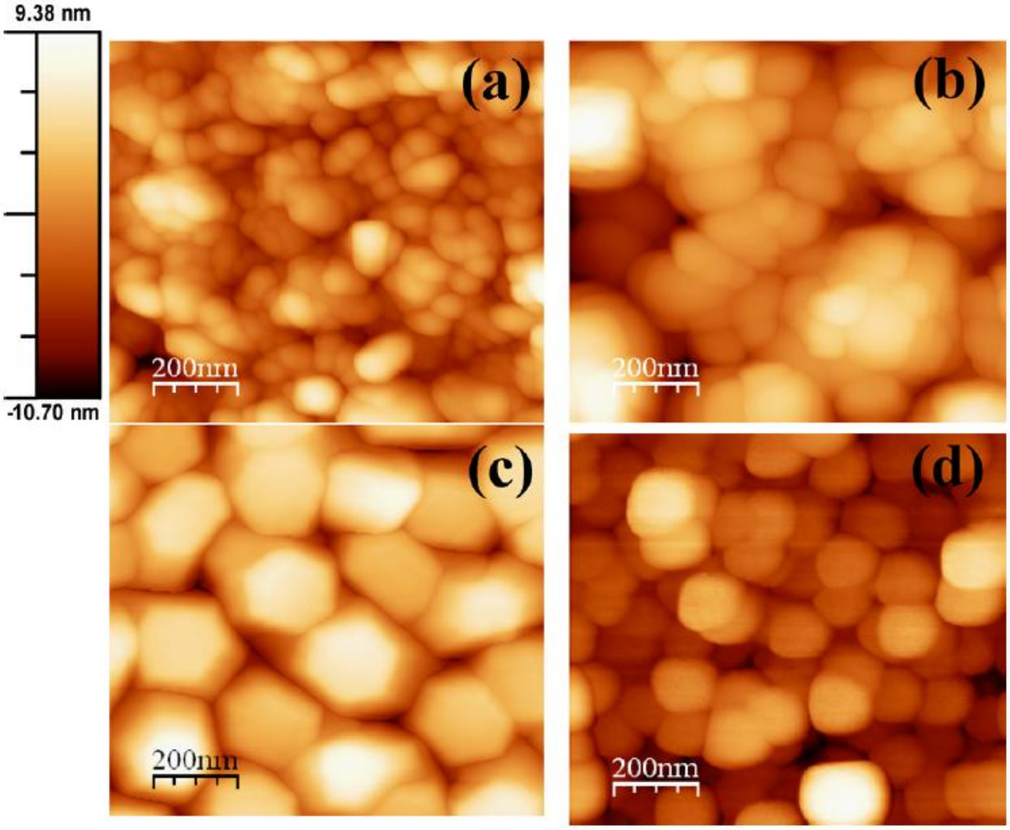

**Fig. 3.9** AFM micrograph of the Zr thin films as a function of substrate temperature (a) 300 K, (b) 573 K, (c) 773 K and (d) 873 K.

These results clearly indicate that the film growth is dominated by nucleation at low substrate temperature (<773 K) and particle coarsening at 773 K in agreement with the metallic alloy film grown by magnetron sputtering [226]. The study revealed that the substrate temperature of 773 K could produce well grown hexagonal crystallites of Zr. Both XRD and AFM studies suggest that unlike refractory oxides [227], the metallic films could be prepared even at room temperature because of low crystallization temperature.

TEM studies show that the film deposited in pure argon atmosphere reveal α-hcp Zr phase of equiaxed nanocrystallites of sizes in the range 40-70 nm range (Fig.

3.10 (a)). Film contains hcp-Zr phase and the polycrystalline diffraction pattern (Fig. 3.10 (b)) corresponding to hcp-Zr phase has been indexed (Table 3.2).

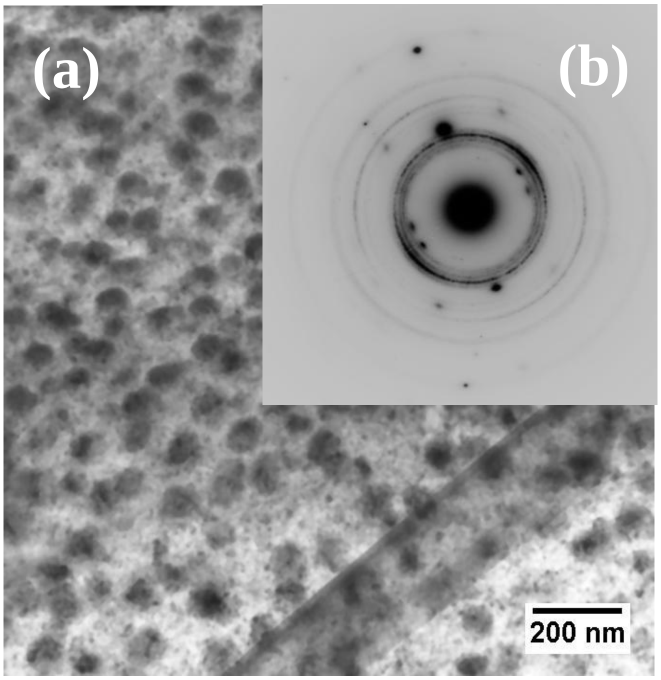

**Fig. 3.10** TEM micrograph of Zr thin films deposited at 673 K (a) Bright field TEM image and (b) Diffraction pattern.

**Table 3.2 Interplanar distance (d) of the Zr film from the SAD pattern of Fig. 3.11**

| **S.No.** | **R($nm^{-1}$)** | **$d_{exp}$ (nm)** | **Zr (hcp) JCPDS# 89-3045** | |
|---|---|---|---|---|
| | | | **d (nm)** | **(hkl)** |
| **1** | ***3.72*** | ***0.269*** | ***0.2799*** | $10\bar{1}0$ |
| **2** | ***3.90*** | ***0.256*** | ***0.2574*** | ***0002*** |
| **3** | ***4.22*** | ***0.237*** | ***0.2459*** | $10\bar{1}1$ |
| **4** | ***4.51*** | ***0.222*** | - | - |
| **5** | ***5.47*** | ***0.183*** | ***0.1895*** | $10\bar{1}2$ |
| **6** | ***5.87*** | ***0.1705*** | - | - |
| **7** | ***6.42*** | ***0.156*** | ***0.1616*** | $11\bar{2}0$ |
| **8** | ***6.8*** | ***0.147*** | ***0.1463*** | $10\bar{1}3$ |
| **9** | ***7.15*** | ***0.140*** | ***0.1399*** | $20\bar{2}0$ |

Fig. 3.11 (a and b) show the high temperature x-ray diffraction (HTXRD) pattern of Zr thin films deposited on Si and D-9 alloy substrates. It indicates that in both the cases Zr films were stable up to 773 K and the films tend to oxidize to form monoclinic $ZrO_2$ and promotes interdiffusion and finally resulting in the decrease of film thickness beyond 773 K. $ZrSi_2$ phase was also noticed at higher temperature. Monoclinic $ZrO_2$ and $ZrSi_2$ phases are shown by symbol (**) and (*), respectively in the Fig. 3.11 (a) and (b), respectively. The lattice parameters (Fig. 3.12) were calculated from the reflections obtained from the HTXRD pattern and it was found to be

$a_T$ (Å) = $3.239 \times 10^{-10} + 1.576 \times 10^{-16}$ (T) + $2.238 \times 10^{-18}$ ($T^2$) and

$c_T$ ( Å) = $5.158 \times 10^{-10} + 1.406 \times 10^{-15}$ (T) +$2.787 \times 10^{-18}$ ($T^2$)

in the temperature range RT-1073 K along the a and c axes, respectively. Second order polynomial fit was used to calculate lattice parameter values.

The average and instantaneous thermal expansion coefficient (Fig. 3.13) of Zr film up to 873 K was calculated using first order derivative of lattice parameter and average CTE values are found to be

$\alpha_{Ta}(K^{-1}) = 5.63 \times 10^{-6} + 1.08 \times 10^{-8} \times (T)$ and

$\alpha_{Tc}(K^{-1}) = 6.25 \times 10^{-6} + 7.36 \times 10^{-8} \times (T)$

along the a and c axis, respectively [ 228] and it is higher than of CTE of the bulk Zr ($5.7\times 10^{-6}$ $K^{-1}$). It is also noticed that average coefficient of the thermal expansion (CTE) was slightly higher than the instantaneous CTE. The average CTE was calculated with the lattice parameter value at room temperatures as a reference. Whereas for the calculation of instantaneous CTE, the lattice parameter values at two successive temperatures were used.

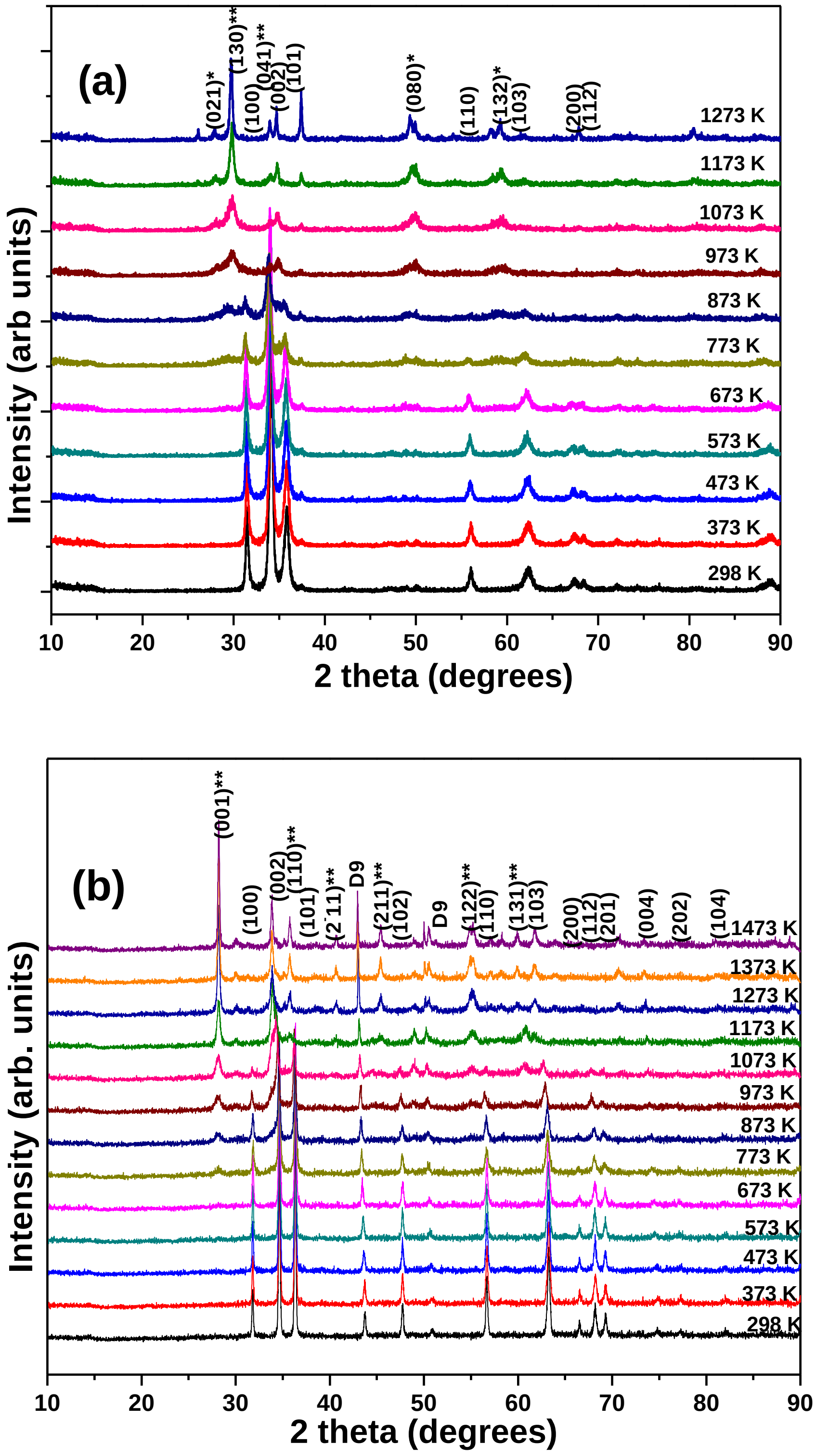

**Fig. 3.11** HTXRD pattern of the Zr films deposited on (a) Si substrate and (b) D-9 alloy substrate as a function of substrate temperature. Monoclinic $ZrO_2$ and $ZrSi_2$ phases are shown by symbol (**) and (*), respectively.

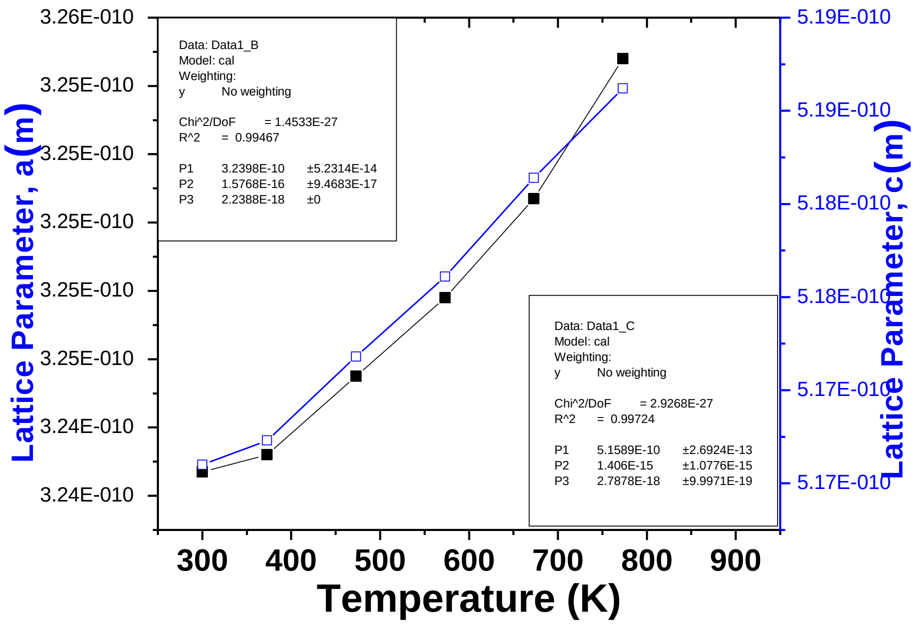

**Fig. 3.12** Variation of lattice parameters *a* and *c* of Zr thin films obtained from HTXRD patterns.

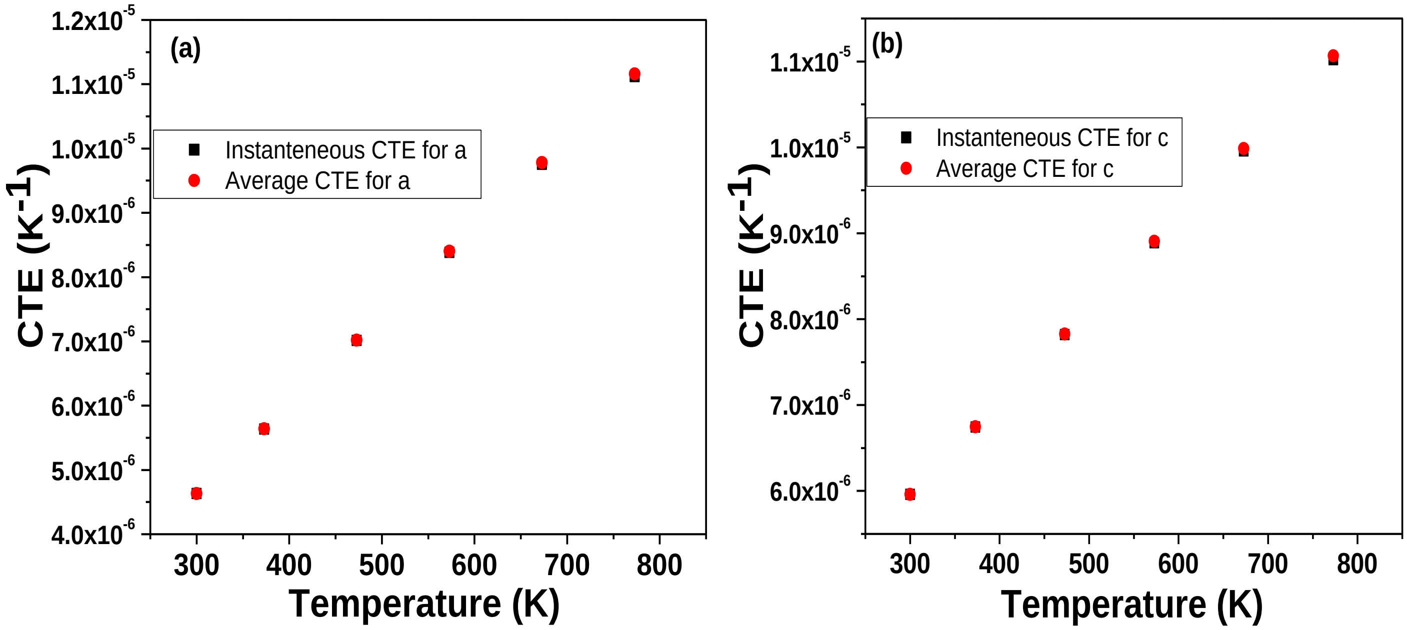

**Fig. 3.13** Variation of average and instantaneous CTE of Zr thin films along (a) a-axis and (b) c-axis as a function of temperature.

### 3.3.3 Nanomechanical Properties

Hardness was determined by microhardness and nanoindentation hardness testers on Zr films of thickness >1 µm deposited on D-9 alloy substrate. The D-9 alloy was chosen in the annealed condition (~ 220VHN) in order to assess the hardness of the film. This material is softer than Si (100) and is used as a clad material for breeder reactors. The microhardness measurements were carried out for the films deposited as a function of substrate temperature using a load of 10 g and the composite hardness was in the range 600–800 VHN. Nanoindentation measurements were also carried out to estimate the hardness of the film. The applied load for nanoindentor was selected such that the indentation depths were in the range from 100 to 150 nm in order to avoid the contribution from the substrate. For measuring hardness and modulus using the nanoindentation method with a Berkovich indenter, indentation load, P, and displacement, h, were continuously recorded during one complete cycle of loading and unloading [229]. Both the microhardness and nanohardness showed a decrease in the hardness for the films with increasing deposition temperature from 300 K to 773 K. For instance, the hardness and elastic modulus of the Zr films was found to be 6.4 and 10.5 GPa and 184, 200 GPa for the films deposited at 773 K and 573 K, respectively.

Scratch test was carried out to determine the films adhesion with the substrate and the film failure, if any. This was further assessed by optical microscopy and scanning electron microscopy during and after the scratch test. The tangential force and acoustic emission signals were measured and recorded during the scratch test process and is used as a supplementary test to identify different film damage levels.

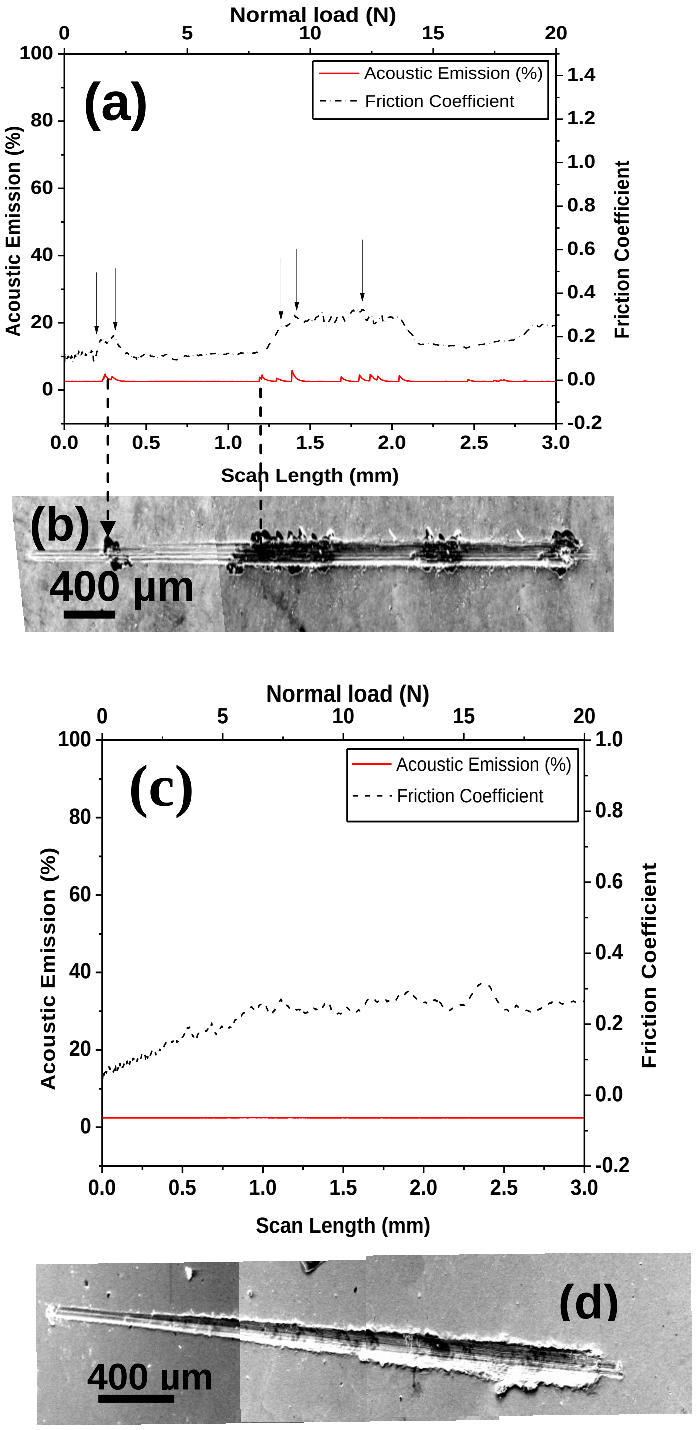

**Fig. 3.14** Scratch test of Zr films on D-9 alloy substrate (a) deposited at 300 K (b) SEM image of the scratch tested region of sample ‘a’, (c) deposited at 773 K and (d) SEM image of the scratch tested region of ‘c’**.**

Scratch tests were carried out with increasing load to determine the critical scratch load and friction coefficient for a given damage level. Scratch test indicates that chipping and flaking of the films depend on the substrate temperature during film deposition. The scratch test was adopted to evaluate the adhesion properties and the critical loads, $Lc_1$ and $Lc_2$. $Lc_1$ is defined as critical load for cohesive failure, whereas $Lc_2$ is defined as critical load for thin film delamination and revealing of the substrate. From the acoustic emission signals, the films deposited at room temperature show failures at first and second critical loads of about ~2 N and 7 N, respectively (Fig. 3.14 (a)) and indicated by arrow, while they do not fail up to a load of 20 N for the films deposited in the temperature range 573–773 K (Fig. 3.14 (c)).

SEM images of the scratch tested regions of the films deposited at 773 K indicate a few debris from the scratched region at loads exceeding 15 N only. Also, the coefficient of friction (COF) of the films remains at about 0.2. However, it rises to higher value (0.3), whenever there is a failure of the films. This is evident from Fig. 3.14(a) in the load range 9–14 N. In contrast, the COF values of the film deposited at 773 K remain at a uniform value in the entire range of the load during scratch indicating an excellent adhesion with the substrate. However, there is a minor difference in the estimated values of the COF of the films deposited at 300 and 773 K owing to the difference in the microstructure.

### 3.3.4 Tribological Studies

Fig. 3.15 shows the coefficient of friction (COF) versus wear distance in Zr thin film deposited on D-9 alloy at 773 K and then wear tested with steel and alumina balls. Steel and alumina counter bodies were chosen due to differences in their hardness values as steel and alumina balls show hardness of 3 and 23 GPa, respectively. The values of the COF of the Zr films on D-9 alloy substrate as a function of wear distance show that during the initial periods of wear testing, the COF rapidly increases to a saturation (peak) value and then gradually reaches a constant value (plateau region). At the beginning of the wear test, there is a severe material transfer between the film and the ball which leads to a rapid increase in the COF value. Beyond the saturation value, the COF remains more or less constant in the plateau region, where the material transfer is slowly reduced and stabilized after the coverage of a large percentage of the test area with the transferred material. In case of failure of the film, the saturation value of the COF varies significantly with wear distance. Fig. 3.15 indicates that the COF of Zr films is lower for the steel ball (100Cr6 steel) than that for the $Al_2O_3$ ball. Fig. 3.16 shows the SEM micrograph of the wear tested region with steel and alumina balls. It is clear that under constant load the width of the wear track is wider with the alumina ball than that of steel ball indicating higher wear rate of the film with the ceramic ball.

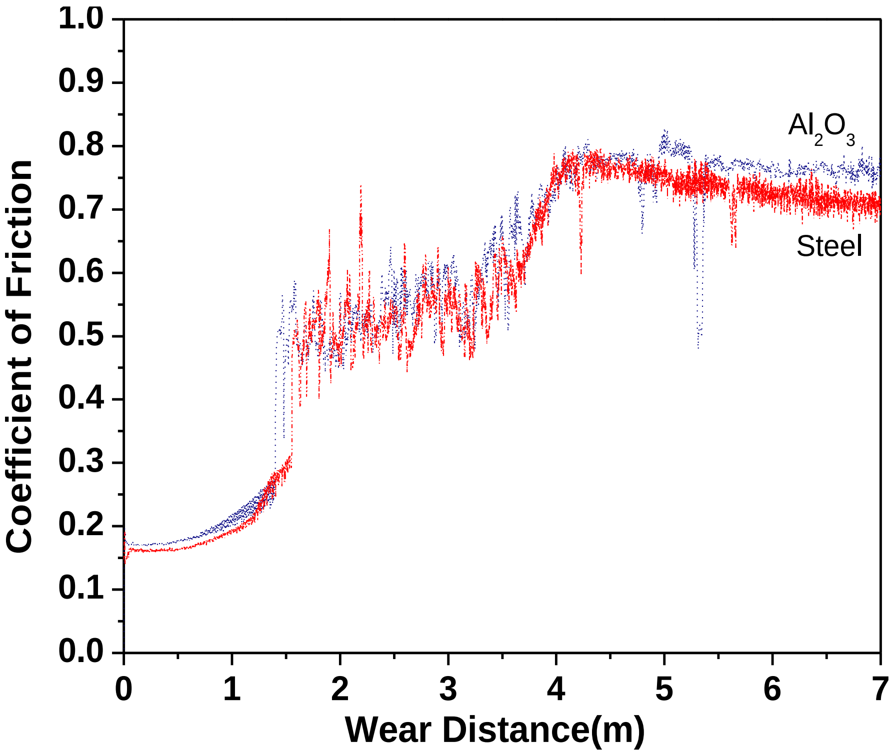

**Fig. 3.15** COF versus wear distance of the Zr thin films deposited on D-9 alloy substrates at 773 K.

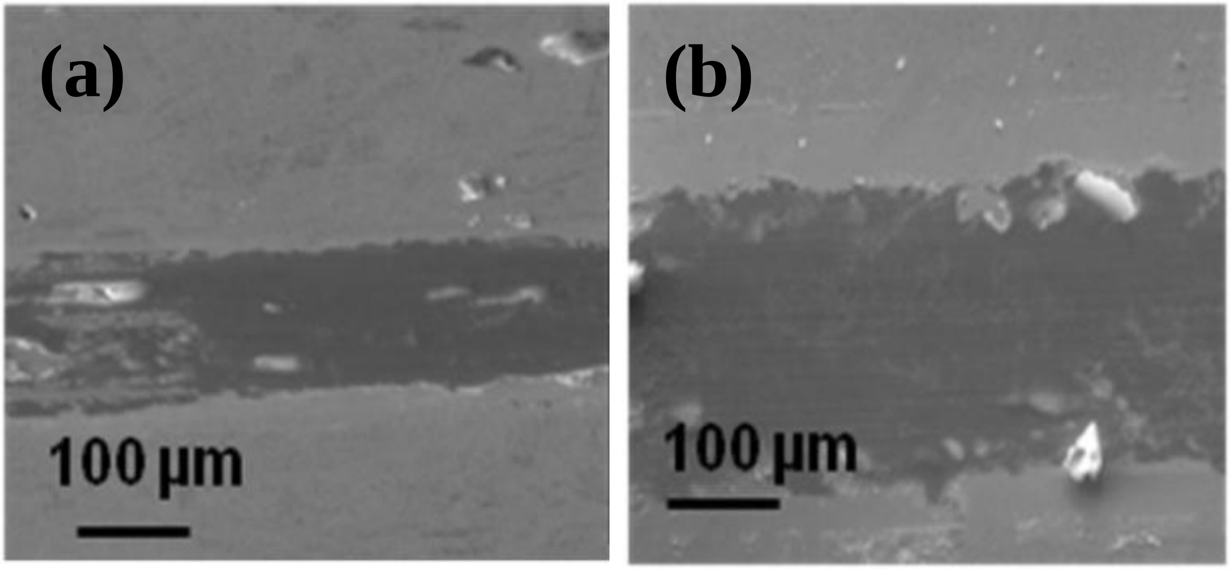

**Fig. 3.16** SEM micrographs of Zr films of the wear tracks obtained with (a) steel and (b) alumina counter bodies.

## 3.4 Discussion

### 3.4.1Effect of Pulse Power Supply Parameters on the Growth Characteristics

The crystallite size and deposition rates of Zr films are significantly influenced by some of the pulse parameters reported in the present work.

The deposition process is usually carried out with pulse frequencies ($f_P$) in the range 50-250 kHz. Increasing the pulse frequency increases the bombardment of target by high energy Ar atoms [40], leading to increased flux of sputtered atoms [231], which results in the decrease in the surface mobility of these species. As a consequence there is a reduction in the crystallite size. The growing film is bombarded by ions of appropriate energy to cause modification of its structure and properties, and the rate of arrival of the ions, and hence the degree of structural modification can be controlled by varying the pulse frequency. Also, the average power dissipated at the target decreases with increasing pulse frequency and at the start of each pulse there is a dead time during which negligible sputtering occurs and the proportion of this dead time increases with increasing pulse frequency and so the deposition rate is lower at a higher frequency [230,232]. The rate of voltage change at the target during the initial stages of the pulse-on period and the maximum negative voltage attained during the pulse-on period is significantly lower at higher frequencies [232]. Since sputtering rate is proportional to power and sputtering yield is proportional to target voltage, both these factors tend to lower the deposition rate at a higher frequency (Fig.3.1(b)).

Pulse width is related to the duty cycle of the pulse and it is indirectly related to pulse frequency also. Duty cycle of any pulse can be defined as the ratio of on time of the pulse (pulse width) and total time (on and off time) of the pulse. Duty cycle is the proportion of time during which supply is operated. It controls the discharge duration of a single pulse and increasing the duty cycle at constant power increases the deposition rate (Fig. 3.2(b)). Duty cycle may provide a useful means for controlling film compositions. This is due to the fact that the duty cycle determine the sputtering duration on each target and the amount of sputtered species. At higher duty cycle, the time for sputtering increases, which reduces the time for discharge for the accumulated species on the target and as a consequence the mobility of the accumulated species in the substrate decreases which leads to a decrease in the crystallite size as seen in the Fig. 3.2(c).

High pulse power in the magnetron sputtering process creates highly energized Ar ions which imparts increased kinetic energy to the sputtered atoms. Therefore, increasing the magnetron discharge power also tends to increase the plasma density. Therefore the surface diffusion of these species is enhanced on the growing surface, which leads to increased crystalline size in these films. Also, the average power dissipated at the target increases with increasing pulse power which increases the deposition rate of the film as seen in Fig. 3.2(b).

### 3.4.2 Microstructural Properties

It has been reported in the section 3.3.2 that the deposition temperature affects some of the microstructural characteristics such as crystallite size, preferred orientation and surface morphology.

The increase in the crystallite size as a function of substrate temperature has been noticed for Si and D-9 alloy substrates but there was more increase in the crystallite size for the films deposited on D-9 alloy substrate than that of the films deposited on Si substrates. This behaviour can be attributed to the increased mobility of the adatoms on the conducting surface of D-9 alloy compared to that of semiconducting substrate [233]. It was also noticed that crystallite size increases up to 773 K and beyond that it decreases. This is inferred from the decrease in broadening of the peaks with increasing substrate temperatures. The increase in the mobility of the adatoms with increasing substrate temperature has promoted a significant increase in the size of the crystallites. However at temperature >773 K, there is a reduction in the crystallite size possibly due to the inter-diffusion of Si to the zirconium films and is evident from the reduction in the intensity of the reflections of Zr deposited at 873 K (Fig. 3.4). The latter behavior has been reported in thin films coated on Si substrates at higher temperatures [178]. It is also noticed that the crystallite size obtained in TEM shows a lower value than those obtained from XRD analysis. It is because the Scherrer formula used to calculate the crystallite size does not take strain into account, though the X-ray peak broadening is caused by crystallite size and strain.

Polycrystalline films deposited on substrates generally show a preferred orientation which depends on the crystal structure, deposition methods and deposition conditions. Preferred orientation mainly depends on the energy of different crystallites and on the balance between thermodynamics and kinetics. Equation 2.2 gives the idea about preferred orientation in the films. Texture coefficient is unity if the film is randomly oriented and it is higher than one, if the film becomes textured. The texture coefficient was calculated from the reflections present in the XRD pattern at different temperature and qualitatively it indicates that there is a change in the preferred orientation of the films with increasing substrate temperature. From the higher intensity of (002) reflection, it is noticed that with increase in the substrate temperature, [001] orientation decreases slightly. Since, thin films of Zr were prepared under non-equilibrium conditions and there is a possibility that as a function of substrate temperature [001] plane is more preferred based on free energy considerations.

Cross sectional SEM micrograph shows a columnar structure for Zr thin films deposited at 773 K. Such columnar structures are reported to be promoted at $T_s/T_m \leq 0.3$ [234], where $T_s$ is the substrate temperature (773 K) and $T_m$ is the melting point of the material (melting point of Zr ~ 2123 K). Metallic films such as Ti deposited under the condition of limited atomic mobility also have exhibited a similar columnar morphology [235].

The roughness and other microstructural property is also affected by deposition conditions, for instance, the root mean square (RMS) roughness decreases from ~ 20 nm to ~ 4 nm for the increase in the substrate temperature from 300 K to 773 K. The decrease in the rms roughness may be due to the densification of the films with increasing temperature. These results clearly indicate that the film growth is dominated by nucleation at low substrate temperature (<773 K) and particle coarsening at 773 K in agreement with the metallic alloy film grown by magnetron sputtering [226].

It is also important to study the thermal expansion behaviour of Zr films for any technological applications. Thermal expansion of a solid is a consequence of an-harmonicity of the interatomic potentials [236], which are significantly influenced by the material structure. The displacement of individual atoms from their equilibrium sites with temperature depends additionally on structural imperfections, which influence the system behavior (e.g. vibrational frequencies). The value of CTE increases as a function of temperature in the present study is in agreement with several metallic materials [237]. However, the CTE of Zr thin films are found to be higher than that of the bulk Zr due to the grain boundary structure in thin films [238].

### 3.4.3 Nanomechanical and Tribological Properties

The two important nanomechanical properties measured using indentation techniques are the hardness (H) and the elastic modulus (E). During indenter withdrawal, only the elastic portion of the displacement is recovered which facilitates the use of an elastic solution in modeling the contact pressure [239-240,196]. The elastic modulus of the indented sample can be inferred from the initial unloading contact stiffness. Nanoindentation hardness is obtained from the indentation load divided by the projected contact area of the indentation.

It is noticed that there is a decrease in hardness of Zr film deposited with increasing substrate temperature. The decreased hardness for the Zr films could be correlated with the stress relaxation in larger crystallites formed at higher growth temperatures. Also, the hardness is known to depend on the crystallite size according to Hall–Petch relation and it generally increases with decrease in crystallite or grain size [241]. In the scratch test, the load at which material fails catastrophically is a measure of scratch resistance. The better performance of the Zr films prepared at higher temperature could be related to the increased inter-diffusion of the substrate elements with increasing substrate temperature. This could possibly help for adhesion of the film with the substrate.

When a wear particle is liberated from the surface, it can influence the tribological behaviour of the contacts in two ways. Loose wear debris in the contact surface may influence friction and wear, although the wear debris may also attach to the counter bodies to form a transfer layer on the surface under investigation. The amount of wear is usually directly proportional to the applied load W and the sliding distance x and inversely proportional to the hardness to the surface being worn away. Thus wear volume $\gamma$ is given by

$$\gamma = \frac{kWx}{H}$$

Where, k- dimensional less wear coefficient dependent on the material pair and their surface cleanliness.

Surface morphology of the wear tracks obtained with steel and alumina balls tested at ambient conditions indicates that the width of the tracks obtained on Zr films is narrower with steel ball than that obtained with alumina ball due to high rate of deformation obtained with the ceramic ball of hardness 23 GPa. Wear tracks contain several scorings with the films tested with ceramic ball than that obtained with steel ball. It is suggested that plastic deformation of the film due to ploughing is the dominant mechanism of friction for thin soft coatings under low loads. There was no indication of any damage to the substrate in these experiments. The COF of the Zr films obtained using the ceramic balls show a slightly higher COF than that obtained using the steel ball (100 Cr6 steel). It is suggested that the increased hardness of the ceramic balls could offer severe abrasive wear and results in the higher values of the COF.

### 3.5 Conclusions

The present study has illustrated that magnetron sputtering could be used for the development of Zr films on metallic and semiconducting substrates to obtain desired mechanical properties.

- The role of pulsed parameters on the microstructure is significant on the crystallite size and deposition rate.
- Formation of α hcp phase of zirconium with [001] preferred orientation is noticed in the temperature range 300–873 K. It is found that crystallite size increases with increasing temperature. The increase in mobility of the adatoms with increasing substrate temperature has caused an increase in the size of the crystallites at temperatures ≤773 K.
- HTXRD showed that Zr films were stable up to 773 K. The average thermal expansion coefficient of Zr film is found to be $\alpha_{Ta}(K^{-1}) = 5.63 \times 10^{-6} + 1.08 \times 10^{-8} \times (T)$ and $\alpha_{Tc}(K^{-1}) = 6.25 \times 10^{-6} + 7.36 \times 10^{-8} \times (T)$ along the a and c axis, respectively.
- Nanoindentation and microhardness measurements showed that the hardness of the films is in the range 6–10 GPa. Scratch test results indicated that the films deposited at higher substrate temperature have better adhesion. The load for the first critical failure is 20 N for the films deposited at 773 K compared to that of 7 N for the film deposited at room temperature.

- Tribological measurement indicates that films tested with steel ball showed a slight decrease in the COF values than for the film tested with alumina ball due to its decreased hardness value.

.

# Chapter 4

# *Microstructural, Nanomechanical and Tribological Properties of ZrN Thin Films*

## 4.1 Introduction

Ceramic hard coatings are of great interest in a number of technological applications due to their improved physical, chemical and mechanical properties [242-245]. Especially, hard nitride coatings are extensively used in many types of cutting operations, where they enhance tool life, improve surface finish and increase productivity [246-247]. ZrN which has a high melting point of 3253 K and a high hardness value of 15 GPa has been found to be suitable for tribological application. Also, ZrN-coated tools have shown significant advantages over TiN coated tools during drilling tests as well as better corrosion and mechanical properties [248-254]. There are a few papers where tribological properties of this coating have been reported [252-253,255-257]. However, the effect of sliding counter body on friction, wear and deformation of ZrN films has not been fully understood.

In the present work, an investigation on sputter deposited ZrN films on Si (100) from a zirconium target in a mixture of Ar/$N_2$ pulsed direct current (DC) magnetron discharges is carried out. Since some of the physical properties of zirconium nitrides highly depend on the microstructure and nitrogen content of the films, the effect of nitrogen flow on the microstructure and nanomechanical properties is investigated. A comparative study of tribological properties of ZrN films deposited on titanium modified austenitic stainless steel (D-9 alloy) substrates by the pulsed direct current (DC) magnetron sputtering is also studied. The effect of substrate temperature on tribological behaviour of ZrN films in correlation with microstructural properties using sliding bodies such as steel, alumina ($Al_2O_3$) and sapphire ($Si_3N_4$) balls is reported.

## 4.2 Experimental Procedure

ZrN thin films of ~0.5–1 µm thickness were deposited on Si (100) substrates with native oxide film and D-9 alloy substrates from a zirconium target using argon and nitrogen gas mixture. The deposition pressure was kept at $7.5 \times 10^{-1}$ Pa. A RPG-50 asymmetric bipolar pulsed DC power supply was used as an electrical power source at 100 kHz, 100 W with a duty cycle of 20% for the thin film deposition. The deposition conditions are given in Table 4.1. In order to see the effect of process parameter such as substrate temperature and nitrogen flow rate on the microstructure and other properties like hardness and wear, ZrN films were deposited on Si and D-9 alloy substrates as a function of these process parameters. XRD, Raman spectroscopy, TEM and AFM were used for microstructural characterization. Nano-indentation and tribometry techniques were used for nanomechanical and tribological chatracterisation of these films. Details of experimental procedure and sample preparation for TEM have been discussed in Chapter 2.

**Table 4.1: Deposition parameters of ZrN films**

| | |
|---|---|
| *Base pressure* | *$8\times 10^{-4}$ Pa* |
| *Operating pressure* | *$7.5\times10^{-1}$ Pa* |
| *Target voltage* | *205–320 V* |
| *Substrate temperature* | *300–873 K* |
| *Pulse power* | *100 W* |
| *Duty cycle* | *20%* |
| *Pulse frequency* | *100 kHz* |
| *Argon flow rate* | *50-40 sccm* |
| *Nitrogen flow rate* | *0-10 sccm* |

## 4.3 Characterisation of ZrN Thin Films

In the following sections, the effect of the substrate temperature and nitrogen flow rate on the microstructure of the ZrN films are discussed. The results on nanomechanical and tribological properties are also presented.

### 4.3.1 Microstructural Characterisation

#### 4.3.1.1 Effect of substrate temperature

The effect of substrate temperature on the microstructure of the ZrN thin films was characterized by X-ray diffraction. Fig. 4.1(a) and (b) show the XRD patterns of the ZrN films deposited on Si (100) and D-9 alloy substrates respectively, at nitrogen flow rate of 1 sccm and in the temperature range 300–873 K. Only a single phase ZrN with (111), (200), (220), and (311) reflections corresponding to fcc structure was observed in accordance with JCPDS File No. 35-0753. The XRD patterns show an increased intensity for (200) reflection indicating a (200) preferred orientation of the films. A slight shift in the 2θ of the diffraction peaks to lower side is also observed with increasing substrate temperature. Determination of the lattice parameter of ZrN films showed a slight increase from 4.57 to 4.59 ± 0.002 Å in the temperature range 300–873 K. The full width at half maximum (FWHM) of the (200) reflection was used to estimate the crystallite size using Scherrer's equation. However, strain in the films was not taken into consideration while measuring the crystallite size. Fig. 4.1(c) shows that the crystallite size of D-9 alloy substrate increases with increasing substrate temperature up to 673 K and at temperatures ≥773 K, the sizes remain at lower values. The average crystallite size was found to be lower for the films deposited on Si substrate than that deposited on metallic D-9 alloy substrate. Though the deposition time of 1 hour was followed in all the experiments, the thickness obtained on D-9 alloy substrate is slightly lower than that obtained on Si (100) substrate. This is evident from the reflections of D-9 alloy shown in Fig. 4.1 (b).

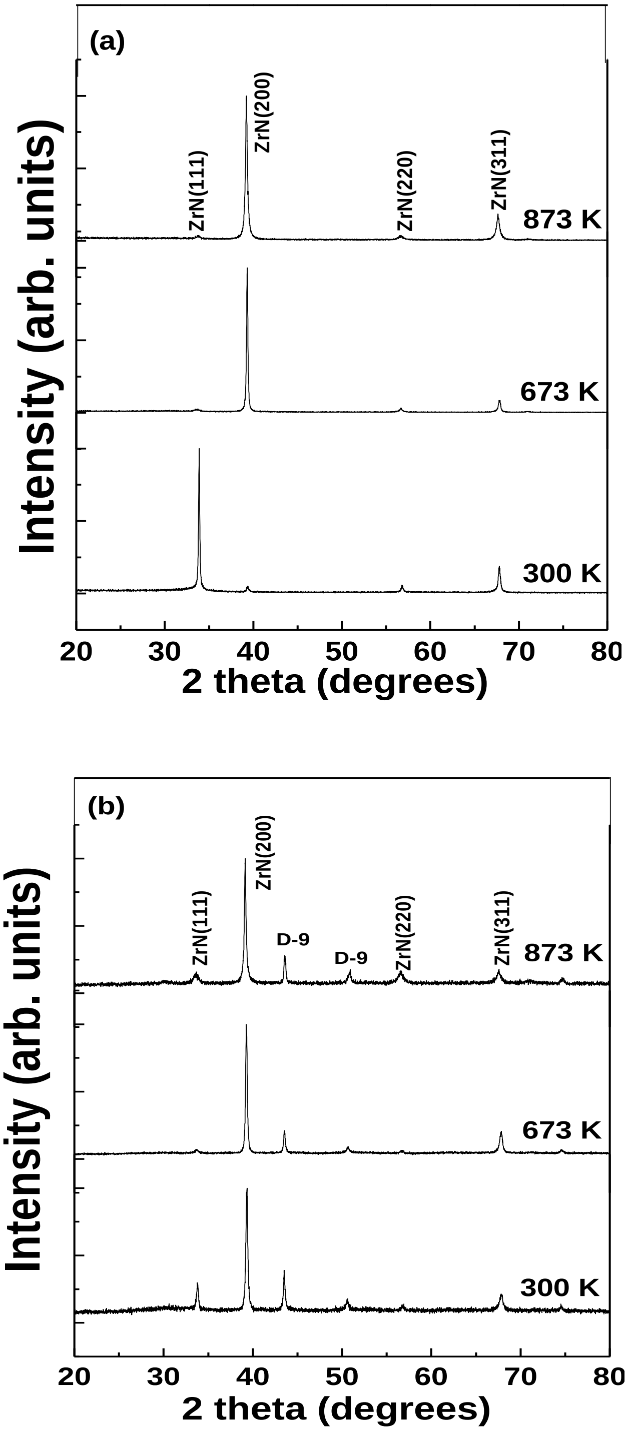

**Fig. 4.1** XRD pattern of ZrN thin films deposited on (a) Si(100) substrate, (b) D-9 alloy substrate.

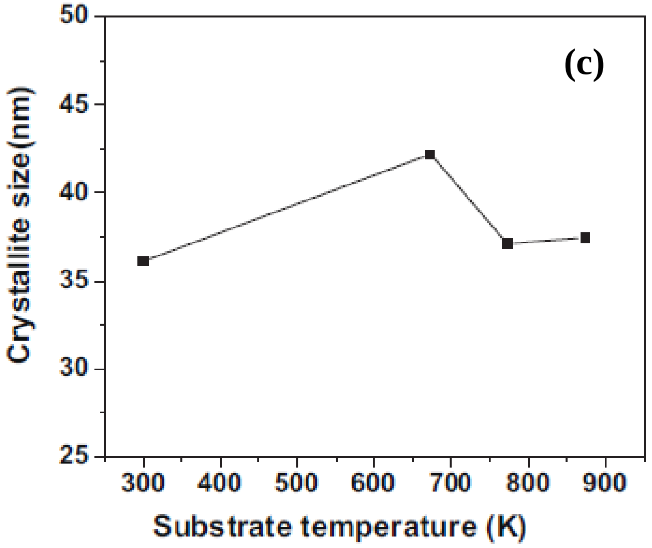

**Fig. 4.1** (c) A plot showing crystallite size versus substrate temperature of ZrN films.

The average surface roughness of the as deposited films was also measured with an atomic force microscope (AFM) and it is found to decrease from 5 nm to 2 nm for the substrate temperature from 300 K to 873 K because of the increased crystallite size and densification with the increasing substrate temperature [258]. Similar results were observed for the Zr films reported in the previous Chapter.

### 4.3.1.2 Effect of nitrogen flow rate

The ZrN films were deposited on Si (100) substrate at 773 K by reactive sputtering as a function of nitrogen flow rates in the range 0.5 - 10 sccm for a constant time of deposition of 60 minutes. The thickness and the deposition rate were found to decrease with increasing flow rate of nitrogen (Fig.4.2). Typical thickness of the films was in the range 0.4-0.8 µm. Films showed golden colour for the films deposited at nitrogen flow rates ≤ 1 sccm and exhibited light gray colour for those deposited at nitrogen flow rate > 1 sccm.

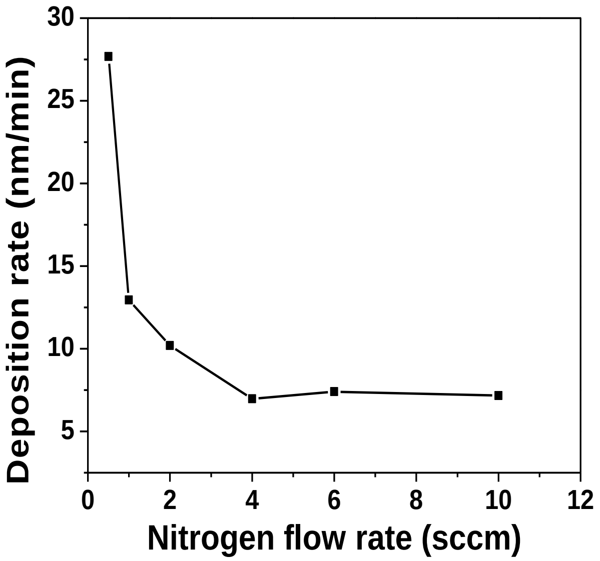

**Fig. 4.2** Deposition rate versus nitrogen flow rate of ZrN films.

XRD patterns (Fig. 4.3 a) show that films deposited in pure argon atmosphere are polycrystalline and exhibit α- Zr phase with (002), (101), (102), (103), (200) and (112) reflections corresponding to hcp structure. It has been reported that the crystalline films of Zr could be formed even at room temperature [259]. It is noticed that films deposited at lower flow rates of nitrogen ( ≤ 1sccm) show (111), (200), (220), (311) and (222) planes corresponding to fcc- ZrN phase. The films deposited at nitrogen flow rates >1 sccm show broadening and reduction in the intensities of (111), (220) and (311) reflections. In addition to the formation of ZrN phase, broad reflections of (111), (511) and (042) corresponding to o- $Zr_3N_4$ phase is identified (Fig 4.3 a) in accordance with the JCPDS file no: 87-0843 [26,68]. It is also noticed that at nitrogen flow rate of 2 sccm, (111) reflection corresponding to $Zr_3N_4$ appears, which is not seen at >2 sccm flow rate of nitrogen. As the nitrogen flow rate increases up to 10 sccm, the films are found to be poorly crystallized.

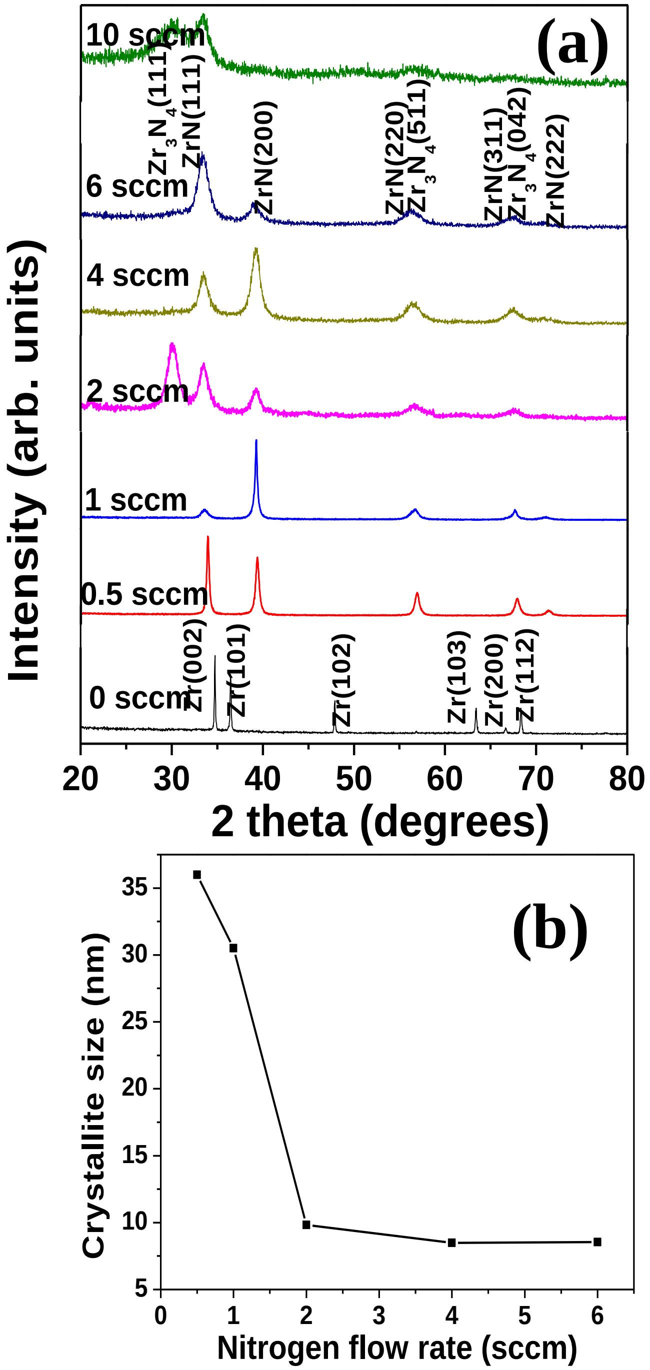

**Fig. 4.3** (a) XRD pattern of ZrN thin films deposited on Si (100) substrate and (b) Crystallite size versus nitrogen flow rate used for the deposition of ZrN films.

The lattice parameter *a* was found to be in the range 4.573-4.602 ±0.003 Å. It was noticed that there is slight increase in the lattice parameter as a function of nitrogen flow rate. The influence of nitrogen flow rate on the intensities of the peaks of ZrN is also noticed. The preferred orientation of the film as a function of nitrogen flow rate was assessed from the intensities corresponding to (111) and (200) planes of the ZrN films. Films show (111) preferred orientation at nitrogen flow rates < 1 sccm and show (200) orientation at nitrogen flow rates ≥ 1 sccm. The film tends to become more polycrystalline with slight increase in the intensity for (111) reflection at the nitrogen flow rate of 6 sccm.

Also, the flow rate of nitrogen shows a significant influence on the crystallite size in ZrN thin films. The crystallite size of Zr deposited with pure argon is ~40 nm, and it decreases from ~35 nm to ~10 nm with an increase in the nitrogen flow rate from 0.5 to 2 sccm (Fig. 4.3 b) and beyond that it remains constant. The above crystallite sizes were calculated using Scherrer's formula which does not take strain into consideration and only the strongest reflection of Zr and ZrN was used to determine the crystallite size.

Figure 4.4 shows the Raman spectra of the films deposited in the nitrogen flow rate range of 1 to 4 sccm. The spectra indicates the Raman peaks at 170 $cm^{-1}$, 209 $cm^{-1}$, 499 $cm^{-1}$ , 710 $cm^{-1}$ and 980 $cm^{-1}$ of ZrN. The peak positions obtained from the film is found to be consistent with the reported values of ZrN [260]. It is also seen that at higher nitrogen flow rates, Raman lines at 710 $cm^{-1}$and 980 $cm^{-1}$ tend to disappear indicating the tendency for loss of crystallinity of ZrN**.**

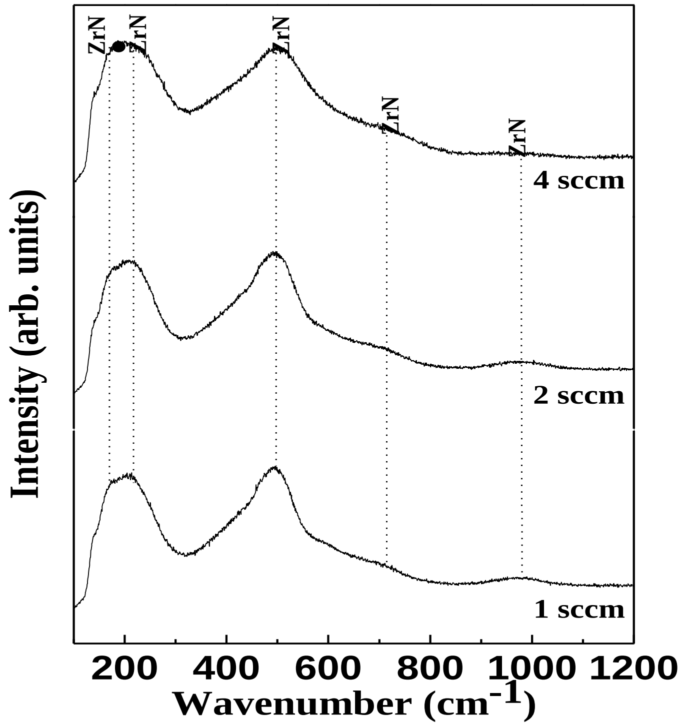

**Fig. 4.4** Raman spectra of ZrN thin films as a function of nitrogen flow rate.

Elements such as zirconium, nitrogen, oxygen, and carbon as a function of nitrogen flow rates were identified in the films by assigning the corresponding XPS peaks. Fig. 4.5(a) is the representative XPS spectra at 1 sccm flow of nitrogen showing the photo-electron peaks from Zr, N, O and C. After removing the surface contaminants through argon ion sputtering, the high resolution spectra were recorded for each individual photo electron peak.

Fig. 4.5 (b) and (c) show the high resolution XPS spectra corresponding to Zr 3d and N 1s, respectively obtained after cleaning the film surface by sputtering for 60 seconds. After deconvolution, the main Zr 3d peak is found to consist of individual peaks corresponding to ZrN and $ZrO_2$. In addition, evidence is obtained for the contribution from a phase having chemistry intermediate between ZrN and $ZrO_2$.

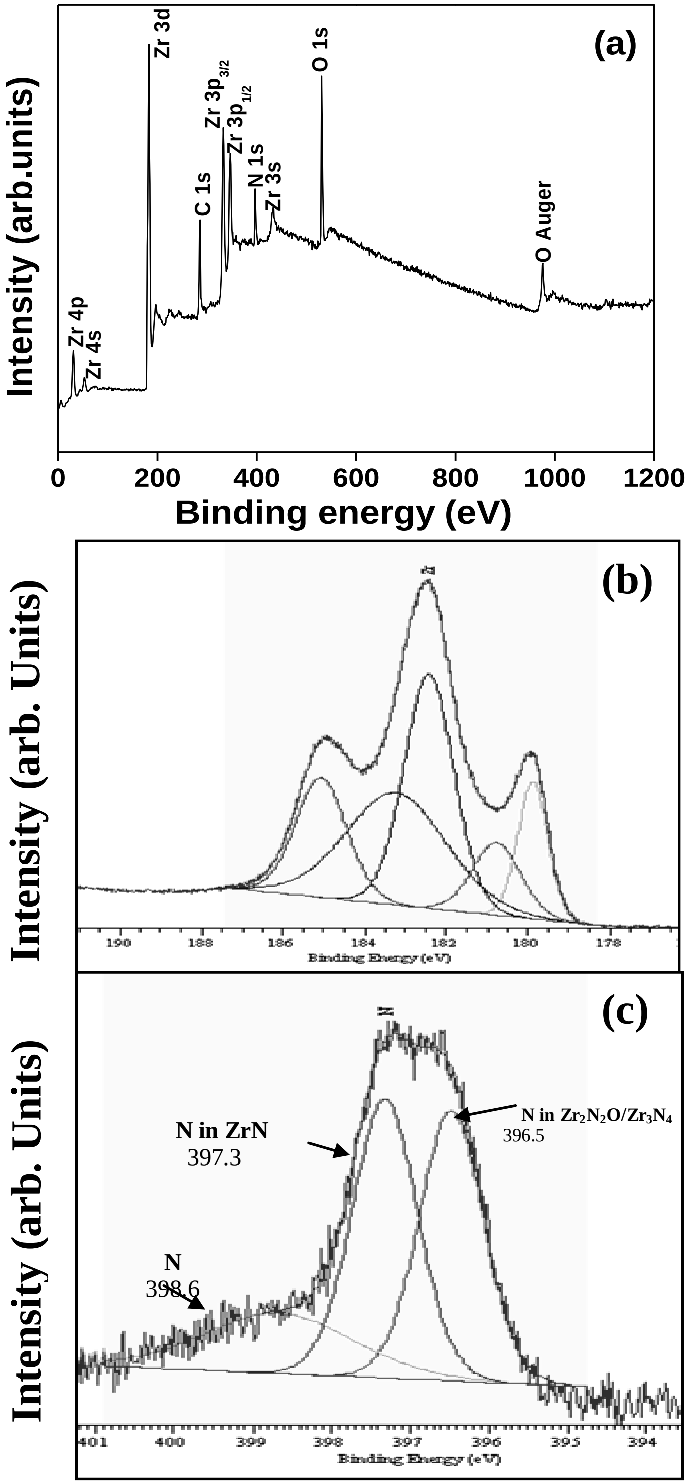

**Fig. 4.5** (a) XPS spectrum of ZrN film deposited at 773 K, 1 sccm showing the presence of Zr,N,O and C in the as deposited films, (b) De-convoluted spectra of Zr after in-situ sputter cleaning and (c) De-convoluted spectra of N after in-situ sputter cleaning.

Comparing the binding energy values with the available information in the literature on oxidized ZrN films [261-263], this phase is found to be related to an oxy-nitride such as $Zr_2N_2O$. Binding energy values for Zr, ZrN, $ZrO_2$ and $Zr_2N_2O$ obtained in this study compared well with the already reported values in the literature [264-267]. Based on similar analysis carried out on all the specimens, it is observed that the metallic phase of Zr is present only at the nitrogen flow rate $\leq 1$ sccm and a slight shift in the binding energies of ZrN is noticed at higher flow rates of nitrogen. High resolution N 1s spectra is found to be asymmetric with contribution from nitrogen peaks corresponding to ZrN at 397.3 eV [264-266], $Zr_2N_2O$ at 396.5 eV [261,265] and elemental nitrogen at 398.6 eV [261,267].

The elemental nitrogen peak may correspond to adsorbed nitrogen. Zirconium deposited freshly on a substrate is found to react readily with $O_2$, CO, $CO_2$ and hydrocarbons, forming oxides and carbides which are essentially unreactive, and the gettering rate of zirconium for $N_2$ is observed to be smaller than that for $O_2$ [268-269]. Therefore, it is possible that small amounts of Zr-O compounds could form while depositing ZrN in the present study.

TEM studies show that the film deposited at the nitrogen flow rate of 1 sccm reveal fcc-ZrN and small amounts of o- $Zr_3N_4$ phase of equiaxed nanocrystallites of sizes in the range 4-9 nm (Fig. 4.6 a and b). Diffraction pattern corresponding to first, fourth and sixth rings of the inset of Fig. 4.6(b) gave evidence of o- $Zr_3N_4$ phase (Table 4.2). However, $Zr_3N_4$ phase was not identified by XRD in the films deposited at 1 sccm flow of nitrogen due to its lower limit of detection upto 5 wt. %. The films deposited at 2 sccm is seen to be nanostructured with nanocrystallites of sizes in the range 4-9 nm (Fig.

4.7 a & b). It is also seen that film contains fcc-ZrN and o-$Zr_3N_4$ phase and the polycrystalline diffraction patterns corresponding to these phases are shown in the Fig. 4.7 (b). First, fourth and sixth rings of the diffraction pattern give evidence for the presence of o-$Zr_3N_4$ phase. The zirconium nitride film deposited at 4 sccm of nitrogen flow rate is also seen to be nanostructured with nanocrystallites in the range 4-9 nm (Fig. 4.8 a & b) and the film mostly contains fcc-ZrN along with o- $Zr_3N_4$ phase and the diffraction pattern corresponding to these phases have been indexed and the d-spacing are shown in Table 4.2.

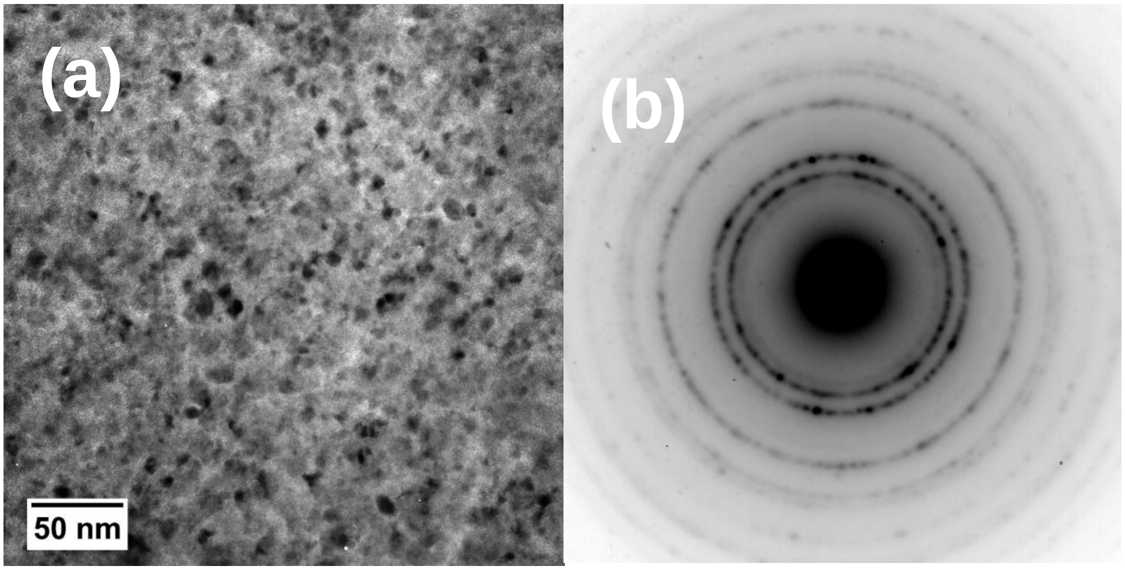

**Fig. 4.6** (a) Bright field TEM image and (b) Diffraction pattern from ZrN film deposited on KCl crystal at 673 K and 1 sccm flow rate of nitrogen.

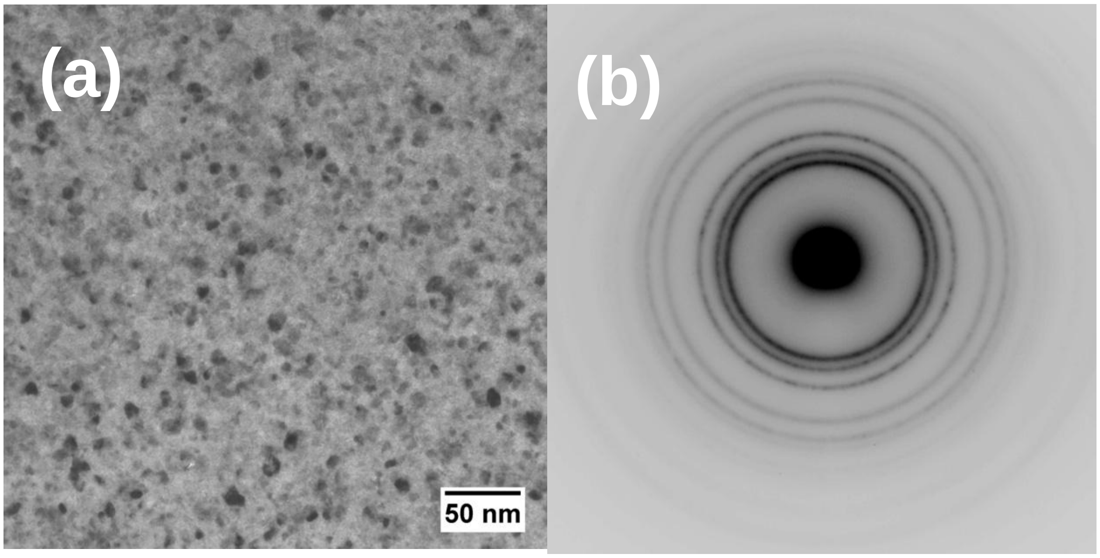

**Fig. 4.7** (a) Bright field TEM image and (b) Diffraction pattern from ZrN film deposited on KCl crystal at 673 K and 2 sccm flow rate of nitrogen.

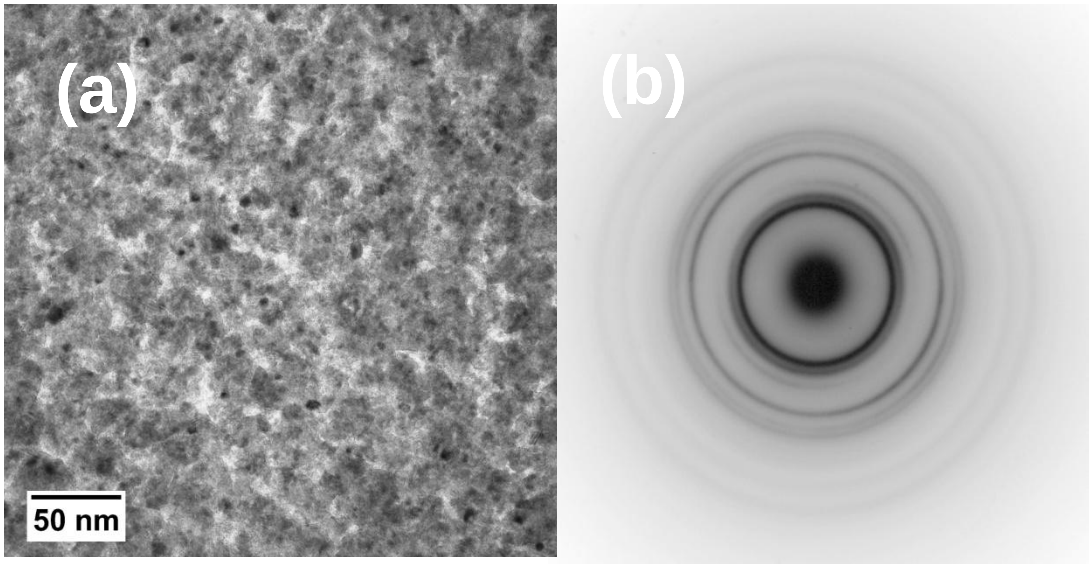

**Fig. 4.8** (a) Bright field TEM image and (b) Diffraction pattern from ZrN film deposited on KCl crystal at 673 K and 4 sccm flow rate of nitrogen.

**Table 4.2 Calculated d-spacings of ZrN and $Zr_3N_4$ phases from the selected area diffraction patterns of the films deposited at 1 and 4 sccm of nitrogen flow rate**

| Ring No. | $d_{exp}$ (nm) | Phases at nitrogen flow rate of 1 sccm | | | | $d_{exp}$ (nm) | Phases at nitrogen flow rate of 4 sccm | | | |
|---|---|---|---|---|---|---|---|---|---|---|
| | | ZrN JCPDS# 65-0972 | | $Zr_3N_4$ JCPDS# 87-0843 | | | ZrN JCPDS# 65-0972 | | $Zr_3N_4$ JCPDS# 87-0843 | |
| | | d (nm) | (hkl) | d (nm) | (hkl) | | d (nm) | (hkl) | d (nm) | (hkl) |
| 1 | 0.289 | - | - | 0.2897 | 111 | 0.302 | - | - | 0.2988 | 111 |
| 2 | 0.261 | 0.2641 | 111 | 0.2606 | 211 | 0.266 | 0.2641 | 111 | 0.2638 | 211 |
| 3 | 0.224 | 0.2287 | 200 | 0.2256 | 131 | 0.232 | 0.2288 | 200 | 0.2355 | 131 |
| 4 | 0.177 | - | - | 0.1773 | 160 | 0.184 | - | - | 0.1838 | 421 |
| 5 | 0.159 | 0.1618 | 220 | 0.1599 | 511 | 0.166 | 0.1618 | 220 | 0.1654 | 511 |
| 6 | 0.150 | - | - | 0.1503 | 360 | 0.157 | - | - | 0.1576 | 360 |
| 7 | 0.135 | 0.1379 | 311 | 0.1349 | 042 | 0.140 | 0.1379 | 311 | 0.1402 | 042 |
| 8 | 0.130 | 0.1321 | 222 | 0.1297 | 650 | 0.118 | 0.1143 | 400 | 0.1181 | 480 |

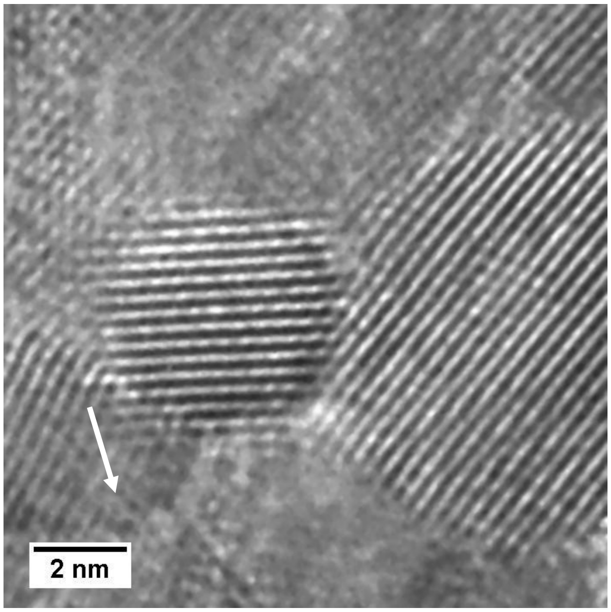

**Fig. 4.9** A typical HREM image of ZrN films deposited on KCl at 4 sccm of nitrogen flow rate at 673 K.

Fig. 4.9 shows the HREM micrograph of the nanocrystalline thin film deposited at 4 sccm containing fcc-ZrN and o-$Zr_3N_4$ nanocrystallites with crystallite sizes in the range 4 - 9 nm. TEM shows lower crystallite size than that obtained from XRD because the Scherrer formula used to calculate the crystallite size does not take strain into account, though the X-ray peak broadening is caused by crystallite size and strain. Besides the formation of secondary phase, lattice bending and dislocations (indicated by an arrow) are noticed within the nanocrystalline grains.

Fig. 4.10 (a) shows the high temperature x-ray diffraction (HTXRD) pattern of ZrN thin films deposited on Si substrates. It indicates that ZrN film is stable up to 973 K and the film tends to oxidize to form monoclinic $ZrO_2$ and promotes interdiffusion and finally resulting in the $ZrSi_2$ beyond 973 K. The lattice parameter (Fig 4.10(b)) was calculated from the reflections obtained from HTXRD patterns and it is found to be $a_T$ (Å) = $4.568 \times 10^{-10} + 3.119 \times 10^{-15}$ (T) + $2.2497 \times 10^{-19}$ ($T^2$) in the temperature range RT-1073 K Second order polynomial fit was used to calculate lattice parameter values.

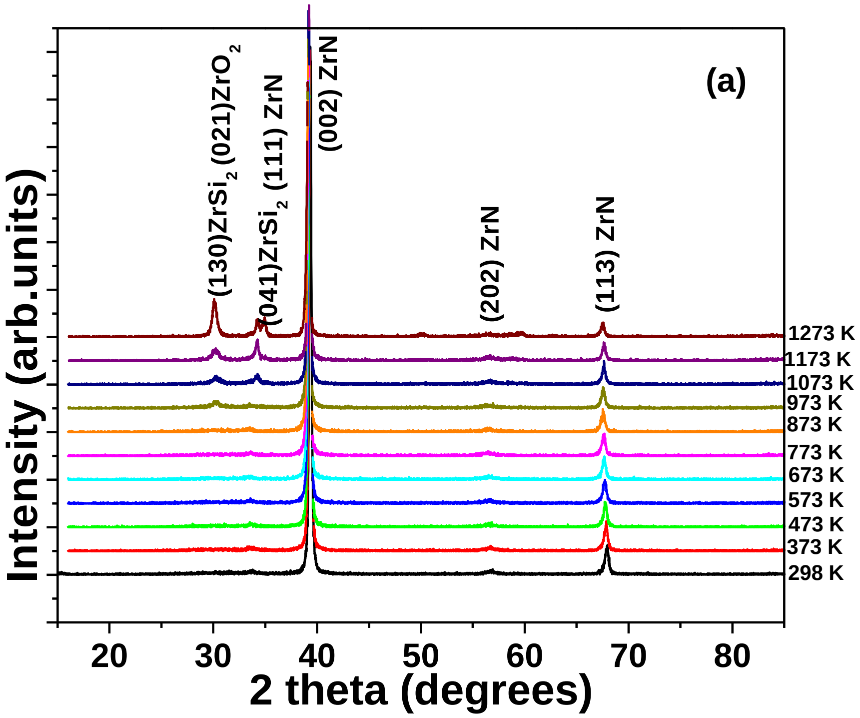

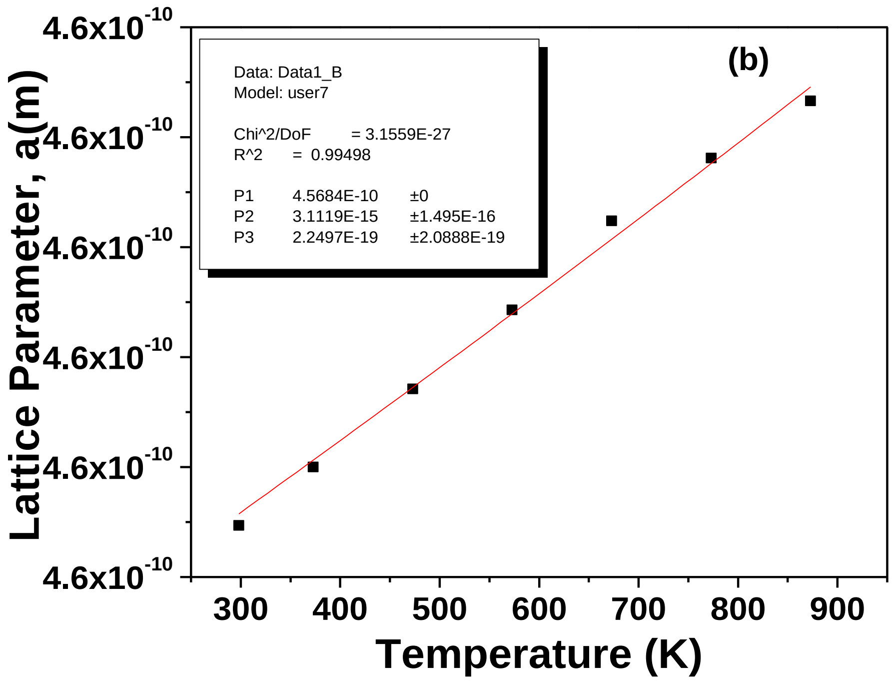

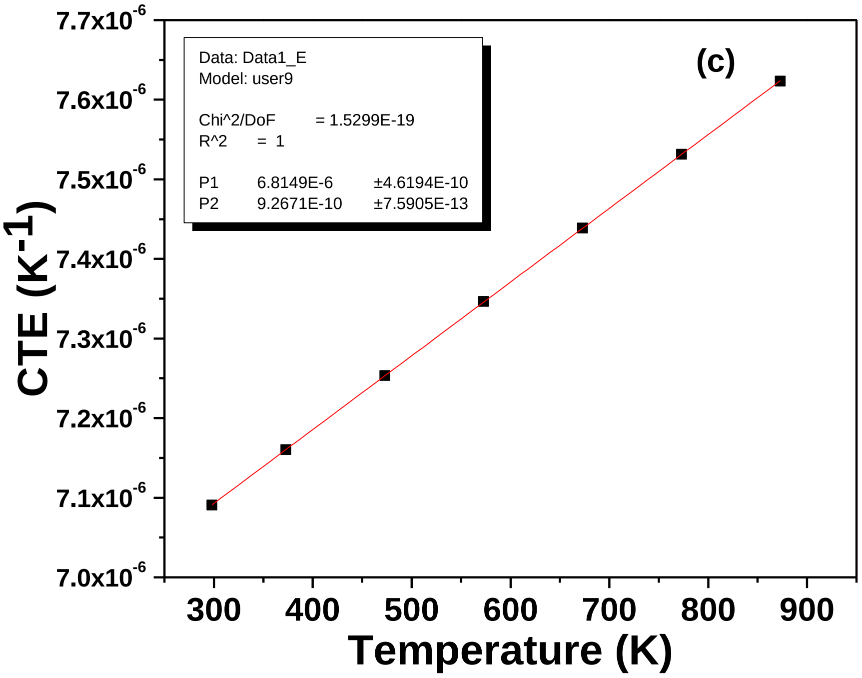

**Fig. 4.10** (a) HTXRD pattern of ZrN films, (b) Lattice parameter as a function of temperature and (c ) Average CTE versus temperature.

The average thermal expansion coefficient (Fig 4.10 c) of ZrN film up to 973 K was calculated using first order derivative of lattice parameter and found to be $\alpha_T$ ($K^{-1}$) = $6.81 \times 10^{-6} + 9.26 \times 10^{-10}$ x (T) and lower than that of the CTE of bulk ZrN ($7.2 \times 10^{-6}$ $K^{-1}$).

### 4.3.2 Nanomechanical Properties

Nano-indentation studies were performed to estimate the mechanical properties of the films. The applied load for nanoindentor was selected such that the indentation depths were in the range 1/10th of the thickness of the film in order to avoid the contribution from the substrate. The indentation load and the displacement were continuously recorded during one complete cycle of loading and unloading [229] for measuring hardness and modulus of the films. The nanohardness and Young's modulus were evaluated using the approach by Oliver and Pharr [196].

The load-displacement response obtained by the nano-indentation contains information about the elastic and plastic deformation of the films. The area between the loading and unloading curves represents the energy dissipation in the films due to plastic deformation. The area under the unloading curve represents the elastic energy for deformation. The hardness is derived from the peak load and the projected area of indentation, while reduced Young's modulus is obtained from the stiffness measured from the slope of the upper portion of the unloading curve [270].

The nanohardness of ZrN thin films deposited on D-9 alloy was measured as a function of the nitrogen flow rate from 0 to 10 sccm. This metallic substrate is softer (~2GPa) than Si (~8-10 GPa) and is used as a clad material for breeder reactors [271].

Also, the structural information of the films obtained from D-9 alloy is similar to that on Si substrate.

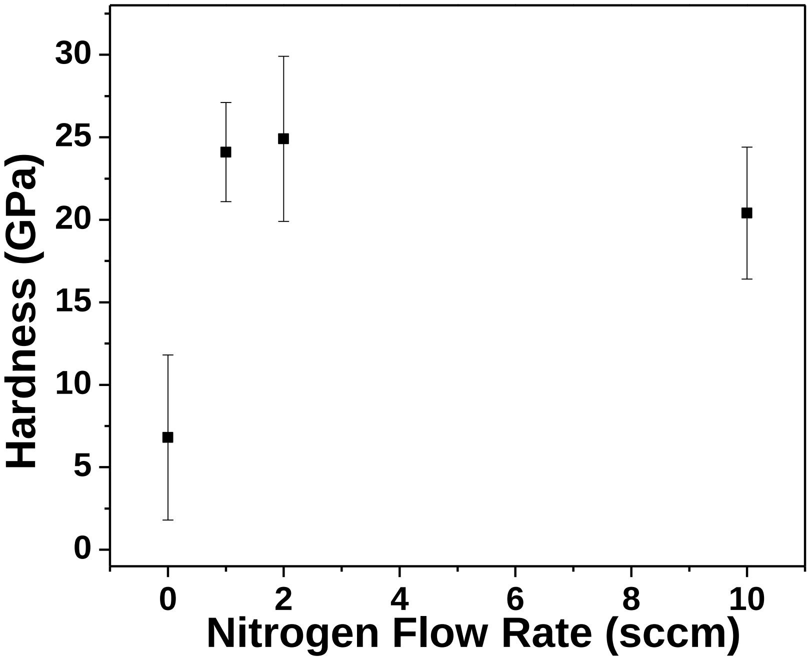

**Fig. 4.11** Hardness ( H) plot as a function of nitrogen flow rate of the films deposited at 773 K.

The average hardness and Young's modulus values of Zr films deposited in pure argon were 6.8 ± 2.7 GPa and 190 ± 25 GPa [258], respectively. It is observed that the values of hardness and Young's modulus of the Zr-N films were in the range of 21-26 GPa ± 3 GPa and 300-440 GPa ± 52 GPa, respectively (Fig 4.11 and Fig 4.12). However, hardness are significantly higher than that of the bulk hardness of ZrN (14.7 GPa) reported in the literature [8]. The calculated value of the Young's modulus from the present study is in agreement with that of Torok et al. [272], who have reported a value of 460 GPa from the flexural resonance frequency of the reactive magnetron sputtered coatings deposited on steel substrates.

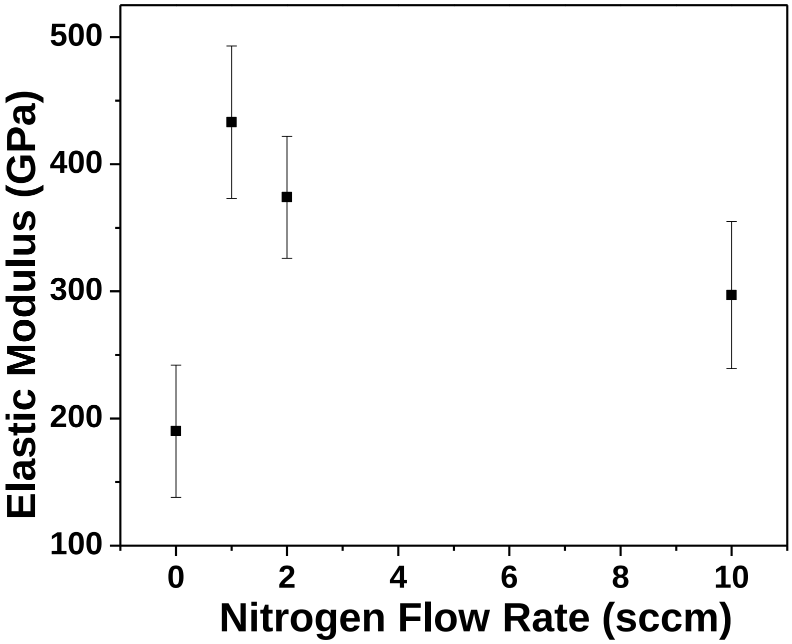

**Fig. 4.12** Young's modulus (E) as a function of the nitrogen flow rate of the films deposited at 773 K.

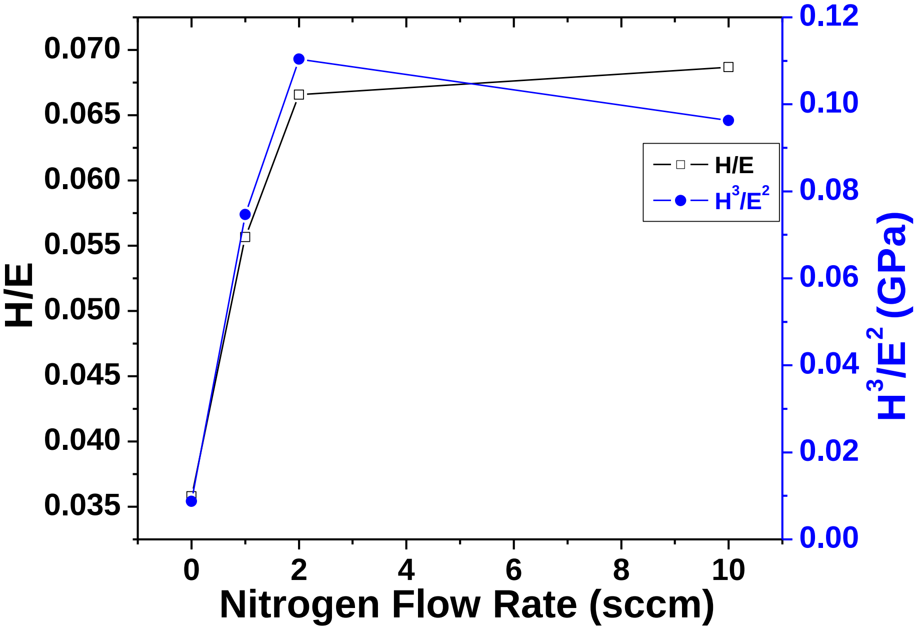

**Fig. 4.13** H/E and $H^3/E^2$ as a function of nitrogen flow rate of the films deposited at 773 K.

Fig. 4.13 shows the values of H/E and $H^3/E^2$ of the ZrN thin films as a function of nitrogen flow rate. In contrast to $H^3/E^2$, the variation of H/E is not very significant for the nitrogen flow rate ≥ 2sccm. $H^3/E^2$ of ZrN films has a value 0.01 for the films deposited in pure argon and it increases to 0.11 for the films formed at 1 sccm and then decreases to 0.095 for 10 sccm of nitrogen flow rate.

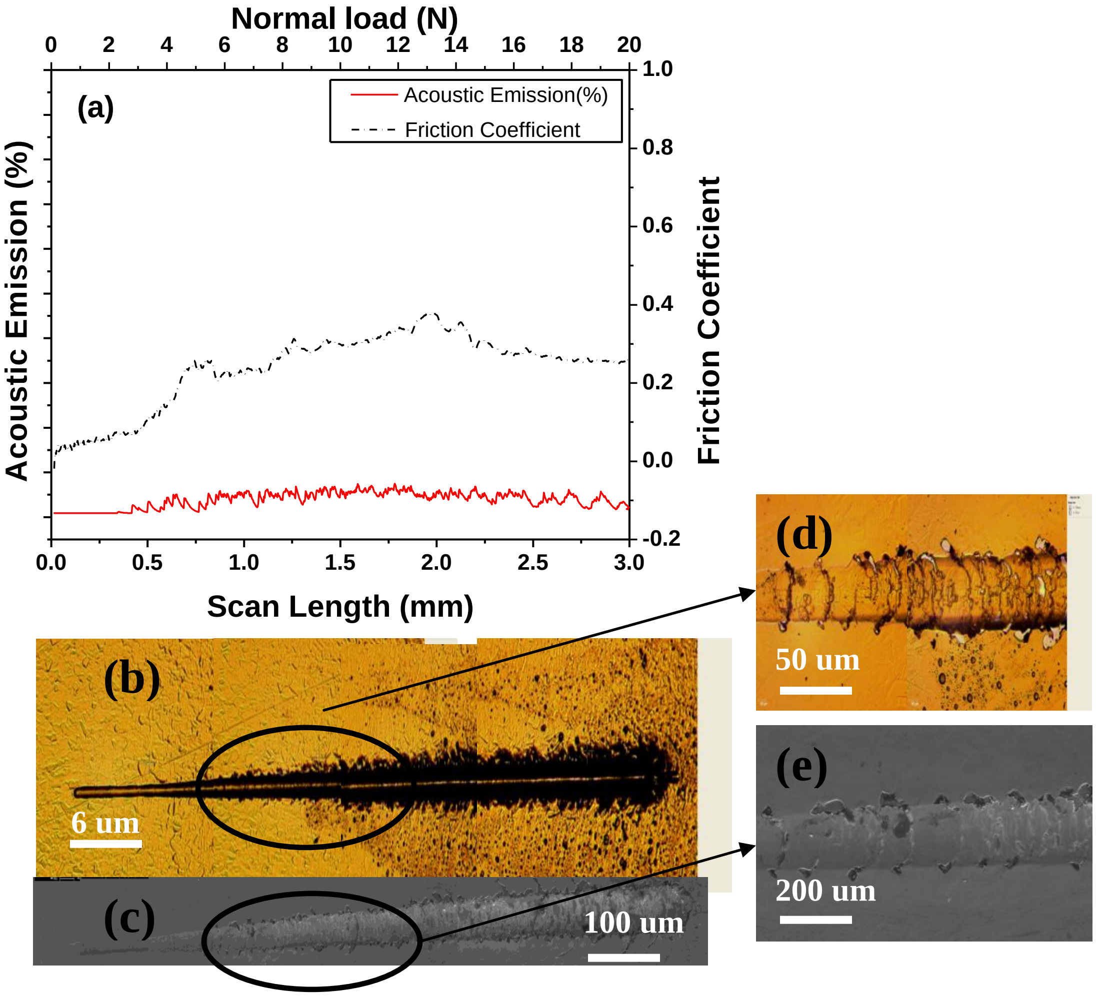

**Fig. 4.14** Scratch test of ZrN films deposited at 773 K and 1 sccm flow rate of nitrogen (a) acoustic emission and friction coefficient as a function of scan length, (b) optical image of scratch tested region, (c) SEM image of scratch tested region, (d) Magnified image of marked region of ‘b’ and (e) Magnified image of marked region of ‘c’.

Scratch test was carried out to examine the film adhesion with the substrate and the film failure, if any. Scratch tested region was further assessed by optical microscopy and scanning electron microscopy during and after the scratch test. The tangential force and acoustic emission signals were measured and recorded during the scratch test process and used as a supplementary test to identify different film damage levels. Scratch tests were performed with increasing load to determine the critical scratch load and friction coefficient for a given damage level. A typical scratch test result for the ZrN films deposited at 773 K and 1 sccm flow rate of nitrogen are shown in Fig. 4.14 (a). From the Fig. 4.14 (a), it is evident that during the failure there is a change in the friction coefficient value. From the acoustic emission signals and friction coefficient curves first and second critical loads are found to be about ~4.6 N and 4.8 N, respectively. Fig. 4.14 (b) and Fig 4.14 (c) show the optical and SEM image corresponding to scratch tested region, respectively. Magnified images of a portion of the optical and SEM image are also shown in the insets (Fig. 4.14 (d) and (e)) corresponding to the first and second critical failure regions. The exposure of the substrate in these images indicates the film failure.

### 4.3.3 Tribological Properties

Tribological behaviour of ZrN thin films deposited at various substrate temperatures and nitrogen flow rate is investigated using sliding bodies such as steel, alumina and sapphire balls.

#### 4.3.3.1 Effect of substrate temperature

Fig. 4.15 shows the value of coefficient of friction (COF) of the ZrN films on D-9 alloy substrate deposited at three different substrate temperatures, where (a), (b) and (c) denote the COF curves obtained for the films prepared at 300 K, 673 K and 873 K, respectively. 1,2 and 3 in each figure represent the COF of ZrN films tested with steel, alumina and $Si_3N_4$ balls. The values of the COF (Fig. 4.15 (a)–(c)) indicate that the COF of ZrN films is lower for the steel ball than for the $Al_2O_3$ and $Si_3N_4$ balls. The values of the COF are found to be more or less steady, with the steel ball compared to that of the ceramic balls, especially with the $Si_3N_4$ ball (Fig. 4.15(c)). The COF also shows lower values at 873 K because of the reduced surface roughness of the films with increase in the substrate temperature. It is pointed out that the COF of the ZrN films obtained using the ceramic balls show higher COF than that obtained using the steel ball, irrespective of the deposition temperature. Though, the COF reaches a saturation value at all substrate temperatures, the value of the COF in the plateau region decreases with increasing substrate temperatures. For instance, at 300 K, the COF measured at a sliding distance of about 1 m for the steel, $Al_2O_3$ and $Si_3N_4$ balls are 0.3, 0.6, and 0.8, respectively. In contrast, the COF measured for the films deposited at 873 K for the steel, $Al_2O_3$ and $Si_3N_4$ balls are 0.1. 0.11 and 0.35, respectively.

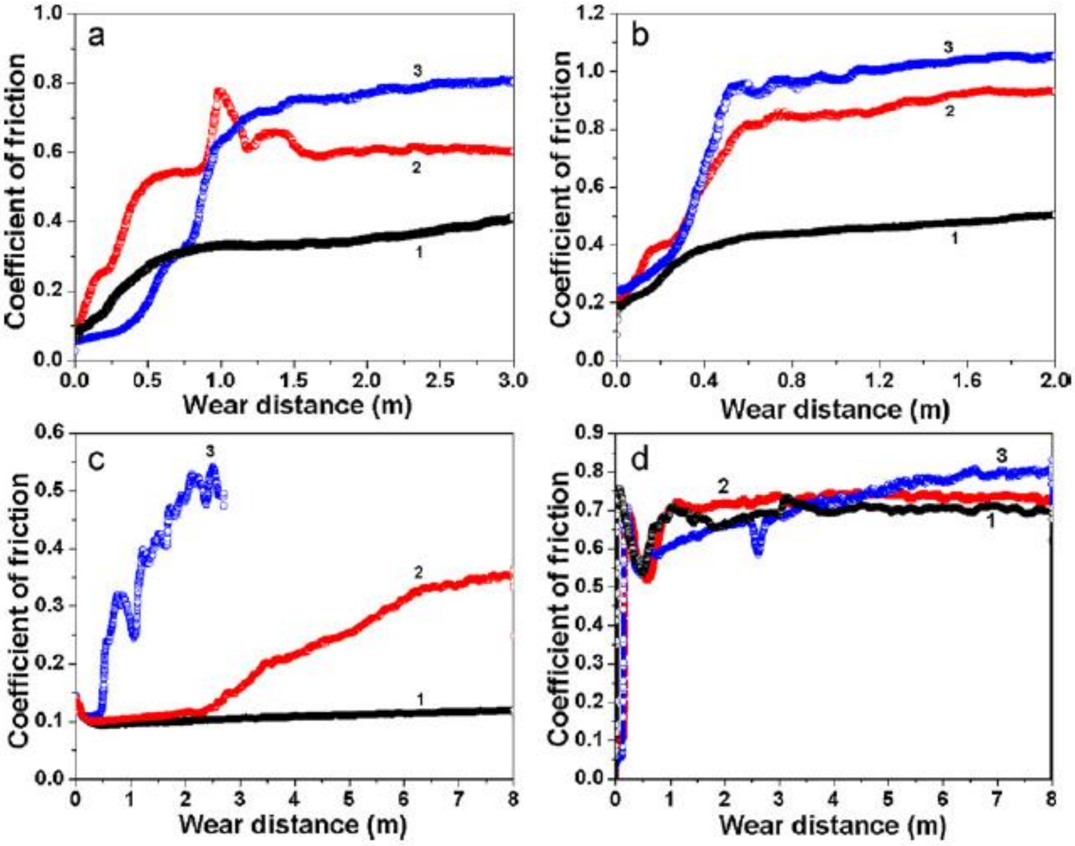

**Fig. 4.15** COF versus wear distance plot of ZrN thin films deposited at 1 sccm flow rate of nitrogen and at (a) 300 K, (b) 673 K, (c) 873 K and (d) COF versus wear distance plot for the films deposited on D-9 alloy substrate.

These values are found to be constant especially with the alumina and steel balls compared to that of the $Si_3N_4$ ball at higher wear distances. The value of the COF is found to be stable and low (0.1) even at higher wear distances for steel ball as is evident from Fig. 4.15 (c). The value of the COF was also measured on the bulk substrate of D-9 alloy and the value is found to be ~0.7 as shown in Fig. 4.15(d). These results clearly point out that there is a reduction in the COF with the deposition of the ZrN film on D-9 alloy. The width of the wear track obtained on the ZrN film is found to be ~100 μm for the steel ball, while it is ~200 μm for the ceramic balls indicating an increased wear loss with the ceramic balls.

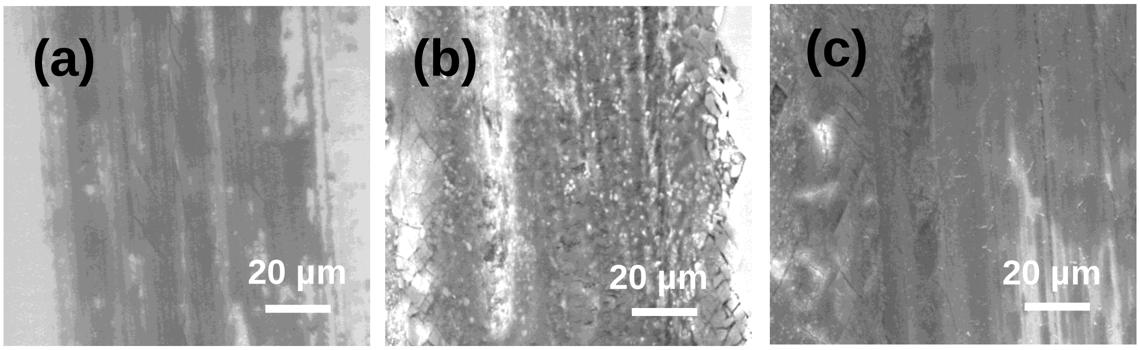

**Fig. 4.16** SEM micrograph of wear track of ZrN films deposited at 300 K ; 1 sccm flow rate of nitrogen and tested with (a) Steel , (b) $Al_2O_3$ and (c) $Si_3N_4$ balls.

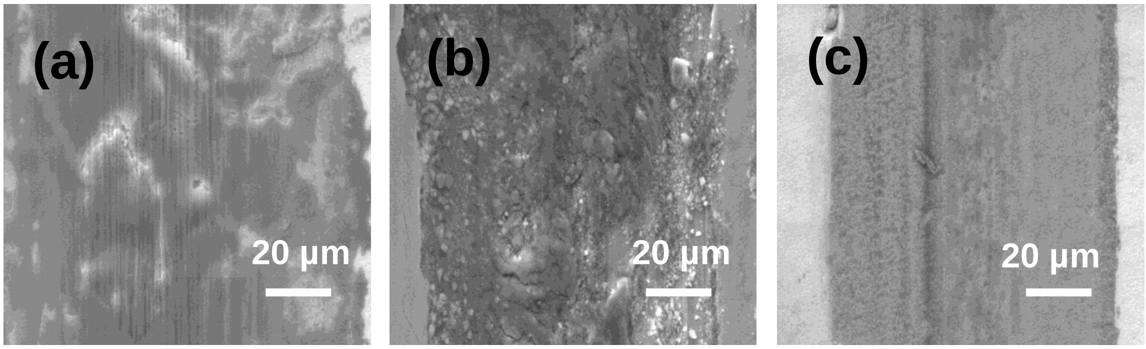

**Fig. 4.17** SEM micrograph of wear track of ZrN films deposited at 873 K ; 1 sccm flow rate of nitrogen and tested with (a) Steel , (b) $Al_2O_3$ and (c) $Si_3N_4$ balls.

It has been observed that oxide layers may form during tribo- testing and the formation of tribo layer offers lower values of COF due to a weak adhesive interaction. In contrast, the ZrN films tested with the ceramic balls show wear particles and severe cracks at the edge of the wear tracks. There is also no tribolayer as is evident from Figs. 4.16(b) and (c) and 4.17(b) and (c).

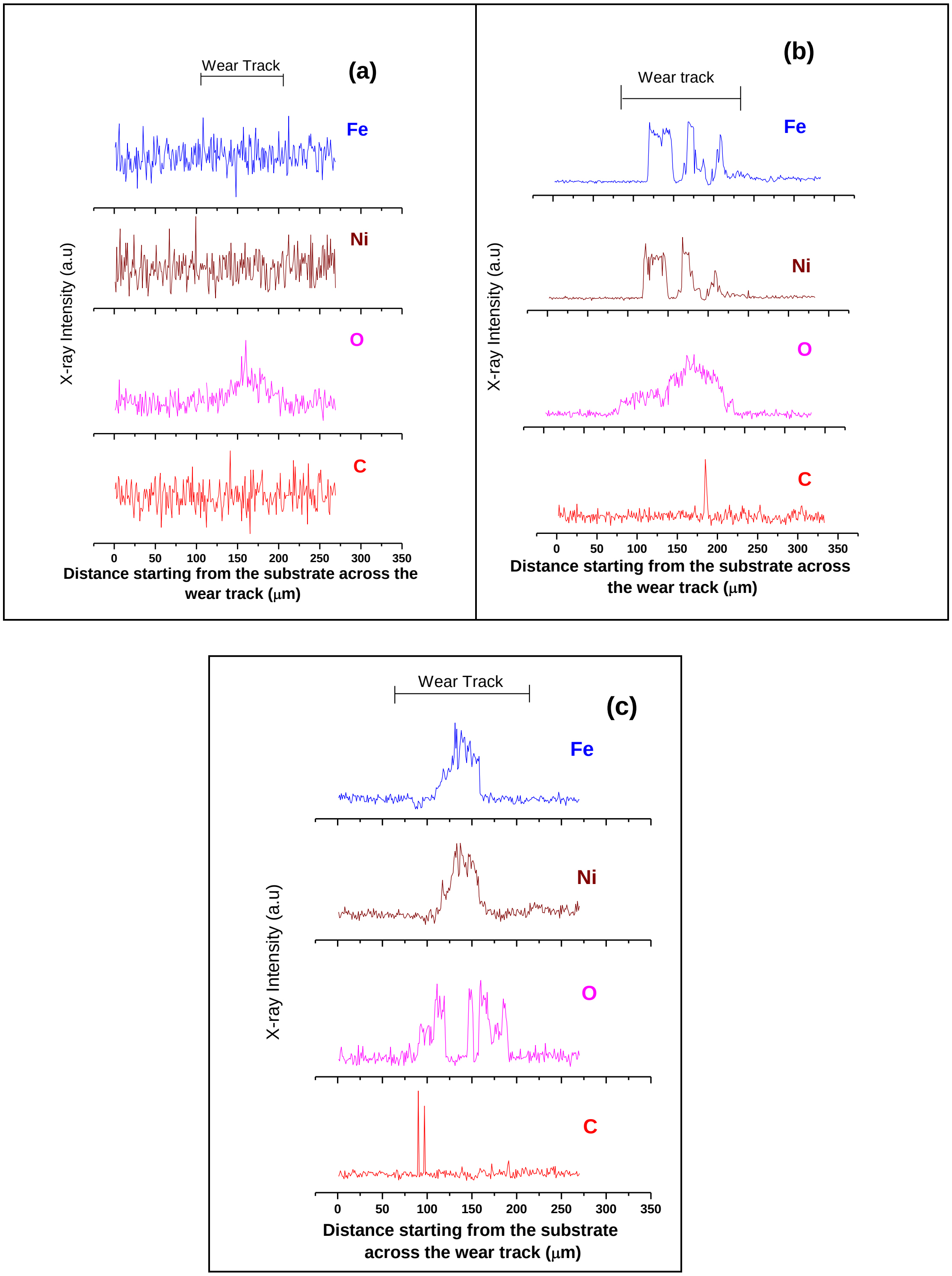

**Fig. 4.18** EPMA analysis across the wear track of ZrN films deposited at 873 K and 1sccm flow rate of nitrogen and tested with (a) Steel, (b) $Al_2O_3$ and (c) $Si_3N_4$ balls.

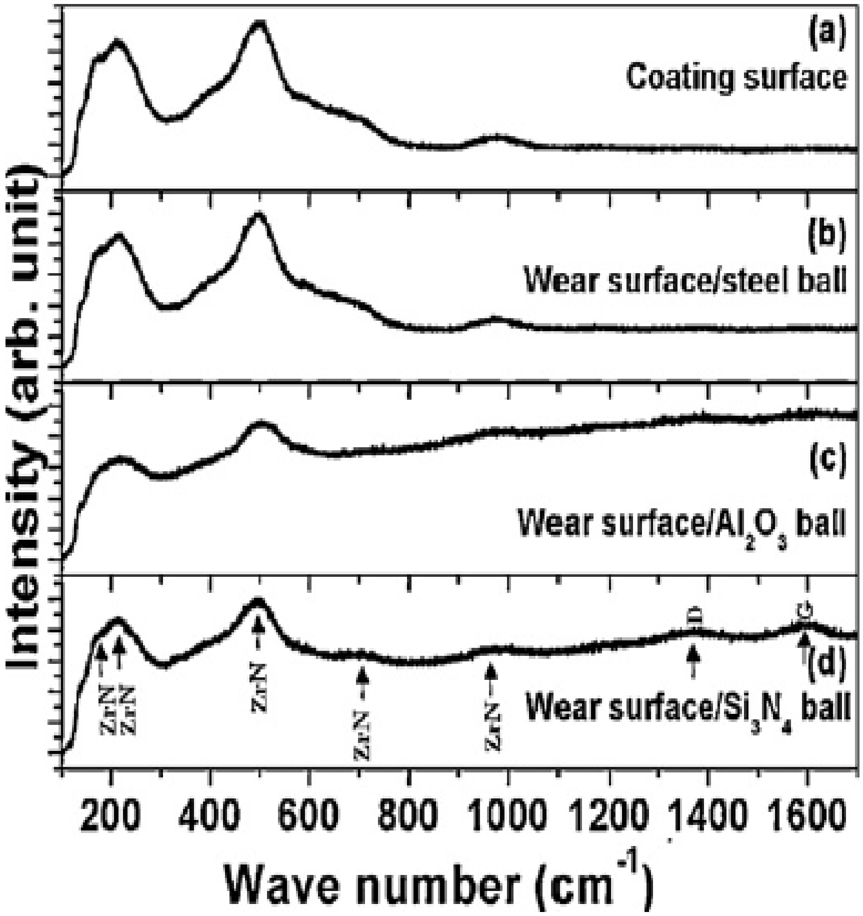

**Fig. 4.19** Raman analysis of ZrN films deposited at 873 K and 1 sccm flow rate of nitrogen.(a) As deposited and tested with (b) Steel, (c) ) $Al_2O_3$ and (d) $Si_3N_4$ ball.

The COF was found to be lower at higher deposition temperature. To understand the failure mechanism EPMA and Raman analysis were carried out for the wear tested samples deposited at 873 K.

EPMA analysis was also performed in order to confirm the elemental distribution in the wear tracks as well as in the as deposited films of ZrN. Fig. 4.18 shows the variation in the X-ray intensity of Fe, Ni, O, and C across the as deposited and wear tested region of the samples. From the figure 4.18 (b) and (c) presence of Fe, Ni, C and O were noticed across the wear track, whereas carbon peak was absent in the wear track of the steel tested sample.

Micro-Raman spectroscopy has been performed to understand the distribution of phases in the wear tracks for the ZrN film deposited at 873 K. The Raman spectroscopy shows dispersion curves leading to a group of 'lines' (bands) due to acoustic transitions in the 150–300 $cm^{-1}$ region and another set of lines appear due to optic modes in the region of 400–650 $cm^{-1}$ as shown in Fig. 4.19. The Raman spectra of ZrN have been reported previously [260], and the Raman lines are found at the frequency of 169 $cm^{-1}$, 209 $cm^{-1}$ and 499 $cm^{-1}$ of ZrN phase as shown in Fig. 4.19(a). At higher spectral region (710 $cm^{-1}$ and 980 $cm^{-1}$), second order weak lines of ZrN are also observed. Broad and weakly developed peaks are found at 1366 $cm^{-1}$ and 1588 $cm^{-1}$ which correspond to the vibrational modes of D and G - lines of graphitic phase [273].

#### 4.3.3.2 Effect of nitrogen flow rate

Fig. 4.20 shows the value of coefficient of friction (COF) of the ZrN films on D-9 alloy substrate deposited at constant substrate temperature of 773 K and at different nitrogen flow rates. Since $Al_2O_3$ and $Si_3N_4$ have hardness of 23 and 25 GPa, respectively and show almost similar behaviour during the wear study of substrate temperature at constant flow rate of nitrogen. Only steel and $Al_2O_3$ balls were used as a counter body to study the wear behaviour of the films.

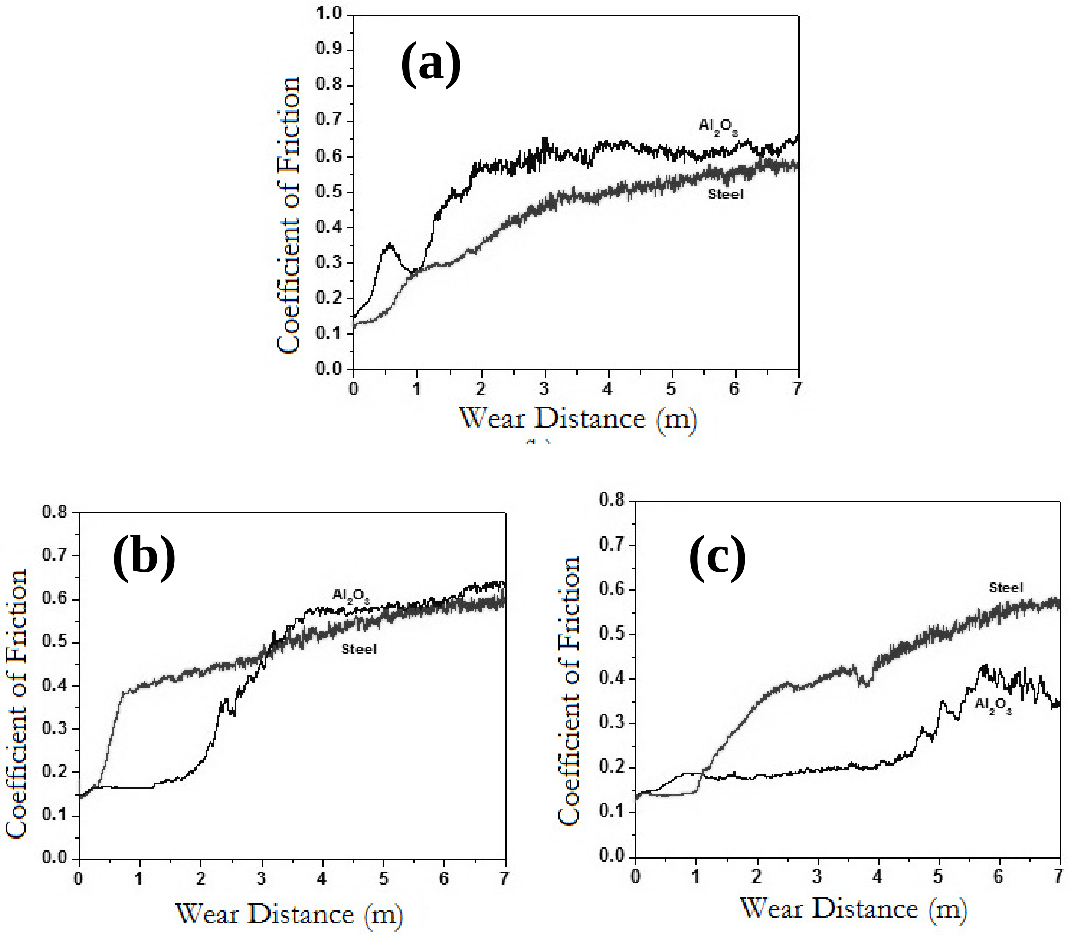

**Fig. 4.20** The COF verses wear distance plot of ZrN thin films deposited at 773 K and at (a) 1 sccm, (b) 2 sccm and (c) 4 sccm flow rate of nitrogen.

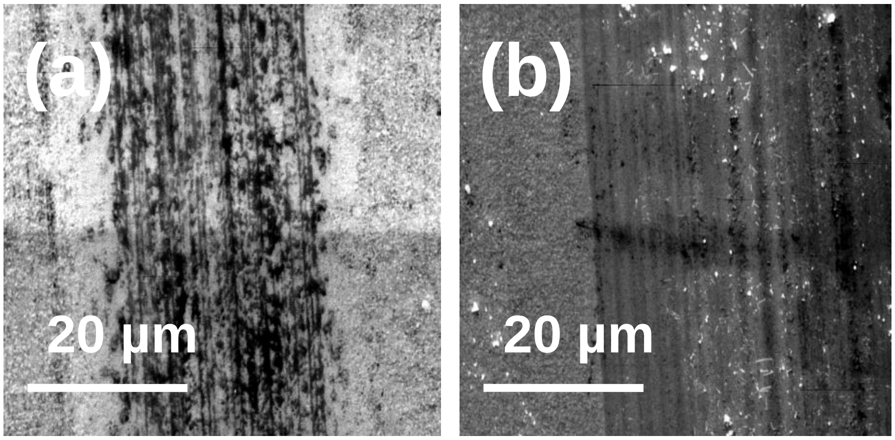

**Fig. 4.21** SEM micrograph of wear tracks of ZrN films tested with (a) Steel and (b) $Al_2O_3$ balls. These films were deposited at 773 K and at nitrogen flow rate of 1 sccm.

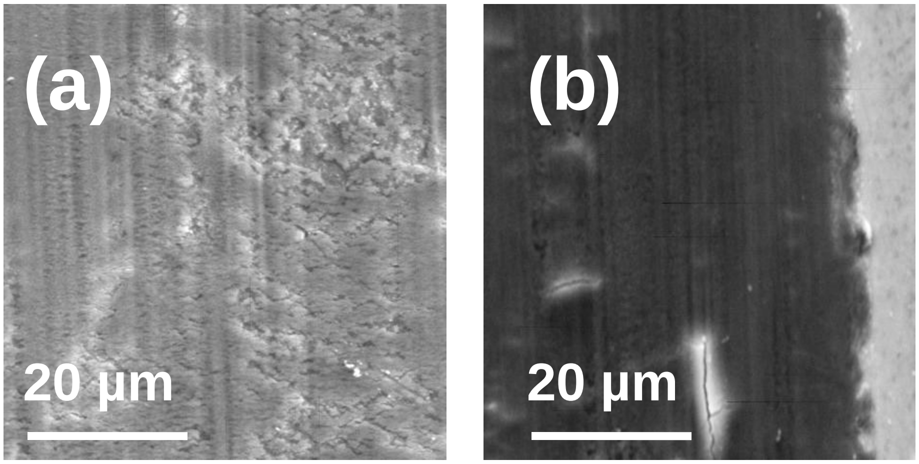

**Fig. 4.22** SEM micrograph of wear tracks of ZrN films tested with (a) Steel and (b) $Al_2O_3$ balls. These films were deposited at 773 K and at nitrogen flow rate of 4 sccm.

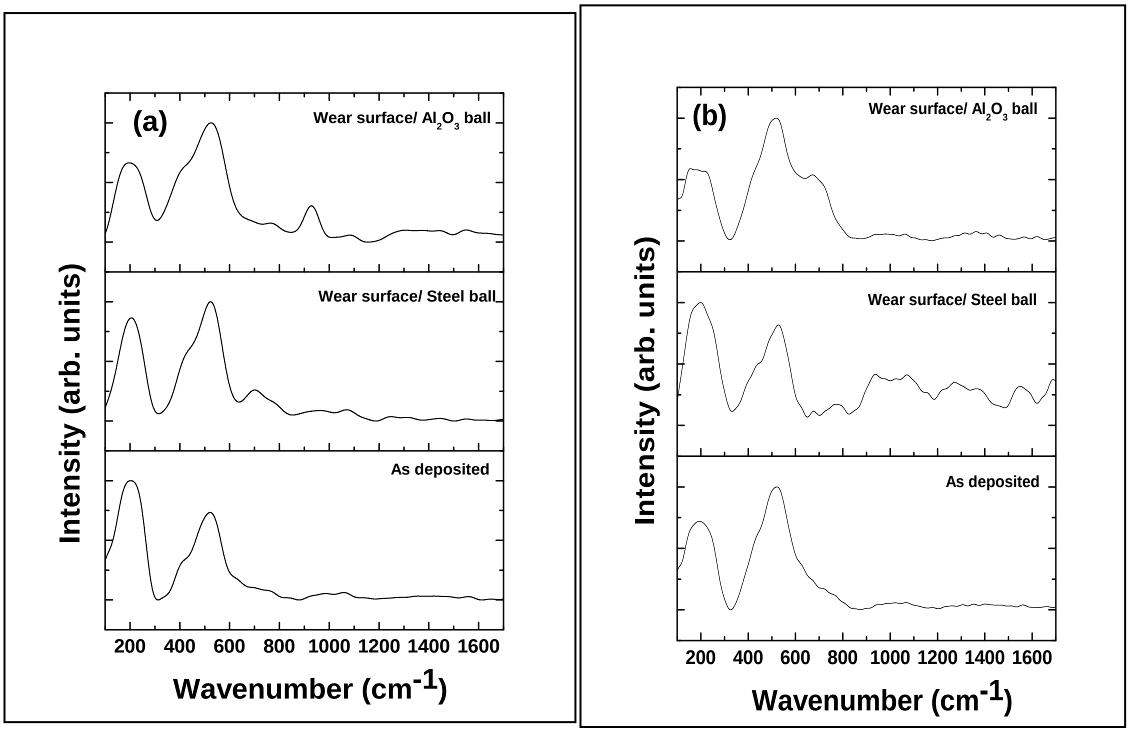

**Fig. 4.23** Raman analysis of ZrN films deposited at 773 K and tested with steel and $Al_2O_3$ balls with (a) 1 sccm and (b) 4 sccm flow rate of nitrogen.

The values of the COF (Fig. 4.20 (a)–(c)) indicate that the COF of ZrN films is lower for the steel ball than for the $Al_2O_3$ balls at 1 and 2 sccm flow of nitrogen, the values of the COF are found to be more with the steel ball compared to that of the ceramic ball, especially at higher flow rate of nitrogen (Fig. 4.20(c)). It is also noticed that the COF reaches a saturation value at all flow rates of nitrogen, the value of the COF in the plateau region decreases with increasing nitrogen flow rate. For instance, at 1 sccm flow rate of nitrogen, the COF measured at a sliding distance of about 1.5 m for the steel and $Al_2O_3$ balls are 0.3 and 0.5, respectively. In contrast, the COF measured for the films deposited at 4 sccm flow rate of nitrogen for the steel and $Al_2O_3$ balls are 0.3 and 0.2, respectively. It is observed that during the initial periods of wear testing, the COF rapidly increases to a saturation (peak) value and then gradually reaches a constant value (plateau region). At the beginning of the wear test, there is a severe material transfer between the film and the ball which leads to a rapid increase in the COF value.

Beyond the saturation value, the COF remains more or less constant in the plateau region, where the material transfer is slowly reduced and stabilized after the coverage of a large percentage of the test area with the transferred material. In case of failure of the films, the saturation value of the COF varies significantly with wear distance.

Fig. 4.21 and 4.22 shows the SEM micrograph of wear tested films deposited at 1 and 4 sccm flow rate of nitrogen, respectively. Fig. 4.21 (a) and 4.22 (a) show the SEM micrographs corresponding to the 773 K, films deposited at 1 sccm and 4 sccm flow rate of nitrogen and tested with steel ball, whereas Fig. 4.21 (b) and 4.22 (b) show the SEM micrograph corresponding to the 773 K, films deposited at 1 sccm and 4sccm flow rate of nitrogen and tested with $Al_2O_3$ ball.

Micro-Raman spectroscopy was performed to understand the distribution of phases in the wear tracks for the ZrN film deposited at 773 K at different nitrogen flow rate. The Raman spectroscopy shows dispersion curves leading to a group of lines (bands) due to acoustic transitions in the region 150–300 $cm^{-1}$ and another set of lines appear due to optic modes in the 400–650 $cm^{-1}$ region as shown in Fig. 4.23. The Raman lines are found at the frequency band of 166 $cm^{-1}$, 209 $cm^{-1}$ and 502 $cm^{-1}$ for ZrN phase as shown in Fig. 4.23(a) and (b). At higher spectral region (710 $cm^{-1}$ and 980 $cm^{-1}$), second order weak peaks of ZrN are also observed. At 4 sccm flow rate of nitrogen and the film tested with $Al_2O_3$ ball shows broad and weakly developed peaks at 1370 $cm^{-1}$ and 1580 $cm^{-1}$ which correspond to the vibrational modes of D and G bands of graphitic phase as reported earlier.

## 4.4 Discussion

### 4.4.1 Microstructural Characterisation

The substrate temperature and nitrogen flow rate have profound influence on the microstructure. It was noticed that there is slight increase in the lattice parameter as a function of nitrogen flow rate as the excess nitrogen can preferentially occupy interstitial positions leading to a monotonous increase of the lattice parameter. When the nitrogen flow rate increases up to 10 sccm, the films are found to be poorly crystallized. This can be explained by the absence of the stable phases in the nitrogen rich zone of Zr-N system. From Fig 4.3 (a) it was noticed that $Zr_3N_4$ phase appears at 2 sccm and not seen at nitrogen flow rate > 2 sccm. This behaviour can be understood since $Zr_3N_4$ phase is a metastable phase. As the nitrogen flow rate increases up to 10 sccm, crystallinity of the films decreases due to the absence of the stable phases in the nitrogen rich zone of Zr-N system.

The increase in the crystallite size with increasing substrate temperature is noticed because of the increased adatom mobility at higher temperatures [274]. With increasing substrate temperature, densification of the films is also promoted due to thermal diffusion. It was also noticed that there is a slight increase in the lattice parameter. This small change in the lattice parameter may be due to stresses present in the films. Initially stress is compressive in nature and the films formed at higher temperature tend to possess tensile stress. This is clearly evident from the change in the lattice parameter with respect to bulk value of ZrN. The average surface roughness of the as deposited films was found to decrease for the substrate temperature from 300 K to 873 K because of the increased crystallite size and densification with the increasing substrate temperature [275]. However there is a decrease in the crystallite size at ≥ 773 K, which could be related to diffusion of Si of the substrate into the growing film in agreement with the results reported in the literature [178].

The decrease in the crystallite size as a function of nitrogen flow rate (Fig 4.3 (b) may be related to structural disordering. In our thin film deposition, the increase of nitrogen partial pressure was accompanied by the decrease of the partial pressure of argon in order to keep the total flow rate constant. As a result, the overall sputtering yield of the target decreased due to lower ionization of molecular nitrogen compared to argon, which causes a continuous decrease in the deposition rate of the films up to 4 sccm and then becomes constant (Fig.4.2). It is suggested that at higher nitrogen flow rates, distortions are produced in the lattice due to increased accommodation of nitrogen atoms.

Therefore, the reduction in the crystallite size with increasing nitrogen flow rate could be related to tendency for amorphization.

Raman spectra (Fig 4.4) also confirm the presence of ZrN phase at different flow rates of nitrogen. In a perfect fcc structure, the first order Raman scattering is forbidden due to selection rules. However in this case due to disorder induced by the deposition technique, the translation symmetry is lost, and all the modes can participate in the scattering. Raman spectra will be an “image” of the density of vibrational states (DVS) [276]. At low frequency range, the bands are attributed to the disorder of single phonons and second order processes, whereas at higher frequencies the asymmetry of the bands is due to the superposed contributions of the disorder of the optical phonons and second order combination of acoustic and optical processes [277]. In this case also the broadening of the bands indicates the disorder of the crystals. The as-deposited ZrN film presents a Raman spectrum with the typical broadened bands, due to the disorder induced by N atoms [278]. However in this case we could not get significant change as a function of the nitrogen flow rate up to 4 sccm.

Thermal expansion of a solid is a consequence of an-harmonicity of the interatomic potentials, which are significantly influenced by the material structure. The value of the CTE increases (Fig 4.10 (b)) as a function of temperature, which is similar to metallic system. The CTE of ZrN thin films are found to be comparable with the value of the CTE of bulk ZrN.

### 4.4.2 Nanomechanical Characterisation

A protective film such as ZrN not only requires high hardness but also high resistance to plastic deformation during contact events. The ratio, H/E and $H^3/E^2$ have been increasingly applied to evaluate the resistance to plastic deformation from the values of H and E [201]. The increased value of $H^3/E^2$ (Fig 4.13), gives information on the resistance of the material to plastic deformation. From the values of $H^3/E^2$, it is evident that ZrN films deposited at 2 sccm of nitrogen flow rate could offer higher resistance to plastic deformation. The variation in the resistance to plastic deformation could be discussed in terms of the microstructure. In the present work, the mean crystallite size is significantly reduced as nitrogen flow rate is increased and this results in the increase in the hardness value for the films deposited up to 2 sccm of nitrogen flow rate. However, above 2 sccm of nitrogen flow rate, films show poor crystallinity and also the formation of impurity phase of $Zr_3N_4$. The present study indicates that the reduction in the value of resistance to plastic deformation at higher nitrogen flow rates may be related to the change in the microstructure, especially, the crystallite size and formation of secondary phase.

Scratch test indicates (Fig. 4.14) that films are adherent up to 4.6 N. Generally, acoustic emission curve (Fig. 4.14 (a)) gives the idea about film failure. The acoustic emission curve is smooth and when film loss occurs, the signal can increase either suddenly or steadily as a function of load. The “shoulder” can be correlated to cracking or to the onset of the cohesive failure. These effects are directly related to the tool life. Cohesive and adhesive failures of the films are noticed at 4.6 and 4.8 N, respectively. It is also clear from the SEM micrograph of the scratch tested region that showed flaking at

4.6 N due to the cohesive failure and exposure of the substrate at 4.8 N due to adhesive failure.

### 4.4.3 Tribological Behaviour of ZrN Thin Films

Tribological characterization of the ZrN films tested with ceramic balls show higher COF than that of the steel balls irrespective of deposition temperature. Also the value of the COF for the films deposited at higher temperature and tested with steel ball is lower (Fig 4.15). The behaviour of the above curves can be qualitatively explained in the following manner: during the initial periods of wear testing, the COF rapidly increases to a saturation (peak) value and then gradually reaches a steady value (plateau region). At the beginning of the wear test, there is a severe material transfer between the film and the ball which leads to a rapid increase in the COF. Beyond the saturation value, the COF remains more or less constant in the plateau region, where the material transfer is slowly reduced and stabilized after a large percentage of the test area is covered with the transferred material. In case of failure of the films, the saturation value of the COF varies significantly with wear distance and is more evident with the films tested with the $Si_3N_4$ ball.

It is suggested that the increased hardness of the ceramic balls could offer severe abrasive wear and result in the higher values of the COF. The changes in the wear behaviour of the ZrN films with the sliding bodies can be explained from the morphology, composition and phase distribution of the of wear tracks. Typical surface morphology of the wear tracks obtained with the three sliding bodies for the film deposited at 300 K and 873 K are shown in Figs. 4.16 and 4.17, respectively. Using the steel ball, the wear surfaces of the films are found to be plastically deformed leading to the formation of smooth surfaces as shown in Figs. 4.16(a) and 4.17(a). In this case, a modified smooth tribolayer is non-uniformly formed on the ZrN film. It is also reported that the wear testing with the steel ball generates lower amount of wear particles due to the formation of a smooth surface layer [279].

The formation of tribofilm can be qualitatively explained by the following process. Initial sliding contact can take place on a limited number of surface asperities, i.e. the top points of the growth defect grains protruding upon the film surface. The concentrated compressive and tangential loads result in prompt fracture of these grains leading to the generation of first wear particles, This process continue until all the protruding grains inside the wear track are wornoff. Meanwhile, some of the wear particles entrapped within the sliding contact zone work as a ‘third body’ to make special contributions to the tribo-system. Firstly, the sliding and rolling motion of the wear particles result in high-stress abrasive wear of the film. Secondly, these particles are further broken themselves into progressively smaller sizes. Then taking into account of the increased surface to volume ratio of the wear debris and the strong ionic chemical bonding of the ZrN, high compressive and shear loading as well as frictional heating in the sliding contact zone, would promote both the self agglomeration of the fine wear debris into clusters and the ionic adhesion of the clusters to the worn surface, which eventually leads to the formation a continuous film to attach on the parent worn surface. Afterwards, further sliding is more restricted within the tribofilm and results in continuous powdering or amorphorisation. The friction curve shows that the coefficient of friction is about 0.1 -0.3 in the temperature range 300 – 873 K and for the films tested with steel balls in the beginning prior to the tribofilm formation. Then it is increased to 0.5 – 0.6 for the films tested with ceramic balls due to the entrapped wear particles arising from the mechanical wear. The high friction arises from the severe shear deformation and adhesive interaction of the tribofilms. Such adhesive interaction is attributed to the ionic bonding of the tribofilm. It is known that adhesive interaction is one of the major components forming the frictional resistance in a sliding process. The adhesive interaction depends on the inter-atomic bonding, for which strong ionic, metallic and covalent bondings result in strong adhesion whereas weak bonding, such as van der Waals inter-molecule forces, lead to weak adhesion [ 280].

With the $Si_3N_4$ ball, the films are subjected to severe abrasive wear (Fig. 4.16(c)) and the latter is evident from the distribution of fine wear particles (Fig. 4.17(c)). The observation of the increased wear rate of the films with the ceramic balls by SEM could be related to significant increase in the COF values. It is also reported that such ceramic balls can easily react with moisture and form oxides of the respective metals and cause a change in the wear mechanism [281].

The intensity profiles of the elements across the wear tracks show a non-uniform distribution of the elements due to the wear testing. It is clear from Fig. 4.18 that there is an increase in the amount of oxygen in the wear track for all the samples, while the carbon is absent in the wear track tested with the steel ball. Also, the films tested with the ceramic balls show more enrichment in the substrate elements such as Fe, Ni and C (Fig. 4.18(b) and (c)). The observation of a significant quantity of the substrate elements in the samples tested with the ceramic balls indicates that the surface of the substrate is exposed as a consequence of cracking and delamination of the film. It is suggested that the ceramic balls which cause severe deformation of the films seem to promote carbon segregation to the surface of the substrate during the tribo-testing.

Position of these peaks obtained at 170 $cm^{-1}$, 211 $cm^{-1}$and 503 $cm^{-1}$ from the wear tracks is found to be shifted slightly towards the higher wave number for the films tested with all the three sliding balls as shown in Fig. 4.19(b)–(d). A slight shift in the position of these peaks to higher wave number could be related to accumulation of tribo induced stress. In addition, there is a broadening and reduction in the intensity of the peaks indicating a tendency to amorphisation due to tribo-induced structural disordering and defect accumulation. Formation of these bands is clearly observed in Fig. 4.19(c) and (d). Pashechko and Lenik [282] have reported the segregation of C, B, and Si to the wear tested surface due to thermal diffusion activated by frictional heating in accordance with our EPMA data for carbon. Therefore, it is reasonable to consider the segregation of carbon from the substrate to the wear tested surface due to tribo-induced heating activated by contacting stress of the hard ceramic balls.

However, the above peaks are not observed in the wear tested surface formed with steel ball. Hertzian contact stress for the tribo-system of ZrN/steel ball is found to be lower (0.98 GPa) and this stress may not be adequate to segregate the carbon to the surface. However, this stress is found to be 1.84 GPa and 2.27 GPa for ZrN/$Al_2O_3$ and ZrN/$Si_3N_4$ tribo systems, respectively. It is possible that with increase in the contact stress of the ceramic balls, the temperature of the contacting surfaces also increases which may further promote the segregation of the carbon from the substrate to the surface. Though, the amount of such carbon phases formed using the ceramic balls in the present study is minimal, the role of such phases on the tribological properties of materials is still ambiguous and may need further investigation.

The COF value is lower for the films deposited at 1 sccm of nitrogen flow rate and tested with the steel. In contrast the films deposited at 4 sccm flow rate of nitrogen shows higher COF value with the steel ball than that obtained with $Al_2O_3$ ball ( Fig 4.20). This behaviour may be attributed to the presence of insulating impurity phase of $Si_3N_4$ along with ZrN present in the films deposited at higher flow rate of nitrogen. Micro-Raman spectroscopy has been performed to understand the distribution of phases in the wear tracks for the ZrN film. A slight shift in the position of Raman peaks to higher wave number has been related to accumulation of tribo-induced stress. In addition, there was a broadening and reduction in the intensity of the peaks indicating a tendency to amorphisation due to tribo-induced structural disordering and defect accumulation.

## 4.5 Conclusions

ZrN films were deposited on Si and D-9 alloy substrates at different substrate temperatures, as a function of nitrogen flow rate using the pulsed magnetron sputtering technique.

(i) The nanostructured crystalline films with (200) preferred orientation were observed at all deposition temperatures. Films deposited up to 1 sccm of nitrogen flow rate showed a single phase fcc-ZrN, while films deposited at nitrogen flow rate > 1 sccm and up to 6 sccm revealed  the growth of ZrN along with $Zr_3N_4$ secondary phase. Films deposited > 6 sccm have poor crystallinity.

(ii) TEM studies also confirmed the presence of ZrN along with small amount of o-$Zr_3N_4$ phase at higher nitrogen flow rates. However, XPS analysis of these films indicated the presence of $ZrO_2$ along with ZrN phase.

(iii) HTXRD study showed that ZrN films were stable up to 1073 K. The average linear thermal expansion coefficient of ZrN film was found to be $\alpha_T(K^{-1}) = 6.81 \times 10^{-6} + 9.26 \times 10^{-10}$ x (T)

(iv) The effect of nitrogen flow rate on the nanomechnical properties indicated an enhancement in hardness and elastic modulus and showed a peak value for the resistance to plastic deformation at lower flow rates of nitrogen.

(v) The tribological properties of these films were found to be influenced by the deposition temperature and sliding counter bodies. The COF is found to be lower at 873 K and with steel ball. EPMA techniques suggested an increased amount of elements such as Fe, Ni and C, while Raman spectroscopy indicated the presence of carbon related phases in the wear tracks obtained using the ceramic balls. At higher flow rate of nitrogen, steel ball shows higher COF than that obtained at lower flow rates of nitrogen. The variation in the COF has been also discussed in relation with the microstructure of the wear tracks.

# Chapter 5

# *Studies of Alloyed ZrAlN Thin Films*

## 5.1 Introduction

Among the ternary M–Al–N (M = transition metal) systems, Ti–Al–N and Cr–Al–N coatings have been the most widely investigated [56-66], whereas a very few studies have been devoted to the Zr–Al–N system [67-69]. ZrN has a lower coefficient of friction than TiN and other transition metal nitrides, and is relatively hard. However, its poor oxidation resistance hampers a broader range of applications. Therefore, alloying ZrN with Al was suggested in order to improve the oxidation resistance and possibly also the mechanical properties [283]. The crystal structure of ZrN is B1 fcc structure and it is similar to TiN. However, there is a difference in the lattice parameter values of ZrN and TiN. Also, ZrN has a larger lattice parameter (a = 4.58 Å JCPDS: 30-0753) than that of TiN (a = 4.24 Å JCPDS: 38-1420). It is also reported that the lattice parameter value of AlN is ~4.05 Å (JCPDS: 46-1200). Therefore, the mismatch between ZrN and AlN is higher than that of TiN, if forced into the B1 structure. AlN is immiscible in TiN and ZrN, and experiments indicate that the driving force for segregation is larger in the case of Zr-Al-N. However, alloyed ZrAlN films with lower concentration of Al exhibit fcc structure similar to ZrN [133].

Thermal expansion of material plays an important role in the areas of microelectronics and microelectromechanical systems (MEMS). There are several problems that arise from the thermal expansion effect. For instance, the mismatch of thermal expansion between the thin films and the substrate may lead to residual stresses in the thin films [284-286]. Thus, the electronic devices as well as the micromachined structures will be damaged or deformed by this effect. On the other hand, the thermal expansion effect can be exploited to drive microactuators [287-288]. In order to design micromachined components as well as microelectronics devices properly, it is necessary to characterize the coefficient of thermal expansion (CTE) for thin film materials. There are several techniques used to measure the CTE of bulk materials. However, the thickness of the films are too small to be determined using the conventional optical techniques [289-292]. The X-ray diffraction method can be used to measure the CTE of thin film materials but it is only appropriate for crystalline structures [293-295].

In this Chapter, the studies of alloyed thin films of ZrAlN deposited on Si and D-9 alloy substrate have been presented. In the present work, four different compositions of alloyed films of $Zr_{1-x}Al_xN_y$ ($Zr_{0.47}N_{0.53}$, $Zr_{0.34}Al_{0.13}N_{0.53}$, $Zr_{0.25}Al_{0.28}N_{0.47}$ and $Zr_{0.20}Al_{0.36}N_{0.44}$) have been studied to understand their mechanical, tribological and thermal expansion properties. These compositions have been selected based on the equilibrium phase diagram of Zr-Al-N system, which suggests that Al is in the solid solution up to 42 at.%. In the present study only alloyed films of ZrAlN have been investigated, therefore two extreme and one intermediate compositions of Al were selected.

## 5.2 Experimental Methods

ZrAl and alloyed films of ZrAlN were deposited on Si (100) and D-9 alloy substrates by sputtering from composite targets of Zr-Al and ZrN-Al.

ZrAl films with 13 at.% of Al was prepared by placing a suitable Al strip of 1 mm thickness and surface area of ~ 5.7 $cm^2$ over Zr target of ~ 45.34 $cm^2$. This composition was realized by trial and error based on the composition obtained from EPMA analysis. In addition, alloyed ZrAlN thin films were also prepared on Si (100) and D-9 alloy substrates by sputtering from a composite target of ZrN - Al target using a single pulsed power supply in a gas mixture of argon and nitrogen. In order to study the effect of Al addition on the properties of ZrAlN thin films, films with different Al concentrations were prepared at 773 K and nitrogen flow rate of 0.2 sccm. The experimental conditions are given in Table 5.1.

**Table 5.1 Deposition parameters of ZrAl and ZrAlN thin films**

| | |
|---|---|
| *Base pressure* | *8 x10$^{-4}$ Pa* |
| *Operating pressure* | *7.5 x10$^{-1}$ Pa* |
| *Substrate to target distance* | *60 mm* |
| *Target voltage* | *220 - 320 V* |
| *Substrate temperature* | *300-773 K* |
| *Pulse power* | *100 W* |
| *Duty cycle* | *20%* |
| *Pulse frequency* | *100 kHz* |
| *Argon flow rate* | *50-40 sccm (with Zr target);*<br>*50-48 sccm (with ZrN target)* |
| *Nitrogen flow rate* | *0-10 sccm (with Zr target);*<br>*0-2 sccm (with ZrN target)* |
| *Al Area* | *2.85 to 22.8 cm$^2$* |

The surface area of Al strip was varied from 2.85 to 22.8 cm$^2$ over zirconium nitride target of 45.34 cm$^2$ to realize the above alloyed films. The effect of substrate temperature, nitrogen flow rate at constant Al composition and Al addition at constant temperature and nitrogen flow rate on the microstructure, nanomechanical and tribological properties were also studied.

In addition to EPMA analysis, the composition of ZrAlN films was determined by proton elastic back scattering (PEBS), which is sensitive for light elements [296]. An analyzing beam of ${}_1H^+$ at energy of 2.1 MeV, backscattered by 165º, was used during the backscattering measurements. The experimental spectra were fitted using SIMNRA code [297]. SIMNRA is a Microsoft Windows program for the simulation of back or forward scattering spectra for ion beam analysis with MeV ions. SIMNRA is mainly intended for the simulation of spectra with non-Rutherford backscattering cross-sections,
nuclear reactions and elastic recoil detection analysis.

## 5.3 Characterisation of ZrAl and Alloyed ZrAlN Films

Firstly, the results of ZrAl and alloyed ZrAlN thin films sputtered from the composite target of Zr-Al on Si and D-9 alloy substrate are given. Secondly, the results of alloyed ZrAlN thin films prepared from a composite target of ZrN-Al as a function of processing condition and Al addition are presented. The last section discusses the thermal expansion behaviour and phase stability of the alloyed films.

### 5.3.1 ZrAl and Alloyed ZrAlN Thin Films Prepared from Composite Target of Zr-Al

Fig. 5.1 (a) shows the XRD pattern of ZrAl thin film deposited on Si (100) substrate as a function of substrate temperature in the range 300-773 K. These films were deposited by sputtering from a composite target of Zr-Al. The composite target of Zr-Al was prepared by an Al strip of surface area 5.7 cm$^2$ on Zr target as discussed in Chapter 2. The composition of these films were estimated by EPMA and it was found to be (12.6 at. %) 13 at. % of Al present in the film. The films were generally polycrystalline in

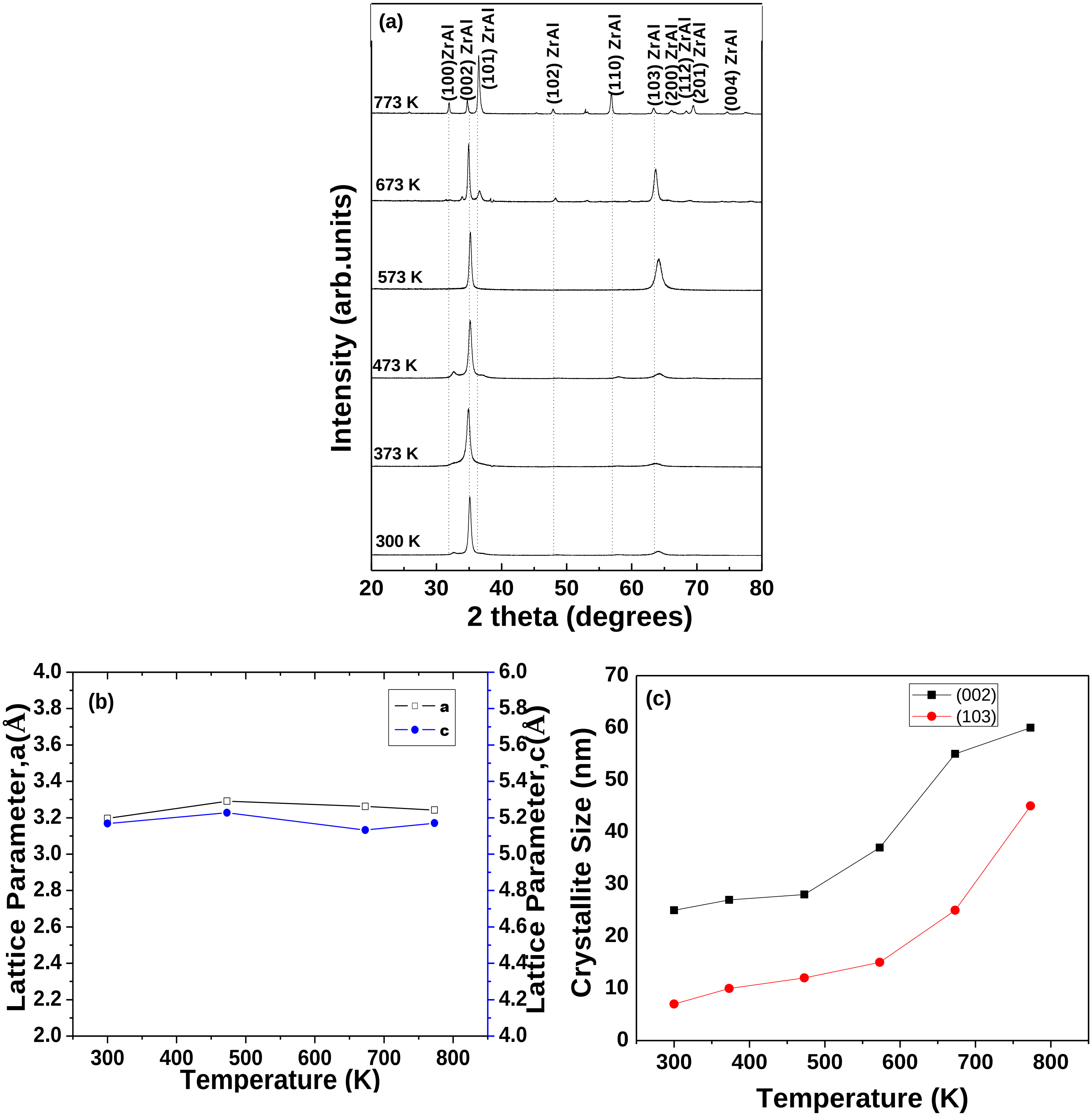

**Fig. 5.1 (a)** XRD pattern of ZrAl (13 at.% Al) thin films as a function of substrate temperature, (b) Lattice parameters and (c) Crystallite size variation.

nature and were crystalline even at room temperature. Formation of α - ZrAl phase of zirconium with [001] preferred orientation was noticed in the temperature range 300–773 K. It was found that crystallite size increased with increasing temperature up to 773 K. No traces of Al was noticed indicating the fact that Al atoms formed solid solution with Zr. Two strong peaks (002) and (103) of ZrAl were observed at all substrate temperatures and were used to calculate the crystallite size. It is also evident that at 773 K, the films were well crystalline. Similar behaviour has been reported for transition metal nitrides [271].

Fig. 5.1 (b) and (c) show the lattice parameters and crystallite size of ZrAl films as a function of substrate temperature. The lattice parameter values of ZrAl thin films were $a$ = 3.195-3.262 ±0.002 Å and $c$ = 5.131-5.170 ± 0.002 Å. The crystallite size was calculated using full width at half maximum (FWHM) of (002) and (103) reflection of XRD pattern and it was found to be increasing with increasing substrate temperature.

Fig.5.2 (a) shows the XRD pattern of ZrAlN thin films deposited on Si (100) substrate as a function of nitrogen flow rate in the range of 1-10 sccm and at 773 K. With addition of small amount of nitrogen, only fcc - ZrAlN phase was noticed at nitrogen flow rate ≤ 2 sccm. Also, a slight shift towards higher angle side in the 2θ values is also noticed. From the figure it is clear that as the nitrogen flow rate increases, film crystallinity decreases and films deposited at nitrogen flow rate >2 sccm of nitrogen are found to be x-ray amorphous. The broad peak seen above $32^{o}$ (2θ) also tends to shift toward lower angle. The crystalline size was calculated for the plane (200) and it was found to be decreasing with increasing flow rate of nitrogen (Fig. 5.2 (b)).

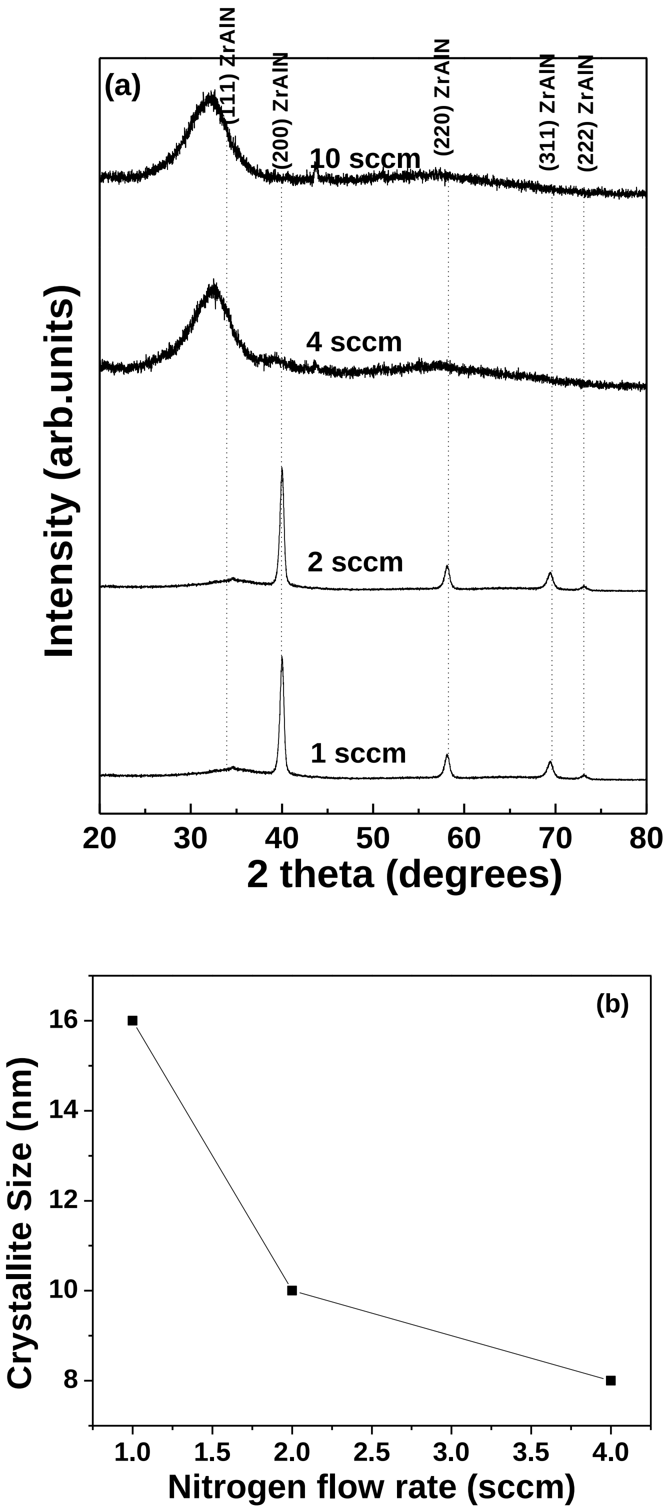

**Fig. 5.2** (a) XRD pattern of ZrAlN (13 at. % Al) thin films and (b) Crystallite size variation as a function of nitrogen flow rate.

Fig. 5.3 (a) and (b) show the AFM micrograph of ZrAl and ZrAlN thin films deposited on Si substrate. AFM micrograph shows a uniform surface morphology and the films are more crystalline at 773 K (Fig. 5.3 (a)) than at room temperature. It is also noticed that as the nitrogen flow rate increases films are tending to amorphisation (Fig. 5.3 b) in accordance with XRD results**.**

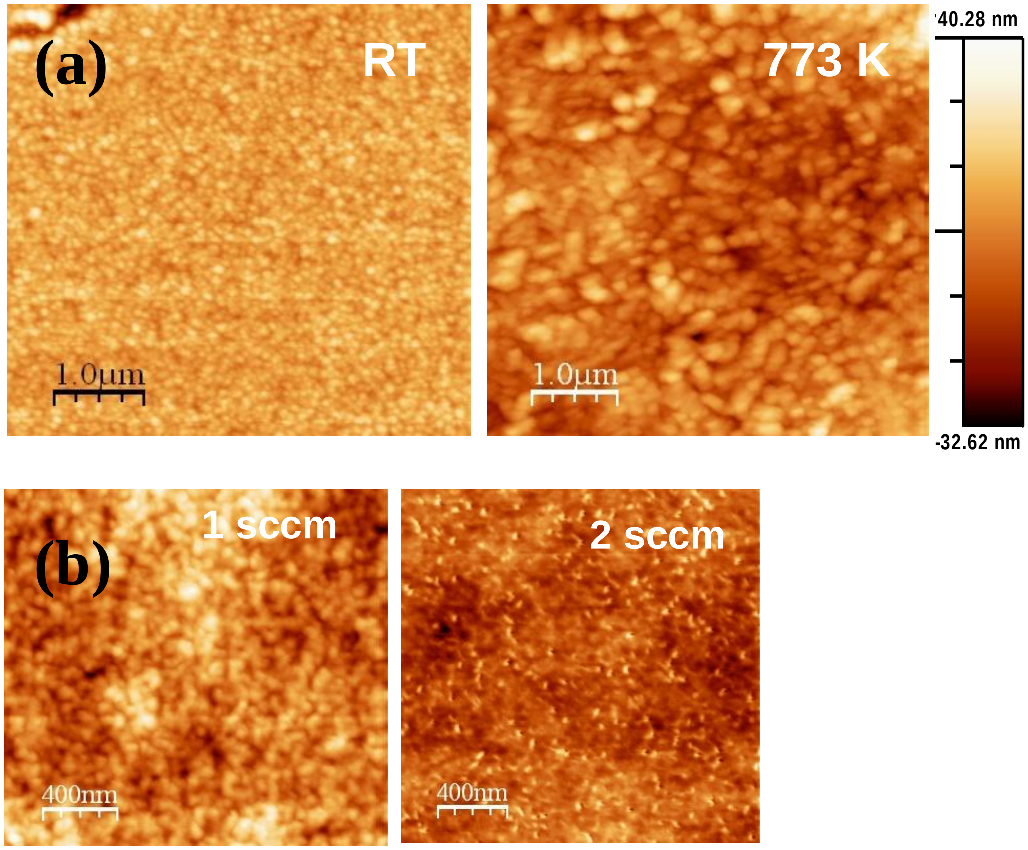

**Fig. 5.3** AFM micrographs of (a) ZrAl (13 at. % Al ) thin films as a function of substrate temperature and (b) ZrAlN (13 at. % Al) films at 773 K and as a function of nitrogen flow rate.

The hardness and elastic modulus of the ZrAlN (13 at.%Al ) thin films were measured by nano-indentation method (Fig. 5.4). The figure shows that hardness and elastic modulus of the zirconium aluminum nitride thin films increase with the increase in the nitrogen flow rate ≤ 2 sccm. Beyond 2 sccm flow rate of $N_2$, both the hardness and

Young's modulus are decreased possibly due to the formation of x-ray amorphous ZrAlN.

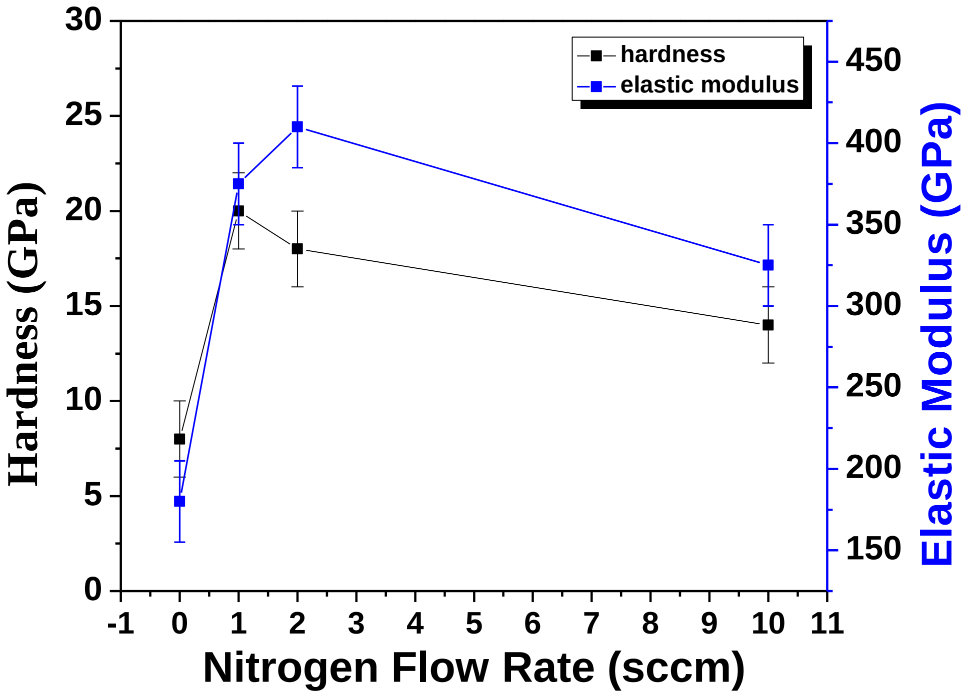

**Fig. 5.4** Hardness and elastic modulus of ZrAlN (13 at.%Al) thin films as a function of nitrogen flow rate.

### 5.3.2 Preparation of ZrAlN Thin Films from ZrN-Al Composite Target

Alloyed ZrAlN thin films were prepared by co sputtering of ZrN-Al composite target. The behaviour of ZrAlN films were studied as a function of processing parameters ( substrate temperature and nitrogen flow rate) and Al addition.

#### 5.3.2.1 Effect of substrate temperature

The growth characteristics of ZrAlN (13 at.% Al) as a function of temperature was studied at constant flow rate of 0.2 sccm of nitrogen.

Fig. 5.5 (a) shows the XRD pattern of ZrAlN thin films deposited on Si (100) substrate and at 0.2 sccm flow rate of nitrogen in the range 300 – 873 K. Only the reflections of (111), (200), (220), (311) and (222) corresponding to fcc- ZrAlN was noticed. At 300 K, films were poorly crystalline and as the substrate temperature increased the crystallinity also improved.

The lattice parameter (Fig. 5.5 (b)) was calculated using unit cell program. Determination of the lattice parameter of ZrAlN films showed a slight increase from 4.490 to 4.494 ± 0.002 Å in the temperature range 300–873 K, and were found to be lower than the lattice parameter value of ZrN. The full width at half maximum of the (200) reflection was used to estimate the crystallite size using Scherrer's equation. However, strain in the films was not taken into consideration while measuring the crystallite size. The crystallite size was found to be increasing up to 773 K and then decreasing at 873 K.

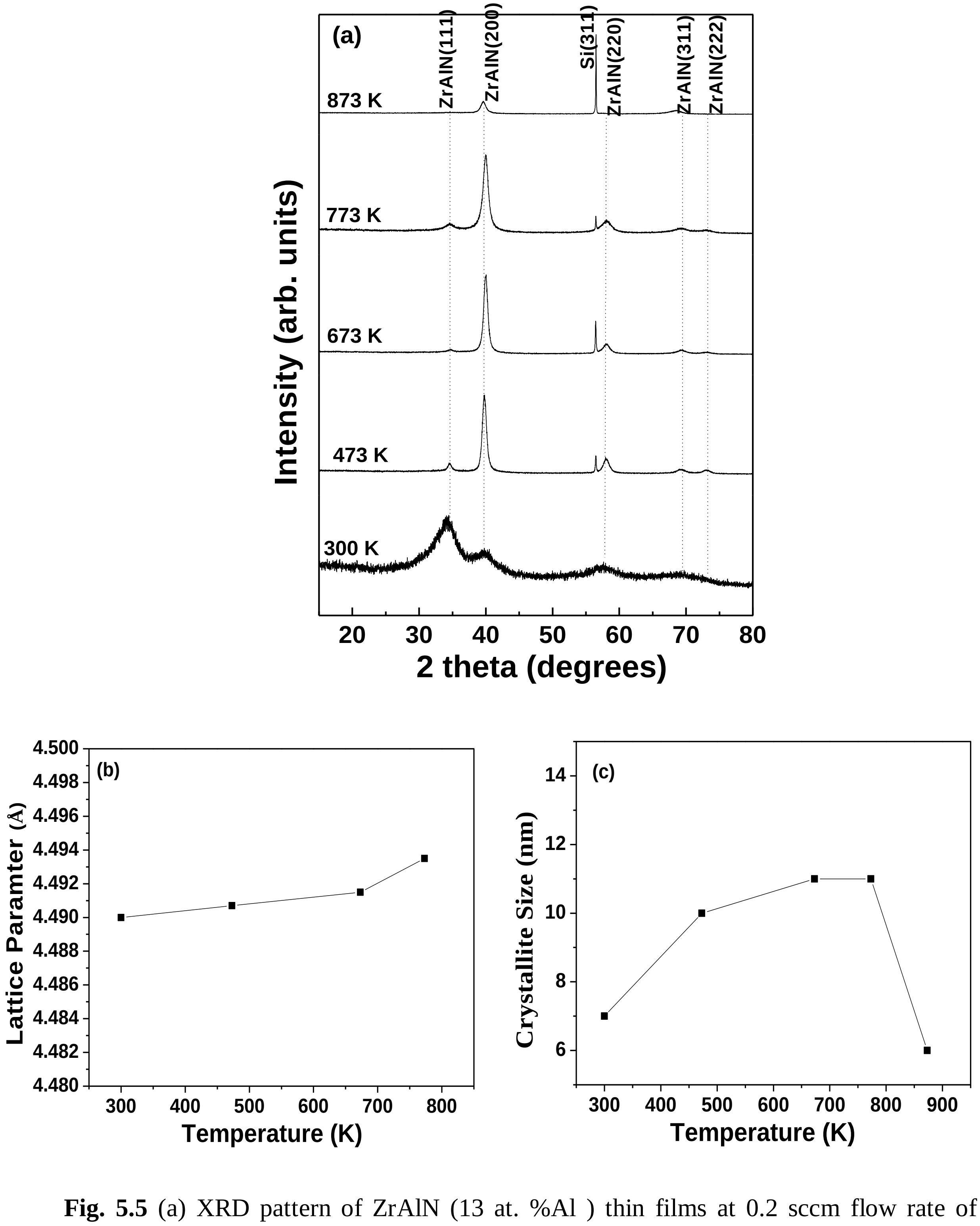

**Fig. 5.5** (a) XRD pattern of ZrAlN (13 at. %Al ) thin films at 0.2 sccm flow rate of nitrogen as a function of substrate temperature, (b) Lattice parameter versus temperature and (c) Crystallite size versus temperature.

### 5.3.2.2 Effect of nitrogen flow rate

The ZrAlN (13 at. %Al) films were deposited at 773 K by reactive sputtering in the mixture of nitrogen and argon as a function of nitrogen flow rates in the range 0 - 2 sccm for a constant time of deposition.

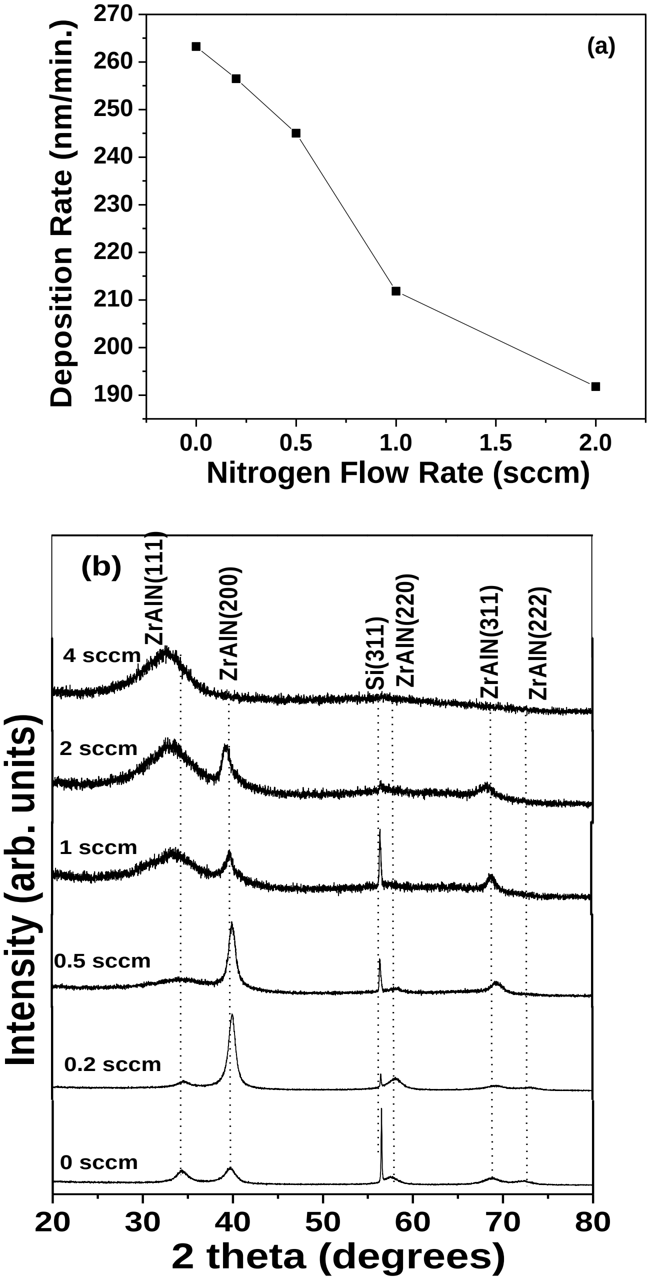

**Fig. 5.6** (a) Deposition rate and (b) XRD pattern of ZrAlN films as a function of nitrogen flow rate.

Substrate temperature was selected at 773 K, since at this temperature well grown crystallite was noticed. The thickness and the deposition rate were found to decrease with increasing flow rate of nitrogen (Fig.5.6 (a)). Typical thicknesses of the films were in the range 1-2 µm. Films showed light golden colour for the films deposited at nitrogen flow rates ≤ 0.2 sccm and exhibited light gray colour for those deposited at nitrogen flow rate > 0.2 sccm. Fig. 5.6 (b) shows the XRD pattern of ZrAlN (13 at. %Al) thin films deposited at 773 K; in varying flow rate of nitrogen in the range of 0 to 4 sccm. It is noticed that films deposited at lower flow rates of nitrogen ( ≤ 0.2 sccm) show (111), (200), (220) , (311) and (222) planes corresponding to fcc- ZrAlN phase. The films deposited at nitrogen flow rates >0.2 sccm show broadening and reduction in the intensities of (111) and (311) reflections. Films show (200) orientation at nitrogen flow rates ≤ 0.5 sccm and beyond 0.5 sccm flow rate of nitrogen, intensity of (200) reflection also decreases significantly and at 4 sccm flow rate of nitrogen it disappears. Also, the crystallite size of the films decreases with increasing nitrogen flow rate.

The Raman spectra of the films deposited in the nitrogen flow rate range of 0 to 2 sccm is shown in Fig. 5.7 and indicates the presence of ZrAlN phase. The spectra show the frequency band at 172 cm$^{-1}$, 210 cm$^{-1}$ and 510 cm$^{-1}$ of ZrAlN. The band positions obtained from the film is found to be consistent with the reported values of ZrN [32]. There is a slight shift in the Raman band from the ZrN band positions noticed due to Al content of 13 at.% of Al content. Also, with increasing nitrogen flow rate broadening in the Raman band is also present.

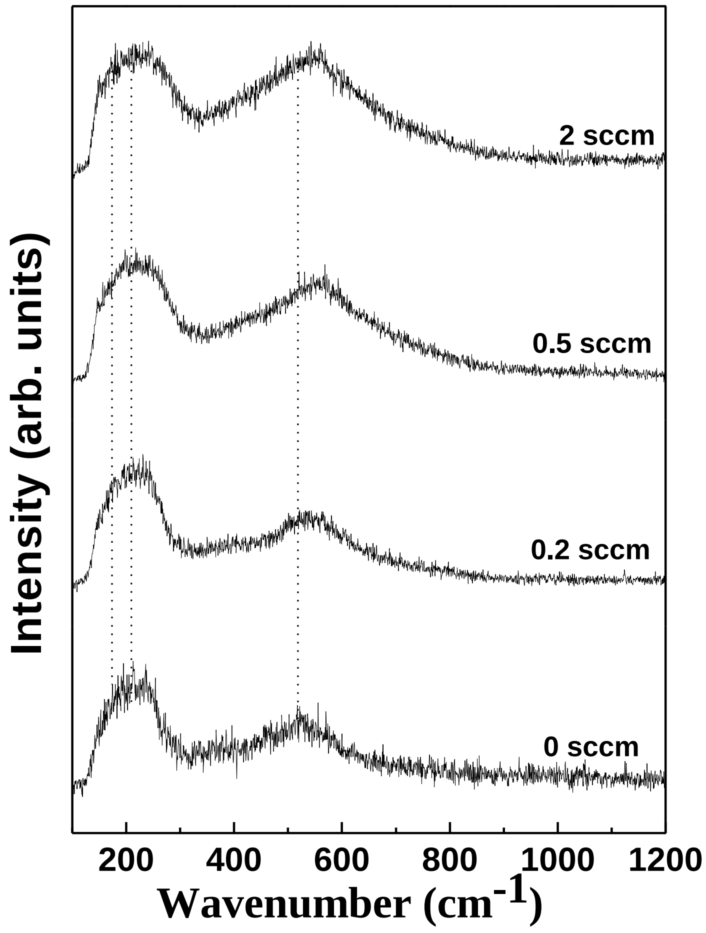

**Fig. 5.7** Raman spectra of ZrAlN thin films as a function of nitrogen flow rate.

### 5.3.2.3 Effect of Al addition

In order to study the effect of Al addition on the ZrAlN films, the substrate temperature and nitrogen flow rate were kept constant at 773 K and 0.2 sccm, respectively, based on the experimental results reported in earlier sections.

The composition of the films was determined by PEBS and EPMA. PEBS analysis was carried out for all the films to determine the elemental composition in the film. The experimental data was fitted using SIMNRA code [296]. Typical PEBS curves for the Al percentage of 13 at.% and 28 at. % respectively, are shown in Fig. 5.8 (a) and (b). EPMA analysis was also carried out for ZrAlN thin films to get the composition of the films. The elemental composition obtained from PEBS and EPMA study are given in Table 5.2 and 5.3 respectively. An histogram for the variation in the Zr, Al and N are also shown in the Fig. 5.9.

**Table 5.2 Elemental composition (at.%) obtained from PEBS**

| **Area of Al strip (cm$^2$)** | **Zr** | **Al** | **N** | **O** | **Si** |
|---|---|---|---|---|---|
| **0** | 45.0 | 0 | 52.0 | 0 | 0 |
| **5.7** | 36.0 | 15.0 | 49.0 | 0 | 0 |
| **11.4** | 26.5 | 24.5 | 45.0 | 0 | 5 |
| **22.8** | 18.0 | 30.0 | 39.0 | 8 | 5 |

**Table 5.3 Elemental composition obtained from EPMA**

| **Area of Al strip (cm$^2$)** | **Zr** | | **Al** | | **N** | | **Standard deviation (%)** | | |
|---|---|---|---|---|---|---|---|---|---|
| | wt% | at.% | wt% | at.% | wt% | at.% | Zr | Al | N |
| **0** | 82.4 | 46.5 | 0 | 0 | 14.6 | 53.5 | 0.45 | 0 | 3.45 |
| **5.7** | 72.6 | 33.8 | 7.8 | 12.6 | 17.6 | 53.6 | 0.49 | 0.37 | 3.03 |
| **11.4** | 61.4 | 24.9 | 20.7 | 28.4 | 17.7 | 46.7 | 0.55 | 0.22 | 2.92 |
| **22.8** | 51.2 | 20.5 | 26.4 | 35.7 | 16.8 | 43.8 | 0.61 | 0.19 | 3.06 |

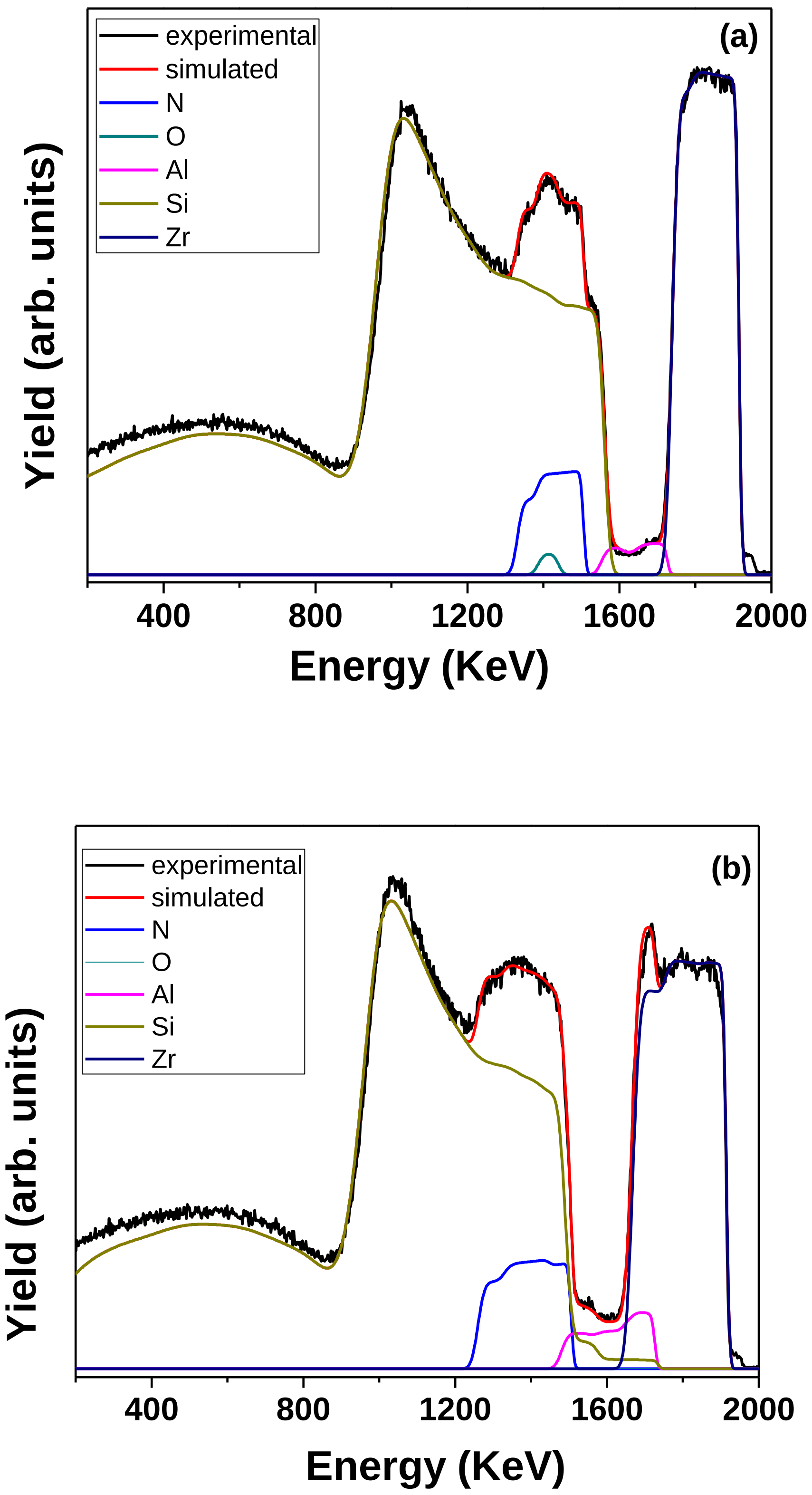

**Fig. 5.8** PEBS curve for (a) 13 at. % Al and (b) 28 at. % Al containing ZrAlN films.

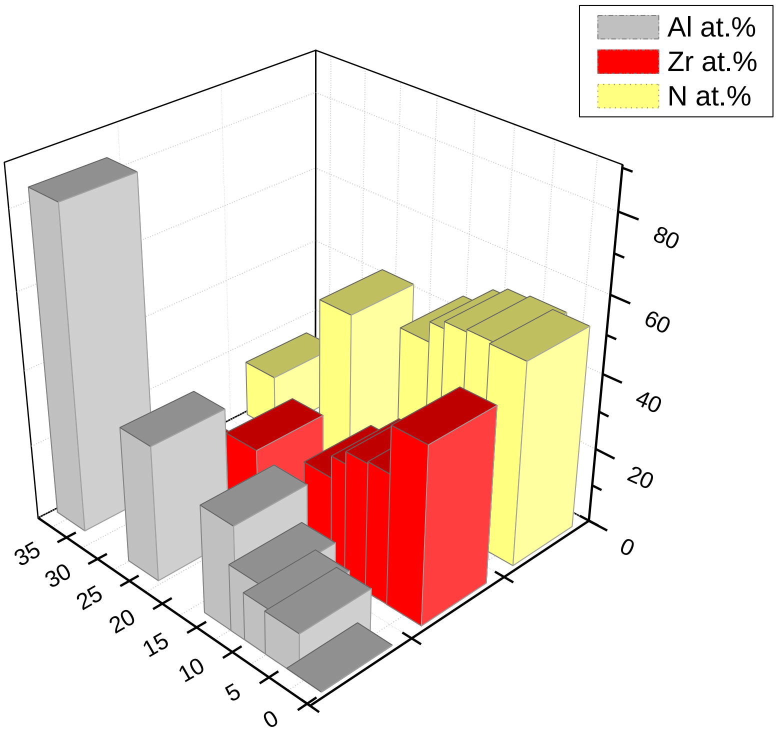

**Fig. 5.9** Histogram of the elements of Zr, Al and N obtained for the ZrAlN films from EPMA analysis.

The thickness and the deposition rate were found to increase slightly with increasing Al concentration (Fig.5.10 (a)). Typical thickness of the films was in the range 1-2 µm. Films showed golden colour for the films deposited at 0% of Al and exhibited light gray to dark gray colour as the Al content increased up to 36 at. %. Fig. 5.10 (b) shows the XRD pattern of ZrAlN thin films with different amounts of Al deposited on Si (100) substrate at nitrogen flow rate 0.2 sccm and substrate temperature of 773 K.

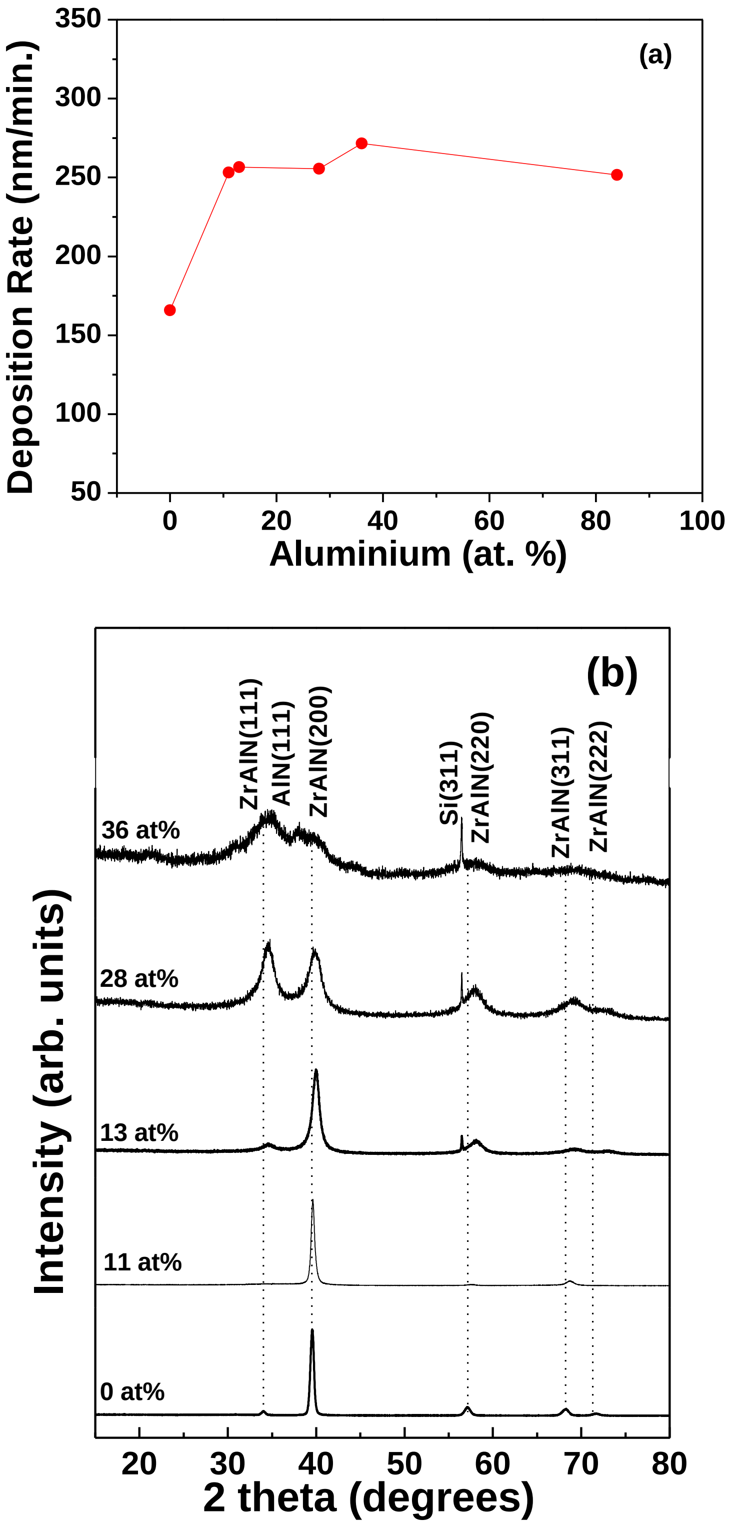

**Fig.5.10** (a) Deposition rate of ZrAlN thin films with Al addition and (b) XRD pattern of ZrAlN films as a function of Al deposited at 773 K and 0.2 sccm of nitrogen flow rate.

ZrAlN was noticed with the reflections of (111), (200), (220), (311) and (222) corresponding to fcc structure. No traces of Al were present in the XRD pattern. As the Al at. % increased up to 28 at. % of Al, reduction in the intensity and peak broadening was noticed for the (200), (220) and (311) reflections. At 36 at. % of Al, there was a severe peak broadening for lower angle reflections and ZrAlN tended to form x-ray amorphous structure. In addition, a weak reflection of (111) of AlN was also noticed

The lattice parameter, *a* of any alloyed films were deduced from ZrAlN film. Fig. 5.11 (a) showed a linear relationship, $a=a_0 - 0.0028\ x$ (where $a_0=0.455$ nm for ZrN and x is the concentration of Al in at. %. It was also found that the value of lattice parameter decreased with increasing Al content. The crystallite sizes were calculated from (200) and (111) reflection of the ZrAlN patterns. The crystallite size of the ZrN films for (200) reflection deposited without any Al addition was ~32 nm, and it decreased from ~32 nm to ~3 nm with an increase in the Al content from 0 to 36 at. % (Fig. 5.11 (b)). The above crystallite sizes were calculated using Scherrer’s formula which does not take strain into consideration.

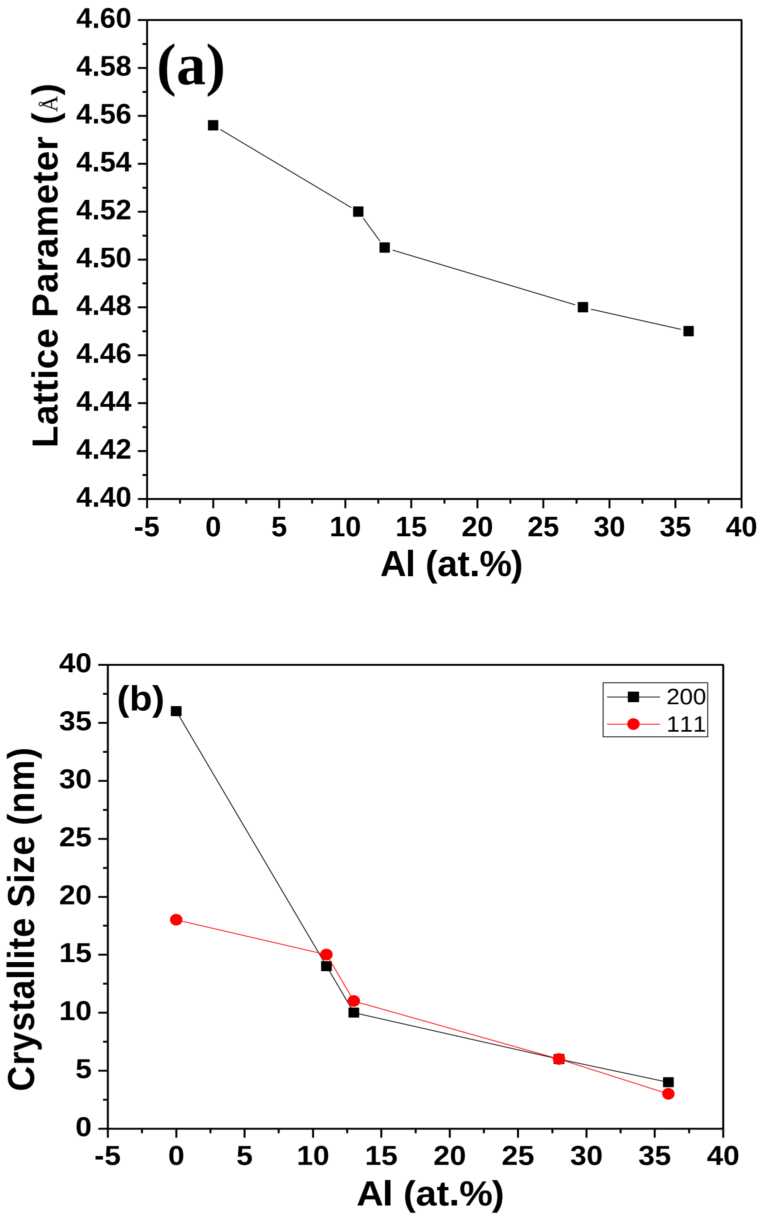

**Fig. 5.11** (a) Lattice parameter and (b) Crystallite size variation as a function of Al content.

Raman analysis (Fig. 5.12) also showed alloyed ZrAlN peaks and there was a shift in the Raman peaks as Al concentration increases up to 36 at. %. The spectra indicate the frequency band of 172 cm$^{-1}$, 210 cm$^{-1}$, 510 cm$^{-1}$ and 980 cm$^{-1}$ of ZrN. The band positions obtained from the film is found to be consistent with the reported values of ZrN.

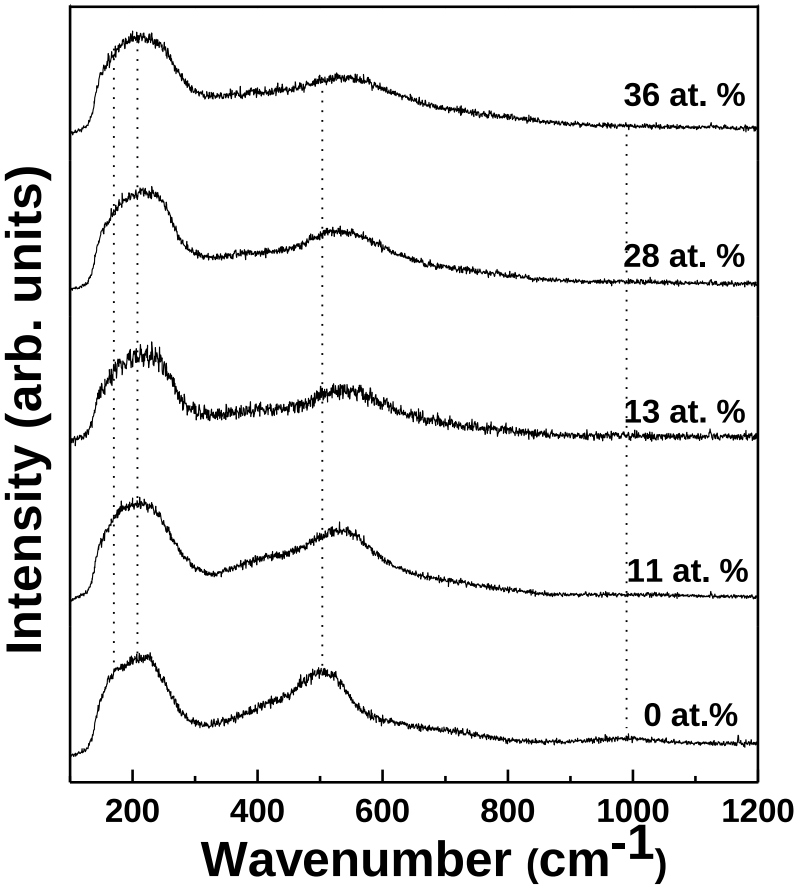

**Fig.5.12** Raman spectra of ZrAlN films as a function of Al content.

The variation in surface morphology and crystallite size using AFM have been also investigated (Fig. 5.13) and it is found that as the Al % increased, the crystallite size decreased. It was also noticed that at higher percentage of Al, the crystallites formed agglomerates and grew in size. Unlike XRD, the crystallite sizes could not be measured accurately owing to the overlapping of the crystallites. Also, the films did not contain any cracks in any of the above films.

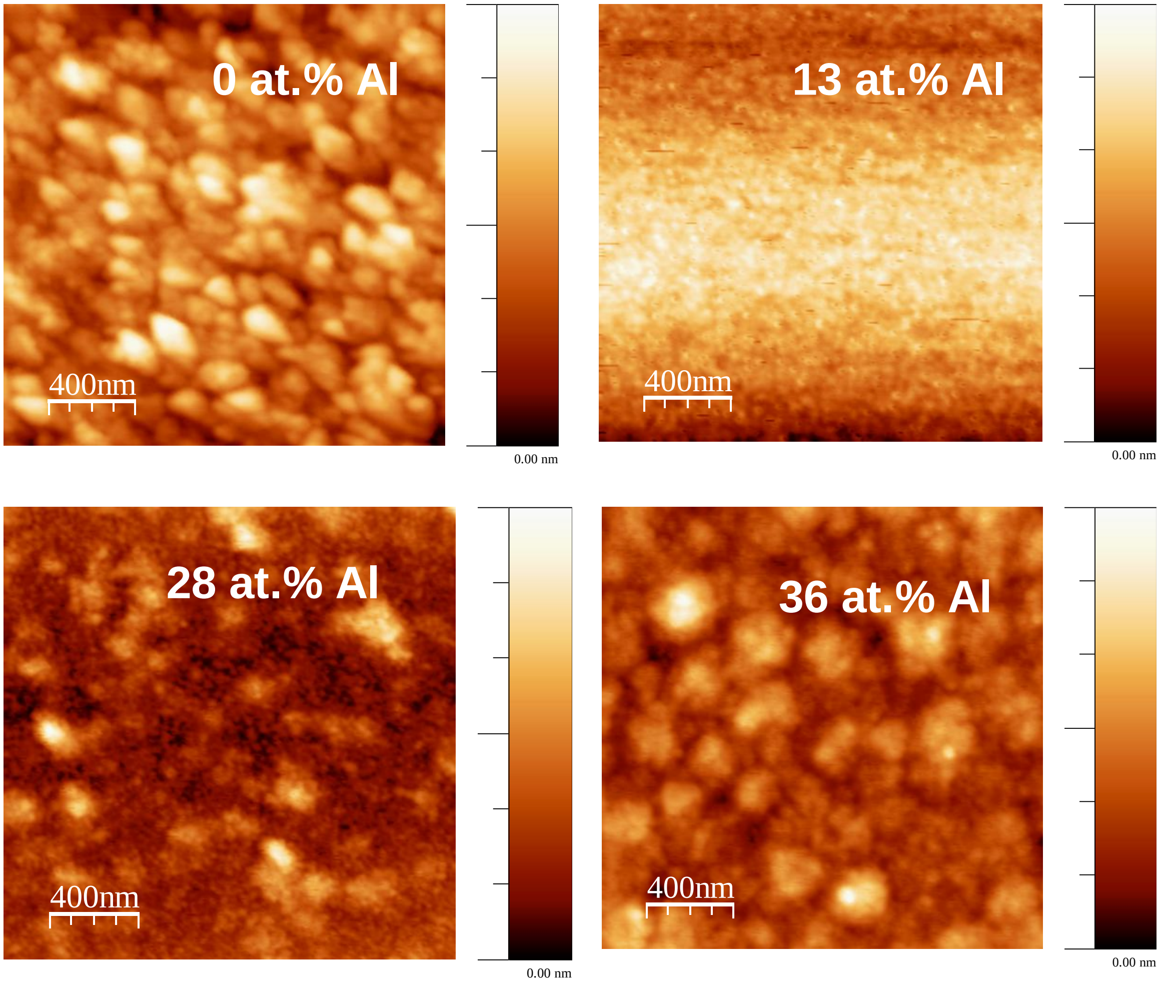

**Fig. 5.13** AFM micrographs of ZrAlN films with different Al contents.

TEM studies show that the ZrAlN with 28 at. % of Al film deposited at 773 K and 0.2 sccm flow rate of nitrogen reveal fcc-ZrAlN phase of equiaxed nanocrystallites of sizes in the range 2-6 nm (Fig. 5.14 (a)). Diffraction pattern corresponding to first, second and third rings of the inset of Fig. 5.14 (a) gives evidence of $SiO_2$, $ZrO_2$ and ZrAlN phase (Table 5.4). Similar SAD pattern were obtained at different regions of the sample.

**Table 5.4 Calculated d-spacings of different phases obtained in the ZrAlN (28 at.% Al) from the selected area diffraction patterns of the films deposited at 773 K and nitrogen flow rate of 0.2 sccm**

| S. No. | R($nm^{-1}$) | d(nm) | ZrN(cF8) (04-004-2860) | | $ZrO_2$(mP12) (01-070-2491) | | $SiO_2$(hP9) (00-012-0708) | |
|---|---|---|---|---|---|---|---|---|
| | | | d(nm) | hkl | d(nm) | hkl | d(nm) | hkl |
| **1** | 2.742 | 0.3647 | - | - | - | - | 0.338 | 101 |
| **2** | 3.160 | 0.3164 | - | - | 0.3164 | -111 | - | - |
| **3** | 4.408 | 0.2268 | 0.2292 | 200 | - | - | - | - |

**Table 5.5 Calculated d-spacings of different phases obtained in the ZrAlN (36 at.% Al) from the selected area diffraction patterns of the films deposited at 773 K and nitrogen flow rate of 0.2 sccm**

| S. No. | R($nm^{-1}$) | d(nm) | ZrN(cF8) (04-004-2860) | | $SiO_2$(hP9) (00-012-0708) | | AlN(cF8) (00-046-1200) | |
|---|---|---|---|---|---|---|---|---|
| | | | d(nm) | hkl | d(nm) | hkl | d(nm) | hkl |
| **1** | 2.95 | 0.3390 | - | - | 0.338 | 101 | - | - |
| **2** | 3.42 | 0.2924 | 0.2647 | 111 | - | - | - | - |
| **3** | 4.81 | 0.2079 | 0.2292 | 200 | - | - | 0.2023 | 200 |
| **4** | 5.89 | 0.1698 | 0.1621 | 220 | - | - | - | - |
| **5** | 6.80 | 0.1470 | 0.1382 | 311 | - | - | 0.1430 | 220 |

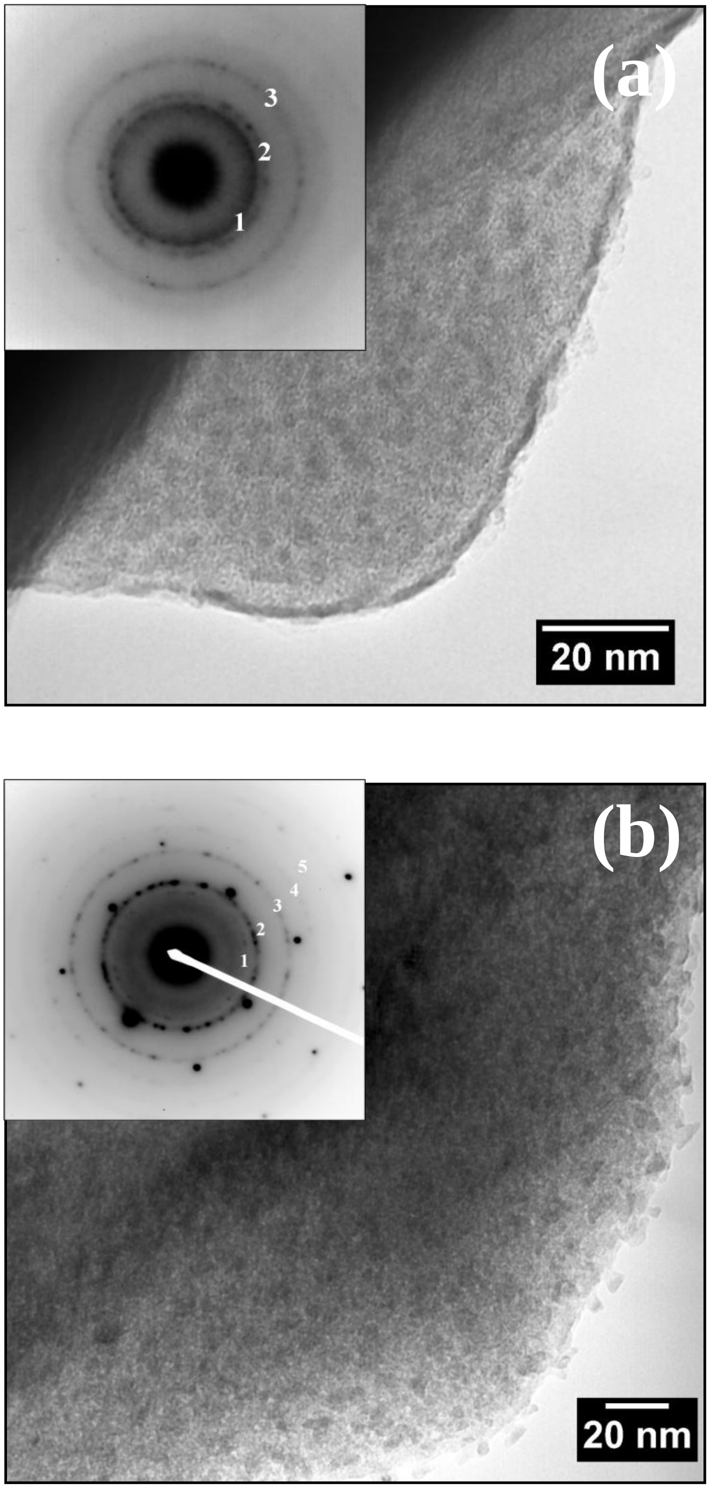

**Fig. 5.14** Bright field TEM images from (a) $Zr_{0.25}Al_{0.28}N_{0.47}$ and (b) $Zr_{0.20}Al_{0.36}N_{0.44}$ film deposited at 773 K and nitrogen flow rate of 0.2 sccm. The corresponding selected area diffraction patterns are shown in the inset.

Fig. 5.14 (b) shows TEM results on the ZrAlN films with 36 at. % Al deposited at 773 K and 0.2 sccm flow rate of nitrogen. It reveals fcc-ZrAlN and AlN phase of equiaxed nanocrystallites of sizes in the range 2-6 nm (Fig. 5.14 (b)). Diffraction pattern corresponding to second and fourth rings of the inset of Fig. 5.14 (b) gives evidence of ZrAlN phase (Table 5.5). Third and fifth ring of the diffraction pattern shown in the inset correspond to AlN phase. It is clear small amount of AlN phase is noticed with ZrAlN films with 36 at. % of Al content.

### 5.3.3 Thermal Expansion Behaviour of ZrAlN Thin Films

The phase stability and linear thermal expansion behaviour of alloyed ZrAlN thin films with different Al concentration $Zr_{0.34}Al_{0.13}N_{0.53}$, and $Zr_{0.25}Al_{0.28}N_{0.47}$ were investigated. Fig. 5.15 (a) shows the HTXRD pattern of $Zr_{0.34}Al_{0.13}N_{0.53}$ in the temperature range of 300-1473 K. The figure also shows that addition of 13 at. % of Al did not promote the formation of any oxide phase of Zr. However, there is a slight inter-diffusion of the film as it is evident from the reduction in the peak intensities of (200) and (311) reflections. The plot of lattice parameter and CTE as a function of temperature are also shown in Fig. 5.15 (b) and (c), respectively. Second order polynomial fit was used for the non linear fitting of the lattice parameter. Average and instantaneous CTE was calculated and it was found that average CTE was slightly higher than that of instantaneous CTE.

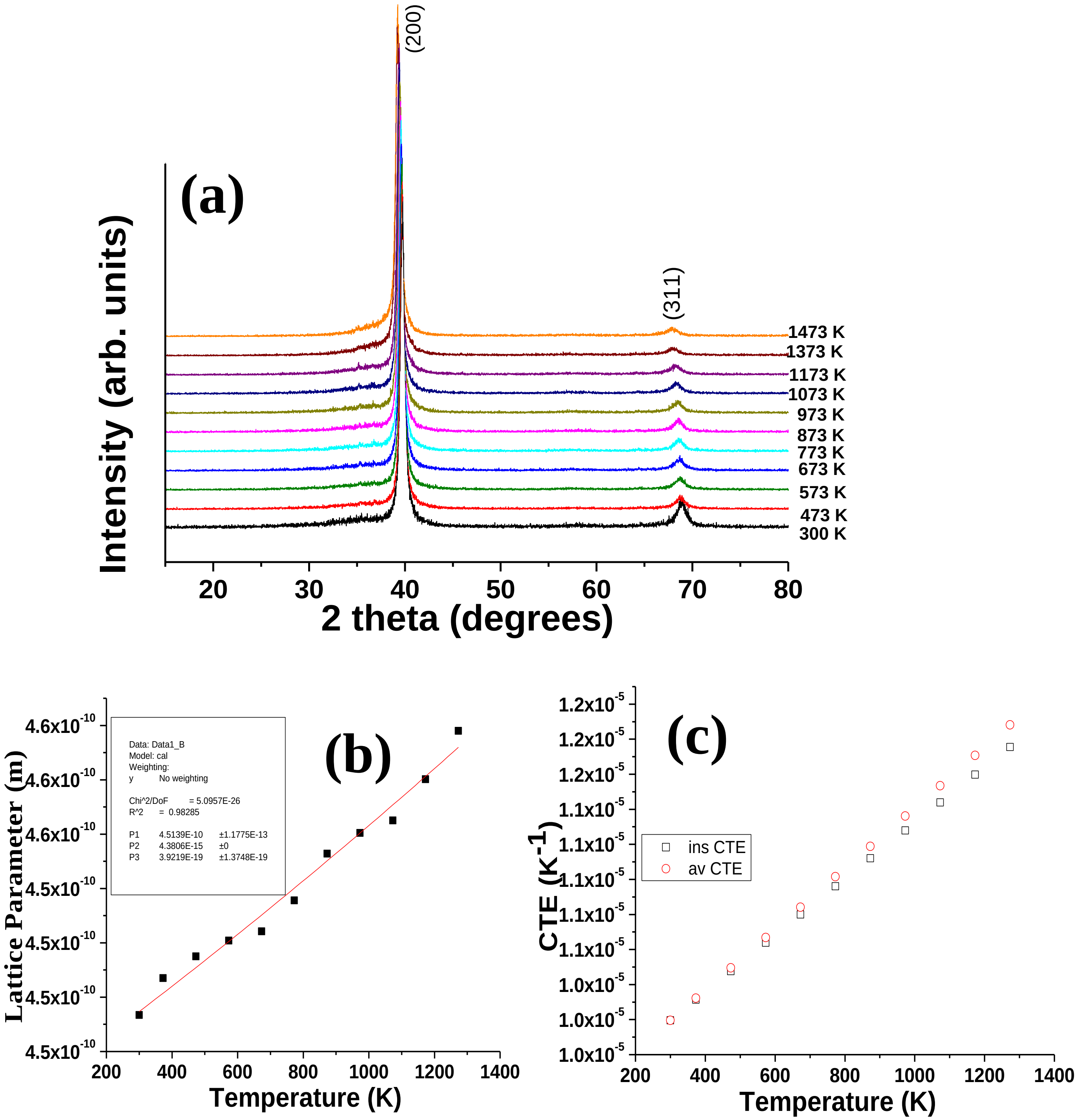

**Fig. 5.15** (a) HTXRD pattern of $Zr_{0.34}Al_{0.13}N_{0.53}$ films, (b) Variation in the lattice parameter and (c) CTE of the films as a function of temperature.

The lattice parameter of $Zr_{0.34}Al_{0.13}N_{0.53}$ was found to be:

$$a_T(\text{Å}) = 4.513 \times 10^{-10} + 4.381 \times 10^{-15} (T) + 3.922 \times 10^{-19}(T^2)$$

in the temperature range 300-1373 K and the average linear thermal expansion coefficients are found to be:

$$\alpha_T (K^{-1}) = 9.3 \times 10^{-6} +2.7 \times 10^{-9} (T)$$

Fig. 5.16 (a) shows the HTXRD pattern of $Zr_{0.25}Al_{0.28}N_{0.47}$ in the temperature range of 300-1373 K. Lattice parameter and CTE versus temperature plots are also shown in Fig. 5.16 (b) and (c) respectively. Second order polynomial fit was used for the non linear fitting of the lattice parameter. Average and instantaneous CTE was calculated and it is found that average CTE was slightly lower than that of instantaneous CTE. The thermal expansion coefficient was determined from the change in the lattice parameter as a function of temperature. It was found that the ZrAlN thin film was stable up to 1373 K and there was no signature for the formation of any secondary phase. The following is the lattice parameter of $Zr_{0.25}Al_{0.28}N_{0.47}$. It is in the temperature range 300-1373 K:

$$a_T(\text{Å}) = 4.454 \times 10^{-10} + 4.139 \times 10^{-15} (T) + 9.416 \times 10^{-19} (T^2)$$

and the average linear thermal expansion coefficient were found to be:

$$\alpha_T(K^{-1}) = 10.01 \times 10^{-6} +1.9 \times 10^{-9} (T)$$

The CTE values of alloyed ZrAlN thin films show higher values for the 13 and 28 at. % of Al alloyed films of ZrAlN than that of the ZrN films ($7.2 \times 10^{-6}$ $K^{-1}$) reported in the previous chapter.

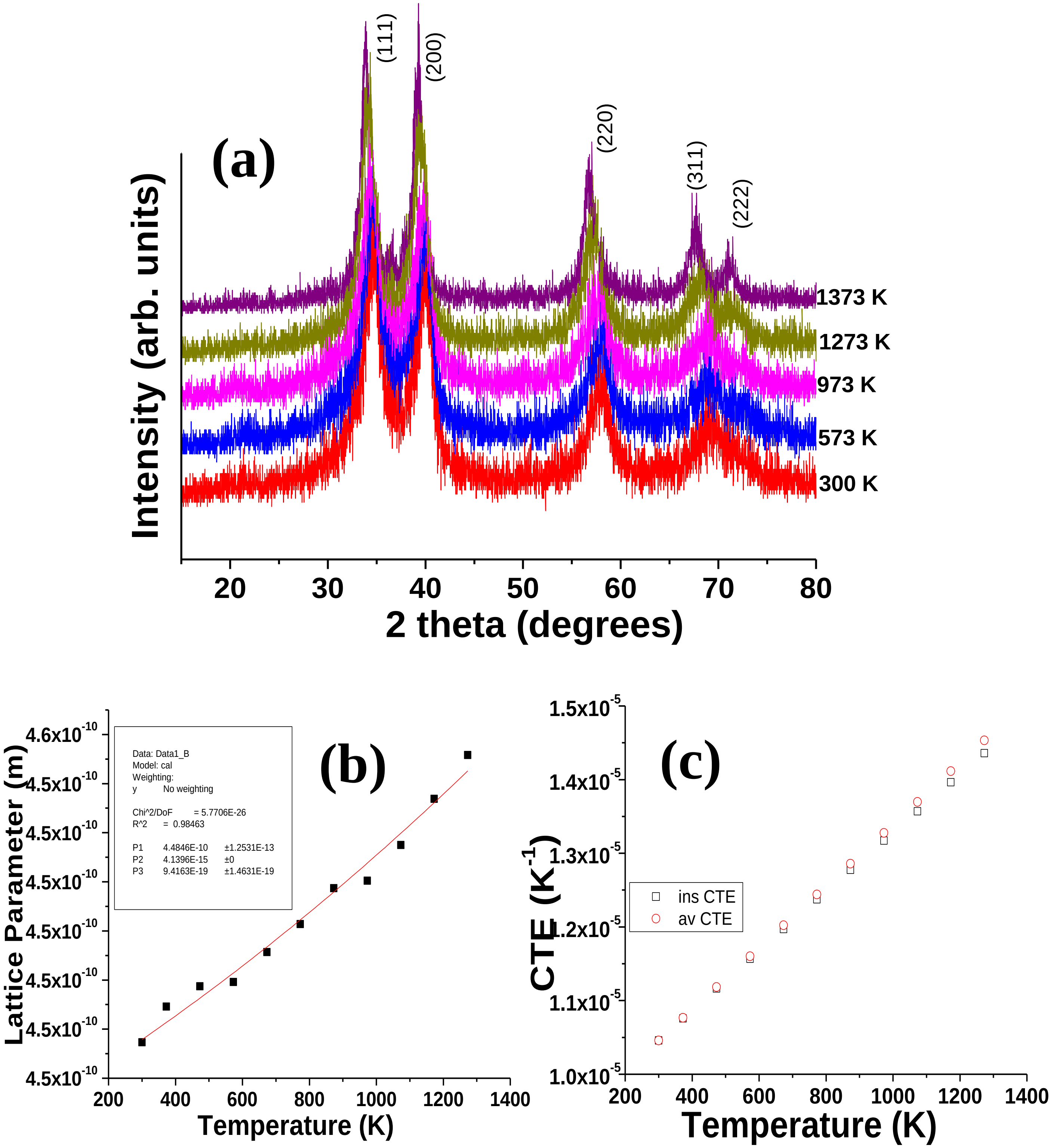

**Fig. 5.16** (a) HTXRD pattern of $Zr_{0.25}Al_{0.28}N_{0.47}$ films, (b) Variation in the lattice parameter and (c) CTE of the films as a function of temperature.

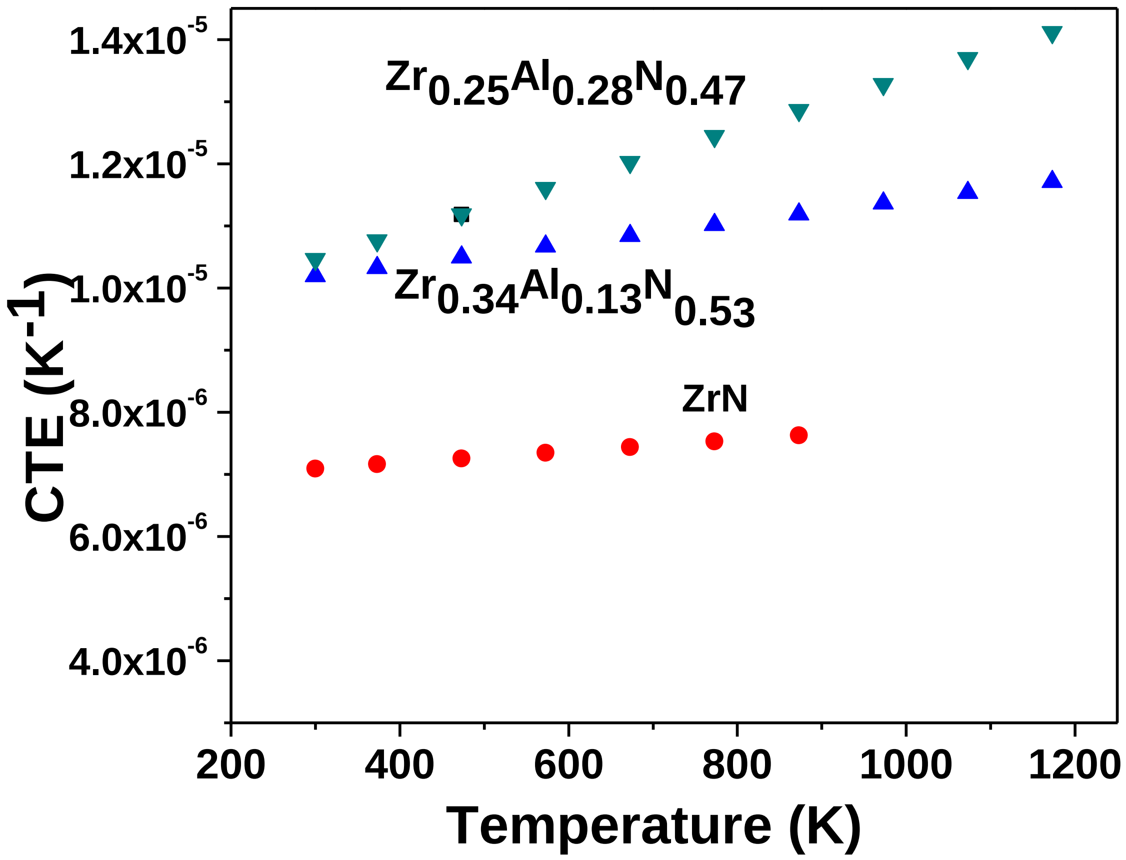

**Fig. 5.17** A comparative plots of average CTE of ZrN and ZrAlN alloyed thin films as a function of temperature.

Fig. 5.17 presents a comparative data of the CTE for ZrN and alloyed ZrAlN thin films measured in the present investigation. From the figure it is clear that Al addition increases the CTE compared to that of ZrN films.

### 5.3.4 Nanomechanical Properties of Alloyed ZrAlN Thin Films

Nano-indentation measurements were carried out to estimate the mechanical properties of the films. The indentation load and displacement were continuously recorded during one complete cycle of loading and unloading [229] for measuring the hardness and modulus of the films. The nanohardness and Young's modulus were evaluated using the approach by Oliver and Pharr [196].

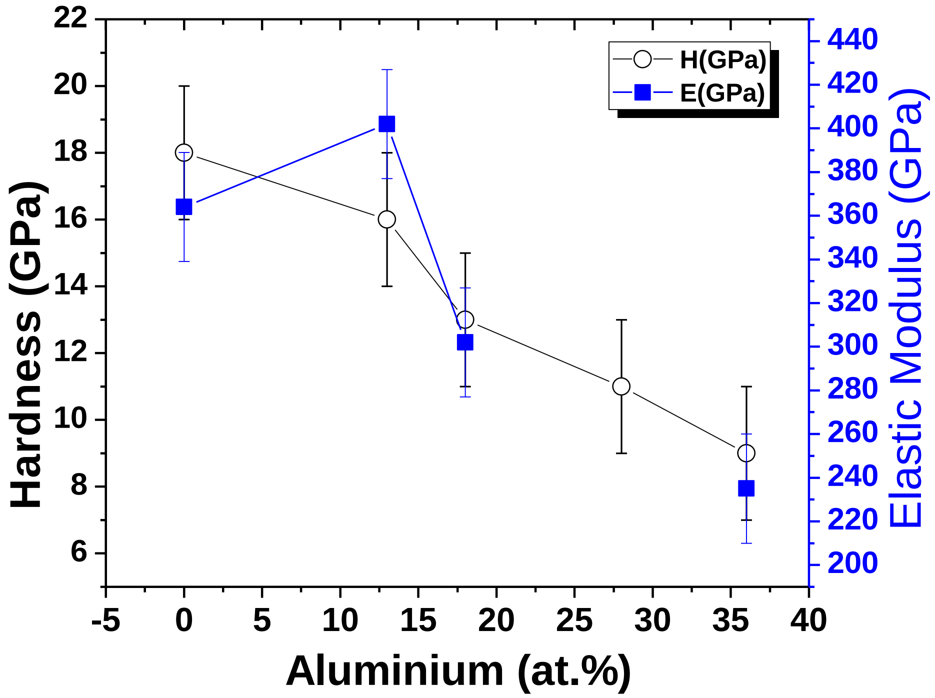

**Fig. 5.18** Hardness and elastic modulus of the alloyed ZrAlN films deposited on D-9 alloy at 773 K and nitrogen flow rate of 0.2 sccm.

The load displacement response obtained by nano-indentation contains information about the elastic and plastic deformation of the films. The nanohardness of ZrAlN thin films deposited on D-9 alloy was measured with various amount of Al.

It is observed that the values of hardness and Young's modulus of the ZrAlN films were in the range 9-18 GPa ± 2 GPa and 235-364 GPa ± 25 GPa, respectively (Fig. 5.18 ). It is also noticed that with increasing Al addition, hardness value decreases.

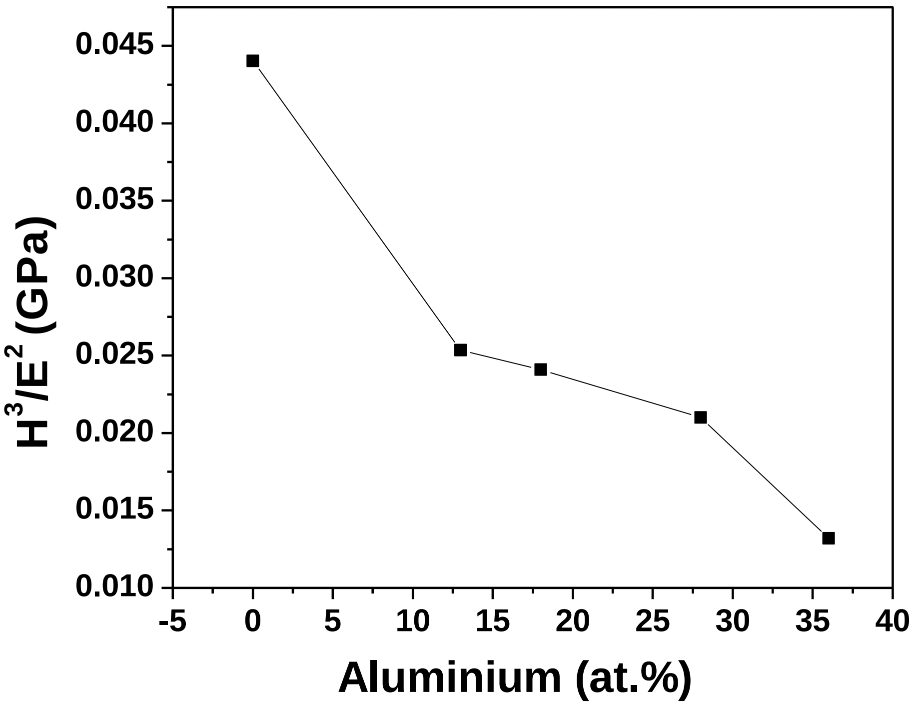

**Fig. 5.19** $H^3/E^2$ values of ZrAlN alloyed films as a function of Al content.

Fig. 5.19 shows the values of $H^3/E^2$ of the ZrAlN thin films as a function of Al. $H^3/E^2$ of ZrAlN films has a value 0.025 for the films with 13 at. % of Al. It is also noticed that $H^3/E^2$ value decreases with Al addition. This suggests that the resistance to plastic deformation decreases as the Al content increases.

Scratch test was carried out to determine the films adhesion with the substrate and the film failure, if any. After scratch test, tested region was further assessed by optical microscopy and scanning electron microscopy. The tangential force, friction coefficient and acoustic emission signals were measured as a function of scratch length and used as a supplementary test to identify different film damage levels.

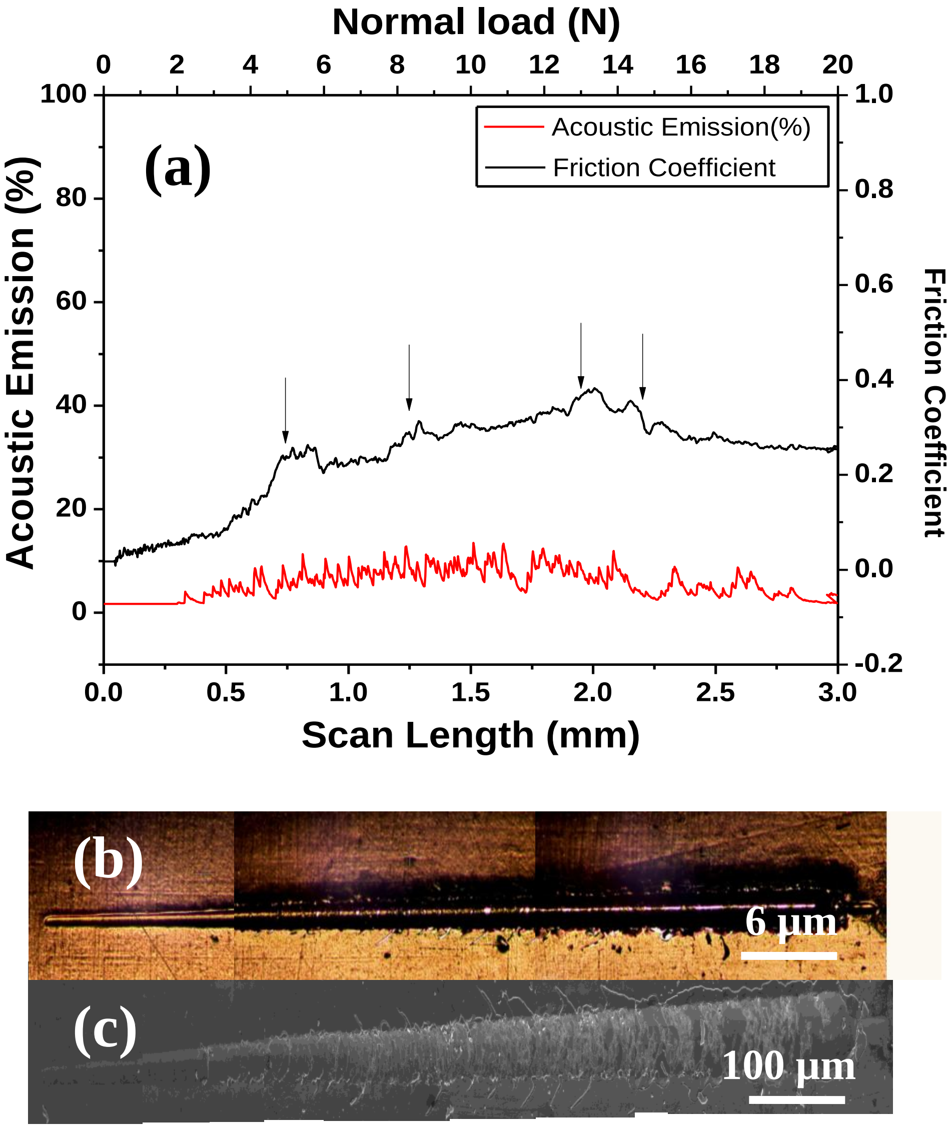

**Fig. 5.20** (a) Scratch test result of $Zr_{0.34}Al_{0.13}N_{0.53}$ films, (b) optical micrograph of scratch tested region and (c) SEM micrograph of the corresponding scratch tested region.

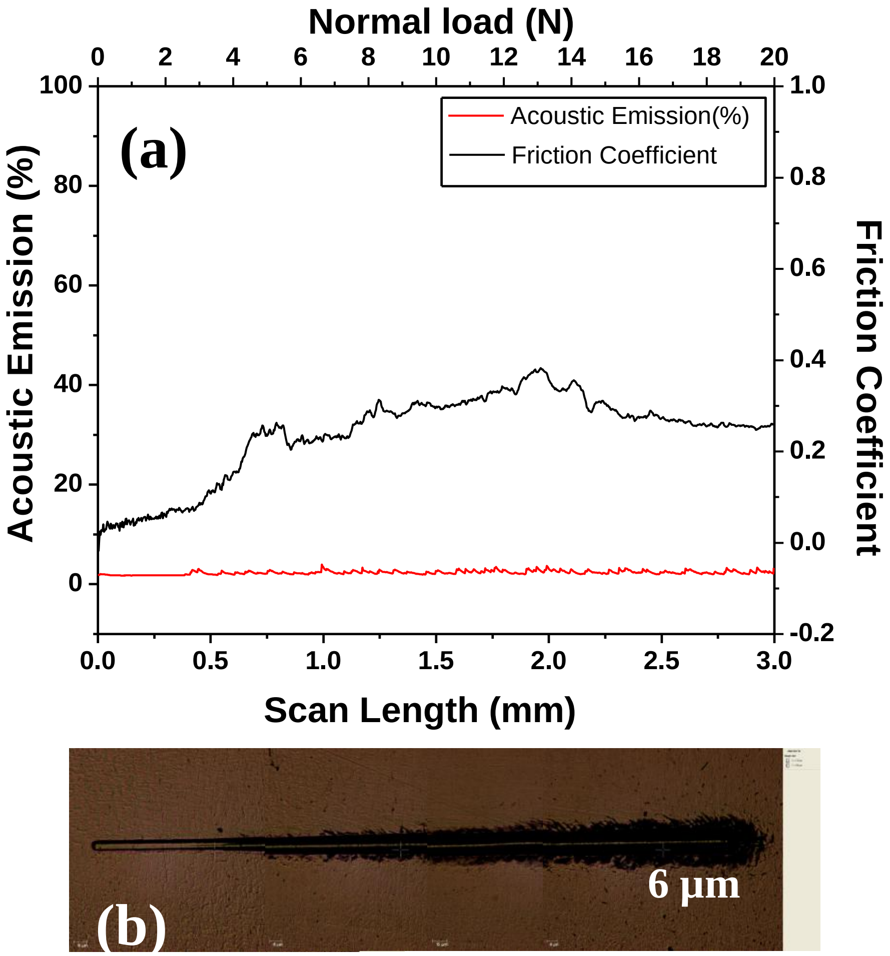

**Fig. 5.21** (a) Scratch test result of $Zr_{0.20}Al_{0.36}N_{0.44}$ films and (b) Optical micrograph of scratch tested region.

Fig. 5.20 (a) shows scratch test results for the ZrAlN films with 13 at. % of Al. Scratch tests were carried out with progressive load to determine the critical scratch load and friction coefficient for a given damage level. Fig. 5.21 (a) shows scratch test results for the ZrAlN films with 36 at. % of Al. From the acoustic emission signals and friction coefficient curves, first critical loads for $Zr_{0.34}Al_{0.13}N_{0.53}$ and $Zr_{0.20}Al_{0.36}N_{0.44}$ films was about ~ 4.9 N and 4.2 N, respectively. Fig. 5.20 (b) and Fig. 5.21 (b) show the optical images taken during the scratch testing. A typical SEM image corresponding to scratch tested region is also shown in Fig. 5.20 (c) for the $Zr_{0.34}Al_{0.13}N_{0.53}$ film. Both optical and SEM images of the scratch test regions indicate chipping and flaking of film close to the region where there is a change in the friction coefficient as a function of normal load. From the Fig. 5.20 and 5.21, it is evident that during the failure there is a change in the friction coefficient value as indicated by arrows. However, the variation in the acoustic signal as a function of scan length is more with $Zr_{0.34}Al_{0.13}N_{0.53t}$ than that of $Zr_{0.20}Al_{0.36}N_{0.44}$ films.

### 5.3.5 Tribological Behaviour of Alloyed ZrAlN Films

Fig. 5.22 shows the COF versus wear distance plots of $Zr_{0.47}N_{0.53}$, $Zr_{0.34}Al_{0.13}N_{0.53}$, $Zr_{0.25}Al_{0.28}N_{0.47}$ and $Zr_{0.20}Al_{0.36}N_{0.44}$ alloyed films of ZrAlN. It is seen that the COF values initially increase and then saturates after 2 meter of wear distance. The COF values were tested with steel and $Al_2O_3$ counterbodies. Tribological studies of the ZrAlN thin film showed that the COF of ZrAlN thin films is lower for the steel ball (100Cr6 steel) than that for the $Al_2O_3$ ball irrespective of Al concentration.

The COF values were measured at 5 meter of wear distance for all the composition and it was found to be 0.7, 0.65, 0.75 and 0.55 for steel balls and 0.7, 0.85, 0.9 and 0.75 for $Al_2O_3$ balls for $Zr_{0.47}N_{0.53}$, $Zr_{0.34}Al_{0.13}N_{0.53}$, $Zr_{0.25}Al_{0.28}N_{0.47}$ and $Zr_{0.20}Al_{0.36}N_{0.44}$ compositions respectively. Though the COF value obtained from the alumina ball is always higher than those obtained with steel ball, no clear trend is obtained for the COF with increasing amount of Al addition in the present work. The behaviour measured from wear test appeared to be quite complex and not fully understood.

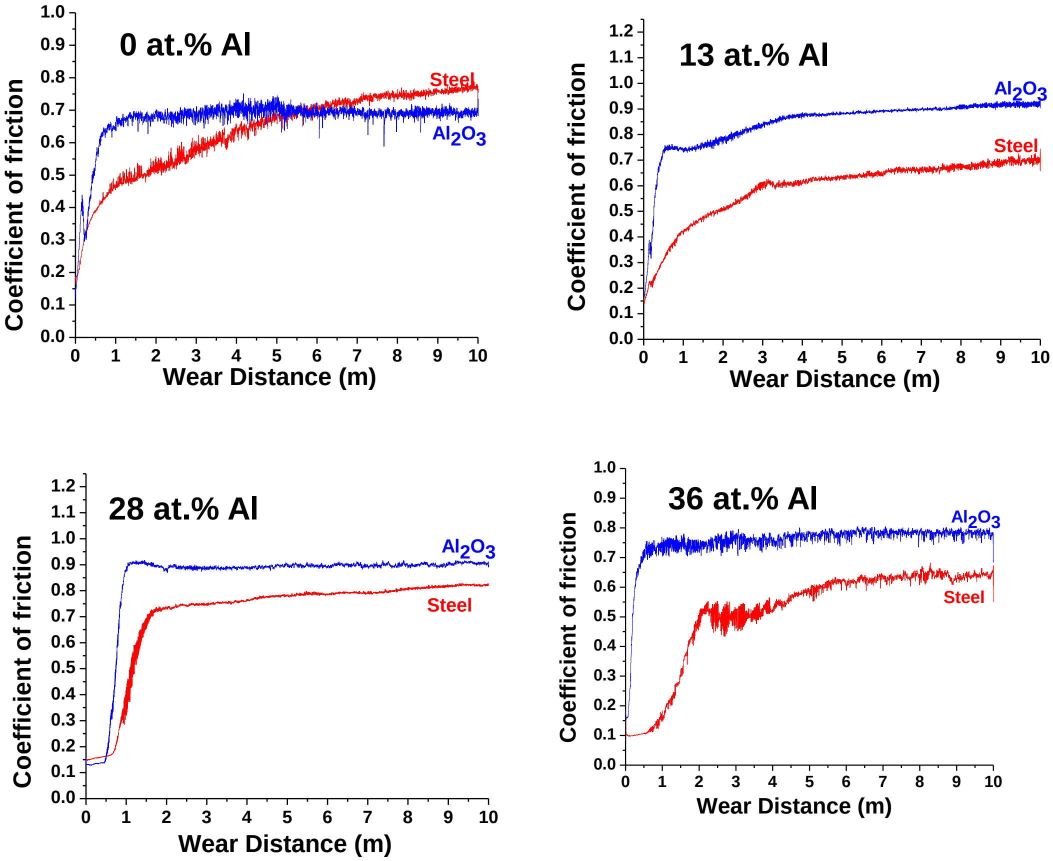

**Fig. 5.22** COF versus wear distance plots of $Zr_{0.47}N_{0.53}$, $Zr_{0.34}Al_{0.13}N_{0.53}$, $Zr_{0.25}Al_{0.28}N_{0.47}$ and $Zr_{0.20}Al_{0.36}N_{0.44}$ films of ZrAlN.

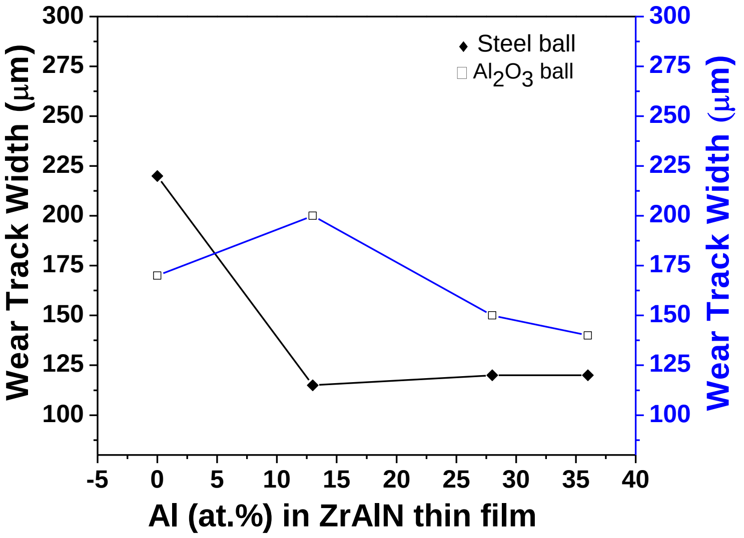

**Fig. 5.23** Wear track width versus Al concentration in the ZrAlN thin films tested with steel and alumina balls.

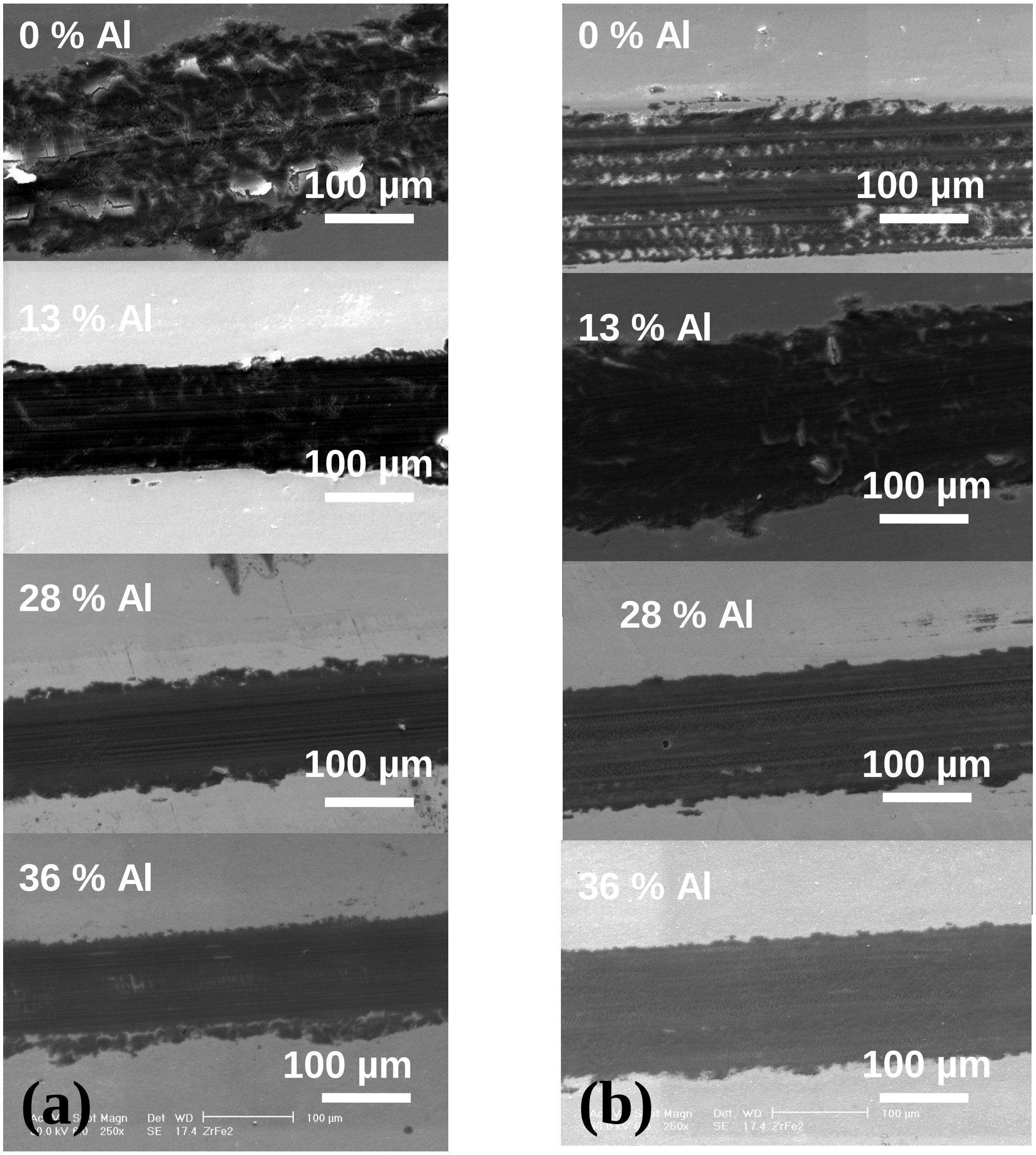

**Fig. 5.24** SEM micrograpg of wear tracks tested with (a) steel and (b) alumina balls for ZrAlN alloyed films.

Fig. 5.23 shows a plot between change in the wear track width as a function of Al concentration for the films tested with steel and alumina balls. Wear rates could not be directly measured due to inaccuracy in the measurement of the depth inside the wear track. Width of the wear track can be qualitatively related to wear rate. The wear rates measured for ZrN using steel and alumina balls were generally higher than that of ZrAlN alloyed films. The wear rate decreased significantly to lower values with addition of Al concentration and remains steady at higher Al concentration. The pot clearly demonstrates that the wear rates are significantly higher with $Al_2O_3$ ball than those obtained with steel ball. There is a slight increase in the COF values at higher concentration of Al for both the balls. SEM micrograph of wear tested region is also shown in Fig.5.24. From Fig. 5.24 (a) and (b), it is clear that track widths are higher with $Al_2O_3$ tested samples than that of steel ball tested samples.

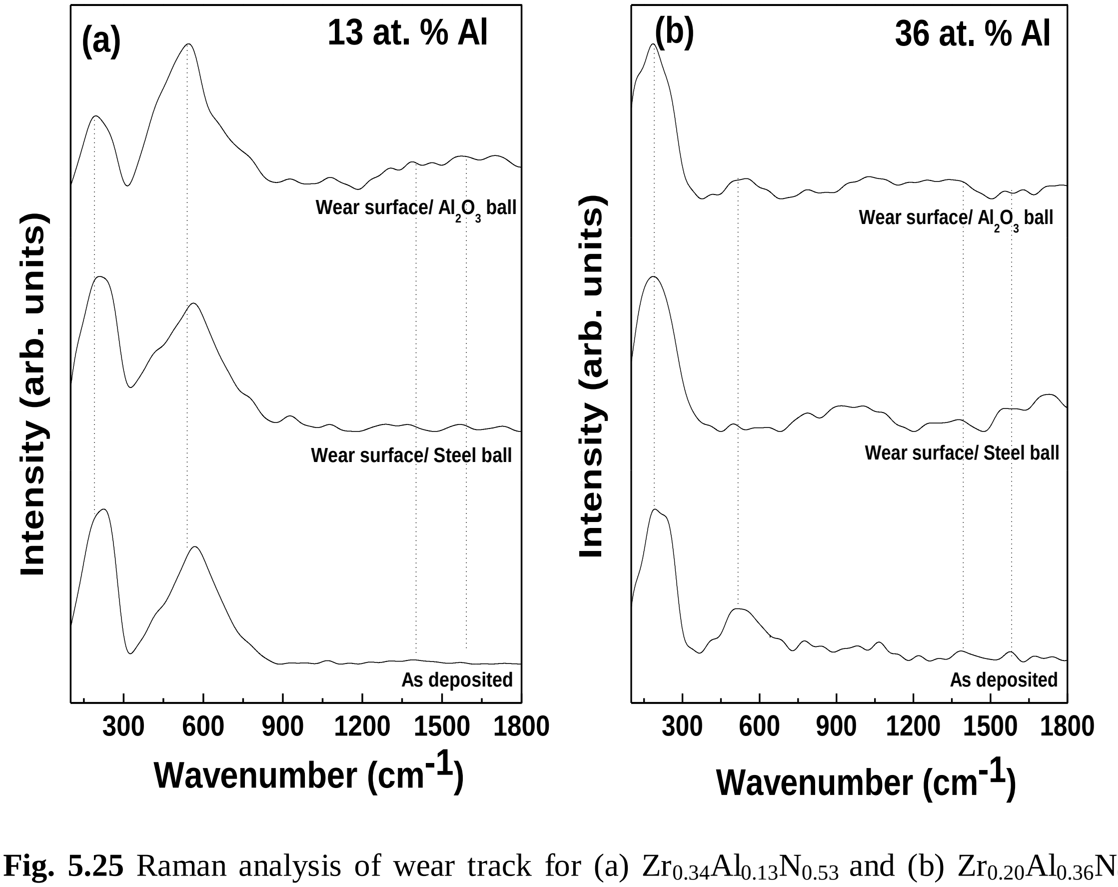

**Fig. 5.25** Raman analysis of wear track for (a) $Zr_{0.34}Al_{0.13}N_{0.53}$ and (b) $Zr_{0.20}Al_{0.36}N_{0.44}$ alloyed films.

In order to understand the wear track morphology, Raman analysis was also carried out inside the wear tracks in all the samples. Fig. 5.25 shows the Raman curves for two extreme cases of alloyed films of ZrAlN. It is observed that the prominent Raman band of ZrAlN observed at 212 $cm^{-1}$, 550 $cm^{-1}$, 720 $cm^{-1}$ for 13 at. % of Al and slightly shifted to 200 $cm^{-1}$, 512 $cm^{-1}$ for 36 at. % of Al added film. It is also seen that films tested with alumina balls show higher order Raman band at 1360 $cm^{-1}$ and 1582 $cm^{-1}$, which may correspond to carbon segregation from the substrate as observed for ZrN thin films. Also, with higher addition of Al content intensity of Raman bands decrease.

## 5.4 Discussion

### 5.4.1 Growth Characteristics of ZrAl from Zr-Al Target and a Comparative Study of ZrAlN Films from Zr-Al and ZrN-Al Composite Targets.

ZrAl films were synthesized from the composite target of Zr-Al prior to the synthesis of ZrAlN films to understand the growth process of ZrAl (13 at. %) film.

The crystallite size of ZrAl thin films were found to be increasing with increasing temperature (Fig. 5.1 (b)). This behaviour can be explained with the increase in mobility of the adatoms with increasing substrate temperature. Similar behaviour has been also reported for other transition metal nitrides.

The decrease in the crystallite size as a function of nitrogen flow rate (Fig 5.2 (b) is due to structural disordering leading to amorphization. As the nitrogen flow rate increases, the overall sputtering yield of the target decreased due to lower ionization of molecular nitrogen compared to argon, which causes a continuous decrease in the deposition rate of the films. It is suggested that at higher nitrogen flow rates, distortions are produced in the lattice due to increased accommodation of nitrogen atoms. Therefore, the reduction in the crystallite size with increasing nitrogen flow rate could be related to tendency for amorphization.

A comparative study was made for alloyed ZrAlN (13 at.%) films deposited at constant temperature of 773 K from the composite target of Zr-Al and ZrN-Al. It was found that ZrAlN films sputtered with Zr target needed 1 sccm flow rate of nitrogen, whereas films sputtered with ZrN-Al target consumed only 0.2 sccm flow rate of nitrogen to obtain alloyed film of ZrAlN. This is obvious because of the sputtering from a N rich target. Excess nitrogen was required for the films sputtered with Zr –Al target, in order to obtain the stoichiometric ZrAlN films.

The variation in crystallite size was showing similar trend for the ZrAlN films sputtered from both the targets. Raman spectra (Fig 5.7) also confirmed the presence of ZrAlN phases at different flow rate of nitrogen. The as-deposited ZrAlN film showed Raman spectrum with the typical broadened bands due to the disorder induced by N vacancies [278].

A significant increase in the hardness and elastic modulus (Fig. 5.4) is found at lower $N_2$ flow rates of 1 to 2 sccm. Beyond 2 sccm flow rate of $N_2$, both the hardness and Young’s modulus are decreased. The observed low hardness at 0 sccm of nitrogen is due to the metallic phase formation of ZrAl (hcp structure). This phase when converted into ZrAlN ( fcc structure) at 1-2sccm of nitrogen flow rate, shows a large increase in hardness and elastic modulus and > 2 sccm of nitrogen, this phase gets distorted and has a tendency to form amorphous phase as evident from XRD analysis. The formation of amorphous like ZrAlN shows a decreasing hardness and elastic modulus, however higher than the nano mechanical properties of metallic phase of ZrAl.

### 5.4.2 Effect of Al Addition on Thermal Expansion, Nanomechanical and Tribological Properties of ZrAlN Alloyed Films

The addition of Al has shown significant influence on the thermal, nanomechanical and tribological properties. To study the effect of Al addition, ZrAlN films were deposited at 773 K and 0.2 sccm of nitrogen flow rate as these processing conditions promote films with good crystalinity.

The addition of Al was substituted in the cationic sub-lattice of Zr leading to a single phase with shrinkage of the lattice because of the lower ionic radius of Al (0.5Å) compared to that of Zr (1.6 Å) upto an Al concentration of 36 at.%. Therefore lattice parameter values were found to be decreasing (Fig. 5.11(a)) for the Al concentration range $0 \leq x \leq 0.36$. Besides the formation of ZrAlN, a weak reflection of AlN for ZrAlN films with 36 at. % Al indicated an onset of phase separation in accordance with the phase diagram for Zr-Al-N system as explained in Chapter 1.

In the present work, the CTE of alloyed ZrAlN films was calculated and it was found to be higher than that of CTE values of ZrN films. In general, thermal expansion of a solid is a consequence of an-harmonicity of the interatomic potentials [298], which are significantly influenced by the material structure. The displacement of individual atoms from their equilibrium sites with temperature depends additionally on structural imperfections, which dramatically influence the atomic behavior (e.g. vibrational frequencies). Structural defects such as vacancies, interstitials and dislocations locally alter the interatomic potential as they induce strain fields and change the chemical environment in their vicinity. The reduction in grain size influences the number of atoms in grain boundary and the volume fraction of the defective GB area. This means that the higher the volume fraction of GB the more pronounced is the effect on the thermal properties of the whole system [238]. Since the atoms in the GB region have lower average coordination numbers than the atoms in the grain interior, and are thus more weakly bonded, their interatomic potential becomes shallower and more asymmetric [299]. Due to the necessary enhancement of thermal vibration and anharmonicity of the interatomic potential, the thermal expansion of the nanocrystalline material is higher than that of the single crystal material. The enhancement of CTE is indeed more pronounced for lower grain sizes, since the contribution of GB atoms to thermal expansion increases dramatically with increasing volume fraction.

There are, however, additional effects which can affect thermal expansion. For instance, defective GB enhances the heat capacity of nanocrystalline materials [300], which in turn contributes to increased thermal expansion according to the Gruneisen relation. Porosity is also expected to alter the thermal expansion of a solid. All these effects should be taken into account and discussed before offering an interpretation of the variation in CTE compared with the coarse-grained polycrystalline and single crystal counterparts.

The CTE of the films is, however, not only a structure dependent but also a stress-dependent parameter, since internal stress modifies the interatomic equilibrium positions and thus the anharmonic thermal vibrational amplitudes. High compressive stresses are known to reduce the CTE by restricting the vibrational movement of atoms [298]. Tensile stress, on the other hand, tends to increase the interatomic distances and contributes to the pronounced anharmonicity of the interatomic potential around the minimum. However, in the case of thin films under compressive stress, which is predominantly related to the local volume change due to irradiation-induced defect generation, the film is not compressed in the same way. Although the defect concentration in the films is sufficient to explain the development of relatively high compressive stresses, the local change in the atomic arrangement seems not to affect the CTE on the macroscopic scale [298].

In the case of nanocrystalline materials atoms at the surface of a crystal or at an incoherent interface (grain boundary) are not saturated with respect to their bonding states and their coordination number (i.e. the number of nearest neighbours) is less than that of bulk materials. Hence, the curve of potential energy per atom versus interatomic distance for a surface/interface atom shows a less deep potential energy minimum well than for a bulk material. Consequently, in view of the asymmetry of the potential energy minimum wells, the thermal expansion pertaining to the surface/ interface atoms of the crystal is larger than for the bulk atoms [237]. Theoretically it has been shown that the potential energy well is less deep and more asymmetric for surface atoms than for the atoms in the bulk [300]. The smaller the crystal, the larger the ratio of the number of surface/interface atoms and therefore smaller crystals show larger average linear coefficient of thermal expansion. Therefore in the present work, the CTE of ZrAlN is significantly higher than that of bulk ZrN (7.2 x $10^{-6}$ $K^{-1}$).

The ratio $H^3/E^2$ has been increasingly applied to evaluate the resistance to plastic deformation from the values of H and E [201]. The increased value of $H^3/E^2$ (Fig 5.19), gives information on the resistance of the material to plastic deformation. From the values of $H^3/E^2$, it is evident that ZrAlN films deposited with lower Al % could offer higher resistance to plastic deformation. The variation in the resistance to plastic deformation could be discussed in terms of the microstructure. In the present work, the mean crystallite size is significantly reduced as Al concentration is increased and this should result in the increase in the hardness value for the films deposited at higher Al %. However, in this case the hardness values were found to be decreasing (Fig.5.18) due to the presence of higher amount of a soft phase in the matrix. In addition, at higher Al concentration, the crystallite sizes are quite low and may not follow the Hall-Petch relation [301-302]. For too small grain sizes however, the Hall-Petch relation is no longer valid and the hardness can even decrease according to the inverse Hall-Petch relation [303]. For magnetron sputtered CrN thin films, the hardness has been observed to decrease when the grain size is below ~15 nm [304]. Also ZrN thin films exhibit a decreased hardness when the grain size is reduced to below ~5 nm [305]. The reason for the decreased hardness may be due to the increased grain boundary sliding [306-307] as the volume fraction of boundaries increases with decreased grain size. A small grain size also results in an overall increased porosity of the film. In addition, dislocation motion through several grains or enhanced grain boundary diffusion can reduce the hardness [308]. The present study indicates a reduction in the hardness and a low value of resistance to plastic deformation at higher Al concentration. This may be related to very low crystallite size and the presence of large amount of the soft phase of Al.

Scratch test is intended to assess the mechanical integrity, failure modes, and adhesion strength of hard films on a metal or ceramic substrate. The test method does not measure the fundamental “adhesion strength” of the bond between the film and the substrate. Rather, the test method gives a quantitative engineering measurement of the practical (extrinsic) adhesion strength and damage resistance of the film-substrate system as a function of the applied normal force. The adhesion strength and the damage modes depend on the complex interaction of the coating/substrate properties (hardness, fracture strength, modulus of elasticity, damage mechanisms, microstructure, flaw population, surface roughness, and so forth) and the test parameters (stylus properties and geometry, loading rate, displacement rate). Brittle damage events (cracking, delamination, chipping, spalling, buckling, and so forth) can produce high frequency elastic waves in the coating and substrate which can be detected by acoustic emission (AE) originating from the films. As the applied normal force increases in the scratch test, film damage events occur with increasing frequency and severity and the resulting elastic waves can be detected. It should be noted that the changes in acoustic emission events at given normal force levels cannot discriminate apriori between the different damage events and coating failure modes.

Scratch test indicates (Fig 5.19(a)) that films are intact up to 4.6 N. Generally acoustic emission curve (Fig. 5.19 (b)) gives the idea about film failure. At low loads the curve is smooth and when film loss occurs, the signal increases suddenly as a function of the load. The “shoulder” can be correlated to cracking or the onset of the cohesive failure. Cohesive and adhesive failure of the films were noticed at 4.6 and 4.3 N respectively for the ZrAlN films with 13 and 36 at. % of Al respectively.

However, the COF values were slightly lower than the COF values of ZrN thin films. Similar behaviour was also reported by López and Staia [309]. Low values of the COF (0.5–0.6) at 973 K for $Zr_{0:72}Al_{0:28}N$ and $Zr_{0:42}Al_{0:58}N$ were also reported in the literature and it was explained with the presence of Fe oxides in the wear tracks [310]. They also reported that at 300 K, there was generally an increased wear rate for all the ZrAlN films which decreased with low Al content if the temperature is increased to 773

K. This behaviour was similar to observation made in the case TiAlN [311] and HfAlN [312].

In our case it is suggested that the increased hardness of the ceramic balls could offer severe abrasive wear and result in the higher values of the COF than that of steel balls. This is also evident from the wider wear tracks obtained with the alumina balls than that of steel balls.

## 5.5 Conclusions

ZrAl and alloyed ZrAlN films were deposited on Si (100) and D-9 alloy substrate from the composite targets of Zr-Al and ZrN-Al. The effect of deposition temperature and nitrogen flow rate was studied at constant Al content of 13 at. %. Also, the effect of Al addition on the microstructural, thermal expansion behaviour, nanomechanical and tribological properties were reported at 773 K and 0.2 sccm flow rate of nitrogen.

- Only α-phase of ZrAl with [001] preferred orientation was noticed in the temperature range 300–773 K. It was found that the crystallite size increases with increasing temperature.
- It was found that (Zr,Al) N is in solid solution up to 36 at. % of Al. ZrAlN thin films were a single phasic fcc structure. As the Al content was increased up to 36 at. % , lattice parameter decreased due to the substitution of Zr by Al of lower atomic radius.
- High temperature results of $Zr_{1-x}Al_xN_y$ thin films indicated that the addition of Al improved the phase stability at higher temperature. The average linear thermal

expansion coefficient of $Zr_{1-x}Al_xN_y$ thin films showed an increase in the thermal expansion coefficient with increasing Al content up to 28 at.%Al.

- It was also observed that values of hardness and Young's modulus of the alloyed ZrAlN films were in the range of 9-18 GPa and 235-364 GPa, respectively as a function of Al in the range of 0 to 36 at. %.
- Tribological studies of the alloyed ZrAlN thin film showed that the COF of ZrAlN films was lower for the steel ball (100Cr6 steel) than that for the $Al_2O_3$ ball up to 36 at. % of Al. However, no clear trend was observed in the COF value as a function of Al content.

# Chapter 6

# *Summary, Conclusions and Future Directions*

## 6. 1 Summary and Conclusions

Pulsed DC magnetron sputtering technique has been used to deposit the Zr, ZrN and alloyed films of ZrAlN on Si (100) substrates with native oxide film and D-9 alloy substrates. Following are the summary and conclusions obtained from the investigations on Zr, ZrN and alloyed ZrAlN films:

### 6.1.1 Zr thin films

The present study has demonstrated that magnetron sputtering could be used for the development of Zr films on metallic and semiconducting substrates to obtain desired mechanical properties.

(i) The role of pulsed parameters such as pulse frequency, duty cycle and pulse power of the pulsed DC power source was investigated on the deposition rate and crystallite size of the Zr films. Higher pulse frequencies and duty cycle have been found to produce lower crystallite size. The reduction in the mobility of the sputtered species caused the production of crystallites of lower sizes. Whereas, deposition rate has been found to decrease with in increasing pulse frequencies and increase with increasing duty cycle. The effect of pulsed power in the range 50-125 W indicated an increase in both the deposition rate and the crystallite size with increasing pulse power energy.

(ii) Formation of α-hcp phase of zirconium with [0 0 1] preferred orientation was noticed in the temperature range 300–873 K.

(iii) The increase in the crystallite size as a function of substrate temperature has been noticed for Si and D-9 alloy substrates but the increase in the crystallite size of the films deposited on D-9 alloy substrate was higher than that of the films deposited on Si substrates. This behaviour can be attributed to the increased mobility of the adatoms on the conducting surface of D-9 alloy compared to that of semiconducting substrate.

(iv) HTXRD showed that Zr films were stable up to 773 K. The average thermal expansion coefficient of Zr film is found to be $\alpha_{Ta}(K^{-1}) = 5.63 \times 10^{-6} + 1.08 \times 10^{-8} \times (T)$ and $\alpha_{Tc}(K^{-1}) = 6.25 \times 10^{-6} + 7.36 \times 10^{-8} \times (T)$ along the a and c axis, respectively. The increase in the value of the CTE as a function of temperature in the present study is in agreement with several metallic materials.

(v) Nanoindentation and microhardness measurements showed that the hardness of the films was in the range 6–10 GPa for films deposited in the temperature of 300-873 K. The decreased hardness of the Zr films deposited at higher temperature could be correlated with the stress relaxation in larger crystallites formed at higher growth temperatures. Scratch test results indicated that the films have better adhesion at higher substrate temperature. The load for the first critical failure was 20 N for the films deposited at 773 K compared to that of 7 N for the film deposited at room temperature. The better performance of the Zr films prepared at higher temperature could be related to better adhesion of the film with the substrate.

(vi) Tribological measurement indicates that films tested with steel and alumina balls showed a very small increase in the COF values for the films tested with alumina balls due to their increased hardness value. It is suggested that plastic deformation of the film due to ploughing is the dominant mechanism of friction for thin soft coatings under low loads.

### 6.1.2 ZrN thin films

ZrN films were deposited on Si (100) and D-9 alloy substrates at different substrate temperatures as a function of nitrogen flow rate using the pulsed magnetron sputtering technique.

(i) The substrate temperature and nitrogen flow rate have shown profound influence on the microstructure. The nanostructured crystalline films with (2 0 0) preferred orientation were observed at all deposition temperatures. Films deposited up to 1 sccm of nitrogen flow rate showed single phase fcc-ZrN, while films deposited at nitrogen flow rate > 1 sccm and up to 6 sccm revealed the growth of ZrN along with $Zr_3N_4$ secondary phase. Films deposited > 6 sccm have poor crystallinity. TEM studies also confirmed the presence of ZrN along with small amount of o-$Zr_3N_4$ phase at higher nitrogen flow rates. The increase in the crystallite size with increasing substrate temperature was noticed because of increased adatom mobility at higher temperatures. In contrast, there was a decrease in the crystallite size as a function of nitrogen flow rate due to structural disordering. It is suggested that at higher nitrogen flow rates, distortions could be produced in the lattice due to increased accommodation of nitrogen atoms which results in the reduction in the crystallite size and tendency for amorphization .

(ii) HTXRD study showed that ZrN films were stable up to 1073 K. The average linear thermal expansion coefficient of ZrN film was found to be $\alpha_T(K^{-1}) = 6.81 \times 10^{-6} + 9.26 \times 10^{-10} \times (T)$.

(iii) The effect of nitrogen flow rate on the nanomechnical properties indicated an enhancement in hardness (25 GPa) and elastic modulus (460 GPa) and showed a peak value for the resistance to plastic deformation ($H^3/E^2$) at 2 sccm of nitrogen flow rate. However, above 2 sccm of nitrogen flow rate, there is a reduction in the value of resistance to plastic deformation because of the change in the microstructure, especially, the crystallite size and formation of secondary phase.

(iv) The tribological properties of these films were found to be influenced by the deposition temperature and sliding counter bodies. The COF was found to be lower at higher deposition temperature and with steel ball regardless of the deposition temperature. EPMA suggested an increased amount of elements such as Fe, Ni and C, while Raman spectroscopy indicated the presence of carbon related phases in the wear tracks obtained using the ceramic balls. At higher flow rates of nitrogen, the steel ball showed higher COF than that obtained at lower flow rates of nitrogen. The variation in the COF was also discussed in relation with the difference in the microstructure of the wear track obtained with steel ball and ceramic balls.

### 6.1.3 ZrAlN alloyed thin films

ZrAl and ZrAlN films were deposited on Si (100) and D-9 alloy substrates from the composite targets of Zr-Al and ZrN-Al. The content of Al of the alloyed films was varied by clamping Al strips of different surface area on the targets of Zr and ZrN. The effect of deposition temperature and nitrogen flow rate was studied at constant Al content of 13 at. %. Also, the effect of Al addition on the microstructural, thermal expansion behaviour, nanomechanical and tribological properties were reported at 773 K and 0.2 sccm flow rate of nitrogen. The following are the important conclusions on alloyed films:

(i) Only α-phase of ZrAl with [0 0 1] preferred orientation was noticed in the temperature range 300–773 K, when deposited with high pure argon as the sputter gas. It was found that the crystallite size increased with increasing temperature.

(ii) (Zr,Al) N formed solid solution up to 36 at. % of Al. ZrAlN thin films were single phasic fcc structure. As the Al content was increased up to 36 at. %, lattice parameter decreased due to the substitution of Zr with ionic radius of 1.6 Å by Al of lower atomic radius (0.5Å). Besides, with 36 at. % of Al addition, the presence of a small amount of AlN phase was also noticed. This may be due to the onset of phase separation in ZrAlN due to solubility limit of Al in Zr-N system.

(iii) High temperature results of $Zr_{1-x}Al_xN_y$ thin films indicated that the addition of Al improved the phase stability at higher temperature. The average linear thermal expansion coefficient of $Zr_{1-x}Al_xN_y$ thin films showed an increase in the thermal expansion coefficient with increasing Al content up to 28 at.%Al than that of ZrN films. Since, the crystallite size of ZrAlN was found to be decreasing with Al addition, an increasing CTE was noticed due to the increased grain boundary effects. Therefore, in the present work, for instance with 13 at. % Al the CTE of ZrAlN ($9.3 \times 10^{-6}$ $K^{-1}$ ) was significantly higher than that of the bulk ZrN ($7.2 \times 10^{-6}$ $K^{-1}$).

(iv) The hardness and Young's modulus of the alloyed ZrAlN films were found to decrease from 18 GPa to 9 GPa and from 364 GPa to 265 GPa, respectively as a function of Al in the range of 0 to 36 at. %. As a consequence, the resistance to plastic deformation ($H^3/E^2$) also was found to decrease with Al addition. This may be related to very low crystallite size (< 10 nm) and presence of large amount of the soft phase of Al.

(v) Tribological studies of the alloyed ZrAlN thin film showed that the COF of ZrAlN films was lower for the steel ball (100Cr6 steel) than that for the $Al_2O_3$ ball up to 36 at. % of Al because the ceramic balls produce severe abrasive wear and resulted in the higher values of the COF than that of steel balls. This was also evident from the wider wear tracks obtained with the alumina balls than that of steel balls.

## 6. 2 Future Directions

(i) There are reports which suggest that very small amount of Al addition (≤ 5 at. % Al) could increase the hardness of alloyed films of ZrAlN. We could not perform the experiments with lower content of Al because of the practical limitation in the preparation of the composite target and sputtering from a single power source.

(ii) Though, a few reports suggest better oxidation resistance for Al alloyed ZrN films, a systematic investigation on the oxidation resistance of ZrAlN must be taken up.

(iii) Synthesis of Zr/ZrN and ZrN/ZrAlN multilayers will be investigated with the support of HRTEM to understand the mechanical properties as a function of bilayer thickness.

## References:

[1] Handbook of physical vapor deposition (pvd) processing, Donald M. Mattox, Noyes publication, Westwood, New Jersey, U.S.A., (1997).

[2] R.D.Arnell,H. Backer and J.W.Bradley, Surf. Coat. Technol., 174-175 (2003) 779.

[3] F.A.Cotton and G.Wilkinson, Advanced Inorganic Chemistry, Interscience Publishers, New York (1972).

[4] F. Benesovsky, R.Kiefer and P.Ettmayer, Nitrideds in Kirk-Othmer's Encyclopedia of Industrial Chemistry, 4th Ed., John Wiley & Sons (1993).

[5] P.Ettmayer and W. Lengauer, Nitrides in Ullmann's Encyclopedia of Industrial Chemistry, 5th Ed.,Vol. 15, VCH (1985).

[6] S.Hampshire, Ceramics in Material Science and Technology, Vol. 11, VCH, New York (1994).

[7] P.Haussinger, P. Leitgeb and G.Ruckborn, Nitrogen in Ullmann's Encyclopedia of Industrial Chemistry, 5th Ed.,Vol. 15, VCH (1985).

[8] L.E.Toth, Transition Metal Carbides and Nitrides. Academic Press, New York, (1971).

[9] Hugh O. Pierson, Handbook of refractory carbides and nitrides, Noyes publication, westwood, New jersey, U.S.A.(1996).

[10] Zhenghua An, Chuanling Men, Zhengkui Xu, Paul K. Chu, Chenglu Lin, Surf. Coat. Technol. 196 (2005) 130.

[11] K. Kamiya., T. Yoko,. M. Bessho,., J. Mat. Sci. 14 (1979)70.

[12] H. G. Tompkins, J. Appl. Phys.70 ( 1991) 3876.

[13] K.G.Grigorov, G.I.Grigorov, M.Stoyanova, J.L.Vignes, J.P.Langeron and P. Denjean , Appl Phys A 55 (1992)502.

[14] C. W. Colling, J.G. Choi, L. Thompson, J. Catal. 160 ( 1996) 3542.

[15] A.Massinon, J.A., Odriozola, Ph Bastians, R.Conanec, R. Marchand, Y. Laurent, P.Grange, Appl. Catal. A 137( 1996) 9.

[16] Albert Irudayaraj A. and Kalainathan S. , Journal of Crystal Research. Technology 43 (2008) 709.

[17]. Aouadi S.M. Bohnhoff A. Sodergren M. Mihut D. Rohde S.L. Xu J. Mishra S.R. (2006) Surf. Coat. Technol. 201(2006) 418.

[18]Mayumi B. Takeyama, Takaomi Itoi, Eiji Aoyagi, Atsushi Noy, Applied Surface Science 190 (2002) 450.

[19] W. D Sproul, J. Vac. Sci. Technol. A 4 (1986) 2874.

[20] J. Vetter, R. Rochotzki, Thin Solid Films 192 (1990) 253.

[21] S. Kanamori, Thin Solid Films 136 (1986) 195.

[22] M. Ostring, S Nygren, C. S. Petersson, H. Norström, R. Buchta, H.O. Blom, S. Berg Thin solid films 145 (1986) 81.

[23] K. Hinode, Y. Homma, M. Horiuchi, T. Takahashi, J. Vac. Sci. Technol. A15 (1997) 2017.

[24] P. J. Matin, R. P. Netterfield, W. G Sainty, Vaccum 32 (1982) 359.

[25] B. Karlsson, R. P. Shimshock, B. O. Serphin, Phys. Scr. 25(1982) 775.

[26] B. Karlsson, C. G. Ribbing, SPIE 324 ( 1982) 52.

[27] C. G. Ribbing, A. Roos, SPIE 3133 ( 1997) 148.

[28] P. Panjan, A. Zabkar, B. Navinsek, et al., Vacuum 40, 161 (1990).

[29] A. Mumtaz, W. H Class, J. Vac. Sci. Technol. 20 ( 1982) 345.

[30] P. C. Johnson, H. Rawdhawa, Surf. Coat. Technol. 33 ( 1997) 53.

[31] M. Molariur, A. S. Korhnen, E. Harju, R. Lappalainen, Surf. Coat. Technol. 33 (1987) 117.

[32] M. Nose, T. Nage, M. Yokota, S. Saji, M. Zhou, M. Nakoda, Surf. Coat. Technol. 116 (1999) 296.

[33] L. Pichon, T. Girardeau, A. Straboni, F. Lignou, J. Perrie´re, J.M. Frige´rio, Nucl. Instr. Meth. Phys. Res. B147 (1999) 378.

[34] B.O. Johansson, H.T.G. Hentzell, J.M.E. Harper, J.J. Cuomo, J. Mater. Res. 1 (1986) 442.

[35] M. Yoshitake, T. Yotsuya, S. Ogawa, Jpn. J. Appl. Phys. 31 (1992) 4002.

[36] L. Pichon, T. Girardeau, A. Straboni, F. Lignou, P. Gue´rin, J. Perrie`re, Appl. Surf. Sci. 150 (1999) 115.

[37] A.D. Katnani, K.I. Papathomas, J. Vat. Sci. Technol. A5(4) ( 1987) 1335.

[38] J.C. Francois, Y. Massiani, P. Gravier, J. Grimblot, L.Gengembre, Thin Solid Films, 223 ( 1993) 223.

[39] S. Horita, M. Kobayashi, H. Akahori, T. Hata, Surf. Coat. Technol. 66 (1994) 318.

[40] A.J. Perry, J.P. Schaffer, J. Brunner, W.D. Sproul, Surf. Coat. Technol. 49 (1991) 188.

[41] P.C. Johnson, H. Randhawa, Surf. Coat. Technol. 33 (1987) 53.

[42] M. Diserens, J. Patscheider, F. Lévy, Surf. Coat. Technol. 108-109 (1998)241.

[43] S. Veprek, J. Vac. Sci. Technol., A 17 (1999) 2401.

[44] J. Musil, Surf. Coat. Technol. 125 (2000) 322.

[45] F.J. Espinoza-Beltrán, O.Che-Soberanis, L. García-González, J. Morales-Hernández, Thin Solid Films 437 (1–2) (2003) 170.

[46] D. Pilloud, J.F. Pierson, A.P. Marques, A. Cavaleiro, Surf. Coat. Technol.180–181 (2004) 352.

[47] T. Mae, M. Nose, M. Zhou, T. Nagae, K. Shimamura, Surf. Coat. Technol.142–144 (2001) 954.

[48] J. Musil, P. Karvánková, J. Kasl, Surf. Coat. Technol. 139 (2001) 101.

[49] J. Musil, P. Zeman, H. Hrubý, P.H. Mayrhofer, Surf. Coat. Technol. 120–121 (1999) 179.

[50] M. Benkahoul, C.S. Sandu, N. Tabet, M. Parlinska-Wojtan, A. Karimi, F.Lévy, Surf. Coat. Technol. 188–189 (2004) 435.

[51] F. Vaz, L. Rebouta, B. Almeida, P. Goudeau, J. Pacaud, J.P. Rivière, J.Bessa e Sousa, Surf. Coat. Technol. 120–121 (1999) 166.

[52] C.S. Sandu, R. Sanjinés, M. Benkahoul, M. Parlinska-Wojtan, A. Karimi,F. Lévy, Thin Solid Films 496 (2006) 336.

[53] J. Patscheider, T. Zehnder, M. Diserens, Surf. Coat. Technol. 146–147(2001) 201.

[54] E. Martinez, R. Sanjines, O. Banakh, F. Levy, Thin Solid Films 447–448(2004) 332.

[55] R. Sanjinés, M. Benkahoul, C.S. Sandu, F. Lévy, J. Appl. Phys. 98 (2005)123511.

[56] O. Knotek, M. Böhmer, T. Leyendecker, J. Vac. Sci. Technol., A, Vac.Surf. Films 4 (1986) 2695.

[57] H.A. Jehn, S. Hofmann, V.E. Rückborn, D. Münz, J. Vac. Sci. Technol., A,Vac. Surf. Films 4 (1986) 2701.

[58] D. McIntyre, J.E. Greene, G. Hakansson, J.E. Sundgren, W.D. Münz, J.Appl. Phys. 67 (1990) 1542.

[59] J. Musil, F. Hruby, Thin Solid Films 365 (2000) 104.

[60] A. Kimura, H. Hasegawa, K. Yamada, T. Suzzuki, Surf. Coat. Technol. 120(1999) 438.

[61] Y. Tanaka, T.M. Gür, M. Kelly, S.B. Hagstrom, T. Ikeda, K. Wakihira, H.Sato, J. Vac. Sci. Technol., A, Vac. Surf. Films 10 (1992) 1749.

[62] J. Probst, U. Gbureck, R. Thull, Surf. Coat. Technol. 148 (2001) 226.

[63] W.D. Münz, J. Vac. Sci. Technol., A, Vac. Surf. Films 4 (1986) 2717.

[64] L.A. Donohue, I.J. Smith, W.D. Münz, I. Petrov, J.E. Greene, Surf. Coat.Technol. 94–95 (1997) 226.

[65] Y. Makino, K. Nogi, Surf. Coat. Technol. 98 (1998) 1008.

[66] O. Banakh, P.E. Schmid, R. Sanjinés, F. Lévy, Surf. Coat. Technol.163–164 (2002) 57.

[67] H. Holleck, Surf. Coat. Technol. 36 (1988) 151.

[68] R. Lamni, E. Martinez, S.G. Springer, R. Sanjinés, P.E. Schmid, F. Lévy,Thin Solid Films 447–448 (2004) 316.

[69] R. Lamni, R. Sanjinés, F. Lévy, Thin Solid Films 478 (2005) 170.

[70] L. Hultman, Vacuum 57 (2000) 1.

[71] A. Hörling, H. Ultman, M. Oden, J. Sjölén, L. Karlsson, J. Vac. Sci.Technol., A, Vac. Surf. Films, 20 (2002) 1815.

[72] P.H. Mayrhofer, A. Hörling, L. Karlsson, J. Sjölén, T. Larsson, C. Mitterer,L. Hultman, Appl. Phys. Lett. 83 (2003) 2049.

[73] S.K. Sikka, Y.K. Vohra, R. Chidambaram, Prog. Mater. Sci. 27 (1982) 245.

[74] A. Jayarama, W. Klement Jr., G.C. Kennedy, Phys. Rev 131 (1963) 644.

[75] P.W. Bridgman, Proc. Am. Acad. Arts Sci 76 (1948) 55-71.

[76] P.W. Bridgman, Proc. Am. Acad. Arts Sci. 81 (1952) 165.

[77] G. Jyoti, S.C. Gupta, J. Phys. Condens. Matter 6 (1994) 10273.

[78] H. Xia, A.L. Ruoff, Y.K. Vohra, Phys. Rev B 44 (18) (1991) 10374.

[79] G. Jyoti, K.D. Joshi, S.C. Gupta, S.K. Sikka, Philos. Mag. Lett. 75 (5)(1997) 291.

[80] A.V. Dobromyslov, N.I. Taltus, Fiz. Metal. M 5 (1990) 108.

[81] S.G. Song, G.T. GrayIII, Philos. Mag. A 71 (2) (1995) 275.

[82] L. Ming, M.H. Manghnani, K.W. Katahara, J. Appl. Phys. 52 (3)(1981) 1332.

[83] H. Dammak, A. Dunlop, D. Lesueur, Nucl. Inst. Methods. B 107(1996) 204.

[84] H. Dammak, These, Ecole Polytechnique, Palaiseau, France, 1994.

[85] A.V. Dobromyslov, N.V. Kazantseva, Scripta Mater. 37 (5) (1997) 615.

[86] P. Gaunt, J.W. Christian, Acta Metall. 7 (1959) 534.

[87] E.J. Rapperport, Acta Metall. 7 (1959) 254.

[88] L. Kaufman, Acta Metall. 7 (1959) 575.

[89] E.S. Fisher, C.J. Renken, Phys. Rev. 135 (2A) (1964) A 482.

[90] D.O. Northwood, I.M. London, L.E. Bahen, J. Nucl. Mater. 55 (1975) 299.

[91] E. Tenckhoff, ASTM, Philadelphia, PA, (1988), 55.

[92] R.A. Lebensohn, C.N. Tome, Acta Metall. Mater. 41 (1993) 2611.

[93] G.C. Kaschner, G.T. Gray III, Metall. Mater. Trans., A 31 (2000) 1997.

[94] A. Baudry, P. Boyer, M. Brunel, J. Magn. Mater. 185 (1998) 309.

[95] D.J. Li, M.X. Wang, J.J. Zhang, Mater. Sci. Eng. A 423 (2006)116.

[96] L. Smardz, J. Alloys Compd. 395 (2005) 17.

[97] Y. Zhao, J. Zhang, C. Pantea, J. Qian, L.L. Daemen, Phys. Rev. B 71 (2005)184119.

[98] S. Ramanathan, C.-M. Park, P.C. McIntyre, J. Appl. Phys. 91 (2002)4521.

[99] S. Niyomsoan, W. Grant, D.L. Olson, B. Mishra, Thin Solid Films 415 (2002) 187.

[100] S. Miyazaki, M. Narasaki, M. Ogasawara, M. Hirose, Solid State Electron. 46 (2002) 1679.

[101] N.L. Zhang, Z.T. Song, Q. Wan, Q.W. Shen, C.L. Lin, Appl. Surf. Sci. 202 (2002) 126.

[102] H.M. Benia, M. Guemmaz, G. Schmerber, A. Mosser, J.C. Parlebas, Appl. Surf. Sci. 200 (2002) 231.

[103] L.Q. Shi, G.Q. Yan, J.Y. Zhou, S.Z. Luo, S.M. Peng, W. Ding, X.G. Long, J. Vac. Sci.Technol. A 20 (2002) 1840.

[104] L. Pichon, T. Girardeau, F. Lignou, A. Straboni, Thin Solid Films 342 (1999) 93.

[105] D. Pilloud, J.F. Pierson, C. Rousselot, F. Palmino, Scripta Mater. 53 (2005) 1031.

[106] J. Chakraborty, K. Kishor Kumar, S. Mukherjee, S.K. Ray, Thin Solid Films 516 (2008) 8479.

[107] M. Balaceanu , T. Petreus , V. Braic , C.N. Zoita , A. Vladescu , C.E. Cotrutz , M. Braic, Surf. Coat. Technol. 204 (2010) 2046.

[108] H.O. Pierson, New Jersey, USA, 1996, 181.

[109] Kendall J. Hollis ,International Thermal Spray & Surface Engineering, Editors, Robert Gansert, William Jarosinski, Nov. 2010, 5 (4).

[110] Abbasi F., Etaati G.R., Afarideh H., Koohi-Fayegh R., Aslani G.R, Iranian J.Phys.Res. .3, No.2. (2002)101.

[111] Abbasi Davani F., Koohi Fayegh R., Afaride H., Etaati G.R., Aslani G.R., Radiation Measurement 37 (2003) 237.

[112] L. Pichon, T. Girardeau, A. Straboni, F. Lignou, P. Guerin, Applied Surface Science 150 (1999) 115.

[113] H.A. Jehn, Surf. Coat. Technol 131(2000) 433.

[114] R. Hubler, Surf. Coat. Technol 158 (2002) 680.

[115] Z.G. Zhang, O. Rapaud, N. Allain, D. Mercs, M. Baraket, C. Dong , C. Coddet, Applied Surface Science 255(2009) 4020.

[116] M. Nose, M. Zhou, E. Honbo, M. Yokota, S. Saji, Surf. Coat. Technol. 142 (2001)211.

[117] C. Mitterer, F. Holler, D. Reitberger, E. Badisch, M. Stoiber, C. Lugmair, R Nöbauer, Th Müller, R Kullmer, Surf. Coat. Technol 163-164 (2003) 716.

[118] J.A. Berr´ıos-Ort´ıza, J.G. La Barbera-Sosaa, D.G. Teerb, E.S. Puchi-Cabreraa, Surf. Coat. Technol. 179 (2004) 145.

[119] K.A. Gruss , T. Zheleva , R.F. Davis, T.R. Watkins, Surf. Coat. Technol .107 (1998) 115.

[120] E. Kelesoglu, C. Mitterer, M. U¨rgen, Surf. Coat. Technol. 160 (2002) 82.

[121]A. Ravi Shankar , B. Prabhakara Reddy , Vipin Chawla , M. Jeya Preyanga ,Ramesh Chandra , U. Kamachi Mudali, Surf. Coat. Technol. 204 (2010) 3214.

[122] Wen-Jun Chou, Ge-Ping Yu, Jia-Hong Huang, Surf. Coat. Technol. 167 (2003) 1.

[123] L. Hultman, Vacuum 57(2000) 1.

[124] A. Hörling, H. Ultman, M. Oden, J. Sjölén, L. Karlsson, J. Vac. Sci. Technol., A, Vac.Surf. Films 20 (2002) 1815.

[125] P.H. Mayrhofer, A. Hörling, L. Karlsson, J. Sjölén, T. Larsson, C. Mitterer,
L. Hultman, Appl. Phys. Lett. 83 (2003) 2049.

[126] S.H. Sheng, R.F. Zhang, S. Veprek, Acta Mater. 56 (2008) 968.

[127] B. Alling, A. Karimi, I.A. Abrikosov, Surf. Coat. Technol. 203 (2008) 883.

[128] H.W. Hugosson, H. H쪳gberg, M. Ahlgren, M. Rodmar, T.I. Selinder, J.Appl. Phys. 93 (2003) 4505.

[129] Holleck H. J Vac Sci Technol. A 4 (1986) 2661.

[130] Berg G, Friedrich C, Broszeit E, Berger C. In: Riedel R, editor. Handbook of ceramic hard materials. Weinheim: Wiley-VCH; (2000) 965.

[131] Li DJ. Sci Chin Ser E: Technol Sci 49 (2006) 576.

[132] Lamni R, Sanjine´s R, Parlinska-Wojtan M, Karimi A, Le´vy F. J Vac. Sci. Technol. A 23(4) (2005) 593.

[133]H. Klostermann, F. Fietzke, T. Modes and O. Zywitzki, Rev.adv. Mater. Sci. 15 (2007) 33.

[134] P. Holubar, M. Jilek and M. Sima, Surf. Coat.Technol. 133-134 (2000) 145.

[135] J. Patscheider, T. Zehnder and M. Disserens, Surf. Coat. Technol. 146-147 (2001) 201.

[136] Hillert M, Cohen M, Averbach BL. Acta Metall. 9 (1961)536.

[137] Ditchek B, Schwartz LH. Annu Rev Mater Sci. 9 (1979)219.

[138] Cahn JW, Hillard JE. J. Chem. Phys. 28 (1958) 258.

[139] Cahn JW. Acta Metall. 9 (1961)795.

[140] Cahn JW. Acta Metall. 11 (1963)1275.

[141] Cahn JW. Trans. Metall. Soc AIME 242 (1968)166.

[142] Cahn JW. Scand J. Metallurg. 20 (1991)9.

[143] Porter DA, Easterling KE. Phase Transformations in Metals and Alloys. 2nd ed. Cheltenham: Nelson Thornes; 2001.

[144] Alling B, Ruban AV, Karimi A, Peil OE, Simak SI, Hultman L, et al. Phys Rev B 75 (2007) 045123.

[145] Mayrhofer PH, Music D, Schneider JM. Appl. Phys. Lett. 88 (2006) 071922.

[146] Mayrhofer PH, Fischer FD, Bo¨hm HJ, Mitterer C, Schneider JM. Acta Mater 55 (2007) 1441.

[147] S.H. Sheng, R.F. Zhang, S. Veprek, Acta Materialia 56 (2008) 968.

[148] H. Holleck, Surf. Coat. Technol. 36 (1988) 151.

[149] Hugh O. Pierson, Handbook of Chemical Vapor Deposition (CVD)(Second Edition),Principles, Technology, and Applications © 1999 William Andrew Inc. ISBN: 978-0-8155-1432-9.

[150] Bowden F.P. and Tabor B. (1950) 'The Friction and Lubrication of Solids',the Friction and Lubrication of Solids, Clarendon Press, Oxford

[151] J.E. Mahan and A. Vantomme, J. Vac. Sci. Technol. A, 15 (1997) 1976.

[152] R.N. Tait, J. Vac. Sci. Technol. B, 16(1998) 1222.

[153] R.V. Stuart and G.K. Wehner, J. Appl. Phys., 35 (1964) 1819.

[154] R.V. Stuart and G.K. Wehner, Trans 9th National Vacuum Symp.. 160 (1963).

[155] M.J. Grapperhous, Z. Krivokapic and M. Kushner, J. Appl. Phys. 83, (1998) 35.

[156] A. Lousa, E. Martinez, J. Esteve, E. Pascual, Thin Solid Films 35-356 (1999) 210.

[157] A. Thobor, C. Rousselot, C. Clement, Jamal Takadoum, Nicolas Martin, Rosendo Sanjines, Francis Levy Surf. Coat. Technol. 124 (2000) 210.

[158] T. Migita, R. Kamei, T. Tanaka, K. Kawabata, Appl. Surf. Sci. 169-170 (2001) 362.

[159] J.F. Pierson, E. Tomasella, Ph. Bauer, Thin Solid Films 408 (2002) 26.

[160] E. Ribeiro, A. Malczyk, S. Carvalho, et al., Surf. Coat. Technol.151-152 (2002) 515.

[161] J.A. Thtnton and A.S. Penfold, Thin Film Processes, J. Vossen eds., Academic Press, New York, Chapters 2-3 (1978).

[162] D.B. Fraser, Thin Film Processes, J. Vossen eds. Academic Press, New York, Chapters 2-3 (1978).

[163] ] R.K. Waits, Thin Film Processes, J. Vossen eds. Academic Press, New York, Chapters 2-4 (1978).

[164] R.K. Waits, J. Vac. Sci. Technol., 15 (1978) 179.

[165] R.D. Arnell, P.J. Kelly, J.W. Bradley, Surf. Coat. Technol. 188 (2004) 158.

[166] Johan Bohlmark, Chris Christou, P. Arutiun, Ehiasarian, Ulf Helmersson, Jones Alami, J. Vac. Sci. Technol. A 23 (2005) 18.

[167] W. Somkhunthot, T. Burinprakhon, I. Thomas, T. Seetawan, V. Amornkitbamrung, Elektrika 9 (2007) 20.

[168] J.M. Schneider and W.D. Sproul, Handbook of Thin Film Process Technology.IOP, Bristol,A5. 1 (1995).

[169] H. Ohsaki, Y. Tachibana, J. Shimizu and T. Oyama, Thin Solid Films, 281-282, 213 (1996).

[170] W.M. Posadowski, Thin Solid Films, 343-344 (1999) 85.

[171] R.A. Sholl, Surf. Coat. Technol. 7 (1997) 93.

[172] P.I. Kelly, O.A. Abu-Zeid, R.D. Arnell and J.Tong, Surf. Coat. Technol. 86-87(1996) 28 .

[173] P. Frach, U. Heisig, C. Gottfried and H. Walde, Sur. Coat. Technol, 59(1993) 177.

[174] A. Belkind, A. Frelich and R. Scholl, J. Vac. Sci. Technol. A, 17, 1934 (199).

[175] D.R. Lide,ed. Handbook of Chemistry and Physics, 81st edition,CRC Press, Boca Raton, FL, 955-966 (2000).

[176] H. Akazawa and Y. Murata, Surf. Sci., 207, L971 (1989).

[177] K.S. Sree Harsha,Principle of Physical Vapour Deposition of Thin Films, (2006) ISBN: 978-0-08-044699-8 .

[178] T. Elangovan, P. Kuppusami, R. Thirumurugesan, V. Ganesan, E. Mohandas, D. Mangalaraj, Mater. Sci. Eng. B 167 (2010) 17.

[179] Materials R&D for Prototype Fast Breeder Reactor, Proceedings of the seminar, January 1-2, 2003, IGCAR, kalpakkam, Editors S.L. Mannan and M.D. Mathew.

[180] T. J. B. Holland, S. A. T. Redfern, J. Appl. Cryst. 30 (1997) 84.

[181] B.D. Cullity & S.R. Stock, Elements of X-Ray Diffraction, 3rd Ed., Prentice-Hall Inc., (2001) 167.

[182] P. Scherrer, Göttinger Nachrichten Gesell., 2 (1918) 98.

[183] J. D. James, J. A. Spittle, S.G. R. Brown, R. W. Evans, Meas. Sci. Technol. 12 (2001) R1-R15.

[184] M. A. White, Cryst. Eng. (1999) 273.

[185] E. Meyer, Prog. Surf. Sci. 41 (1992) 3.

[186] Nader Jalili, Karthik Lakxminarayana, Mechatronics 14 (2004) 907.

[187] G. Binnig, C. F. Quate and C. H. Gerber, Phy. Rev. Lett. 56 (6) (1986) 930.

[188] D. Shindo, K. Hiraga, “High-resolution Electron Microscopy for Material science” Springer publication (ISBN 4-431-70234-2).

[189] David J Smith, Rep. Prog. Phys. 60 (1997) 1513.

[190] Gwenael Gouadec, Philippe Colomban, Prog. Cryst. Growth Charact. Mater. 53 (2007) 1.

[191] “Introductory Raman spectroscopy” John R. Ferraro, Kazuo Nakamoto and Chris W. Brown, Elsevier Publication (2003), ISBN No: 978-0-12-254105-6.

[192] M. F. Doerner and W. D. Nix, J. Mater. Res. **1**, 601 (1986).

[193] J. L. Loubet, J. M. Georges, and G. Meille, ASTM STP 889, edited by P. J. Blau and B. R. Lawn (American Society for Testing and Materials, Philadelphia, PA, (1986) 72.

[194] P. Parakala, R. A. Mirshams, S. Nasrazadani, K. Lian. Department of Engineering Technology, University of North Texas, Denton, TX 76203

[195] C. Fischer-Cripps. Nanoindentation (New York, Springer, 2002) 1-9.

[196] W. C. Oliver and G. M. Pharr. Journal of Materials Research (1992) 1564.

[197]T.L. Oberle, Properties Influencing Wear of Metals, J. Metals 3 (1951) 438.

[198] Halling, Surface Films in Tribology, Tribologia 1 (2) (1982) 15.

[199] Matthews, Proceedings of the 1st Conference on Materials Engineering, The University of Leeds, UK, July 1984, Institution of Metallurgists,1984 p. 175, ISBN: 0-901-46224-1.

[200] Rebholz, A. Leyland, J.M. Schneider, A.A. Voevodin, A.Matthews, Surf. Coat.Technol. 120-121 (1999) 412.

[201] T.Y. Tsui, G.M. Pharr, W.C. Oliver, C.S. Bhatia, R.L. White, S. Anders, A. Anders, I. G. Brown: Mater. Res. Soc. Symp. Proc. (1995) 383.

[202] K.J. Hollis, Adv. Mater. Process. (November–December) (2010) 57.

[203] J. Csikai, Handbook of Fast Neutron Generators, CRC Press Inc., Boca Raton, Florida, 1987.

[204] C. Bonetti, Nucl. Instr. and Meth. 203 (1982) 595.

[205] G. Stengl, H. Vonach, Nucl. Instr. and Meth. 140 (1977) 197.

[206] J. Pivarc, Atomki Kazlem and nyek 18 (1976) 463.

[207] F.M. Bacon, R.J. Walko, D.F. Cowgill, A.A. Riedel, IEEE Trans. Nucl. Sci. NS-28 (2) (1981).

[208] D.W. Heikkinen, C.M. Logan, IEEE Trans. Nucl. Sci.NS-30 (2) (1983).

[209] K. Fiebiger, Z. Angew. Phys. 9 (1957) 213.

[210] O. Reifenschweiler, Philips Res. Rep. 16 (1961) 401.

[211] H.H. Barsfall, in: Proc. Int. Conf. on Fast Neutron Physics, May 26-31, 1986, Dubrovnik, 188.

[212] J.C. Crawford, W. Bauer, ANL-CTR-75 4 (1975) 227.

[213] B.M. Bahal, HU. Fanger, GKSS 82/E/22, Geesthacht,(1982).

[214] A. Pavlik, G. Winkler, INDC(AUS)-Oll/LI. IAEA, Vienna, (1986).

[215] K. Kudo, N. Takeda, Matiullah, A. Fukuda, S.M. Qaim (Ed), in: Proc. on Nuclear Data for Science and Technology, Springer, Berlin, (1992) 533.

[216] K. Kudo, T. Kinoshita, Fusion Eng. Des. 10 (1989) 145.

[217] M. Drosg, Nucl. Sci. Eng. 106 (1990) 279.

[218] J. Roth, R. Behrisch, W. Mijller, W. Ottenberger, Nucl. Fusion 30 (1990) 441.

[219] R. Weisbeck, J. Angew. Phys. 12 (1960) 34.

[220] D. Kamke, H. Kriiger, 2. Naturforsch. A 18 (1963) 52.

[221] S.M. Kabir , 1973, 109 , 533-536. IEEE NPSS (Toronto), UOIT, Oshawa, ON, 25 & 26 June, 2010 International Workshop on Real Time Measurement, Instrumentation & Control [RTMIC] 2-9

[222] M. Guillaume, G. Delfiore, G. Weber and M. Cuypers, 92 (1971) 571.

[223] M.T. Laugier, Thin Solid Films 76 (1981) 289.

[224] M.T. Laugier, Thin Solid Films 117 (1984) 243.

[225] J. Smolik, K. Zdunek, B. Larisch, Vacuum 55 (1999) 45.

[226] C. Padmaprabhu, P. Kuppusami, A. Singh, E. Mohandas, V.S. Raghunathan, Scripta Mater. 44 (2001) 1837.

[227] G.Balakrishnan, P. Kuppusami, S.Tripura Sundari, R.Thirumurugesan, V.Ganesan, E.Mohandas, D. Sastikumar, Thin Solid Films 518 (2010) 3898.

[228] Akash Singh, P.Kuppusami, N.Kumar, E.Mohandas and S.Dash, Surface Modification Technologies XXVI Edited by T. S. Sudarshan, Michel Jeandin and Vincent Fridrici( Publisher, Valardocs, 2013) (2013 ) 55.

[229] J.L. Loubet, J.M. Georges, O. Marchesini, G. Meille, ASME J. Tribol. 106 (1984) 43.

[230] Y.T. Pei, C.Q. Chen, K.P. Shaha, J.Th.M. De Hosson, J.W. Bradley, S.A. Voronin, M.Cada, Acta Mater. 56 (2008) 696.

[231] Y.T. Pei, K.P. Shaha, C.Q. Chen, R. van der Hulst, A.A. Turkin, D.I. Vainshtein, J.Th.M. De Hosson, Acta Mater. 57 (2009) 5156.

[232] P.J. Kelly, A.A. Onifade, Y. Zhou, G.C.B. Clarke, M. Audronis, J.W. Bradley, Plasma Processes Polym. 4 (2007) 246.

[233] Arup Dasgupta, P. Kuppusami, V.S. Falix Lawrence, P. Raghunathan, Premkumar S Antony, K.S. Nagaraja, Mater. Sci. Eng. A 374 (1–2) (2004) 362.

[234] J.A. Thornton, Ann. Rev. Mater. Sci. 7 (1977) 239.

[235] Arup Dasgupta, Akash Singh, Pradyumna Kumar Parida, P. Kuppusami, S. Saroja, M. Vijayalakshmi, Bull. Mater. Sci., 34 (2011) 483.

[236] T.H.K.Barron, Materials Park, OH: ASM International; 1998.

[237] Y. Kuru, M. Wohlschlögel, U. Welzel , E.J. Mittemeijer, Surf. Coat. Technol. 202 (2008) 2306.

[238] R. Daniel, D. Holec, M. Bartosik, J. Keckes, C. Mitterer, Acta Materialia 59 (2011) 6631.

[239] B. Bhushan, Handbook of micro/nanotribology. 2nd ed. Boca Raton (FL), CRC Press 1999.

[240] G.M. Pharr, Mater Sci Eng, A 253 (1998)151.

[241] S.E. Hsu, G.R. Edwards, J.C. Shyne, O.D. Sherby, J. Mater. Sci. 12 (1977) 131.

[242] F. Klocke, T. Krieg, Ann.CIRP 48 (2) (1999) 515.

[243] H.G. Prengel, W.R. Pfouts, A.T. Santhanam, Surf. Coat. Technol. 102 (1998) 183.

[244] E. Uhlmann, U. Lachmund, M. Brucher, Surf. Coat. Technol. 131 (2000) 395.

[245] N.M. Renevier, N. Lobiondo, V.C. Fox, D.G. Teer, J. Hampshire, Surf. Coat. Technol. 123 (2000) 84.

[246] C. Ducros, V. Benevent, F. Sanchette, Surf. Coat. Technol. 163–164 (2003) 681.

[247] W. Kalss, A. Reiter, V. Derflinger, C. Gey, J.L. Endrino, Int. J. Refract. Met. Hard Mater. 24 (5) (2006)399.

[248] D. Pilloud, A.S. Dehlinger, J.F. Pierson, A. Roman, L. Pichon, Surf. Coat. Technol. 174–175 (174) (2003) 338.

[249] A. Erdem, E. Sabri Kayali, C. Huseyin, Tribol. Int. 39 (2006) 297.

[250] E. Budke, J. Krempel-Hesse, H. Maidhof, H. Schussler, Surf. Coat. Technol. 112 (1999) 108.

[251] J. Ramos Henry, B. Valmoria Nicomedes, Vacuum 73 (2004) 549.

[252] G. Lopez, M.H. Staia, Surf. Coat. Technol. 200 (7) (2005) 2092.

[253] C. Brugnoni, F. Lanza, G. Macchi, R. Muler, E. Parnisari, M.F. Stroosnijder, Surf. Coat. Technol. 100–101 (1998) 23.

[254] E. Gariboldi, J. Mater.Process. Technol. 134 (3) (2003) 287.

[255] L.B. Jonsson, T. Nyberg, I. Katardjiev, S. Berg, Thin Solid Films 365 (2000) 43.

[256] D. Jianxin, L. Jianhua, Z. Jinlong, S. Wenlong, Int. J. Refract. Met. Hard Mater. 26 (2008) 164.

[257] M.A. Augera, J.J. Araiza, C. Falcony, O. Sfchez, J.M. Albella, Vacuum 81 (2007) 1462.

[258] Akash Singh, P. Kuppusami, R. Thirumurugesan, R. Ramaseshan, M. Kamruddin, S. Dash, V. Ganesan, E. Mohandas, Appl. Surf. Sci.257 (2011) 9909.

[259] Akash Singh, M. Geetha, N. Kumar, P. Kuppusami, R. Thirumurugesan, E. Mohandas, V. Kamaraj,Transactions of the Indian Institute of Metals 64 (2011 ) 37.

[260] C.P. Constable, J. Yarwood, W.D. Munz, , Surf. Coat. Technol 116–119 (1999) 155.

[261] I. Milošev, H.H. Strehblow, B. Navinšek, Thin Solid Films 303 (1997) 246.

[262] P. Prieto, L. Galán, J.M. Sanz, Surf. Interface Anal. 21 (1994) 395.

[263] D.I. Bazhanov, A.A. Knizhnik, A.A. Safonov, A.A. Bagatur'yants, M.W.Stoker, A.A. Korkin, J. Appl. Phys. 97 (2005) 044108.

[264] H. Höchst, R.D. Bringans, P. Steiner, Th. Wolf, Phys. Rev., B 25 (1982) 7183.

[265] I. Bertóti, Surf. Coat. Technol. 151–152 (2002) 194.

[266] M. Del Re, R. Gouttebaron, J.P. Dauchot, P. Leclère, G. Terwagne, M.Hecq, Surf. Coat. Technol. 174–175 (2003) 240.

[267] P. Prieto, P.L. Galán, J.M. Sanz, Phys. Rev. B 47 (1993) 1613.

[268] U. Bardi,G.A. Somorjai, P.N. Ross, J. Vac. Sci. Technol. A 1 (1983) 1213.

[269] M. Nagasaka, J. Vac. Sci. Technol. 13 (1976) 676.

[270] P. Kuppusami, H.Murakami and T. Ohmura, Surface Engineering 21 (1) (2005) 53.

[271] Akash Singh, N. Kumar, P. Kuppusami, T.N. Prasanthi, P. Chandramohan, S. Dash, M.P. Srinivasan, E. Mohandas, A.K. Tyagi, Wear 280–281(2012) 22.

[272] E. Torok, A.J. Perry, L. Chollet, W.D. Sproul, Thin Solid Films 153 (1987) 37.

[273] A. Erdemir, C. Bindal, G.R. Fenske, C. Zuikner, P. Wilbur, ICMCTF96 Conf., 22–26 April, San Diego, 1996.

[274] Y.M. Kim, Y.M. Chung, M.J. Jung, J. Musil, J.G. Han, Surf. Coat. Technol. 200 (2005) 835.

[275] Z.G. Xiao, T.D. Mantei, Surf. Coat. Technol. 177–178 (177) (2004)389.

[276] A.N. Christensen, O.W. Dietrich, W. Kress, W.D. Teuchert, Phys. Rev., B 19 (1979) 5699.

[277] A. Cassinese, M. Iavarone, R. Vaglio, M. Grimsditch, S. Uran, Phys. Rev., B 62 (2000) 13915.

[278] C. Moura , P. Carvalho, F. Vaz, L. Cunha , E. Alves, Thin Solid Films 515 (2006) 1132–1137.

[279] H. Liu, Q. Xue, Wear 201 (1996) 51.

[280] LUO, Quanshun (2013) Tribofilms in solid lubricants. In: Encyclopedia of Tribology.Springer. ISBN 9780387928968 (In Press).

[281] K. Kato, Tribology of Ceramics, Wear 136 (1990) 117.

[282] M.I. Pashechko, K.S. Lenik, Wear 267 (2009) 1301.

[283] R. Sanjinés, C.S. Sandu, R. Lamni, F. Lévy, Surf. Coat. Technol. 200 (2006) 6308.

[284] S. Wilson, A.T. Alpas, Surf. Coat. Technol. 86–87 (1996)75.

[285] M.L. Mc Connell, D.P. Dowling, N. Donnelly, K. Donnelly, R.V.Flood, Surf. Coat. Technol. 116–119 (1999)1133.

[286] W. Fang, J.A. Wickert, J. Micromech.Microeng. 6 (1996) 301.

[287] M.B. David, V.M. Bright, Proc. SPIE, Micromachined Devices and Components III Austin, TX, Sept 3224 (1997) 296.

[288]] J.W. Suh, S.F. Glander, R.B. Darling, C.W. Storment, G.T.A.Kovacs, , Sens. Actuators, A 58 (1997) 51.

[289] R.V. Jones, Recording optical lever, J. Sci. Instrum. 36 (1959) 90.

[290] J.M. Shapiro, D.R. Taylor, G.M. Graham, Can. J. Phys. 42 (1964) 835.

[291] R.E. Kinzly, Appl. Opt. 6 (1967) 137.

[292] S.F. Jacobs, J.N. Bradford, J.W. Berthold III, Appl. Opt. 9 (1970) 2477.

[293] D.N. Batchelder, R.O. Simmons J. Chem. Phys.41 (1964) 2324.

[294] D.N. Batchelder, R.O. Simmons, J. Appl.Phys. 36 (1965) 2864.

[295] L.H. Van Vlack, Elements of Materials Science and Engineering,Addison-Wesley, Reading, MA, 1989.

[296] E. Ruhala, Nucl. Inst. Meth. B 12 (1985) 447.

[297] http://home.rzg.mpg.de/~mam/.

[298] THK Barron, Generalized theory of thermal expansion of solids. In: Ho CY, Taylor RE, editors. Thermal expansion of solids. Materials Park, OH: ASM International; 1998.

[299] M.Kiguchi , T. Yokoyama , D. Matsumura , H. Kondoh , O. Endo, T. Ohta Phys Rev 2000; B61:14020.

[300] Chen YY, Vao YD, Lin BT, Suo CT, Shui SG, Lin HM. Nanostruct. Mater. 6(1995) 997.

[301] E.O. Hall, Proc. Phys. Soc. Sect. B 64 (1951) 747.

[302] N.J. Petch, J. Iron Steel Inst. 174 (1953).

[303] C.E. Carlton, P.J. Ferreira, Acta Materialia 55 (2007) 3749.

[304] P.H. Mayrhofer, G. Tischler, C. Mitterer, Surf. Coat. Technol. 142-144 (2001) 78.

[305] H.M. Tung, J.H. Huang, D.G. Tsai, C.F. Ai, G.P. Yu, Mater. Sci.Eng. A 500 (2009) 104.

[306] R.W. Siegel, G.E. Fougere, Nanostruct. Mater. 6 (1995) 205.

[307] J. Schiotz, F.D. Di Tolla, K.W. Jacobsen, Nature 391 (1998) 561.

[308] P.H. Mayrhofer, C. Mitterer, L. Hultman, H. Clemens, Prog. Mater. Sci.51 (2006) 1032.

[309] G. López, M. Staia, Surf. Coat. Technol. 200 (2005) 2092.

[310] G. Fontalvo, C. Mitterer, Wear 258 (2005) 1491.

[311] T. Weirather, K. Kutschej, D. Caliskanoglu, R. Cremer, W. Kölker, J. Kohlscheen, C.Mitterer, in: P. Beiss, C. Broeckmann, S. Franke, B. Keysselitz (Eds.), Proceedings of the 8th International Tooling Conference, 2, RWTH Aachen University, Germany, (2009) 881.

[312] R. Franz, C. Mitterer, M. Lechthaler, C. Polzer, J. Vac. Sci. Technol. A 28 (2010) 528.

# List of Publications:

## 1. Publication from the Present Work

### Journal Publications:

[1] A Comparative wear study of sputtered ZrN coatings on Si substrate, **Akash Singh**, M. Geetha, N. Kumar, P. Kuppusami, R. Thirumurugesan, E. Mohandas, V. Kamaraj, ***Transactions of the Indian Institute of Metals*** 64 (2011 )37.

[2] Study of microstructure and nanomechanical properties of zr films prepared by pulsed magnetron sputtering, **Akash Singh**, P. Kuppusami, R. Thirumurugesan, R. Ramaseshan, M. Kamruddin, S. Dash, V. Ganesan and E. Mohandas , ***Applied Surface Science*** 257 (2011) 9909.

[3] Tribological properties of sputter deposited ZrN coatings on titanium modified austenitic stainless steel, **Akash Singh**, N. Kumar, P. Kuppusami, T.N. Prashanthi, P.Chandramohan, S. Dash, M. P. Srinivasan, E. Mohandas and A . K. Tyagi, ***Wear*** 280-281 (2012 ) 22.

[4] Influence of nitrogen flow rate on microstructural and nanomechanical properties of Zr-N thin films prepared by pulsed magnetron sputtering, **Akash Singh**, P. Kuppusami, Shabana Khan, C. Sudha, R. Thirumurugesan, R. Ramaseshan, R. Divakar, E. Mohandas and S. Das, ***Applied Surface Science*** 280 (2013 )117.

[5] Characterisation of ZrAl and ZrAlN thin films prepared by pulsed DC magnetron sputtering, **Akash Singh**, P. Kuppusami, R. Thirumurugesan, R. Ramaseshan, S. Dash and E. Mohandas, ***Transactions of the Indian Institute of Metals*** 66 (2013 ) 363.

[6] Studies of microstructural and nanomechanical properties of ZrAlN thin films prepared by pulsed magnetron sputtering, **Akash Singh**, P. Kuppusami, R. Thirumurugesan, R. Ramaseshan, E. Mohandas and S. Das ( To be communicated to *Surface and Coatings Technology*).

[7] High temperature x-ray diffraction studies of Zr based thin films prepared by magnetron sputtering, **Akash Singh**, P. Kuppusami, R. Thirumurugesan, E. Mohandas (To be communicated to *Journal of Alloys and Compounds*).

## Conference Proceedings

[1] Synthesis and properties of Zr based coatings, **Akash Singh**, P. Kuppusami, N. Kumar, E. Mohandas and S. Dash In Surface Modification Technologies XXVI, (Eds.) T.S. Sudarshan, Michel Jeandin and Vincent Fridrici( Publisher, Valardocs, 2013) (2013 ) 55-63.

## 2. Publication Outside the Present Work

[1] Effect of substrate temperature and oxygen partial pressure on microstructure and optical properties of pulsed laser deposited yttrium oxide thin films, Maneesha Mishra, P. Kuppusami, T.N. Sairam, **Akash Singh**, E. Mohandas ***Applied Surface Science*** 257 (2011 ) 7665.

[2] Electron Microscopy Study of Interface Structure of Titanium Coating on Copper Substrates,Arup Dasgupta, **Akash Singh**, Pradyumna Kumar Parida, R. Ramasehan, P. Kuppusami,S .Saroja, M. Vijayalakshmi, ***Bulletin of Material Science*** 34 (2011 ) 483.

[3] Phase evolution in zirconia thin films prepared by pulsed laser deposition, Maneesha Mishra, P. Kuppusami, **Akash Singh**, S. Ramya and V. Sivasubramanian, E. Mohandas, ***Applied Surface Science*** 258 (2012 ) 5157.

[4] Microstructural characterisation of $ZrO_2/Y_2O_3$ multilayer prepared by pulsed laser deposition, Maneesha Mishra, P. Kuppusami, V. R. Reddy, **Akash Singh**, G. Chinnamma, Chanchal Ghosh, R. Divakar, E. Mohandas, ***Nanoscience Letters*** 3 (2013 ) 4.1.